



HAL
open science

Experimental characterization of PWR fuel assemblies mechanical behavior under hydrodynamic and seismic-like loads

Lorenzo Longo

► **To cite this version:**

Lorenzo Longo. Experimental characterization of PWR fuel assemblies mechanical behavior under hydrodynamic and seismic-like loads. Solid mechanics [physics.class-ph]. Ecole Centrale Marseille, 2023. English. NNT : 2023ECDM0002 . tel-04578317

HAL Id: tel-04578317

<https://theses.hal.science/tel-04578317>

Submitted on 16 May 2024

HAL is a multi-disciplinary open access archive for the deposit and dissemination of scientific research documents, whether they are published or not. The documents may come from teaching and research institutions in France or abroad, or from public or private research centers.

L'archive ouverte pluridisciplinaire **HAL**, est destinée au dépôt et à la diffusion de documents scientifiques de niveau recherche, publiés ou non, émanant des établissements d'enseignement et de recherche français ou étrangers, des laboratoires publics ou privés.



ÉCOLE DOCTORALE 353: SCIENCE POUR L'INGÉNIEUR: MÉCANIQUE, PHYSIQUE, MICRO ET NANOÉLECTRONIQUE

IRPHE - INSTITUT DE RECHERCHE SUR LES PHÉNOMÈNES HORS EQUILIBRE

LMA - LABORATOIRE DE MÉCANIQUE ET D'ACOUSTIQUE

CEA CADARACHE - IRESNE/DTN/STCP - LABORATOIRE D'ESSAIS THERMOHYDRAULIQUES ET HYDROMÉCANIQUES

THÈSE

POUR OBTENIR LE GRADE DE
DOCTEUR DE L'ÉCOLE CENTRALE MÉDITERRANÉE
SPÉCIALITÉ : MÉCANIQUE DES SOLIDES
PRÉSENTÉE ET SOUTENUE PUBLIQUEMENT
PAR

LORENZO LONGO

LE 21 JUIN 2023

EXPERIMENTAL CHARACTERIZATION OF PWR FUEL ASSEMBLIES MECHANICAL BEHAVIOR UNDER HYDRODYNAMIC AND SEISMIC-LIKE LOADS

**Caractérisation expérimentale du comportement mécanique
des assemblages de combustible REP sous charges hydrodynamiques
et sismiques**

DEVANT LE JURY COMPOSÉ PAR:

J. DEGROOTE	Professeur, Ghent University, Gent	Président
A. CAMMI	Professeur Associé, Politecnico di Milano, Milan	Rapporteur
P. MOUSSOU	Ingénieur Chercheur, EDF, Saclay	Rapporteur
P. BARDET	Professeur, GWU, Washington DC	Examineur
M. PUSCAS	Ingénieure Chercheure, CEA, Saclay	Examinatrice
C. ELOY	Professeur, ECM, Marseille	Directeur
G. RICCIARDI	Ingénieur Chercheur, CEA, Cadarache	Co-Directeur
E. SARROUY	Maitresse de Conférence, ECM, Marseille	Superviseure
R. CAPANNA	Professeur Chercheur, GWU, Washington DC	Invité

Acknowledgement

My first thoughts are for my supervisors and directors. Thank you, Emmanuelle and Christophe, for your guidance, your help and for sharing your knowledge. Thank you, Guillaume, for your daily support and teachings, from the most practical and professional to the most scientific. Thank you, Philippe, for welcoming me in your laboratory and for allowing me to expand the boundaries of this project even further, both geographically and scientifically. Thank you, Roberto, you have opened the doors of research for me since my internship and you have been an example to me as a PhD student first and then as a researcher. Thanks to all of you for giving me the tools and time to complete this journey and for trying to set me straight: definitely not an easy job.

If I have achieved this title, it is also thanks to all the members of the jury, who agreed to review my work, correct it when necessary, and stimulate my curiosity even more with their comments and questions. Thank you, Dr. Puscas, thank you Prof. Cammi, thank you Prof. Degroote and thank you Dr. Moussou.

Thank you to the laboratories that welcomed me, LTHC first and LETH later, to all my colleagues, especially the young researchers and the members of the Guinguette, my companions in frustrations and satisfactions. Thanks to Kevin, comrade in the office and in the lab, and thanks to my two interns, Nathan and Hugo. Thank you for your excellent work that has contributed to the construction of this document.

As usual, I won't bother to make a list of all the people who have stood by me during these years, if you are reading this acknowledgement, it means that you care and you have cared about our friendship and so feel thanked, you will certainly have helped me, even unconsciously. I hope I can be of the same help to you.

I would like to close with a quote from one of my favorite musical groups, taken from the song *Ma che film la vita* by *Nomadi*, for which, however, I need to separately thank all my family and in particular my brother Alberto, for the peaceful and fun moments.

Grazie a mia madre per avermi messo al mondo, a mio padre semplice e profondo, grazie agli amici ed alla loro comprensione, ai giorni felici della mia generazione, grazie alle ragazze, a tutte le ragazze.

Contents

Abstract	XII
Resumé	XIV
Introduction	1
1 General context	4
1.1 Pressurized Water Reactor	4
1.2 FSI issues in reactor core	7
1.3 Numerical models for fuel assemblies	10
1.4 Experimental facilities for fuel assemblies FSI	11
1.5 Conclusion	16
2 Keulegan-Carpenter Instabilities for a Rod-Bundle	17
2.1 Introduction	18
2.1.1 Single cylinder	19
2.1.2 Cylinder array	21
2.2 Experimental methods	22
2.2.1 Particle Image Velocimetry	22
2.2.2 Shaking Bundle Facility	24
2.2.3 Data acquisition and processing	25
2.3 Results	30
2.3.1 Synchronization method	31
2.3.2 Results on FOV1: Intraline plane	36
2.3.3 Results on FOV2: Interline plane	41
2.4 Discussion	47
2.5 Conclusions	50

3	Drag coefficient estimation in FSI for PWR fuel assembly bowing	51
3.1	Introduction	53
3.2	Experimental methods	54
3.2.1	Eudore	56
3.2.2	Force measurements	57
3.2.3	Laser Doppler Velocimetry	59
3.3	Experimental results	63
3.3.1	Force	63
3.3.2	Velocity	67
3.4	Analytical model and identification of coefficients	71
3.4.1	Line load model	73
3.4.2	Displacement field under line load u_1 and punctual force u_2	73
3.4.3	Resolution: finding c_N from measurements	74
3.5	Porous Medium Approach	75
3.6	FSCORE numerical resolution	78
3.6.1	Comparison of experimental and numerical results	79
3.7	Conclusions	81
4	Assembly vibrations under seismic-like load	84
4.1	Introduction	85
4.2	Eudore configuration for dynamical experiment	88
4.3	Experimental results and discussion	91
4.4	Numerical model for the Dynamic experiments	98
4.5	Comparison of experimental and numerical results	101
4.6	Conclusions and perspectives	105
5	General conclusion	108
	Nomenclature	110
	Bibliography	113
A	KC threshold for Dynamic experiments	122
A.1	Introduction	122
A.2	Geometrical considerations on Keulegan-Carpenter definition for rod-bundle	123
A.3	Dynamic experiments in stagnant water	124
B	Sensitivity analysis for static simulations	127
C	More results from SBF	130
D	LDV extrapolation	142
E	More results from Eudore Dynamic experiments	144

List of Figures

1.1	PWR vessel internal schematic view (a) and PWR fuel assembly schematic view [USNRC, 2012].	5
1.2	Section of a spacer grid (a) and unit spacer grid set (b). Springs and dimples keep the fuel rods in position [Shin et al., 2008].	6
1.3	Example of assembly bow measurements at Ringhals 3 and Ringhals 4.	8
1.4	Grid broken by fretting (a) [Spykman and Pattberg, 2014] and grid deformation reproduced in lab test (b) [Yvon et al., 2005].	8
1.5	Grafical representation of in-reactor fuel assemblies bow influencing mechanisms. [Wanninger, 2018].	9
1.6	Porous medium approach by Ricciardi et al. [2009a].	12
2.1	TB90 map	20
2.2	PIV scheme. Figure from Raffel et al. [2018]	23
2.3	Shaking Bundle Facility	24
2.4	Flying PIV setup.	26
2.5	PIV measurement on SBF	26
2.6	Fields of view: a) Intraline, left wall and 3 rods are visible; b) Interline, only left wall is visible.	28
2.7	2D velocity fields for a) Intraline and b) Interline; Bypass and Gap lines identifies the domain of analysis.	29
2.8	Synchronisation of assembly velocity signal for $K = 0.82$, $K = 1.13$ and $K = 1.50$ on Intraline (Cases 7, 8 and 9).	31
2.9	Vertical lines on FOV2 Interline.	32
2.10	Axial and Cross velocities behaviour on Bypass lines for $K = 0.82$ (a, d), $K = 1.13$ (b, e) and $K = 1.50$ (c, f). Bundle velocity is dimensionless.	33
2.11	Superposition of Intraline and Interline for cross and axial velocities for Bypass line 1. Bundle velocity is dimensionless.	34

2.12	Superposition cross and axial velocities for Bypass line 3 for Intraline and Interline. Bundle velocity is dimensionless.	35
2.13	Initial transient for Case 9 ($K = 1.50$) on FOV Intraline.	36
2.14	Time evolution of 3 full amplitude oscillations for case 9 ($K = 1.50$) on FOV Intraline.	37
2.15	Spatial PSD evolution	38
2.16	Spatial spectral analysis at full amplitude oscillation for 10 cycles. a) σ of spatial PSD coefficients for Case 7 ($K = 1.50$), both velocities, 1 st Gap line. b) σ 4 th spatial PSD coefficient vs K number.	39
2.17	4 th spatial PSD coefficient evolution for axial and cross velocities.	40
2.18	Comparison of axial (b, c, d) and cross (f, g, h) velocities for different K	41
2.19	Time evolution of 3 complete amplitude oscillations for Case 11 ($K = 1.13$) on FOV Interline.	42
2.20	Time evolution of three full amplitude oscillations for Case 11 ($K = 1.13$) on FOV Interline.	43
2.21	Initial transient for Case 12 ($K = 1.50$) on FOV Interline.	44
2.22	Time evolution of 3 complete full amplitude oscillations for Case 12 ($K = 1.50$) on FOV Interline.	45
2.23	Evolution of average velocities on 1 st gap line for $K = 0.82$ (a, d), $K = 1.13$ (b, e) and $K = 1.50$ (c, f). Axial velocities (a, b, c) and cross velocities (d, e, f).	46
3.1	Eudore experimental facility: a) picture, b) 3D model.	55
3.2	Eudore test section configuration for Static experiments: (a) Vertical section. (b) Cross-section at the 3rd grid level; plus and minus arrows indicate the reference system of the sensors.	57
3.3	LCP configuration	58
3.4	Lateral toolbox on Eudore.	58
3.5	Manholes and toolboxes.	60
3.6	Backscattered LDV scheme.	61
3.7	LDV measurement on Eudore.	62
3.8	LDV measurement points on Eudore	62
3.9	flow-rate and displacement raw data for each experiment on Eudore.	63
3.10	Force data for each experiment on Eudore.	64
3.11	Assembly hysteresis phenomena. Displacement (x axis) vs Force (y axis). Plot from Clément [2014].	65
3.12	Comparison of campaigns 3 and 4, opposite assemblies.	66
3.13	Force results for Campaign 3. Force value per assembly versus flow-rate with absolute errors and relative errors versus flow-rate.	66
3.14	Force results for Campaign 4. Force value per assembly versus flow-rate with absolute errors and relative errors versus flow-rate.	67

3.15	Measured axial velocity profiles [m/s] on planes A (a) and B (b). Blue circles represent the LCP diaphragms.	68
3.16	Axial velocity profile 3D reconstruction on plane A	69
3.17	Axial velocity profile 3D reconstruction on plane B	70
3.18	Axial and Transverse flow rates model.	71
3.19	Axial velocity v and cross velocity u profiles estimation in Eudore for each assembly.	72
3.20	Graphic model for 1 assembly with the transversal line load f indicated. . .	72
3.21	Simulation with FSCORE for a line of 3 Eudore-like assemblies.	78
3.22	Simulated data	79
3.23	Axial velocity profiles [m/s] measured and simulated with homogeneous $c_N = 0.66$	80
3.24	Numerical simulation of velocity fields $V_y(x, y)$ (a) and $V_x(x, y)$ (b) for a 172 m^3/h flow and $c_N = 0.66$	81
3.25	Comparison of force values from simulations and experiments for two different sets of c_N values: left column (a,c,e) separate values for each assembly; right column (b,d,f) identical average value for all assemblies.	82
4.1	Structural characteristics of Eudore assemblies in Icare facility.	87
4.2	Eudore test section configuration for Dynamic experiments: (a) Vertical section. (b) Cross-section at the 3rd grid level.	88
4.3	Control-command software for Dynamic experiments.	89
4.4	Force sensor in Dynamic experiment configuration	90
4.5	Displacement data example for dynamic experiments. Experiment at 5 Hz and 305.5 m^3/h . Left is the displacement for the third grid of the left assembly, Right is the displacement for the third grid of the right assembly.	91
4.6	Displacements and impact forces for left and right assemblies solicited at 5 Hz with a flowrate of 114.5 m^3/h and different amplitudes for LCP.	92
4.7	Impact forces and displacement variations with amplitude and flow-rates at 5 Hz.	94
4.8	Impact forces for left and right assemblies at 4 and 5 Hz with a flow-rate of 114.5 m^3/h for different LCP amplitudes.	95
4.9	Impact forces for left and right assemblies at 4 and 5 Hz in air.	97
4.10	Fuel assembly seen as an equivalent porous beam [Faucher et al., 2021].	99
4.11	Transfer function of Eudore fuel assembly [Faucher et al., 2021].	102
4.12	Numerical and experimental values for displacements and impact forces for assemblies solicited at 5 Hz with a flowrate of 114.5 m^3/h and different LCP amplitudes.	103
4.13	Impact forces and displacement variations with amplitude and flow-rates at 5 Hz.	104

4.14	Numerical and experimental values of impact forces for left and right assemblies at 5 Hz with a flow-rate of 114.5 m ³ /h.	105
4.15	Data acquisition software for Dynamic and Static experiments.	106
A.1	Averaged l	123
A.2	Comparison Left and Right assemblies displacement in stagnant water at different LCP amplitudes.	124
A.3	Impact forces for Left assembly in stagnant water.	125
A.4	Zoom on impact forces for Left assembly in stagnant water.	126
B.1	Simulated data for different c_T ,	127
B.2	Simulated velocity field on Eudore for different penalty coefficients.	128
B.3	Forces on 3 rd grid for different flow-rates and c_N	128
B.4	Simulated data for different panalty coefficient ρ	129
C.1	Case 14, $K = 2.07$ Intraline evolution.	131
C.2	Case 8, $K = 1.13$ Intraline evolution.	132
C.3	Case 7, $K = 0.82$ Intraline evolution.	133
C.4	PSD for case 7 ($K = 0.82$) and 8 ($K = 1.13$) Intraline at steady state.	134
C.5	Standard deviation for 2 nd (a) and 3 rd (b) coefficients.	135
C.6	1 st Coefficient evolution for axial and cross velocities.	136
C.7	2 nd Coefficient evolution for axial and cross velocities.	137
C.8	3 rd Coefficient evolution for axial and cross velocities.	138
C.9	Other coefficients.	138
C.10	Case 11 ($K = 1.13$), Interline evolution.	139
C.11	Other Interline results.	140
C.12	Superposition of Intraline and Interline averaged velocities for 2 nd bypass line for $K = 0.82$, $K = 1.13$ and $K = 1.50$	141
D.1	Polynomial extrapolation of different orders	143
E.1	Force vs amplitudes for Left and Right for 4 and 5 Hz, experimental.	145
E.2	Displacement vs amplitudes for Left and Right for 4 and 5 Hz, experimental.	146
E.3	Comparison simulations and experiments in air for 4 and 5 Hz, experimental.	147
E.4	Comparison simulations and experiments at 114.5 m ³ /h at 5 Hz.	148
E.5	Comparison simulations and experiments at 114.5 m ³ /h at 4 Hz.	148
E.6	Comparison simulations and experiments at 194.5 m ³ /h at 5 Hz.	149
E.7	Comparison simulations and experiments at 194.5 m ³ /h at 4 Hz.	150
E.8	Comparison simulations and experiments at 240.5 m ³ /h at 5 Hz.	151
E.9	Comparison simulations and experiments at 240.5 m ³ /h at 4 Hz.	152
E.10	Comparison simulations and experiments at 305.5 m ³ /h at 5 Hz.	153
E.11	Comparison simulations and experiments at 305.5 m ³ /h at 4 Hz.	154

E.12 Impact forces in air for different amplitudes for Left and Right for 4 and 5 Hz, experimental.	154
E.13 Impact forces at 114.5 m ³ /h for different amplitudes for Left and Right for 4 and 5 Hz, experimental.	155
E.14 Impact forces at 194.5 m ³ /h for different amplitudes for Left and Right for 4 and 5 Hz, experimental.	156
E.15 Impact forces at 240.5 m ³ /h for different amplitudes for Left and Right for 4 and 5 Hz, experimental.	157
E.16 Impact forces at 305.5 m ³ /h for different amplitudes for Left and Right for 4 and 5 Hz, experimental.	158

List of Tables

1.1	Properties of the experimental facilities	15
2.1	Experimental matrix: input parameters	27
2.2	Keulegan-Carpenter numbers	30
2.3	Threshold Keulegan-Carpenter	49
2.4	Parameters for K_{em} calculations	49
3.1	Diaphragm sizes per assembly.	57
3.2	c_N values evaluated for left and central assemblies.	74
3.3	Data differences between simulations and experiments.	81
4.1	Flow-rate conditions for dynamical experiments	89
4.2	Number of impact peaks per LCP amplitude at 5 Hz and $114.5 \text{ m}^3/\text{h}$	96
4.3	Force peaks at 4 Hz for different flow-rates	98
4.4	Force peaks at 5 Hz for different flow-rates	98
4.5	Coefficient for the fluid-structure coupling	102
4.6	Gaps value for numerical simulations	102
A.1	SBF mean critical Keulegan Carpenter number	124
A.2	SBF mean critical Keulegan Carpenter number	125
E.1	Force peaks at 4 Hz	144
E.2	Force peaks at 5 Hz	145
E.3	Displacement in Air , 5 Hz [mm]	145
E.4	Displacement in Air , 4 Hz [mm]	146
E.5	Displacement in $114.5 \text{ m}^3/\text{h}$, 5 Hz [mm]	146
E.6	Displacement in $114.5 \text{ m}^3/\text{h}$, 4 Hz [mm]	146
E.7	Displacement in $194.5 \text{ m}^3/\text{h}$, 5 Hz [mm]	147
E.8	Displacement in $194.5 \text{ m}^3/\text{h}$, 4 Hz [mm]	147

E.9 Displacement in $240.5m^3/h$, 5 Hz [mm]	149
E.10 Displacement in $240.5m^3/h$, 4 Hz [mm]	150
E.11 Displacement in $305.5m^3/h$, 5 Hz [mm]	150
E.12 Displacement in $305.5m^3/h$, 4 Hz [mm]	150

Abstract

Nuclear fuel assemblies in Pressurized Water Reactor (PWR) core are immersed in an axial flow. This flow exerts a hydrodynamic load on the assemblies, and it is responsible for their coupling and vibrations. Furthermore, during an earthquake or a LOCA event (Loss Of Coolant Accident), fuel assemblies are subjected to strong oscillation amplitudes. The hydrodynamic load can deform the assemblies, generating assembly bow, while stronger oscillations, such in a seismic event, can be responsible for assemblies impacts. In order to ensure the reactor core integrity and safety, nuclear industries want to improve the phenomenological knowledge of fluid-structure interactions inside a PWR core. Thus, engineers need numerical models for mechanical behavior of fuel assemblies and experimental campaigns to validate them and define their limits.

The study presented in this document is mainly divided in three experimental campaigns and aim to investigate: the assembly oscillation effects in fluid at rest, the drag phenomena on steady state fuel assemblies under a flow and the assemblies oscillations behavior when immersed in a flow. Two experimental facilities are used: SBF (Shaking Bundle Facility) and Eudore. SBF hosts one full-height surrogate assembly under axial flow on a vibrating table. By using optical technique, the velocity field of the fluid and assembly motion can be measured. Eudore facility uses three reduced assemblies in line, under axial flow with the possibility of applying seismic excitation to the entire test section. The instrumentation developed on Eudore makes it possible to measure the displacements of the assemblies, velocity field of the fluid and the impact forces.

The experiments performed on Eudore are simulated with a numerical calculation tool developed at CEA, named FSCORE, based on a porous medium approach. This approach provides access to an equivalent fluid model and an equivalent structure model defined over the entire domain from the spatial integration of local equations. The equations of motion of the equivalent fluid and of the equivalent structure are established separately, to provide a coupled model taking into account the contacts between assemblies.

With the help of an analytical model, the experimental results obtained on Eudore are used to retrieve the drag coefficient present in FSCORE. Experimental and numerical

results are widely discussed and show good agreement.

Keywords: Fluid-structure interactions, Assembly bowing, Assemblies vibrations, Keulegan-Carpenter, PWR.

Resumé

Les assemblages de combustible nucléaire dans le cœur d'un réacteur à eau pressurisée (REP) sont immergés dans un écoulement axial. Cet écoulement exerce une charge hydrodynamique sur les assemblages et est responsable de leur couplage et de leurs vibrations. De plus, lors d'un tremblement de terre ou d'un événement LOCA (Loss Of Coolant Accident), les assemblages de combustible sont soumis à de fortes oscillations. La charge hydrodynamique peut déformer les assemblages, générant une déformation arquée, tandis que des oscillations plus fortes, comme lors d'un événement sismique, peuvent être à l'origine d'impacts sur les assemblages. Afin de garantir l'intégrité et la sûreté du cœur du réacteur, les industries nucléaires souhaitent améliorer la connaissance phénoménologique des interactions fluide-structure à l'intérieur du cœur d'un réacteur à eau pressurisée. Les ingénieurs ont donc besoin de modèles numériques pour le comportement mécanique et de campagnes expérimentales pour les valider et définir leurs limites.

L'étude présentée dans ce document est principalement divisée en trois campagnes expérimentales visant à étudier : les effets d'oscillation de l'assemblage dans un fluide au repos, les phénomènes de traînée sur les assemblages de combustible en régime permanent sous un écoulement et le comportement des oscillations des assemblages lorsqu'ils sont immergés dans un écoulement. Deux installations expérimentales sont utilisées : SBF (Shaking Bundle Facility) et Eudore. SBF accueille un assemblage fictif de pleine hauteur soumis à un écoulement axial sur une table vibrante. Grâce à des techniques optiques, le champ de vitesse du fluide et le mouvement de l'assemblage peuvent être mesurés. L'installation Eudore utilise trois assemblages réduits en ligne, soumis à un écoulement axial, avec la possibilité d'appliquer une excitation sismique à l'ensemble de la section d'essai. L'instrumentation développée sur Eudore permet de mesurer les déplacements des assemblages, le champ de vitesse du fluide et les forces d'impact.

Les expériences réalisées sur Eudore sont simulées à l'aide d'un outil de calcul numérique développé au CEA, nommé FSCORE, basé sur une approche en milieu poreux. Cette approche permet d'accéder à un modèle de fluide équivalent et à un modèle de structure équivalent définis sur l'ensemble du domaine à partir de l'intégration spatiale d'équations

locales. Les équations de mouvement du fluide équivalent et de la structure équivalente sont établies séparément, pour fournir un modèle couplé fluide-structure prenant en compte les contacts entre les assemblages.

A l'aide d'un modèle analytique, les résultats expérimentaux obtenus sur Eudore sont utilisés pour retrouver le coefficient de traînée présent dans FSCORE. Les résultats expérimentaux et numériques sont largement discutés et montrent un bon accord.

Mots clés : Interactions fluide-structure, Déformation de l'assemblage, Vibrations des assemblages, Keulegan-Carpenter, REP.

Introduction

The present thesis describes the objectives, the operational steps and the results of my PhD project. I have conducted this research work in the period October 2019 - April 2023 mainly at CEA in France and in collaboration with three university laboratories: IRPHE¹ and LMA² of Ecole Centrale Marseille and Thermo-Fluids Lab³ of George Washington University. The CEA is the french Alternative Energies and Atomic Energy Commission, *Commissariat à l'énergie atomique et aux énergies alternatives*⁴. This project has been conducted in Cadarache at the Thermohydraulic and Hydromechanical Testing Laboratory (*Laboratoire d'Essais Thermohydrauliques et Hydromécaniques*). The PhD work that will be presented in the next pages is set in the framework of a joint project, ASSEMBLAGE, between CEA, EDF⁵ and FRAMATOME⁶.

The investigation concerns fluid-structure interaction (FSI) for rod-bundles immersed in a flow, in particular nuclear fuel assemblies. Fuel assemblies are structured group of fuel rods which are long and slender tubes containing pellets of fissionable material. Spacer grids are utilized to bundle the fuel rods in square configuration to form an assembly. The position of the rods into the grids is ensured by springs and dimples. Therefore, fuel assemblies are characterized by a complex geometry and with a highly non-linear mechanical behavior. A PWR (Pressurize Water Reactor) core contains hundreds of fuel assemblies (from 157 for a 900 MW up to 241 for a 1650 MW). The fuel assemblies are disposed side by side in a cylinder array. In the reactor core, the assemblies are immersed in a flow. This flow is responsible for assemblies coupling and vibrations. In case of accidents such as seismic or LOCA events (Loss Of Coolant Accident), fuel assemblies in the reactor core are subjected to strong oscillation amplitudes.

¹Institute for Research on Non-Equilibrium Phenomena, *Institut de recherche sur les phénomènes hors équilibre*. More on <https://irphe.univ-amu.fr/>.

²Laboratory of Mechanics and Acoustics, *Laboratoire de mécanique et d'acoustique*. More on <http://www.lma.cnrs-mrs.fr/>.

³More on <https://blogs.gwu.edu/bardet/>.

⁴More on <https://www.cea.fr/>.

⁵More on <https://www.edf.fr/>.

⁶More on <https://www.framatome.com/>.

The framework of this project in the broadest sense is the understanding of the behavior of the structure in the presence of a flow. In normal operation, the fuel assemblies deform laterally in the core under the effect of the hydraulic forces exerted by the water circulating in the reactor core, the mechanical forces applied by the support system at the top nozzle, irradiation and temperature. These effects can generate assembly bow. In the defined hypothetical transient of an accident, such as a seismic event, stronger oscillations may occur leading to assemblies impacts. Reactor cores are designed with large allowances for this type of events. Deepening the knowledge of FSI is useful for the global physical understanding and may lead to improve the design and to refine the safety demonstration. Thus, engineers need numerical models to simulate assembly mechanical behavior. These models are validated by experimental campaigns which also define the model limits. The work presented in this document is mainly experimental and part of its results are used to validate a numerical model developed at CEA.

At very small scale, the FSI problem is related to the energy transfer between the fluid and the solid and is linked to the Kolmogorov and Taylor flow scales. At larger scale, it is related to assembly coupling, confinement, added mass, resonance frequency, added damping and added stiffness. In the PhD work presented in this document we will focus the investigation on these last effects, neglecting the smaller scales and considering the global assemblies mechanical behavior. The project considers the two industrial issues named above, assembly bow and assemblies vibrations and impacts. Even restricted to large scale, this FSI problem is complex and we will focus on these particular experimental analysis:

- assembly oscillation effects in fluid at rest,
- drag phenomena on steady state fuel assemblies under a flow,
- assemblies oscillations when immersed in a flow.

The assembly oscillation affects fluid dynamics and fluid dynamics affect the assembly mechanical behavior. We want to study the fluid forces with assemblies in steady state to better describe the bowing phenomenon and the fluid forces with oscillating assemblies to have a good prediction of the damping. For this reason several test configurations will be presented. We will evaluate the effects of a cross flow on the assemblies, such as the drag effect in a non-uniform flow and we will study the assembly oscillations under flow in order to understand the involved phenomena during impacts.

In the first case, studying the assembly oscillation effects on the fluid, we will focus on an analysis of fluid dynamics on a scale comparable to the diameter of fuel rods. In the other cases the analysis of fluid forces acting on the assembly will be carried out on an assembly scale. Thanks to a numerical calculation tool developed at CEA, we use the results from experiments with steady state assemblies in the analysis for assemblies vibration experiments.

The thesis is organized in five chapters. The first chapter is a general context for the subject. We explain how a Pressurize Nuclear Reactor works and which are its main components, focusing on the assemblies and related issues. A brief review on the numerical models is presented with a state of the art of the experimental setups developed at CEA. Second, third and fourth chapters refer to the experimental analysis listed above. Therefore, each of these chapters has its own bibliography introduction to the problem. In the second chapter we investigate the Keulegan Carpenter instabilities dependencies to the assembly vibrations in stagnant fluid. We use experimental results retrieved by non-intrusive velocimetry measurements. This part of the research study is set in an international mobility project funded by ISFIN⁷. The experimental setup is named SBF (Shaking Bundle Facility) at the George Washington University. We introduce the setup, the experimental methods and discuss the experimental results. The third chapter concerns assembly bow under hydrodynamic load. The setup in this case is Eudore, which is the state-of-the-art for FSI facility at CEA Cadarache. We measure the force exerted by the flow to the assemblies and the flow velocity profiles. The numerical tool to simulate fluid-structure interactions in a reactor core is presented too. Named FSCORE, it is based on a porous medium approach. Results from numerical simulations with FSCORE show good agreement with experimental results. In the second and third chapters we respectively face two opposite situations. Fluid is stagnant and assembly vibrates in the second chapter while assemblies are in steady state immersed in a flow in the third one. In the fourth chapter we investigate the effect of the superposition of these two conditions: the assemblies are immersed in an axial flow while the whole test section is forced by a seismic-like loading. In this case, the assemblies vibrate inducing cross-flow on the already present axial flow. This represents a different problem. The experimental setup is Eudore, as in the third chapter, with a different configuration. We use FSCORE application to simulate these experiments too. In this sense, results from the third chapter are used to simulate the vibrating experiments. Numerical results are discussed and they show good agreement with experimental ones. Finally, the last chapter is dedicated to the general conclusions and perspectives.

⁷*Institut Sciences de la Fusion et de l'Instrumentation en environnements Nucléaires.* More on <https://www.univ-amu.fr/en/public/institute-fusion-and-instrumentation-sciences-nuclear-environments-isfin>.

Contents

1.1	Pressurized Water Reactor	4
1.2	FSI issues in reactor core	7
1.3	Numerical models for fuel assemblies	10
1.4	Experimental facilities for fuel assemblies FSI	11
1.5	Conclusion	16

Fluid-structure interactions in a nuclear reactor core is a complicated subject. They involve high temperature and pressure flow and structures with complex geometry and a non-linear behavior. In order to deepen our knowledge, we can use theoretical approaches, numerical models and experimental facilities. The purpose of this chapter is to provide the reader with the context of this doctoral project. In the next sections we briefly expose the design of a PWR reactor core and its main components, industrial issues related to FSI for fuel assemblies, and some numerical models previously developed to simulate the mechanical behavior of fuel assemblies. Finally, we will exhibit a summary of the experimental facilities developed at CEA over the past decades to investigate FSI-related phenomena.

1.1 Pressurized Water Reactor

One of the most recognized classification of the reactors is done by considering the employed moderator, which is the element in the reactor that increases the probability to induce fission events slowing down the neutrons. Using this classification, most reactor use water as moderator (95 % of civilian operating reactors [IAEA]) and they are called Water Cooled Reactor (WCR). Among WCR, Light Water Reactor (LWR) are the most common and they are divided mainly into two families: Pressurized Water Reactor (PWR) and Boiling Water Reactor (BWR) in the ratio 70 to 30 (PWR to BWR) [Lombardi, 2012]. The PWR is therefore the most common reactor.

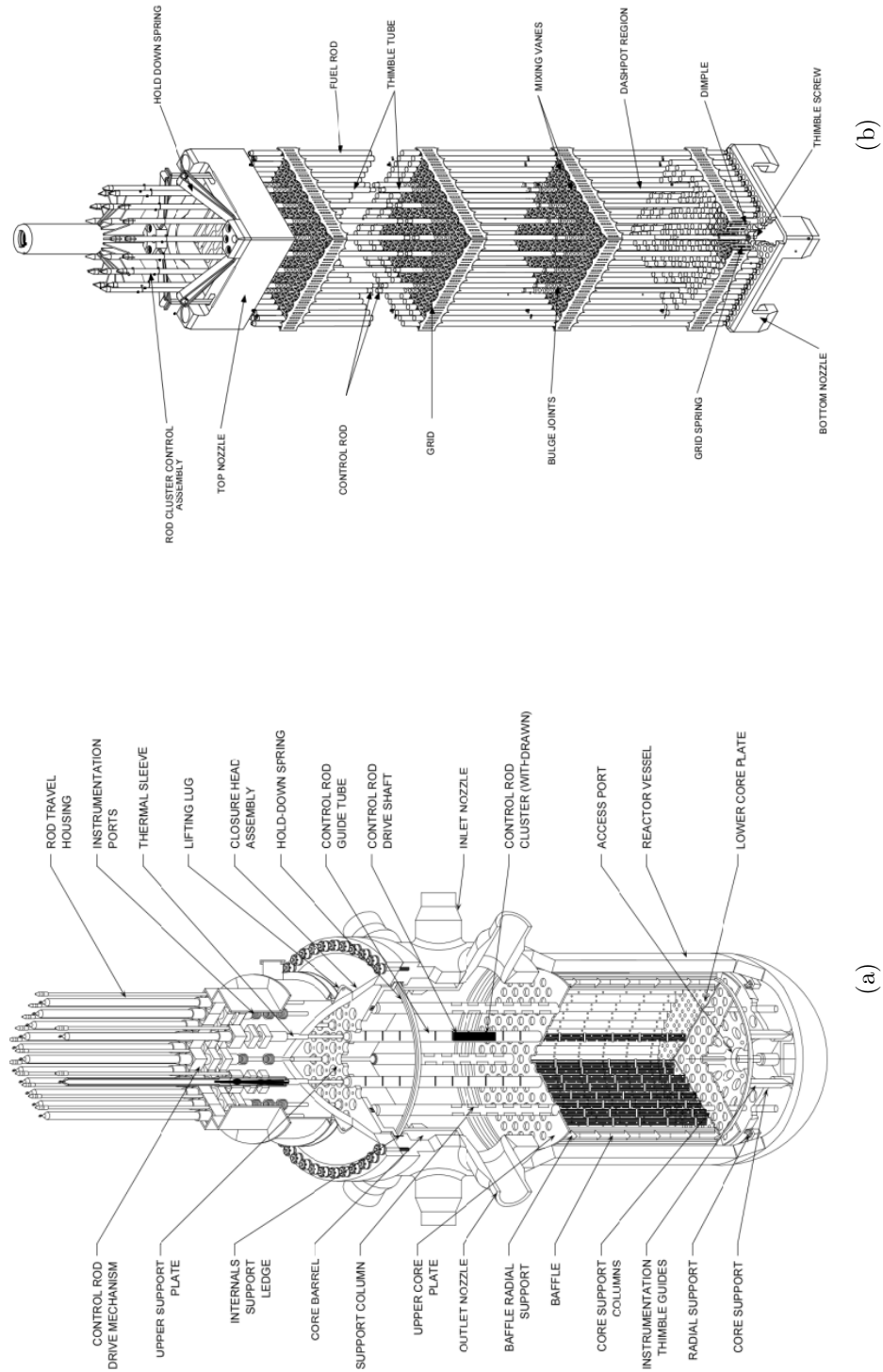


Figure 1.1: PWR vessel internal schematic view (a) and PWR fuel assembly schematic view [USNRC, 2012].

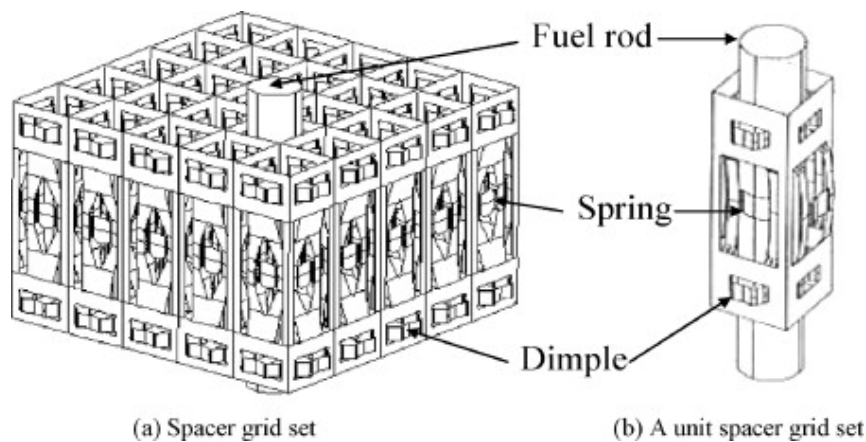


Figure 1.2: Section of a spacer grid (a) and unit spacer grid set (b). Springs and dimples keep the fuel rods in position [Shin et al., 2008].

A PWR is composed of two loops: the primary loop that is radioactive, and the secondary loop that is not. The main element of primary loop is the core, where uranium is stored and the fission reactions occur. The core is hosted in the reactor vessel (Fig. 1.1a) and it supplies the function of a heat generator. A pressurizer keeps the water pressure at 155 *bar*, from which the name *Pressurized* water reactor. The steam generator receives the hot water at 330 °C from the core and cools it down transferring heat to the secondary loop. The water coming out from the steam generator is at 290 °C and it is streamed to the core by means of a pump. Closing the primary loop, the water cooled in the steam generator is again heated up in the core. In the secondary loop the steam generator produces steam by means of the heat transferred from the primary loop. The steam expands in a turbine feeding an electric generator that produces electricity. After the turbine, the steam goes through the condenser, partly returning as liquid water and partly evaporating through the evaporative towers. Since part of the steam mass is lost in the evaporative towers, there is the necessity to reintegrate it, for example by means of a river. Eventually another pump sends the cooled water to the steam generator closing the secondary loop. Further details on nuclear reactions and nuclear plants are available in [Stephenson, 1958, Lewis, 2008, Lombardi, 2012, Murray and Holbert, 2014].

Nuclear fuel in PWR consists of cylindrical pellets of enriched uranium dioxide (UO_2) hosted in a zircaloy tube sealed at both ends and called fuel rod. The fuel rods are thin cylindrical pins with an external diameter of about 10 *mm* and about 4 *m* height, grouped in fuel assemblies. The fuel assembly (Fig. 1.1b) is obtained assembling hundreds of fuel rods, typically in a 17×17 square lattice. In the typical fuel assembly there are 25 guide tubes, 12 *mm* wide cylinders designed for a double purpose: keep the assembly aligned and house the control rods or the measurement instruments. At the bottom and at the top there are two nozzles that hold the assembly in its position inside the core. The control rods are responsible for neutron absorption and consequently for the power regulation generated by fission in the reactor core. Along the height of the fuel assembly there are a dozen of

spacer grids (depending on the model) welded to the guide tube. Fuel rods are supported by springs and dimples present in the spacer grids (Fig. 1.2). The spring force acting on the fuel rods keeps them in position, ensuring a gap of about 3 mm from each other.

To sum up, the PWR core is approximately a cylinder of 4 m diameter, 4 m height and 86 t weight. It is composed of hundreds of fuel assemblies (from 150 to 200) separated by few millimeters and framed between the Lower Core Plate, LCP, and the Upper Core Plate, UCP (Fig. 1.1a). The typical fuel assembly is a 4 m long bar with a square basis of 0.2 m per side, formed by 289 thin rods containing uranium pellets. This sophisticated fundamental element is designed to optimize the fission chain, to allow the measure of neutron fluxes and the control of the reactivity by means of the insertion of the control rods. By means of the fission reactions the core produces a thermal power up to 4500 MW. This heat is transferred to a flux of water at 155 bar with a flow rate up to 1.75 t/s (up to 5 m/s) that enters in the core at 290 °C and gains 30 °C over 4 m; this flow is also highly turbulent, with a Reynolds number $Re = 500000$ at 300 °C. Nuclear reactor cores are very complex, so it is difficult to simulate their behavior without a reliable simplified model.

1.2 FSI issues in reactor core

Along the approximately 30-year-long operative life of a PWR, fuel assemblies need to be replaced periodically. Almost once per year, when the reactor is off and flooded, the fuel assemblies are moved in and out the core in order to better sustain the fission reactions. Thus, the deformation of the assemblies can affect the normal operations of maintenance and operation of the reactor, lengthening its times and costs.

In the reactor core, the flow exerts a fluid load on the assemblies resulting in a change of geometry. Vibrating, the fuel rods slide between springs and dimples and move from their nominal position, leading to deformation of the assembly. Assemblies permanent deformations could prevent or slow down the insertion of control rods, a phenomenon known as Incomplete Rod Insertion (IRI). Apart from this direct effect of assembly deformations, other indirect effects concern thermodynamic and the neutronics of the reactor core [Waninger, 2018, Demazière et al., 2022].

Fig. 1.3a and 1.3b show an example of assembly bow measurements at Ringhals NPP. In these examples the assemblies of two different reactors (3 and 4) bowed with different shapes. In most cases, assembly bow is not an isolated phenomenon but involves more assemblies in the core, generating a collective pattern, as at Ringhals reactor 2 (Fig. 1.3c). Once deformed, the assemblies are no longer aligned, breaking the symmetry in the core. It may happen that edges of grids of opposite assemblies approach or come into contact with each other. In this case, vibration can lead to deformation or even breakage of the spacer grids by fretting. Fig. 1.4a shows a grid corner broken by fretting [Spykman and Pattberg, 2014]. In the event of an accident, vibrations are larger and can lead to impact between assemblies. Fig. 1.4b shows the typical deformation of a real irradiated grid, reproduced

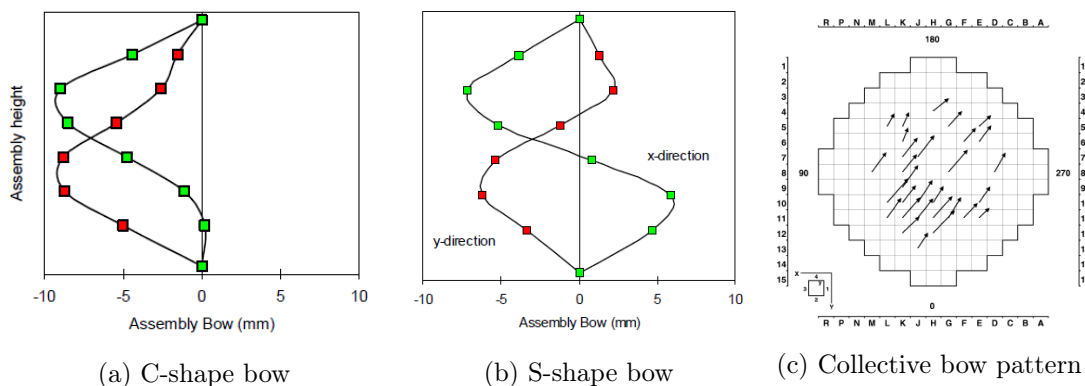


Figure 1.3: Example of assembly bow measurements at Ringhals 3 (a) and Ringhals 4 (b). Collective fuel assembly bow pattern at Ringhals 2 (4th grid height). Here direction x and y are the two lateral dimensions in the core [Andersson et al., 2005].

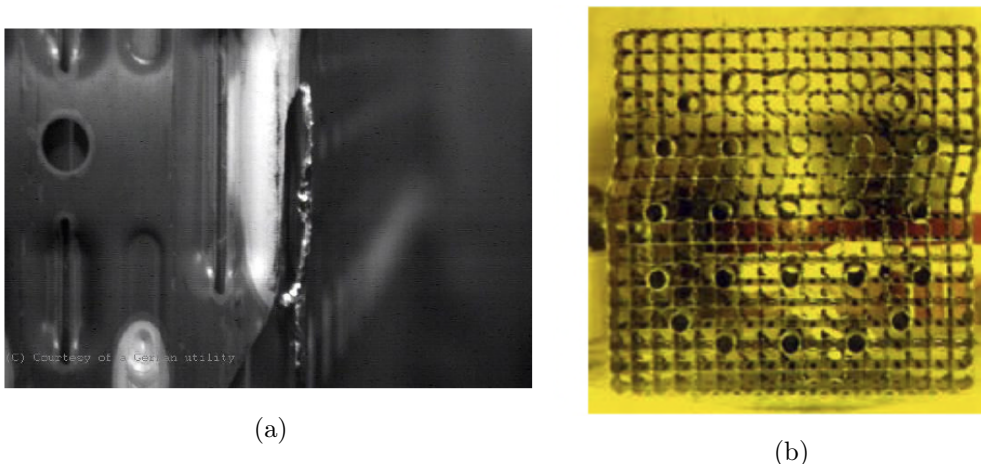


Figure 1.4: Grid broken by fretting (a) [Spykman and Pattberg, 2014] and grid deformation reproduced in lab test (b) [Yvon et al., 2005].

in the laboratory with impact experiments, with 5 mm compression resulting in 1.1 mm of permanent distortion [Yvon et al., 2005].

In his PhD thesis, Wanninger [2018] listed all the fuel assembly bow-inducing and enhancing mechanism in the PWR core. They are summarized below and depicted in Fig. 1.5.

- The holddown force: is the force that compresses the assemblies from the top by the upper core plate to prevent assemblies to lift from the lower core plate due to the effect of the upward coolant flow.
- The structural growth: irradiation growth that is the root cause for increasing hold-down forces.
- The structural creep: once the assembly deforms, neutron irradiation affect the crys-

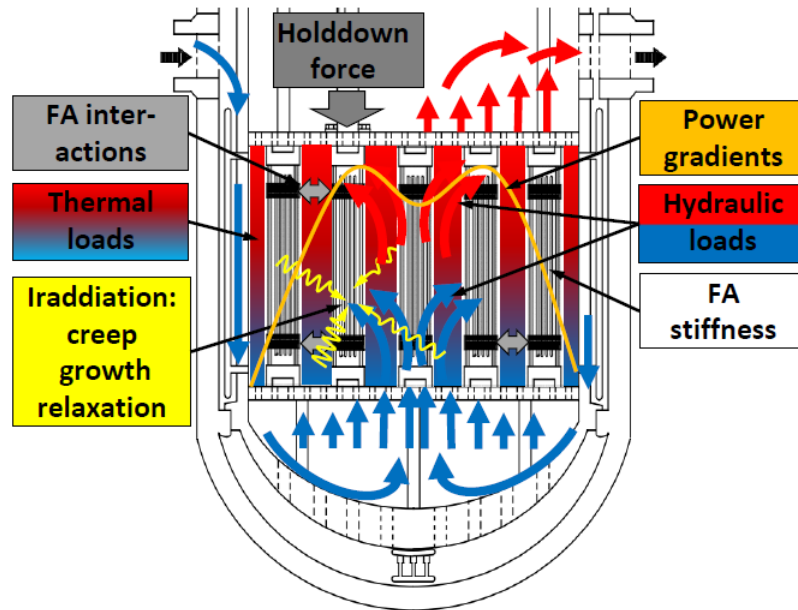


Figure 1.5: Graphical representation of in-reactor fuel assemblies bow influencing mechanisms. [Wanninger, 2018].

tal lattice of the assembly creating plastic deformation.

- The fuel assembly stiffness: it determines the elastic deformation of the assembly. The more the assembly plastically deforms under external load, the higher will be the creep deformation rate. Hence, higher assembly stiffness reduces the susceptibility to lateral bow.
- The structural relaxation: during operation the spring of the spacer grids relax reducing the assembly stiffness and promoting assembly bow but also reducing the bow-enhancing effect due to the holddown force.
- The fast neutron irradiation: it plays a fundamental role in the assembly deformation. Without the contribution of the fast neutron irradiation the creep and relaxation effects would be strongly reduced and no growth would occur.
- The thermal loads: it is a reversible process induced by the temperature gradient. It may lead to internal bending moments and may modify the axial center of rigidity of the fuel assembly.
- The lateral mechanical coupling: once two assemblies are deformed enough to close the gap, they are coupled mechanically in the lateral translational degree of freedom. In this way the bow deformation of a single fuel assembly may propagate over the entire core, creating a bow pattern.
- The lateral hydraulic loads: coolant flow inlet and outlet profile are non-uniform at the lower and upper core plates, inducing a cross-flow in the core as a result of lateral

pressure gradients. Since a certain amount of cross-flow may be desired for heat removal purpose, spacer grids have mixing vanes. They induce flow swirls, increasing the cross-flow and the local heat transfer. The cross-flow induced by the mixing vanes has no preferential direction. In contrast, the one generated by the non-uniform flow condition at the core inlet and outlet exerts a unidirectional hydraulic load on the fuel assemblies, creating bending moment on the structure.

The hydraulic loads may induce permanent deformations as a result of creep and are believed to be one of the major driving mechanisms of the assembly bow. Our analysis focuses on this last mechanism.

1.3 Numerical models for fuel assemblies

According to the French Nuclear Authority, the quadratic addition of LOCA and earthquake effects is considered as the reference accident to design the vessel internals. These accidents are usually considered at the system level, with ad-hoc software such as CATHARE [Valette et al., 2011] or GOTHIC [Papini et al., 2011, Chen et al., 2011]. Instead, we want to focus on the effects of vibration on the internal core components, particularly the assemblies. The core is considered able to work as long as the grids of the fuel assemblies are not damaged. Because of the complexity of the core and the random character of a seismic event, a fine model of the fuel assemblies is not convenient to assess the robustness of grids to seismic events. Performing simulations with all the structures interacting with the fluid would take too long with the currently available simulation tools. A simplified model for the fuel assemblies is therefore needed.

Historically, fluid-structure interactions for slender body as cylinders has been investigated by Stokes [1851], Morison et al. [1950] and Lighthill [1960]. Based on these works, Païdoussis [1966a] studied the dynamic of cylinder immersed in axial flow theoretically and experimentally [Païdoussis, 1966b]. Later on Païdoussis [1973], Païdoussis and Suss [1977], Païdoussis et al. [1977], Païdoussis and Pettigrew [1979] generalized his theory to a cluster of cylinders under axial flow. Recently, Païdoussis model has been used addressing fluid instabilities of cylindrical structures under axial flow [de Langre et al., 2007]. Païdoussis model requires the use of empirical force coefficients to account the effects of the viscous hydrodynamic forces. A different approach is proposed by [De Ridder et al., 2013], that it is based on coupled computational fluid dynamics and computational structural mechanics, minimizing the amount of required empirical input. With this methodology, modal characteristics and elastic instabilities of cylindrical structures are studied with numerical simulations for rods [De Ridder et al., 2013, 2015] and rod-bundles [De Ridder et al., 2017].

Concerning fuel assemblies in reactor core, the first studies in literature aimed at modeling the behavior of a fuel assembly followed a linear approach for simplicity reasons. The behavior of the assembly can be considered linear as long as the involved forces are small: in this case the rods are considered to perfectly fit the grids. Among the linear model, one

which better fits the experimental results is the QUEVAL model, even if it does not represent the physical reality of the problem [Queval and Brochard, 1988, Queval et al., 1991a]. To better model the physical reality of the problem non-linear models have been studied, too. Briefly summing up, theoretical and empirical models have been developed modeling the fuel assembly with one simple Euler-Bernoulli beam [Kim et al., 1981], two beams, one for the rods and one for the guide tube [Fontaine and Politopoulos, 2000], or even more beams [Brochard et al., 1993]. In addition, models have been studied that either take in account or neglect friction between rods and grids, with either linear or non linear spring simulating the contacts between rods and grids or again models with clamped-clamped or free extremities.

It has been experimentally shown that a fuel assembly has a non-linear behavior with regard to stiffness and damping. Brochard et al. [1993] observed the non-linear behavior during vibration and snap back tests. Further experiments showed the presence of hysteresis phenomenon during displacements. The springs and the dimples in the spacers grids are responsible for an observed hysteresis in displacement, which significantly contributes to the mechanical stiffness and damping [Collard et al., 2005, Pisapia, 2004].

Even if the models cited above can fit some of the experimental results, they present some disadvantages. For instance, they cannot represent the damping and frequency variation; they can also become too complex to be used in industrial simulations, or they might need to be adjusted a priori via some parameters. For these reasons they only have a limited usefulness in seismic simulations. Furthermore, all these models do not consider the non-linear fluid-structure interactions effects and therefore cannot model the hydrodynamic coupling between the assemblies.

The state-of-the-art model has been proposed by Ricciardi et al. [2009a]. It takes into account fluid-structure coupling, using porous medium theory. This allows to speed up the simulations and to keep only a few degrees of freedom. In the model (Schematic representation in Fig. 1.6), the equations for the fluid and structure motion are established individually. Then through a porosity coefficient, equivalent fluid and structure are defined over the whole core domain. Finally the empirical model proposed by Païdoussis [1966a] is used to couple the two systems of equations. The model will be explained in more details in Sec. 3.5 and Sec. 4.4.

1.4 Experimental facilities for fuel assemblies FSI

Experimental results are needed to validate numerical models. Many experiments conducted on fluid-structure interactions aimed at identifying hydraulic forces acting on cylinders or cluster of cylinders and can be found in the literature, even with the typical fuel rods and fuel assemblies geometries [Peybernes, 2005, Ferrari et al., 2018, 2020]. Among them, the COLIBRI program is worth mentioning. It aims at investigating the radiation noise related to fuel rods vibrations in an entire reduced scale reactor core [Lamirand et al., 2020a,b]. At the assembly scale, Tanaka et al. [1988] investigated the damping induced by

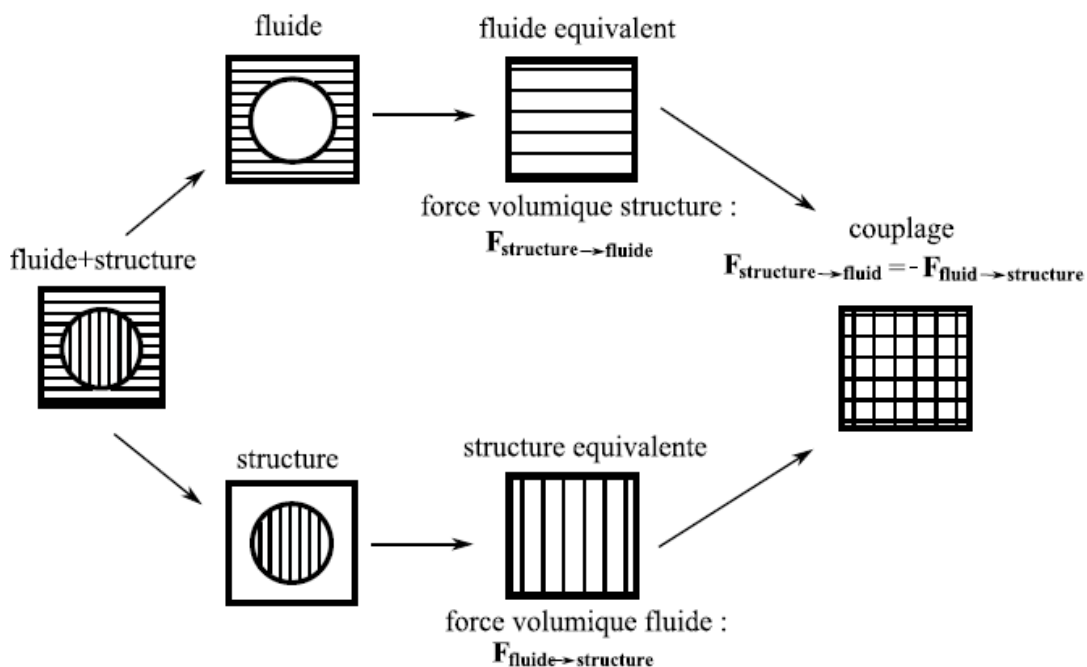


Figure 1.6: Porous medium approach by Ricciardi et al. [2009a].

parallel flow, producing a quantitative explanation for the phenomena, using an isolated cylinder and a rod bundle. Brenneman et al. [2003] used existing experimental data to evaluate the confinement effects on fuel assembly mechanical behavior, showing how the fluid induced damping acts in a relative reference frame and tends to reduce the relative displacements and impact forces between fuel assemblies and baffle walls. More recently, Joly et al. [2021] has proposed an extensive experimental and numerical study on the steady forces exerted upon a cylinder confined in a 3×3 cylinder array in axial flow.

On the other hand, experiments with several assemblies immersed in a flow and under seismic-like load are less common. This kind of experiments have been studied for a long time at CEA, with the first experimental facilities that date back to the beginning of the 90's. Since it would be complicated and expensive to reproduce a real scale nuclear core, different facilities have been constructed during the years scaling some of the parameters (dimensions, number of assemblies, pressure, temperature, etc.). Throughout these years their resemblance to a PWR core increased to the point that in LETH the Hermes facility has real scale dimensions. A brief summary on the older experimental setups is discussed below. Additional information can be found in [Ricciardi, 2008, Clément, 2014, Capanna, 2018].

Eros. In 1990, Eros was the first of a long series of facilities aimed at understanding the phenomena involved in the vibration of the assemblies [Brochard et al., 1993]. This setup consisted in 5 reduced-scale fuel assemblies, with 6×6 fuel rods each, placed on a shaking table. The experiments performed on Eros showed the possibility to model the assemblies

as non-linear beams [Queval et al., 1991b,a].

Echasse. The Echasse setup followed in 1999 with the purpose of measuring the impact forces between two assemblies or between an assembly and the wall. It consisted of two reduced-scale assemblies, with 8×8 fuel rods each, and housed experiments in standing water and in axial flow up to 4.8 m/s. Therefore, the tests were performed in several flow configurations: air, standing water, 2.4 m/s and 4.8 m/s flows. During the experiments, the impacts were caused by a "quick-release" phenomenon: one of the assemblies was removed from its equilibrium position and then quickly released [Collard and Vallory, 2001, Vallory, 1999, 2000].

Cadix. In 2000, new experiments were carried out in the Cadix facility at the EMSI lab (CEA-Saclay). This setup involved, for the first time, 6 full scale fuel assemblies on a shaking table. The tests aimed at measuring the impact forces on full scale assemblies while the table was shaking. They were performed either in air or standing water. The tests evaluated confinement effects and were also used to validate a simulation code developed in parallel [Broc et al., 2001, Queval et al., 2001].

Couplage. In 2006, the first experiments aiming at studying the hydrodynamic coupling between assemblies were carried out on the Couplage setup. It was the first facility arranged in a 2D plane. It has 9 reduced-scale fuel assemblies arranged in square 3×3 lattice, each of which with 4×4 fuel rods held together by only one spacer grid placed in the middle. The central assembly was put in motion by means of a hydraulic jack that imposed a displacement following a sinusoidal signal whose frequency varied from 0 to 4 Hz. Even though the geometry of this experimental facility was not representative of a nuclear reactor core, and even if the assemblies scale was too small to be able to represent a real nuclear fuel assembly, the experiments on Couplage allowed to study coupling forces between the fuel assemblies and to outline the presence of non negligible hydrodynamic interactions between assemblies placed on different rows [Ricciardi, 2008].

Hermes. Hermes is a setup that allows 2 different configuration: P and T. In P configuration, the facility houses 1 full scale 1300 MW PWR fuel assembly and can simulate real operation conditions in a PWR core (155 bar and 330 °C). Such configuration was designed to analyze the pressure drops along real fuel assemblies and to test new designs for fuel assemblies. In T configuration, lower temperature and pressure conditions are used: a pump can supply 1200 m³/h in axial flow and 400 m³/h in cross-flow, at 35 bar and 170 °C. It can handle up to 2 fuel assemblies, one of which is excited by a hydraulic jack. The flow rate is similar to the PWR conditions, the lower temperature allows to provide accurate measurement devices to the test-section. The fuel assembly used in Hermes is made of 25 guide tubes and 264 fuel rods, each having a height of 4.5 m, held together by 10 spacer grids. The force applied by the hydraulic jack is measured by a load cell while

the displacements of its grids are measured with Linear Variable Differential Transformer (LVDT) sensors. Its boundaries house acrylic windows allowing optical fluid measurements with a LDV device [Ricciardi and Boccaccio, 2014, 2015, Ricciardi, 2016].

Icare. Icare facility has been firstly designed and made operative in 2014 during the PhD thesis of Clément [2014]. It aimed at studying the coupling between misaligned assemblies with a design close to the reality. Unlike Couplage, Icare has 4 assemblies in a square lattice 2×2 with the possibility to change their number from 1 single assembly to 4 assemblies. This setup permits to force the vibration of one assembly at different amplitudes, frequencies and heights. Measurements on assemblies displacements are possible by means of LVDT sensors.

Tab. 1.1 summarizes the main characteristics of the facilities.

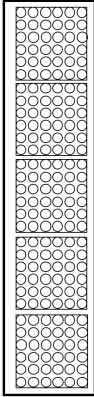
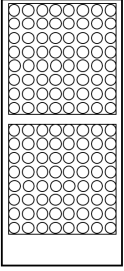
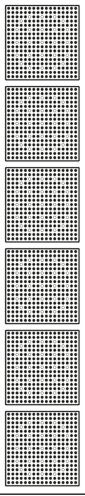
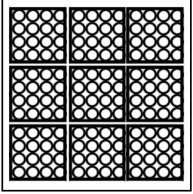
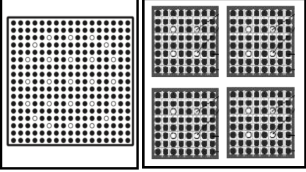
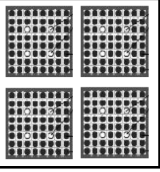
Facility	Section view	Objective	Limitations
Eros		Evaluating impact forces on a line of fuel assemblies	Reduced scale assemblies No water flow
Echasse		Evaluating impact forces under axial flow	Only 2 assemblies Large by-pass
Cadix		Evaluating impact forces on a real fuel assembly	No water flow Assemblies on a single line
Couplage		Evaluating coupling between fuel assemblies	Highly reduced scale assemblies: not representative Assemblies are not free to move
Hermes		Identification of modal parameters of a real fuel assembly (DEDALE campaigns)	Only one fuel assembly
Icare		Study the coupling between misaligned fuel assemblies that have a design close to reality.	Half scale assemblies

Table 1.1: Properties of the experimental facilities. The section views are not in scale but contain the exact number of rods for assembly.

1.5 Conclusion

We have illustrated the working principle and the main components of a PWR core, focusing on the fuel assemblies. Fuel assemblies and interaction with the coolant fluid are the subject of this research. We have presented the two phenomena, assembly bow and assembly vibration, that we will analyze in the following chapters. We have introduced the porous medium approach as a faster solution of core modeling. Finally we have reviewed the principals facilities used at CEA to perform experiment of fluid structure interaction in a PWR core. In the next chapters we will present experimental results obtained in two new facilities, addressing fluid instabilities induced by small amplitude oscillations of fuel assembly, assembly bow and assembly vibrations.

The choice of studying these phenomena was made after several observations. In the literature there is no definition of critical amplitude for oscillations in stagnant fluid of a rod-bundle. Starting from a threshold amplitude, these oscillations induce the creation of vortices in the fluid, which in turn affect the structural behavior of the assembly itself, particularly the damping. In the nominal case for a reactor core we are in the presence of flow. The choice of studying the development of instabilities in the stagnant fluid comes from a simplification of the problem. Indeed, we wanted to separate the mechanical effects due to the presence of the fluid from those due to the presence of the flow and focused on the study of the former.

The experimental campaign for assembly bow was carried out aiming to characterize the hydrodynamic forces acting on reduced-scale assemblies and to identify empirical FSI coefficients by means of an analytical model. These experiments serve to validate the porous medium approach. For this purpose, we used the forces and coefficients identified in the experimental campaign.

The same coefficients were then used, again using the porous medium approach, to numerically simulate the mechanical behavior of fuel assemblies under external vibrations. The results of the latter experimental campaigns are of interest because there are no data in the literature concerning impact forces for an assembly line under axial flow and external vibration.

Keulegan-Carpenter Instabilities for a Rod-Bundle

Contents

2.1	Introduction	18
2.1.1	Single cylinder	19
2.1.2	Cylinder array	21
2.2	Experimental methods	22
2.2.1	Particle Image Velocimetry	22
2.2.2	Shaking Bundle Facility	24
2.2.3	Data acquisition and processing	25
2.3	Results	30
2.3.1	Synchronization method	31
2.3.2	Results on FOV1: Intraline plane	36
2.3.3	Results on FOV2: Interline plane	41
2.4	Discussion	47
2.5	Conclusions	50

Summary

During the normal operations of PWR, fuel assemblies are subjected to an axial flow. However, there are some scenarios in which a loss of flow can happen. Fuel assembly mechanical behavior is affected by the axial flow and changes in still fluid. Furthermore, studying the mechanical behavior in stagnant flow conditions allows us to decouple the effect of the flow by the effect of the fluid only.

The literature is rich of works concerning a single cylinder oscillating in still fluid, but much less or nothing is available on experimental studies rod bundles (assemblies) oscillating in still fluid. The related fluid-structure interactions depend on some force coefficients such as inertial and drag coefficients. In the case of small-amplitude oscillating flow, these

force coefficients depend non-linearly on the Keulegan-Carpenter number (K). K is a dimensionless number that links oscillation velocity, period of oscillation and characteristic size of the solid. In the case of a cylinder or a rod-bundle, this characteristic dimension is the rod diameter. Fluid dynamics with respect to K has threshold phenomena. Above a threshold K_c , fluid instabilities occur and affect the mechanical behavior of rod-bundles and hence the force coefficients describing the fluid-structure interactions equations. The analysis presented in this chapter is devoted to the identification of the threshold K_c for a particular rod-bundle.

Here, we present an experimental investigation on a cylinder array immersed in a stagnant cinnamaldehyde and P-cymene solution, placed on a vibrating table. The purpose of the vibrating table is to set the bundle and the fluid in unidirectional vibration. The bundle is called Shaking Bundle Facility (SBF) and its main feature is the possibility to use a custom flying PIV in MIR condition (Match of Indexes of Refraction). To the author knowledge, this facility is not just the state of the art but even one-of-a-kind. SBF allows to perform non intrusive displacement and velocimetry measurements on a full-height PWR surrogate fuel assembly. As it will be shown, the MIR condition allows to investigate the fluid space between the structures.

The experiments have been performed in 2015, not only with the P-cymene solution, but also with water (not MIR condition). In both cases, they have been performed with still fluid or with of a flow. For the purpose of this study, only the experiments with still fluid have been exploited (they had never been exploited before). The effects of several oscillating amplitude are investigated by studying the velocity fields created by the bundle motion. The study focuses on the temporal and spatial development of fluid instabilities. The velocity fields are investigated on vertical planes lying in the vibrating direction.

The chapter is organized as follows: after introducing the KC instability for rods and rod assemblies, we will explain the PIV technique, then introduce the SBF experimental setup and explain how the measurements were made and processed. We will then illustrate and discuss the experimental results. From the discussion appears that a new definition of Keulegan-Carpenter number for rod-bundle seems needed.

2.1 Introduction

The physics of interactions happening around a moving solid body immersed in a confined fluid still eludes our knowledge, in particular when complex geometries are involved. The complexity increases greatly when both the solid and the fluid are in motion, at high velocities, with complex geometries and nonlinear behaviours. In the last century this subject has been investigated for offshore structures subject to sea currents or ground acceleration ([Rahman and Bhatta \[1993\]](#)), and more recently for steam generators and nuclear reactor cores [[Ricciardi et al., 2009a](#)], where thousands of slender rods interact with a high turbulent flow.

2.1.1 Single cylinder

The study of fluid-structure interaction starts by considering simple bodies with particular symmetries moving slowly in low-density fluids. Then one can increase the complexity by removing body symmetries, changing the moving dynamics or using fluid with different density and properties in general. Stokes [1851] first set out to find the analytical solution for a sphere immersed in a viscous medium. He considered not just fluid density but also fluid viscosity, becoming de facto the first who considered this fluid property both in fluid-dynamics and fluid-structure interaction analysis. Accordingly to Stokes' formula for force on a sphere, a century later Morison et al. [1950] proposed the following expression:

$$f = \frac{1}{2}\rho d c_D |u|u + \frac{1}{4}\rho\pi d^2 c_M \frac{du}{dt}. \quad (2.1)$$

The Morison equation estimates the in-line hydraulic load exerted on a section of a cylinder ($|f| = \text{N/m}$) parallel to the flow direction. This equation is valid for unidirectional conditions both for the flow and the body motion. The expression of the in-line hydraulic load sees two terms: one proportional to the square of the flow velocity u , the drag or resistive force, and one proportional to the flow acceleration du/dt .

The equation proposed by Morison takes into account the fluid density ρ , the rod diameter d and two hydrodynamic coefficients: the drag coefficient c_D and the added mass coefficient c_M . Few years later, Keulegan and Carpenter [1958] wanted to establish how these coefficients depend on the characteristics of the oscillations. They introduced the *period parameter* that became later known as the Keulegan-Carpenter number, K , whose expression is in Eq. 2.2, where u_m is the magnitude of the velocity oscillations ($u(t) = u_m \sin 2\pi ft$) and $T = \frac{1}{f}$ is the oscillation period. Based on dimensional analysis, they established that the hydraulic load and thus the coefficients c_D and c_M depend on the phase, on K and on the Reynolds number Re conventionally defined for particular problem with ν as kinematic viscosity.

$$K := \frac{u_m T}{d} \quad Re := \frac{v_m d}{\nu} \quad \beta := \frac{d^2}{\nu T} = \frac{Re}{K} \quad (2.2)$$

β is called the *frequency parameter* or the *Stokes parameter*. Sarpkaya [2005] shows how Stokes actually used it under some restrictions (linearization, separation, etc.), but it represents the ratio between Re and K , and it can be used wherever Re and K are definable. It should be said, for completeness, that Keulegan and Carpenter [1958] did not find any correlation between the force coefficients and Re , while they did showed a dependence on K . For a greater accuracy on the estimation of the hydraulic load, they also introduced a *reminder function* ΔR taking into account the variation of the force coefficients from their average value during an entire cycle.

Starting from the work of Morison et al. [1950] and Keulegan and Carpenter [1958] and considering other experimental results [Wang, 1968, Honji, 1981, Hall et al., 1984],

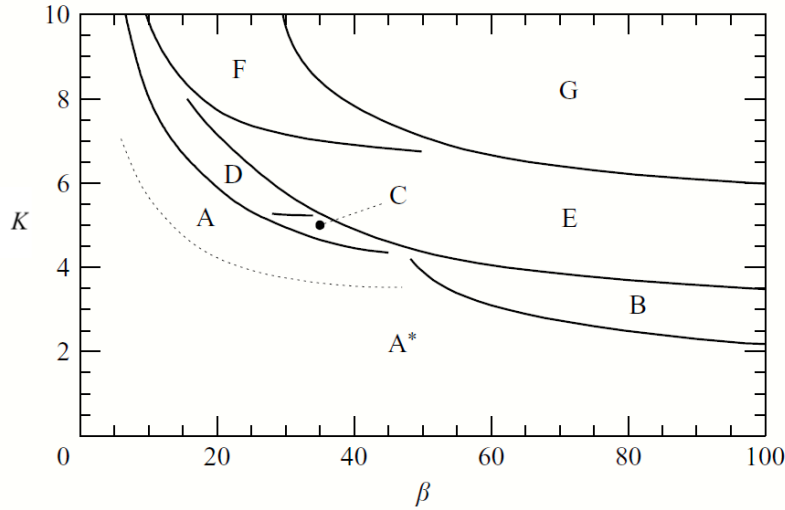


Figure 2.1: Classification of symmetry-breaking flows in the $\beta \in [0, 100] \times K \in [0, 10]$ subset of control space according to [Tatsuno and Bearman \[1990\]](#). Figure from [Elston et al. \[2006\]](#).

[Sarpkaya \[1986\]](#) investigated the relation between the force coefficients and K . The drag coefficient c_D exhibits a threshold behaviour depending on the value of K number; 4 different flow regimes can be identified. For Keulegan-Carpenter numbers smaller than a critical value ($K < K_{cr}$), the flow is laminar and remains stable and attached to the solid. For $K_{cr} < K < K_{md}$ (minimum drag), the laminar flow becomes unstable, eventually leading to separation, turbulence and to the decreasing of c_D to its minimum value. At K_{md} separation occurs and the drag coefficient reaches its minimum value. When the Keulegan-Carpenter number further increases ($K_{md} < K < K^*$), vorticity structures become stable, c_D increases again, and vortex shedding becomes increasingly important as K increases. Finally, for $K > K^*$ the c_D decreases again and the number of shed vortices increases.

[Hall et al. \[1984\]](#) performed an analysis on different oscillating conditions, leading to a threshold $K_H(\beta)$ depending on β , given by Eq. 2.3.

$$K_H(\beta) := 5.78\beta^{-\frac{1}{4}}(1 + 0.21\beta^{-\frac{1}{4}}) \quad (2.3)$$

Later, [Sarpkaya \[2002\]](#) proposed a new correlation (Eq. 2.4) to identify the minimum critical $K_S(\beta)$ at which three-dimensional instabilities occur for large β values: one could note that Eq. 2.3 and 2.4 gave approximately the same result for $\beta \approx 100$.

$$K_S(\beta) := 12.5\beta^{-\frac{2}{5}}. \quad (2.4)$$

Exploring the phase space for a singular cylinder oscillating in a stationary flow, [Tatsuno and Bearman \[1990\]](#) identified 8 flow regimes in a K vs β map in the region $K \in [1.6, 15]$, $\beta \in [5, 160]$. At low K and β the flow is non-separated, aligned with the cylinder motion

and satisfy the symmetry across the plane containing the cylinder axis and the displacement. For larger $K - \beta$ values, three-dimensional instabilities arise. All the letters in Fig. 2.1 correspond to different regimes defined by Tatsuno and Bearman [1990]. With his experimental work, Honji [1981] describes the flow pattern around an oscillating cylinder exhibiting centrifugal 2D and 3D instabilities for $K \in [0, 4]$, $\beta \in [70, 700]$. Elston et al. [2004, 2006] numerically investigated the K - β map in the region $K \in [0, 10]$, $\beta \in [0, 100]$ (Fig. 2.1) finding that part of the flow behaviour can be explained by two-dimensional symmetry-breaking instabilities. More recently, Duclercq et al. [2011] used numerical simulations to investigate the influence of a Re number varying from 40 to 500 at fixed $K = 10$ for a circular cylinder. They find five ranges of Re from the temporal and spectral analyses of the in-line and transverse forces, where the transitions between regimes are characterized by period and aperiodic behaviors, modifications of the distribution of energy in force spectra, and changes in spatio-temporal symmetries.

2.1.2 Cylinder array

Relatively few studies have been carried out to study the force on an oscillating array of cylinders. Price [1995] reviewed the theoretical models addressing fluid-structure instabilities for cylinder arrays in cross flow; he showed that instabilities arise from the interstitial flow in the array and concluded that a good simulation of the vibrational behavior of cylinder arrays is not possible without being able to predict those instabilities. Chang and Tavoularis [2007] simulated isothermal turbulent flow in a 60° sector of a 37-rod bundle, while Anderson et al. [2014] simulated a 3×2 rod bundle investigating fluid-elastic instabilities. Tong et al. [2015] simulated the behaviour of an oscillating flow through a 2×2 rod bundle at rest for different K , Re and gap ratios ($G = g/d$, with g being the gap between the extremities of 2 contiguous cylinders). They explored the parameter domain with: $K \in [1, 12]$, $\beta \in [20, 200]$, $G \in [0.5, 4]$. They mapped the behavior of the c_M and c_D coefficients as a function of K and Re underlying the role played by G . Indeed, for small G , the rod bundle tends to behave as a single, large structure while at larger G the behaviour and magnitude of the drag and inertial coefficients tend to the ones of a single cylinder.

In this chapter, we focus on the experimental study of the flow induced by an oscillating 6×6 rod bundle in an otherwise quiescent fluid. The need for this investigation lies in applications to the nuclear industry, where being able to estimate the forces acting on core elements helps to improve their operation. In fact, the core of a PWR-type reactor consists of tens of thousands of rods (fuel elements) grouped into hundreds of fuel assemblies subjected to a heterogeneous axial flow. Furthermore, the gaps within the rods are relatively small, $G = 0.33$, contributing to amplify coupling and resonance phenomena.

The measurements are carried out with Particle Imaging Velocimetry (PIV), in MIR conditions (Matching of the Refractive Index), allowing to optically investigate the flow dynamics of the whole fluid domain. In the last decade, PIV technique in MIR conditions

has been used by numerous authors such as [Dominguez-Ontiveros et al. \[2009\]](#), [Lee et al. \[2013\]](#) and [Turankok et al. \[2021\]](#). [Nguyen et al. \[2018\]](#) recently performed Stereoscopic-PIV in MIR condition with a facility that hosts a 61 wire-wrapped rod bundle using acrylic and P-cymene, studying the flow interaction with the steady structure. Concerning optical flow measurements and rod bundle vibration, [Capanna et al. \[2021a\]](#) presented an experimental work on two 8×8 rod bundles. One of them was set in vibration and the PIV measurements have been carried out in the gaps between the assemblies. In that case, PIV was not in MIR conditions and the fluid flow within each bundle was not accessible.

In this work, experimental measurements are carried out on an index matched facility installed on a shaking table hosting a full length surrogate bundle, as described by [Weichselbaum \[2016\]](#). To the author's knowledge, to date no other experiment in MIR condition has been performed with assembly in motion. The data presented in this chapter are a first-of-a-kind, showing the flow behaviour for a rod bundle oscillating in a still fluid, both in an oscillating frame of reference.

2.2 Experimental methods

As recalled in Sec. 1.1, the core of a Pressurised Water Reactor (PWR) contains hundreds of rod bundles. The results show in this chapter were obtained with Particle Imaging Velocimetry (PIV) on the Shaking Bundle Facility (SBF) with an acrylic 6×6 rod-bundle at $G = 0.33$. For the sake of clarity the main features of the facility are reported in the next paragraph. A more detailed description of the facility can be found in [Weichselbaum \[2016\]](#).

2.2.1 Particle Image Velocimetry

Particle Image Velocimetry (PIV) is a technique that can provide instantaneous velocity vector measurements in a 2D cross-section of a flow. The technique is applicable to a range of liquid and gaseous flows. More sophisticated techniques can use PIV principles to measure 3D volume of a flow [[Raffel et al., 2018](#), [Weichselbaum et al.](#)]. The fluid is seeded with micrometric particles and the main assumption ruling this technique is for the particles to faithfully follow the flow dynamics, without interfering with it. From the correlation of the seeding particle displacements, the 2D velocity field is retrieved. A typical PIV setup consists of a camera, high power pulsed laser, an optical arrangement to convert the laser output light to a light sheet, tracer particles and a synchronizer. Fig 2.2 illustrates the main working principle of this technique. For an instantaneous measure, two images are taken shortly one after another, with a delay Δt of the order of ms. The images, called frames, show the position of each particle in the laser plane through refraction toward the light captured by the camera. Computing the correlation between the frames, one can retrieve the distance individual particles traveled. The displacement field is thus determined from the motion of the seeding particles between the two images. The velocity field is then

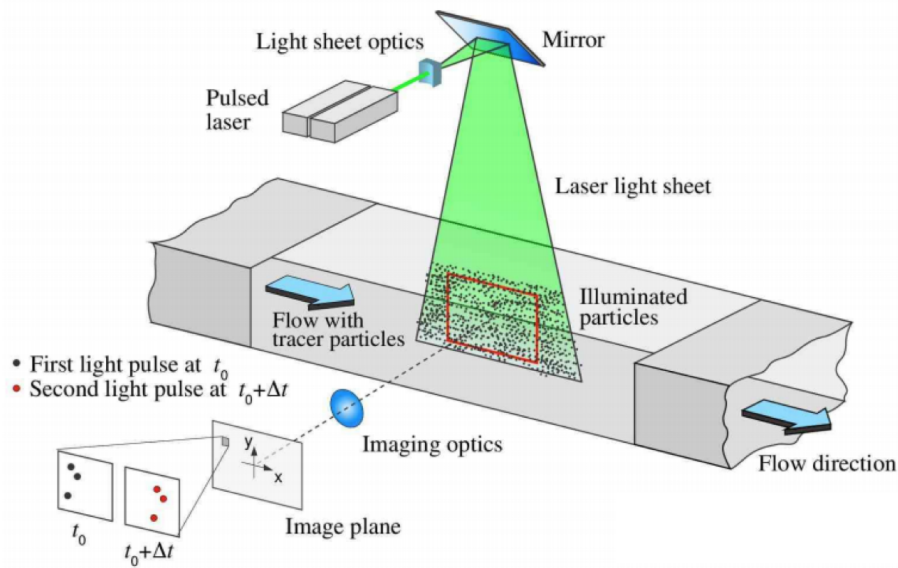


Figure 2.2: PIV scheme. Figure from Raffel et al. [2018]

obtained simply by dividing this displacement field by the time step Δt . The procedure is repeated for all the frames acquired during the measurement, at a fixed acquisition frequency $f_{acq} = 1/\Delta t$.

With PIV one does not track each particle individually, which is a similar but separate technique known as Particle Tracking Velocimetry (PTV). PIV divides each frame into many superposed *interrogation windows*, small enough as not to show any significant velocity gradient within the interrogation area. Rather than from each particles as in PTV, in PIV the displacement field is given by the correlation of the interrogation windows. The particles in the laser sheet reflect the light that is caught by the camera. For each temporal steps the correlation between the intensities of the interrogation windows, in the two frames at t_0 and $t_0 + \Delta t$, gives an average displacement vector. The union of the displacement vectors creates the final image obtained from the PIV processing and thus the velocity field.

A special camera is used so that it can store the first frame fast enough to be ready for the second exposure. To avoid having blurred images while analysing fast flows, laser pulses must be used. They freeze any motion and act as a photographic flash for the digital camera. The light sheet is obtained from the laser beam by simply using spherical and cylindrical lenses in combination. The particles should be as small as possible so that they are able to closely follow the flow. However on the other hand, they may not be too small, because then they will not scatter enough light, and hence produce too weak images. Any particle that follows the flow satisfactorily and scatters enough light to be captured by the camera can be used. The synchronization between the laser and the camera is controlled by the synchroniser.

PIV technique allows the identification of the velocity field in an almost 2D-flow. It is a powerful non intrusive techniques but it suffers from some limitations. For example

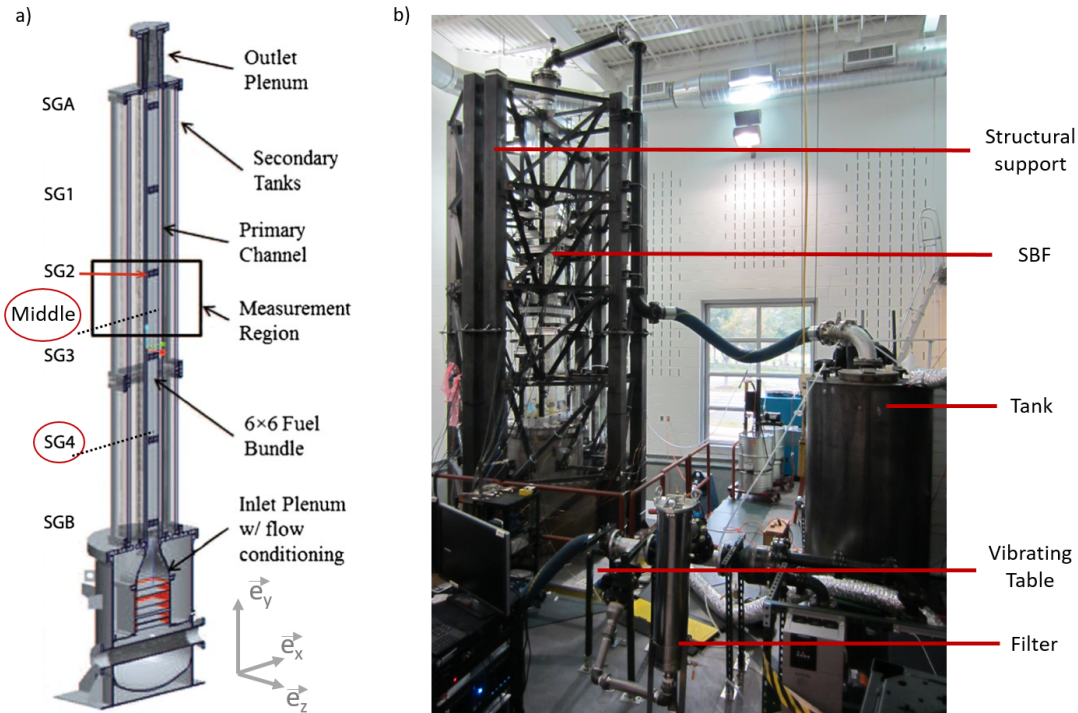


Figure 2.3: Shaking Bundle Facility is connected to a vibrating table. The acrylic rod bundle has 6 spacer grids and it is suspended in two containers one inside the other: *Primary channel* and *Secondary tank*.

the time delay between the laser pulses should be long enough to capture the displacement of the tracer particles and short enough so that the particles with an out-of-plane velocity component do not leave the light sheet. Furthermore, the accuracy of the PIV measurements will drastically improve as the particles follow the flow more closely: small particles are preferred but they can be used only if associated to high power lasers. These and further information on PIV and velocimetry techniques are available in [Raffel et al., 2018, Nagargoje, 2017].

2.2.2 Shaking Bundle Facility

The experimental facility consists of a closed flow loop with a vertical acrylic test section. The test section is installed on a vibrating table, $3 \times 3 \text{ m}^2$, and contains a full height (4 m) 6×6 acrylic bundle held together by 6 spacer grids (Fig. 2.3). The test section is composed by a *primary channel* and a *secondary tank*. The primary channel contains the assembly and is then surrounded by the secondary tank. This last serves as a safety barrier against possible leakages and prevents the Primary channel to undergo large deformations due to vibrations. An inlet plenum ensures the flow is homogeneous and with no memory of the traveled path from the pump to SBF. This is achieved using in the inlet plenum a series of metallic nets with different pitch, which shatter any macro velocity regions formed in the flow. Contrarily to prototypical PWR bundles, which are made of zircaloy, here rods

are made of acrylic. This results in a bundle much lighter than real ones. The use of acrylic materials allows to select a working fluid with the same refractive index. The working fluid selected for SBF is a synthetic oil solution (mainly P-cymene), which is index matched with acrylic at room temperature [Weichselbaum et al., 2015]. The surrogate assembly in SBF preserves the total length and the pitch/diameter ratio $P = p/d$ of a prototypical assembly: $P = 1.33$. The pitch is 19 mm, the rod diameter is $d = 14.25$ mm and the gap is $g = 4.75$ mm. Note that there are not any guide tube. The SBF bundle has been carefully designed to match the natural frequencies of the real fuel assembly, as explained in Bardet and Ricciardi [2016].

The bundle has a square section of 114 mm side, and it is inserted in a rectangular section with a 19 mm gap on the excitation direction x , and a 5 mm gap on the normal direction, z (See Fig. 2.5b). The larger gap in the direction of motion avoids any collision and allows to perform large amplitude shaking tests. The 1st natural frequency of the surrogate bundle in air is about to 2 Hz, matching that of prototypical bundles. In stagnant water, the natural frequency of SBF bundle drops to 1.2 Hz, mainly due to an added mass effect. The added mass effect on the surrogate bundle is larger than for prototypical PWR assemblies. When immersed in P-cymene (lower density than water), SBF first resonant frequency drops to 1.35 Hz while the second proper mode is found at 5.35 Hz for still oil [Weichselbaum, 2016]. At 1.60 mm and 0.04 g acceleration, SBF shaking table reaches full amplitude after a ramp of 4 cycles. The modal response of the system with respect to the lab reference frame is beyond the purpose of this analysis of this document, we will focus instead on the dynamics in the vibrating reference frame. A modal analysis on this rod bundle can be found in Capanna et al. [2022].

2.2.3 Data acquisition and processing

The PIV measurements for these experiments have been performed with a custom *flying* PIV system allowing the camera and the laser planes to move as the vibrating reference frame (Fig. 2.4). Both the primary channel and the secondary tank are filled with P-cymene solution, but only the primary channel is seeded with 30 μm hollow glass spheres, which are neutrally buoyant. The laser sheet comes from a dual cavity Nd:YLF laser with wavelength $\lambda_l = 527$ nm and the camera is used with acquisition frequency $f_{acq} = 256$ fps. Using index matched materials is attractive because light can pass through fluid and solid interfaces without any distortion. In particular, the light has straight path in the whole domain and is not deflected by the fluid-solid interfaces. Thus, velocimetry measurements can be made noninvasively, accessing the whole fluid domain. Depending on the room temperature, the refracting index of acrylic is matched with a solution of P-cymene and cinnamaldehyde (up to 1.6%). Indeed, PMMA has a refractive index $n_D \in [1.490, 1.494]$ and this solution has $n_D \in [1.4698, 1.4715]$ at 298 K [Fort et al., 2015].

We used 2 vertical measurement plane positions: FOV1 *Intraline* and FOV2 *Interline*, as shown in Fig. 2.5b. The laser sheet illuminates separately and alternatively these two

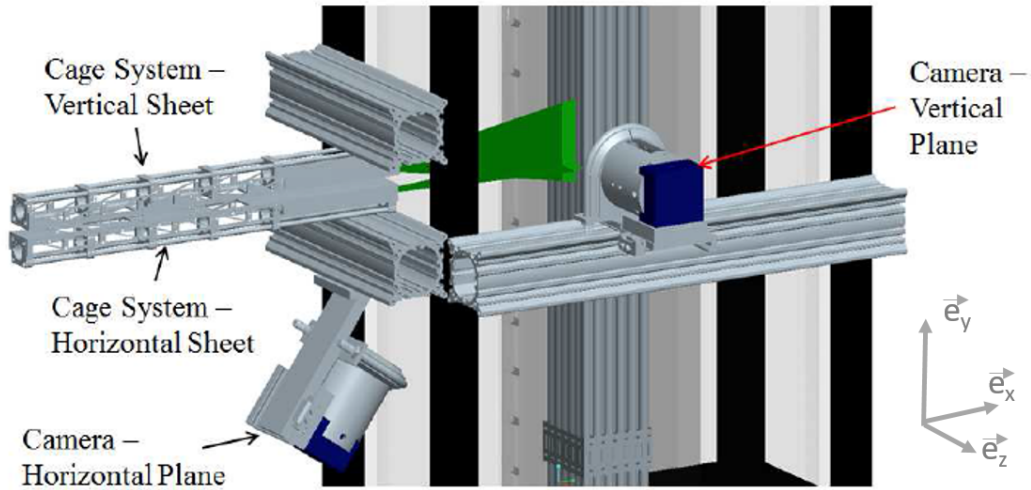


Figure 2.4: Flying PIV setup.

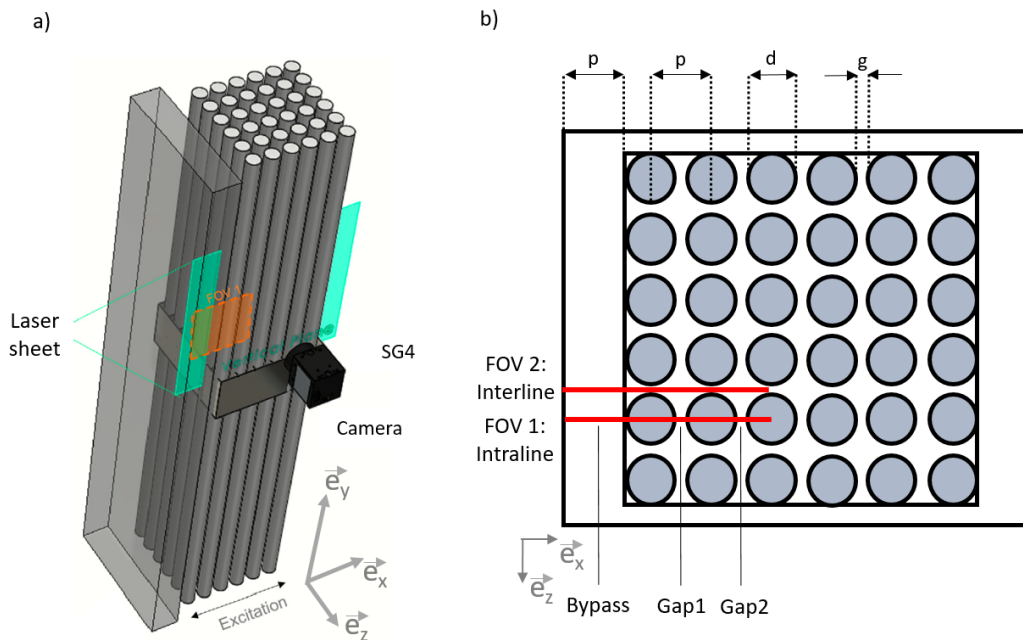


Figure 2.5: PIV measurement on SBF. Measurement regions are vertical plans and concern almost 3 fuel rods over 6, at height *Middle* and *SG4*. a) In this case, the measuring plane is FOV 1 *Intraline* in red. b) Thanks to the refractive index matching, the camera can be focused on two different, planes: *Intraline* is on the second row of rods while *Interline* is within the second and third rows of rods.

Table 2.1: Experimental matrix: input parameters

Case	Forcing Amplitude [mm]	Height		FOV		Mode	
		<i>SG4</i>	<i>Middle</i>	Intraline	Interline	1 st	2 nd
1	2.00	•		•		•	
2	3.00		•	•			•
3	4.00		•	•			•
4	3.00	•		•		•	
5	4.00	•		•		•	
6	5.00	•		•		•	
7	3.00		•	•		•	
8	5.00		•	•		•	
9	7.50		•	•		•	
10	3.00		•			•	
11	5.00		•			•	
12	7.50		•			•	
13	10.0		•	•		•	
14	12.5		•	•		•	

planes. *Intraline* is the measurement plane of the second row of fuel rods, while *Interline* is the measurement plane between the second and third rows of fuel rods. In these experiments the camera Field Of View (FOV) has been chosen in order to follow the motion of almost 3 fuel rods. FOVs for *Intraline* and *Interline* of a single frame are shown in Fig. 2.6. The measurements have been conducted at mid-height *Middle* and above the spacer grid 4 *SG4*. Due to the nature of PIV technique, which produces large amounts of datasets and a time demanding data processing, the analysis needs to be focused on a limited set of experiments. We chose data that allowed us to compare experiments by changing one parameter at a time. Tab. 2.1 shows the experimental matrix with all the parameters for each test. The input parameters are the forcing amplitude of the shaking table, the measurement height level and the oscillating frequency mode, which is chosen close to the 1st (1.30 Hz) and the 2nd (5.35 Hz). All the measurements have been taken on the Intraline but for 3 experiments also the Interline measurements have been provided.

The high speed camera acquires thousands of frames for each experiment. Examining the frame sequence we checked that, the bypass wall shown in Fig. 2.6 remains still, indicating that the camera is indeed in the same reference frame as the test section. In this reference frame, the rods move, hence one needs to isolate the fluid domain by using moving masks for FOV1 Intraline. These are created by following the borders of each fuel rod. The creation of the masks allows to easily track the assembly displacement during the experiment. Once the masks are applied, the calibration of the images is used to convert pixels in mm.

Since the test section is not easily accessible to insert a calibration target, the rod diameter and pitch are used as a calibration reference. Such a calibration does not allow to correct for distortions, which are anyway almost eliminated thanks to the refractive index matching technique.

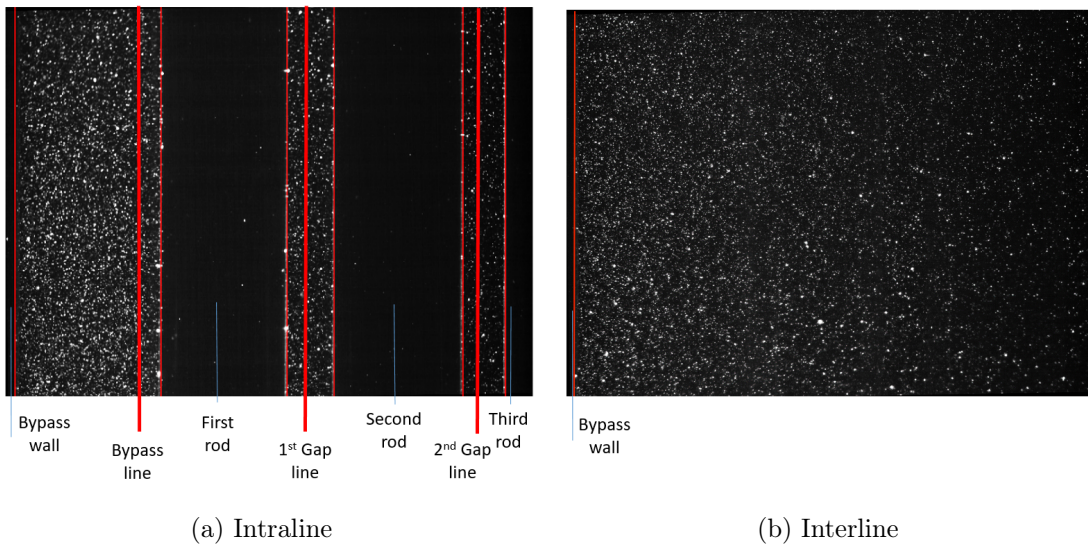


Figure 2.6: Fields of view: a) Intraline, left wall and 3 rods are visible; b) Interline, only left wall is visible.

The main parameters used for the calculations of the vector fields are: square windows, initial interrogation window size 64×64 pixels, final interrogation window size d_I with 32×32 pixels, 2 initial steps, 3 final steps, 50% overlapping, each frame is correlated with its subsequent and the maximum displacement between 2 subsequent frames is set to be $|\Delta X| = 5$ pixels. This satisfies criteria specified by Adrian [1991] for the ratio of the displacement of particle image pairs, $|\Delta X|$, to interrogation size, d_I , $|\Delta X|/d_I \leq 0.25$ for the magnification and data acquisition rate.

The calculation domain is 2-dimensional and the velocity field is:

$$\vec{V}(x, y) = u\vec{e}_x + v\vec{e}_y$$

where u is the velocity component along x (transversal component) and v is the component along y (axial component). As a final result of the processing, Fig. 2.7 shows the two-dimensional velocity field for one frame. PIV errors and confidence parameters can be found on Weichselbaum et al. [2016a].

The data-set for each experiment is three-dimensional: two dimension in space, x and y , and one temporal dimension that is given by the frame number. Thus the velocity field retrieved for each frame is bi-dimensional in space. We want to compare the fluid dynamic in the inner part of the assembly to the fluid dynamic outside the assembly. On the horizontal direction, the gap size remains constant within the assembly, while the bypass size varies during oscillation. Contrarily, the size on the vertical dimension is always the window height. In order to simplify the comparison between gaps and bypass, we focused only on the vertical direction y . Hence the analysis will be performed on three vertical lines: the Bypass and Gap lines indicated in the FOVs (Fig. 2.7) our domain of analysis: Gap

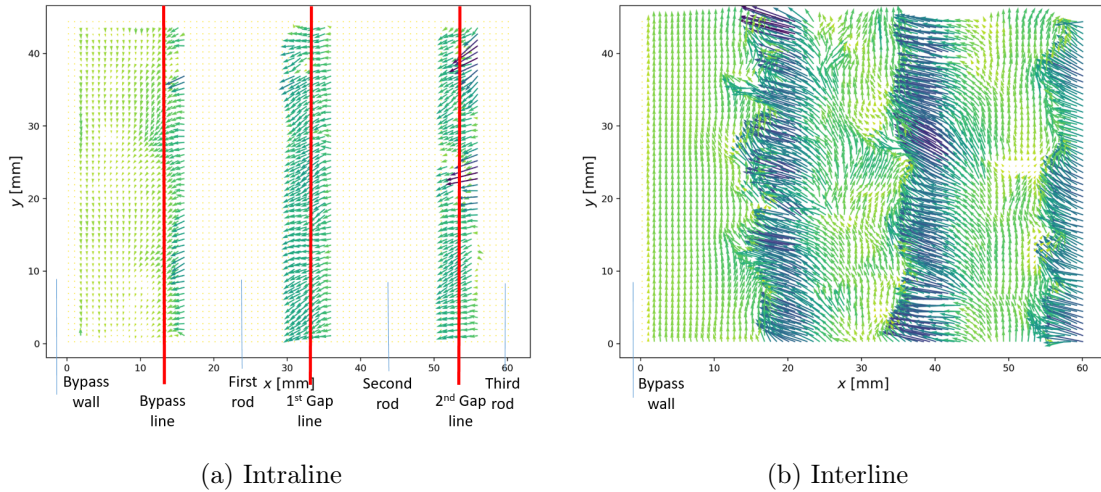


Figure 2.7: 2D velocity fields for a) Intraline and b) Interline; Bypass and Gap lines identifies the domain of analysis.

line is between 2 rods at equal distances and the Bypass line is at half-gap length from the left end of rod 1. Both these imaginary lines will follow the motion of the structure during the analysis. These lines are simply retrieved for the Intraline FOV, while for the Interline FOV they are reconstructed after the synchronization of the experiments. In Interline the rods are not visible, therefore we firstly synchronised Intraline and Interline experiments and then assume that the lines would follow the same path in both cases. To synchronise the 2 sets of experiments, we synchronised the velocity field close to the left wall. In fact, the presence of a impenetrable wall represents a strong boundary condition shared by both the Intraline and Interline FOV. We will deepen the discussion in Sec. 2.3.1.

Other than the velocity we will investigate the spatial Power Spectral Density (PSD) of the velocity on the same lines for both axial and cross velocities. The spatial PSD is calculated in 4 steps for each frame. First the mean velocity ($\bar{u}(t)$ and $\bar{v}(t)$) is subtracted for each line, giving the velocities $u'(y,t)$ and $v'(y,t)$. Then spatial Fourier transforms of $u'(y,t)$ and $v'(y,t)$ are calculated: $\mathcal{F}(u')(\xi,t)$ and $\mathcal{F}(v')(\xi,t)$, where ξ is the spatial frequency. To obtain the PSD, we took the square of the absolute value of these Fourier transforms, normalised by the integral of the Fourier transform and finally multiplied by the square of the standard variation of the velocity value ($\sigma_u(t)$ and $\sigma_v(t)$). Eq. 2.7 shows how the spatial PSD is calculated for each line and frame:

Table 2.2: Keulegan-Carpenter numbers

Case	Bundle Amplitude [mm]	Re	β	K
1	0.39	46.8	272	0.17
2	0.41	202	1120	0.18
3	0.53	262	1120	0.23
4	0.69	82.8	272	0.30
5	0.92	110	272	0.41
6	1.11	133	272	0.49
7	1.85	222	272	0.82
8	2.56	307	272	1.13
9	3.40	408	272	1.50
10	1.85	222	272	0.82
11	2.56	307	272	1.13
12	3.40	408	272	1.50
13	4.09	491	272	1.80
14	4.69	563	272	2.07

$$u'(y, t) = u(y, t) - \bar{u}(t) \qquad v'(y, t) = v(y, t) - \bar{v}(t) \qquad (2.5)$$

$$\sigma_u(t) = \sqrt{\frac{1}{N} \sum_{i=1}^N (u'(y, t)_i - \bar{u}'(t))^2} \qquad \sigma_v(t) = \sqrt{\frac{1}{N} \sum_{i=1}^N (v'(y, t)_i - \bar{v}'(t))^2} \qquad (2.6)$$

$$PSD_u(\xi, t) = \frac{|\mathcal{F}(u')(\xi, t)|^2}{\int \mathcal{F}(u')(\xi, t) d\xi} \sigma_u^2(t) \qquad PSD_v(\xi, t) = \frac{|\mathcal{F}(v')(\xi, t)|^2}{\int \mathcal{F}(v')(\xi, t) d\xi} \sigma_v^2(t) \qquad (2.7)$$

where N is the number of points along direction y . One should note that velocities in Eq. 2.5 and 2.7 depend only on y spatial coordinate because the domain is 1D and x values are fixed by the chosen line.

2.3 Results

Following the motion of the rods recorded by the camera one can retrieve the bundle oscillating amplitude. Knowing the amplitude, Eq. 2.2 allows to calculate the Keulegan-Carpenter number K . Those values are reported in Tab. 2.2. The oscillating amplitude for the assembly is a result of Intraline measurements. Since the PIV is non invasive and does not affect the dynamics of the system, changing both laser sheet position and camera FOV do not affect the bundle amplitude. Therefore, we can assume that for Intraline and Interline measurements with the same input parameters, the bundle oscillating amplitude is the same.

Referring to Tab. 2.1, one could notice that for the same *Forcing Amplitude* imposed to the shaking table we retrieve different *Bundle Amplitude* for the assembly. Under oscillation

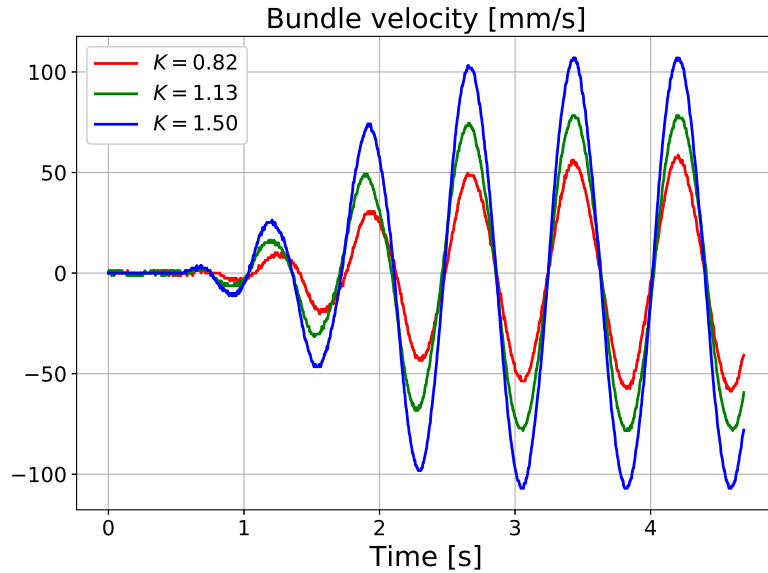


Figure 2.8: Synchronisation of assembly velocity signal for $K = 0.82$, $K = 1.13$ and $K = 1.50$ on Intraline (Cases 7, 8 and 9).

the assembly translates and bows. Therefore rod oscillation amplitude depends on the axial location along the bundle itself, as we expect from a clamped-clamped oscillating beam. Bundle oscillations are larger at *Middle* than at *SG4* (closer to the clamped point). The camera FOV is small enough, approximately 42 mm height \times 60 mm width, that the rod bowing deformation under vibrations can be neglected and rod motion can be considered as a rigid translation. Our experiments are performed in still fluid and we consider the rods translating horizontally, hence we can compare the results obtained at different level positions (*Middle* and *SG4*) as if they were on the same plane at different oscillation amplitudes. Rod bowing could not be neglected at larger FOV and rod deformations would be different on different level positions. With a larger camera FOV or in the presence of an axial flow, the results of different level positions could not be comparable without further considerations.

Weichselbaum et al. [2016b] observed a bundle oscillation amplitude on grid 2 (*SG2*) $A = 1.6$ mm with a forcing amplitude $A_{sbf} = 5.0$ mm and frequency $f = 1.6$ Hz in water. *SG2* is in between *SG1* and *Middle* and for symmetry reasons one could expect *SG1* to move as *SG4*.

2.3.1 Synchronization method

All the experiments with SBF have been carried out between 2015 and 2016, 7 years before the analysis presented in this document. Building the dataset, we decided to collect the highest possible number of significant and well described measurements. Unfortunately the data from the synchroniser were missing. Therefore, for all the experimental data in

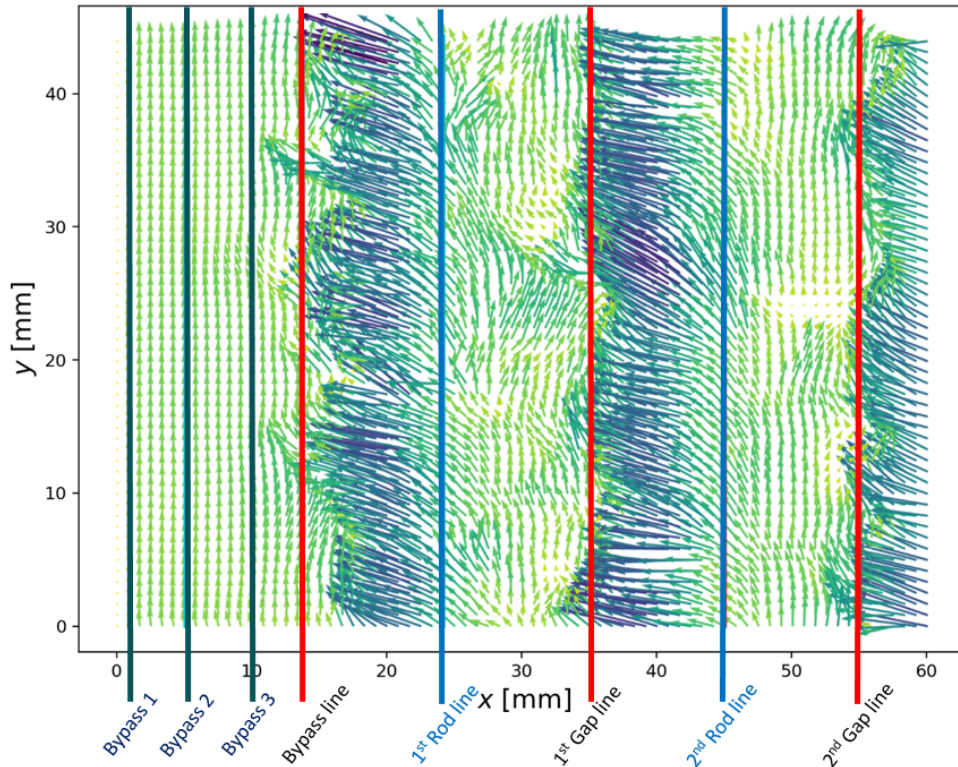


Figure 2.9: Vertical lines on FOV2 Interline.

Tab. 2.1, the time delay between the shaking table and the PIV camera is unknown. In order to have a proper analysis of different experiments, we needed to synchronise the measurements. As illustrated in the following sections, using the frames one can retrieve the bundle motion starting time and can synchronise all the Intraline data by superposition of the bundle motion signals. Fig. 2.8 shows an example of synchronization for experiments at $K = 0.82$, $K = 1.13$ and $K = 1.50$. The method to synchronize also the Interline with the Intraline measurements is a bit more cumbersome and needs a dedicated explanation.

There are basically 2 methods to overcome the Intraline-Interline synchronization problem. The first involves studying velocity fields near a boundary, the second uses the aberration present in the Interline data. Even if the experiments are carried out with matched refractive indexes, the curved shape of the rods induces an optical lens effect. This effect magnify the small difference between the refraction indexes. Thanks to the lens effect, by processing the Interline data one can estimate the position of the rods. However, the difference between the refractive indexes is very small and the lens effect is far to be clear. Therefore estimating the boundary of the rods remains more complicated and it is preferable to use the first method.

The strongest boundary condition in our measurements, is the impermeability of the left wall. The synchronization method consists in locating a vertical domain close to the

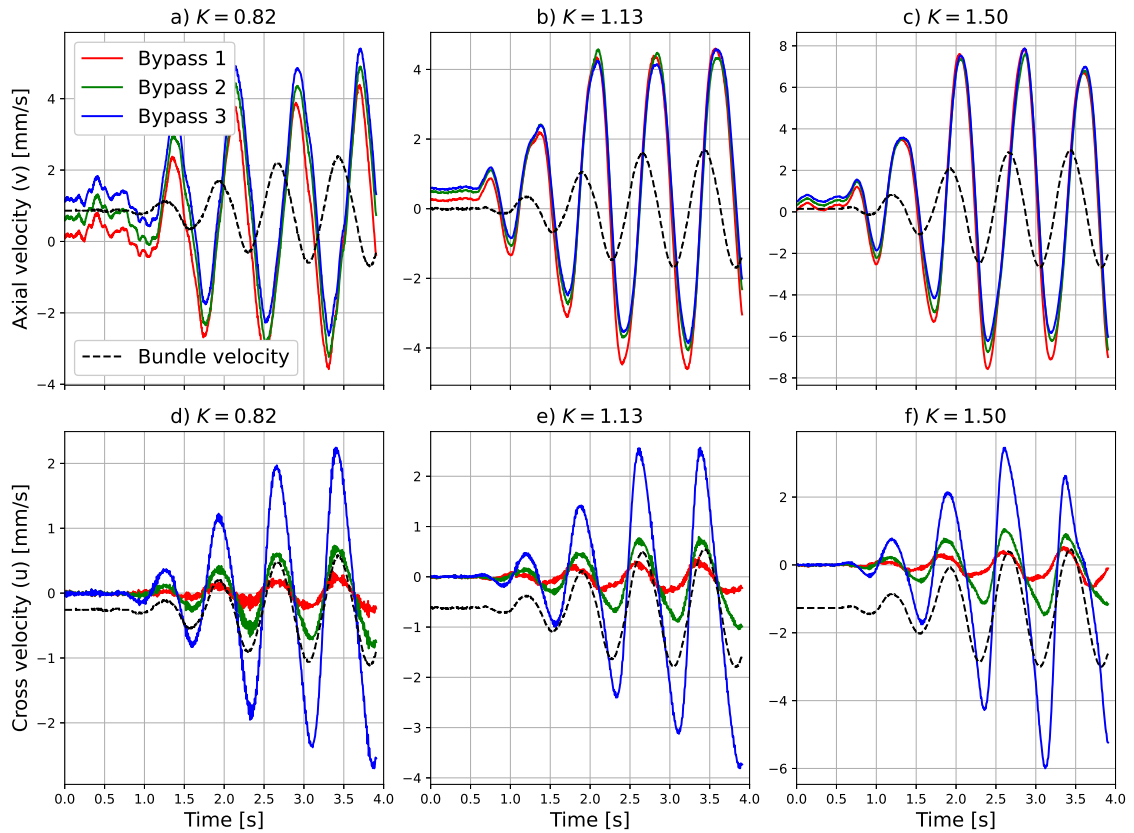


Figure 2.10: Axial and Cross velocities behaviour on Bypass lines for $K = 0.82$ (a, d), $K = 1.13$ (b, e) and $K = 1.50$ (c, f). Bundle velocity is dimensionless.

left wall for Intraline and Interline, and synchronize the velocity fields behaviour on that domain. We assume that the gap ratio G is small enough so that the fluid dynamic sufficiently far from the rod-bundle is not affected by the disposition of the rods inside the bundle.

One can chose different vertical lines in the bypass, as the investigation lines chosen for bypass and gaps. As shown in Fig. 2.9, the first Bypass 1 is the closest to the left wall, the other 2, Bypass 2 and Bypass 3 are equally spaced between Bypass 1 and Bypass line. Fig. 2.9 shows also 2 new vertical lines: 1st Rod and 2nd Rod. Only on Interline plan we can investigate the fluid behaviour just behind the rods; the 2 lines are at half distance between the Bypass and Gap lines.

The synchronization study starts with the data analysis on Intraline. Since the purpose is to synchronize the experiments, the analysis just on the average axial and cross velocities on the Bypass lines is sufficient. Fig. 2.10 shows the behaviour of averaged velocities on the Bypass lines on FOV1 Intraline for different K . The investigated K are the ones with the double FOV Intraline and Interline. On the Intraline (Fig. 2.10), it is clearly visible how the cross velocity strictly follows the bundle velocity and its intensity drastically vanishes approaching the left wall. Bypass line 1 registered averaged cross velocities far lower than

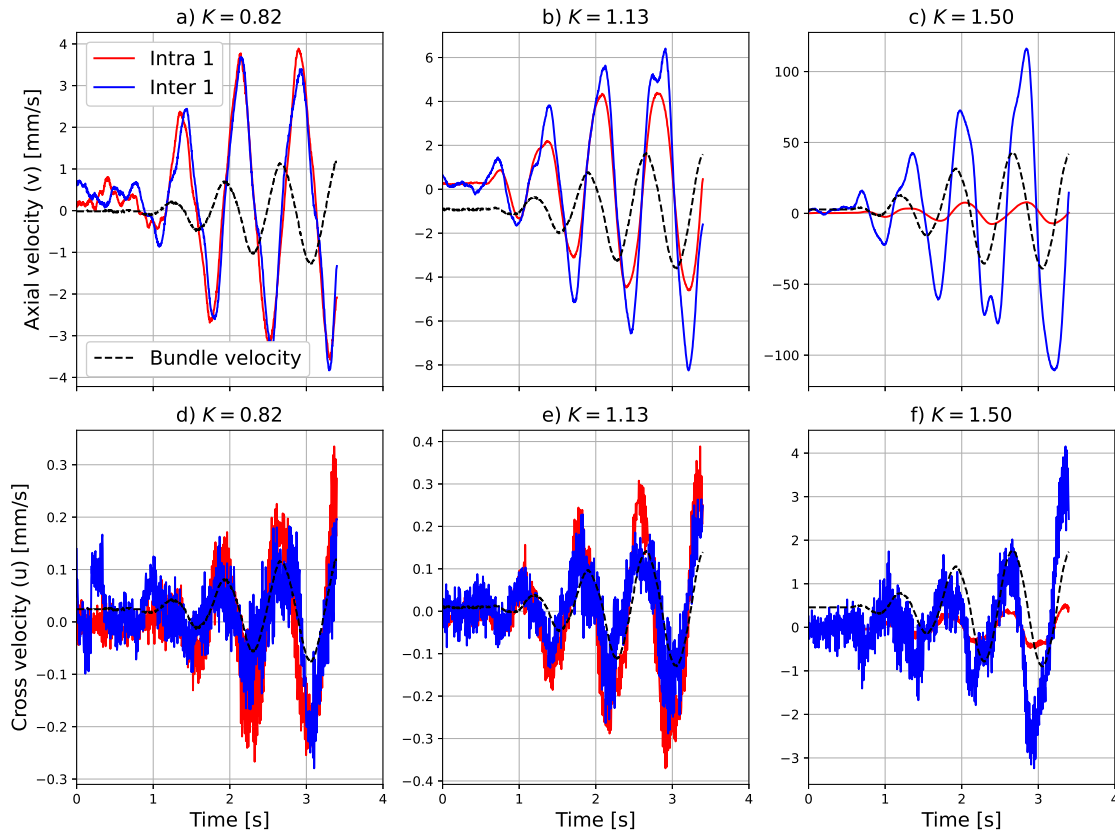


Figure 2.11: Superposition of Intraline and Interline for cross and axial velocities for Bypass line 1. Bundle velocity is dimensionless.

Bypass line 3. Conversely, the axial velocities appear to have all the same intensities for a fixed K . Furthermore the axial velocities present a 90° phase delay with bundle velocity. For $K = 1.50$ axial velocity increases by a factor of 2.

Fig. 2.11 shows the comparison on Bypass line 1 between Intraline and Interline planes when the experiments have already been synchronized. For $K = 0.82$ the axial velocities behave mostly in the same way, proving the basic assumption of low interference of rod presence near the wall. The rods are moving and although the Intraline plane is slightly more affected than the Interline plane, the effect on velocity near the wall is similar. This is expected in the low K limit (low G) especially for this relatively dense bundle. The behaviour of both velocities is the same for Intraline and Interline even on Bypass line 2 (see Fig. C.12). These two lines can thus be used to synchronize the Intraline and Interline experiments.

Close to the rod-bundle, on Bypass line 3, the behaviour of the velocities is not the same anymore. The first assumption of our methods does not hold so close to the bundle and so far from the impermeable wall. As shown in Fig. 2.12, the cross velocity is affected by the presence of the rods and its behaviour is in counter-phase between the 2 experimental planes. At $K = 0.82$, before the threshold, on the Intraline plane the averaged cross velocity

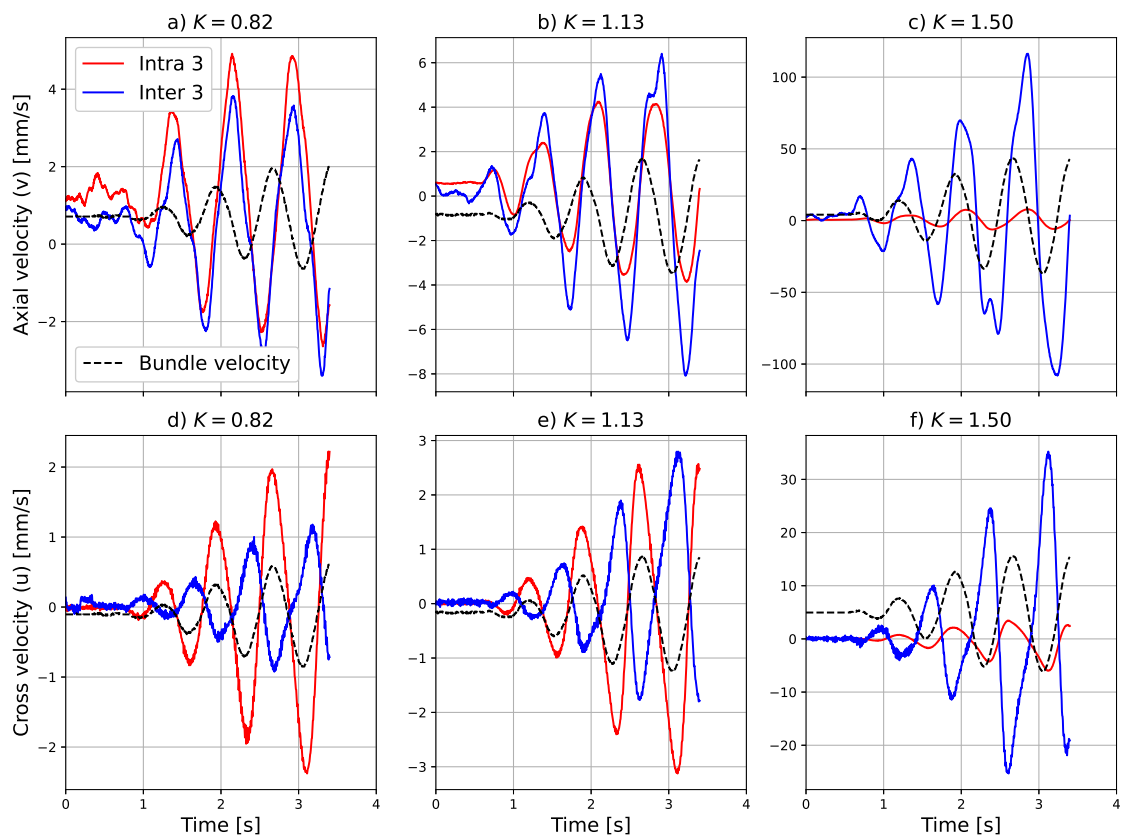


Figure 2.12: Superposition cross and axial velocities for Bypass line 3 for Intraline and Interline. Bundle velocity is dimensionless.

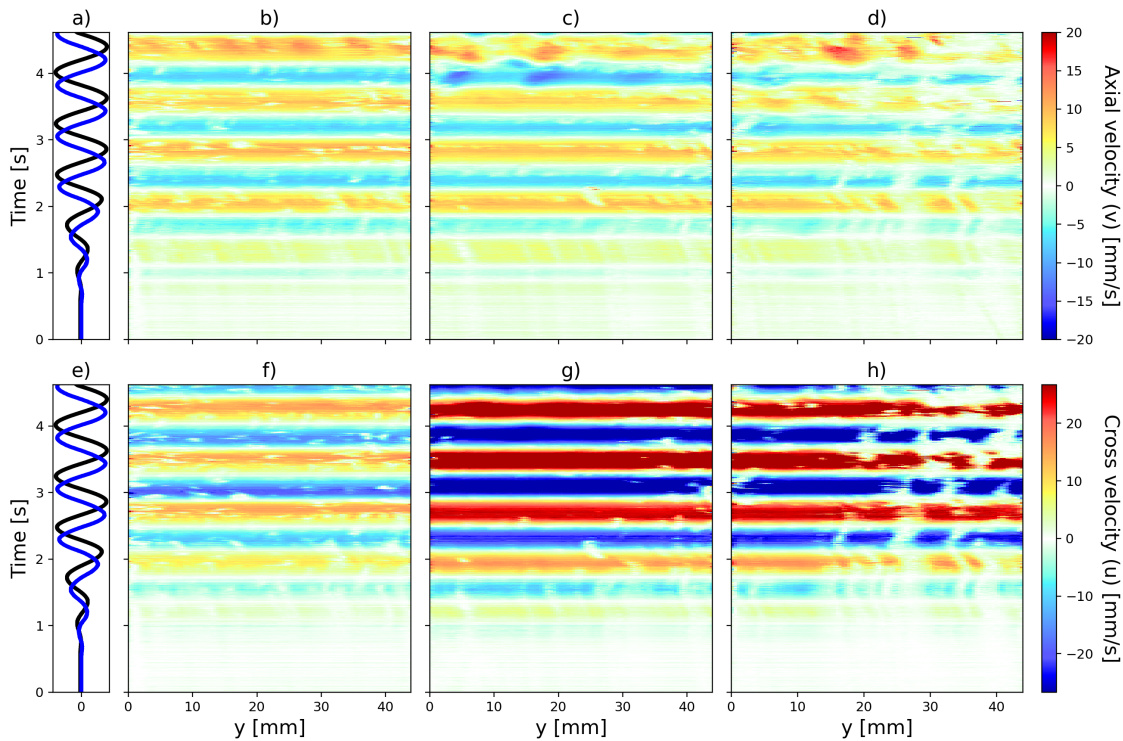


Figure 2.13: Initial transient for Case 9 ($K = 1.50$) on FOV Intraline. In a) and e) the black curve represents the assembly dimensionless displacement along x while the blue line is the assembly dimensionless velocity. Axial velocity on Bypass line b), on 1st Gap line c) and on 2nd Gap line d). Cross velocity on Bypass line f), on 1st Gap line g) and on 2nd Gap line h).

shows greater values. For $K = 1.13$, the velocities are similar in value, while for $K = 1.50$ the velocity on the Interline plane has a higher value with respect to the Intraline plane. The averaged axial velocities have the same intensity on Intraline and Interline planes for $K = 0.82$, while, starting from $K = 1.13$ the highest intensity is on the interline plane. The explosion in value is discussed with a model in section 2.4.

2.3.2 Results on FOV1: Intraline plane

The velocity signal in the Intraline plane starts by a transient stage to eventually reach a stationary full sinusoidal oscillation of the assembly. Starting time has been arbitrarily chosen with assembly at rest, and it is not related to the beginning of shaking table vibrations. Fig. 2.13 shows a color map plot of the velocity in the time-space (t, y) -plane for Case 9 ($K = 1.50$). Both axial and cross velocity profiles are showed along the Bypass line (b and f), the 1st Gap line (c and g) and the 2nd Gap line (d and h). Fig. 2.13a and 2.13e show the normalized displacement and velocity of the assembly along x .

Both axial and cross velocities are affected by the rods' motion. They are driven by the assembly displacement, and in particular on the Gap lines the cross velocity shows a

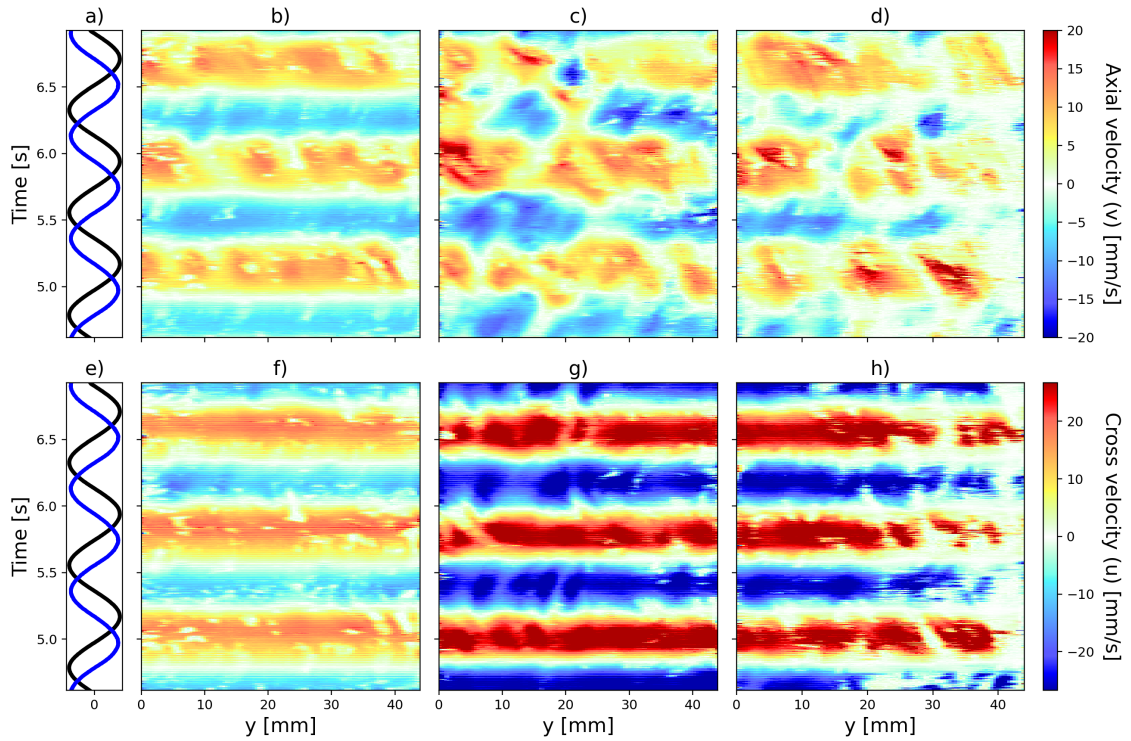


Figure 2.14: Time evolution of 3 full amplitude oscillations for case 9 ($K = 1.50$) on FOV Intraline. In a) and e) the black curve represents the assembly dimensionless displacement along x while the blue line is the assembly dimensionless velocity. Axial velocity on Bypass line b), on 1st Gap line c) and on 2nd Gap line d). Cross velocity on Bypass line f), on 1st Gap line g) and on 2nd Gap line h).

net increase as soon as the assembly reaches maximum displacement. This is naturally attenuated along the Bypass line since the left wall is farther away. As soon as the oscillations begin, we can identify a sinusoidal behaviour for both velocities, especially on the 2nd Gap line, where a sinusoidal pattern is clearly observable. On the third full amplitude oscillation, the velocities in the gaps are not homogeneous along y , which is the signature of vortical structures. The vortices appear sooner in the forcing cycle with increasing K (see Annex C for higher K number). These structures are characterized by higher velocity values.

During the stationary oscillation regime we can see the time evolution of these structures along the lines (Fig. 2.14). The axial velocity field breaks the (x, z) planar motion and becomes three-dimensional. This is evidenced by the complete separation of the velocity regions, accentuated again in the inner part of the rod bundle (Fig. 2.14 for instance).

The analysis of the Power Spectral Density (PSD), allows to outline the spatial frequency distributions and their behavior during the oscillation cycle. Each spatial frequency ξ is associated to a vertical dimension, therefore, the most repeated frequencies would lead to the most common dimension of the flow structure. The spectrogram of the spatial PSD is reported in Fig. 2.15, for both velocities and each line. Fig. 2.15d and Fig. 2.15h

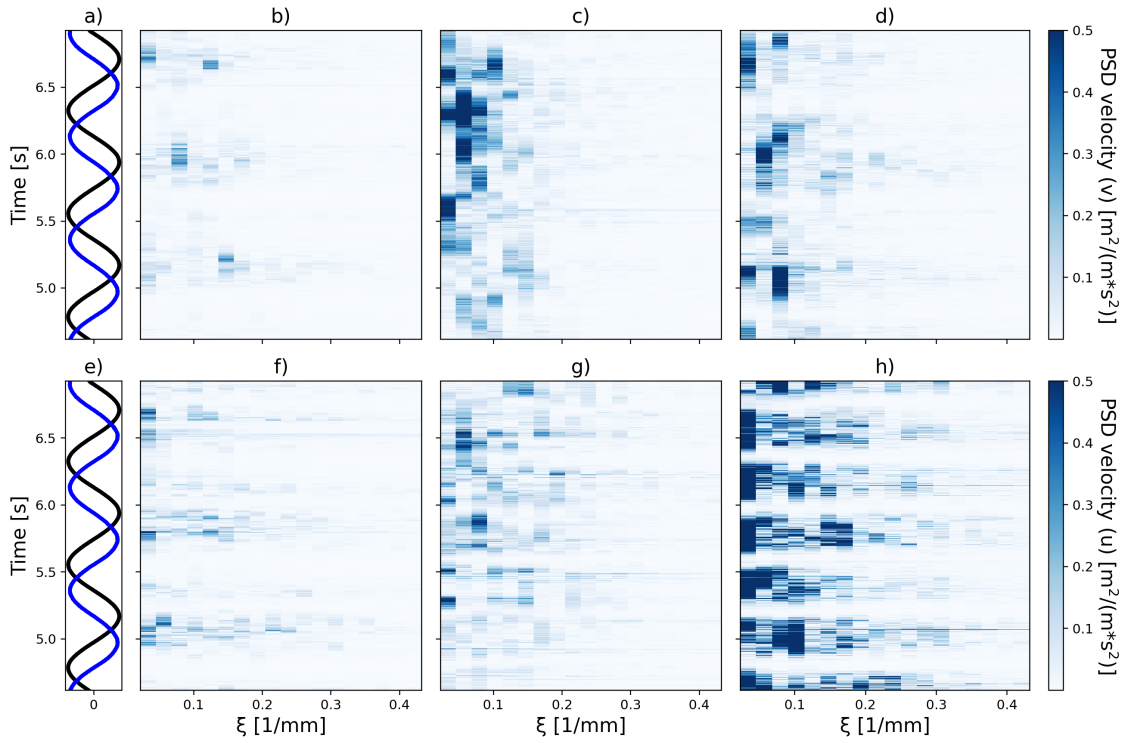


Figure 2.15: Spatial PSD evolution for Case 9 ($K = 1.50$) for 3 cycles at full amplitude oscillation. In a) and e) the black curve represents the assembly dimensionless displacement along y while the blue line is the assembly dimensionless velocity. PSD Axial velocity on Bypass line b), on 1st Gap line c) and on 2nd Gap line d). PSD Cross velocity on Bypass line f), on 1st Gap line g) and on 2nd Gap line h).

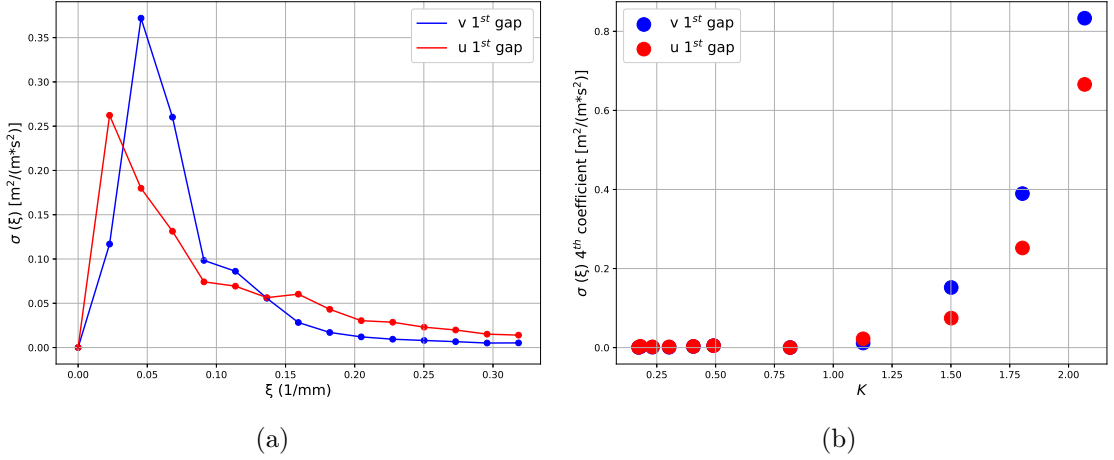


Figure 2.16: Spatial spectral analysis at full amplitude oscillation for 10 cycles. a) σ of spatial PSD coefficients for Case 7 ($K = 1.50$), both velocities, 1st Gap line. b) σ 4th spatial PSD coefficient vs K number.

show higher values over a wider spatial frequency spectrum with respect to the Bypass line (Fig. 2.15b and Fig. 2.15f). We investigated the behavior of the spatial PSD coefficients during a large number of cycles (i.e. 10) to identify the most important spatial frequencies. A method to perform this investigation is to evaluate the temporal standard deviation of spatial PSD: $\sigma_{psd,u}(\xi)$ and $\sigma_{psd,v}(\xi)$, abbreviated $\sigma(\xi)$.

Fig. 2.16a shows $\sigma(\xi)$ for the first spatial PSD frequencies for the 1st Gap line. Regardless of axial or transverse velocity, position in bypass or gaps, we see that the coefficients of greatest significance are in the range $\xi \in [0.02, 0.1]$ mm^{-1} . Even if $\sigma_{psd,u}(\xi)$ and $\sigma_{psd,v}(\xi)$ do not behave in the exact same way, for both of them the range containing most of the fluid dynamics is the same. There are 5 points in that range; excluding the firsts coefficients which corresponds respectively to 0 and to the PIV FOV height (about 42 mm), the other 3 are related to a vertical dimension in the range [10, 21] mm.

One might wonder how these $\sigma(\xi)$ coefficients vary as K changes. Fig. 2.16b shows the $\sigma(\xi)$ 4th coefficient ($\xi \sim 0.07$ mm^{-1}) behaviour for the axial and cross velocities in the 1st gap for 10 cycles at full amplitude oscillations. The $\sigma(\xi)$ 4th coefficient refers to spatial frequency $\xi \sim 0.07$ mm^{-1} , which corresponds to the radius of the cylinder. The plot shows a threshold effect starting at $K_{thr} = 1.13$. This threshold effect is observed for all the coefficients. Furthermore even Bypass and 2nd Gap line show the same behaviour. This results lead us to divide the K in sub-threshold, threshold and over-threshold value for the rod bundle, whenever K is lower or higher than $K_{thr} \sim 1.13$.

We chose the available K around the threshold and we analysed the temporal behaviour of the $\sigma(\xi)$ 4th coefficient value. For $K < K_{thr}$ (Fig. 2.17a-c) the value of the coefficients are a thousand time smaller than $K \geq K_{thr}$. Practically there is no temporal pattern, hence no structure, of any dimensions developed at this level. On the contrary, starting from $K = K_{thr}$ (Fig. 2.17d-f), fluid structures start developing cyclically, in particular the

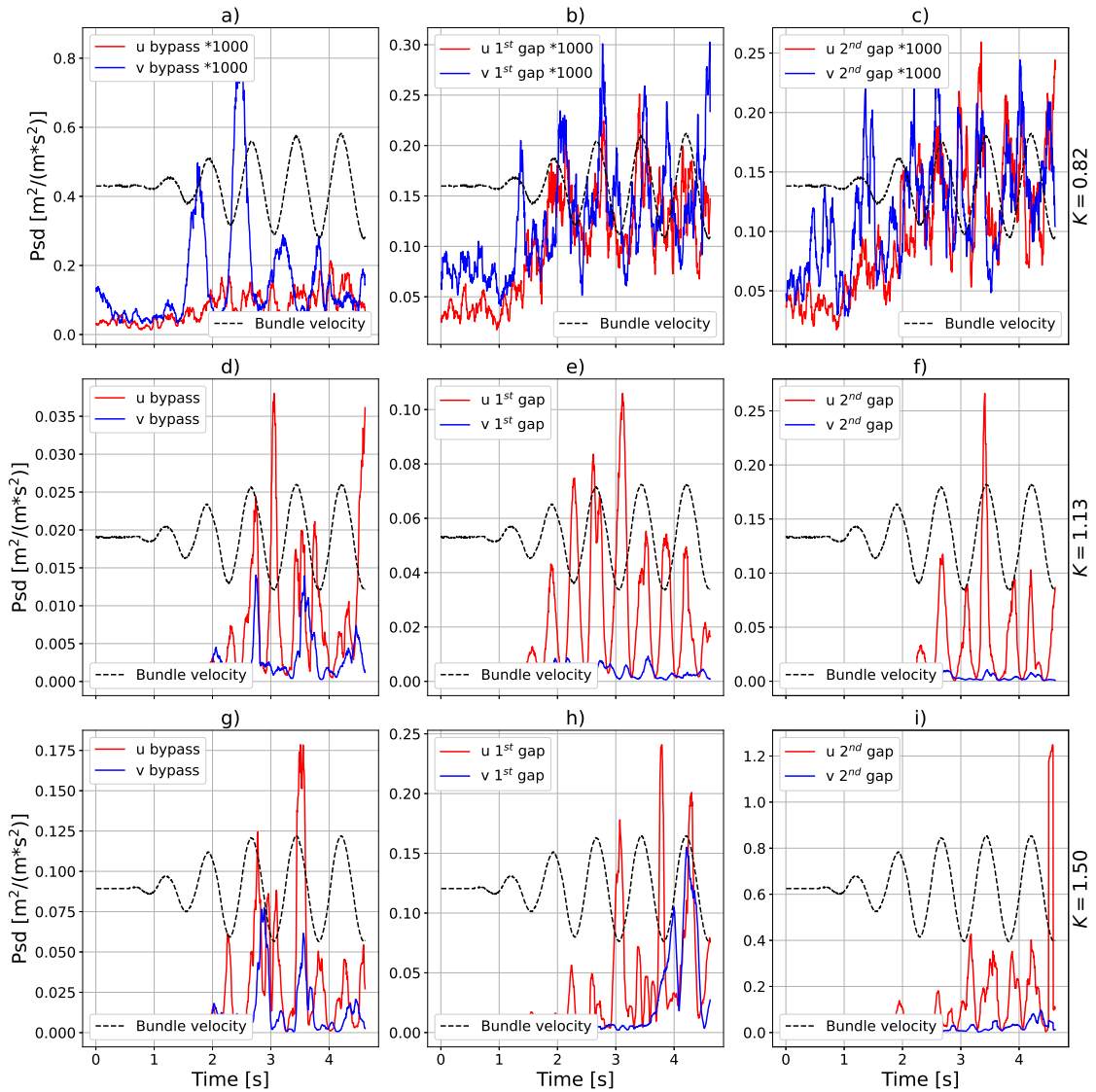


Figure 2.17: 4th spatial PSD coefficient evolution for axial and cross velocities. a) Case 7 ($K = 0.82$), Bypass line. b) Case 7 ($K = 0.82$), 1st Gap line. c) Case 7 ($K = 0.82$), 2nd Gap line. d) Case 8 ($K = 1.13$), Bypass line. e) Case 8 ($K = 1.13$), 1st Gap line. f) Case 8 ($K = 1.13$), 2nd Gap line. g) Case 9 ($K = 1.50$), Bypass line. h) Case 9 ($K = 1.50$), 1st Gap line. i) Case 9 ($K = 1.50$), 2nd Gap line. Bundle velocity is dimensionless.

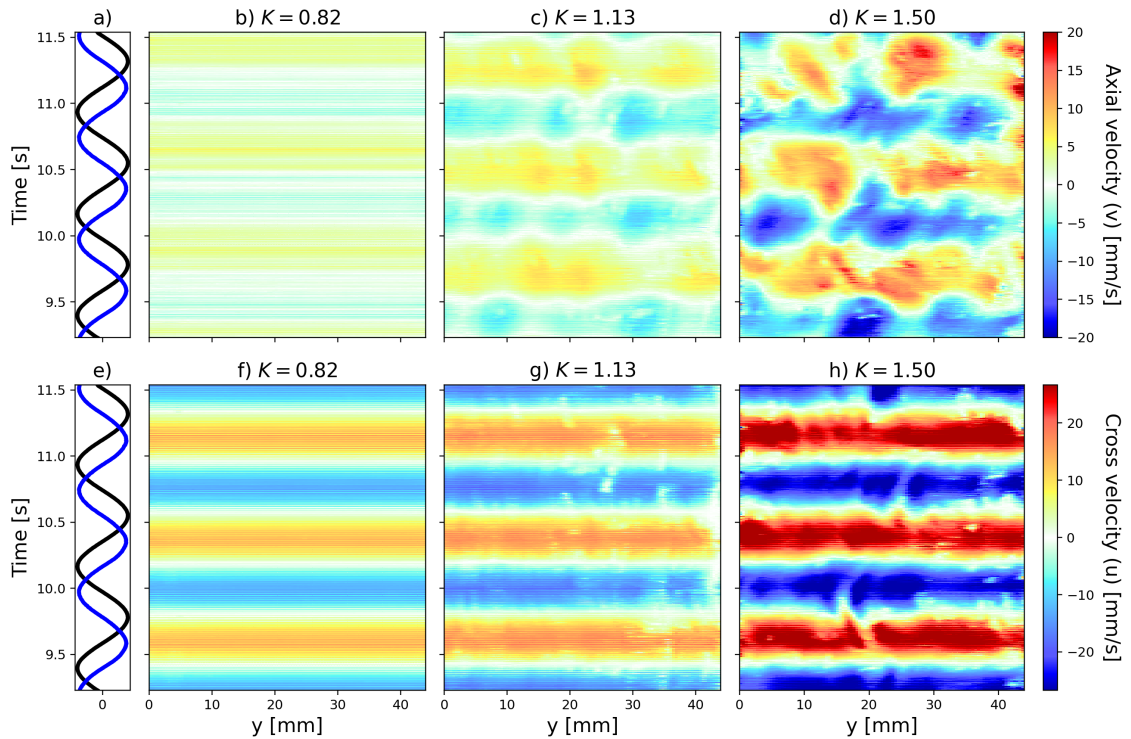


Figure 2.18: Comparison of axial (b, c, d) and cross (f, g, h) velocities for different K .

higher values of the coefficients suggests that this is more pronounced in the 2^{nd} gap. At higher K correspond higher velocities hence higher coefficient values, as in Fig. 2.17g-i for $K = 1.50$. Again, this is common to all the firsts spatial PSD coefficients and remains strongly valid for higher K numbers.

Fig. 2.18 shows the temporal evolution for both velocities, axial and cross, for $K \in \{0.82, 1.13, 1.50\}$. We can see for $K < K_{thr}$ the two-dimensional symmetry hold all along the oscillation, while near the threshold zone the fluid starts to break the symmetry and after the threshold three-dimension flow structures are more and more developed. While this is valid for the axial component of the velocity, the cross component seems to be less affected, barely showing any difference as K changes. The axial velocity behaviour is enhanced as K increases.

2.3.3 Results on FOV2: Interline plane

As explained in section 2.2.3, for the FOV Interline, the two velocities have been investigated following the vertical lines, Bypass and Gaps, identified in their equivalent positions on Intraline. Indeed the rod sections are not visible on this FOV and it is not possible to independently trace the vertical domains, but in this plane, we have the possibility to investigate the lines behind the rods: 1^{st} Rod and 2^{nd} Rod lines.

Figures 2.19 and 2.20 show the axial and cross velocities evolution in time for $K = 1.13$ on the Interline plane. At this K number the vortical structures appear after 5 full

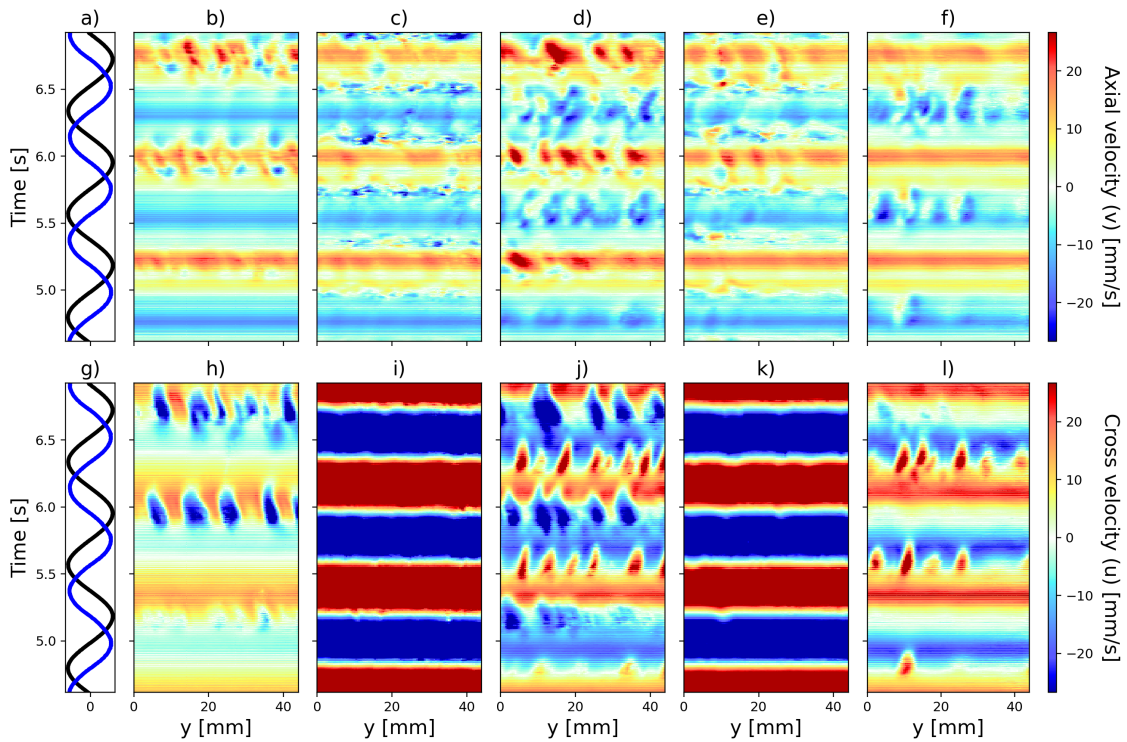


Figure 2.19: Time evolution of 3 complete amplitude oscillations for Case 11 ($K = 1.13$) on FOV Interline. In a) and g) the black curve represents the assembly dimensionless displacement along x while the blue line is the assembly dimensionless velocity. b) Axial velocity on Bypass line. c) Axial velocity between Bypass and 1st Gap lines. d) Axial velocity on 1st Gap line. e) Axial velocity between 2nd Gap and 1st Gap lines. f) Axial velocity on 2nd Gap line. h) Cross velocity on Bypass line. i) Cross velocity between Bypass and 1st Gap lines. j) Cross velocity on 1st Gap line. k) Cross velocity between 2nd Gap and 1st Gap lines. l) Cross velocity on 2nd Gap line.

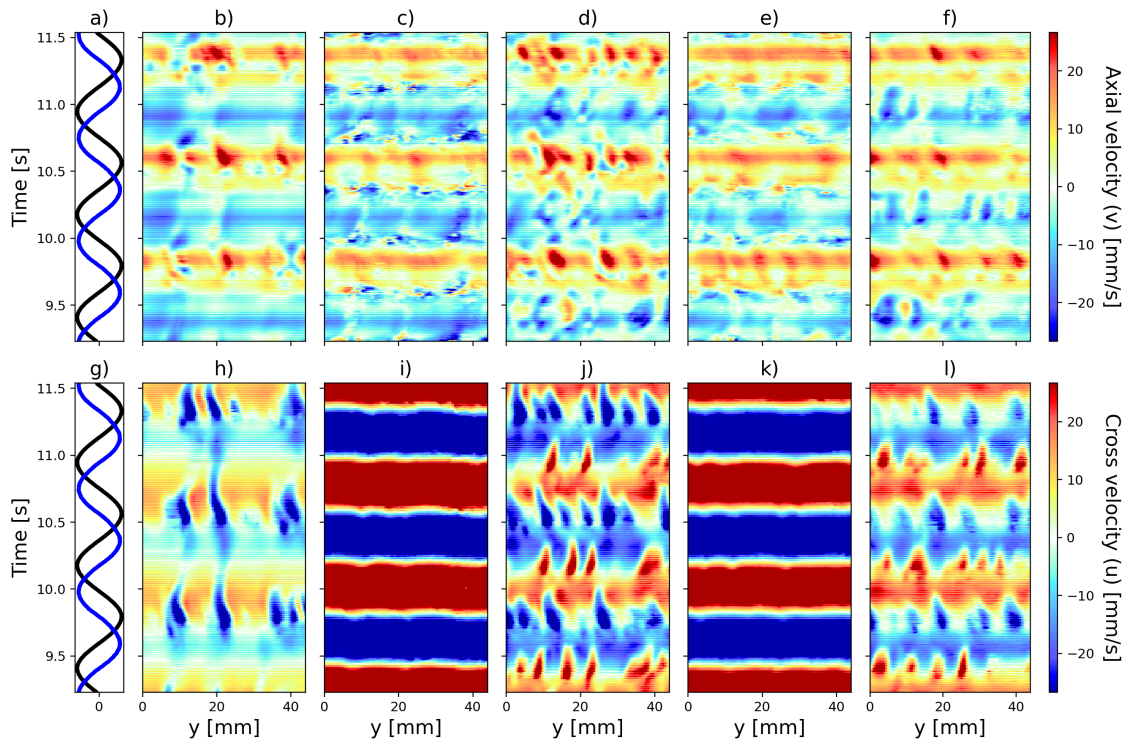


Figure 2.20: Time evolution of three full amplitude oscillations for Case 11 ($K = 1.13$) on FOV Interline. In a) and g) the black curve represents the assembly dimensionless displacement along x while the blue line is the assembly dimensionless velocity. b) Axial velocity on Bypass line. c) Axial velocity between Bypass and 1st Gap lines. d) Axial velocity on 1st Gap line. e) Axial velocity between 2nd Gap and 1st Gap lines. f) Axial velocity on 2nd Gap line. h) Cross velocity on Bypass line. i) Cross velocity between Bypass and 1st Gap lines. j) Cross velocity on 1st Gap line. k) Cross velocity between 2nd Gap and 1st Gap lines. l) Cross velocity on 2nd Gap line.

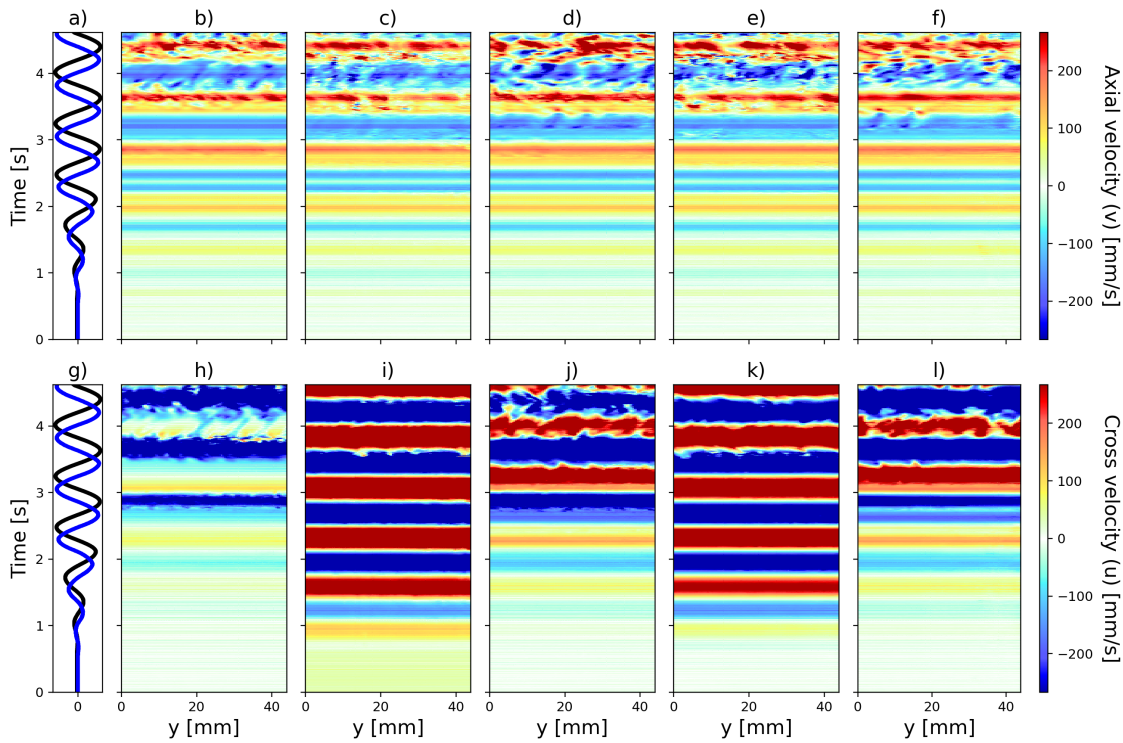


Figure 2.21: Initial transient for Case 12 ($K = 1.50$) on FOV Interline. In a) and g) the black curve represents the assembly dimensionless displacement along x while the blue line is the assembly dimensionless velocity. b) Axial velocity on Bypass line. c) Axial velocity between Bypass and 1st Gap lines. d) Axial velocity on 1st Gap line. e) Axial velocity between 2nd Gap and 1st Gap lines. f) Axial velocity on 2nd Gap line. h) Cross velocity on Bypass line. i) Cross velocity between Bypass and 1st Gap lines. j) Cross velocity on 1st Gap line. k) Cross velocity between 2nd Gap and 1st Gap lines. l) Cross velocity on 2nd Gap line.

amplitude oscillations. In particular on the cross velocity figures, the vortical structures appear to be well separated. This is due to the K number very close to the threshold. The velocity regions begin to develop but they stay separated for several oscillations. These regions are subjected to an axial transportation phenomena in the bypass, while remaining at a fixed distance in the gaps. The cross velocity on the Rods lines strictly follows the bundle velocity, while the axial velocity on the same lines behave as in the Bypass or Gaps lines.

Figures 2.21 and 2.22 show the velocity fields along the lines in FOV Interline at the same relative times as Figures 2.13 and 2.14. In Intraline the vortical structures appear with the first full amplitude oscillation, half cycle before than in the Intraline. Furthermore, Fig. 2.22 shows a more turbulent behaviour than Fig. 2.14. Even at $K = 1.50$ the cross velocity on the Rods lines follows the bundle velocity. The cross velocity reaches higher intensities sooner than on the Bypass and Gaps lines.

The involved velocities are hundreds times higher in Interline than in Intraline for

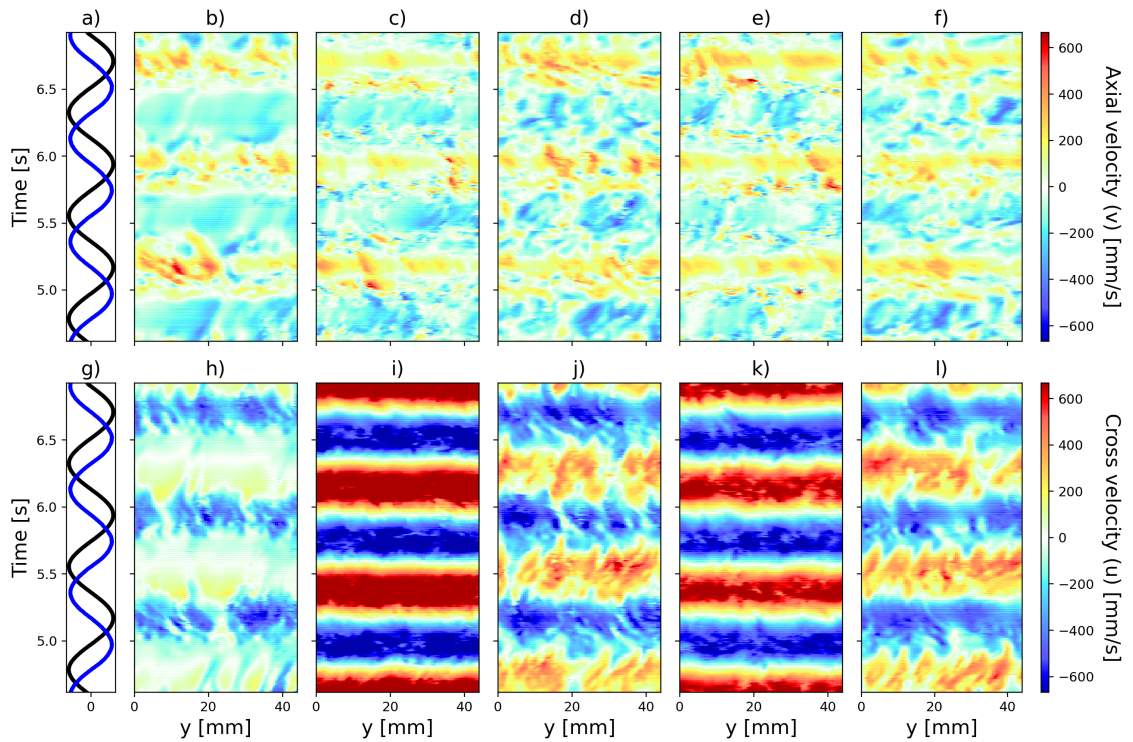


Figure 2.22: Time evolution of 3 complete full amplitude oscillations for Case 12 ($K = 1.50$) on FOV Interline. In a) and g) the black curve represents the assembly dimensionless displacement along x while the blue line is the assembly dimensionless velocity. b) Axial velocity on Bypass line. c) Axial velocity between Bypass and 1st Gap lines. d) Axial velocity on 1st Gap line. e) Axial velocity between 2nd Gap and 1st Gap lines. f) Axial velocity on 2nd Gap line. h) Cross velocity on Bypass line. i) Cross velocity between Bypass and 1st Gap lines. j) Cross velocity on 1st Gap line. k) Cross velocity between 2nd Gap and 1st Gap lines. l) Cross velocity on 2nd Gap line.

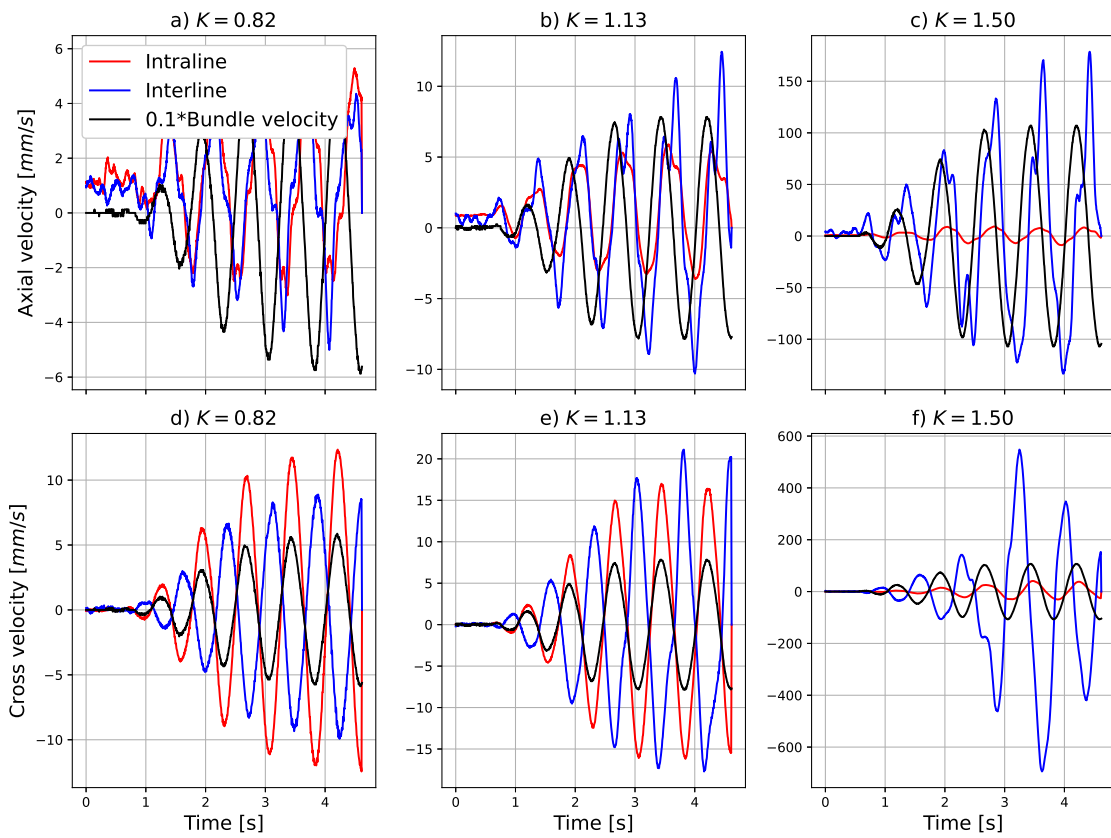


Figure 2.23: Evolution of average velocities on 1st gap line for $K = 0.82$ (a, d), $K = 1.13$ (b, e) and $K = 1.50$ (c, f). Axial velocities (a, b, c) and cross velocities (d, e, f).

$K = 1.50$ but not at lower K . Fig. 2.23 shows the average velocities on 1st gap, for both investigation planes, Intraline and Interline, for $K = 0.82$, $K = 1.13$ and $K = 1.50$. We can see how for $K = 0.82$ and $K = 1.13$ the averaged fluid velocities are smaller than the bundle velocity, even if passing from $K = 0.82$ to $K = 1.13$ the velocity increases non-linearly. Furthermore at $K = 1.13$ we are slightly over threshold and the Interline velocities are bigger than the Intraline velocities, contrary to $K = 0.82$. This pattern is hugely enhanced at $K = 1.50$ where Interline velocities are definitely bigger than in Intraline and even bigger than the bundle velocity, underling some hidden dynamics.

We will discuss these results in the next section. Other results are available in Annex C.

2.4 Discussion

The first observation we are going to discuss concerns the presence of axial velocity even for sub-threshold K , or equivalently, at really small oscillation amplitude. Weichselbaum et al. [2016b] proposed a pressure gradient driven axial flow explanation based on the fact that in this facility the assembly does not simply translate horizontally but it mostly deflects under his first vibration mode. Ricciardi and Boccaccio [2014] observed a higher average velocity in the by-pass than in the assembly gaps in presence of axial flow from a different facility that has the same pitch/diameter ratio. They showed a delay between the fuel assembly displacement and the fluid velocity that decreased with the increase of the axial velocity concluding the phenomenon is related to the fluid convection. Furthermore, the behaviour of the fluid velocity in the bypass was heterogeneous and affected by the presence of the rods on the same line, varying periodically from a lower velocity corresponding to the Intraline to higher values in the Interline. This variation is not present in the inner volume of the assembly, where the fluid appears to be more homogeneous. One should have always in mind that the velocities in the bypass region have to be weighted over a wider domain compared to the inner bundle region. Even if the velocities in bypass have lower values, that does not mean the flux in the by-pass is actually smaller than the one passing through the bundle.

In Weichselbaum's model the time-varying pressure gradient develops when the rigid bundle starts to oscillate under the external forcing. First, a cross flow is induced by a horizontal pressure gradient developed across the bundle width by the flow resistance induced by the rods. In the non-inertial frame of reference moving with the bundle, the bundle sees an oscillatory flow through it. The rods on the edge of the assembly face the incoming flow, the "front" have stagnation lines that develop along their height and, because of viscous effects, the "rear" of the bundle sees a lower pressure. It explains that the transverse pressure fluctuations due to bundle translation scale with the square of the bundle velocity. Then, another pressure gradient arises from the deflection of the rod bundle. At first-mode vibration considered, the displacement is maximal near the center and null at the bundle ends. This vertical deflection of the bundle results in stagnation pressure that varies along the height of the bundle. Indeed the stagnation pressure is

greatest at the point of maximum displacement and null at the bundle extremities (SGA and SGB in Fig. 2.3). Therefore 2 pairs of axial pressure gradients develop pointing in opposing directions, upward and downward. When the assembly moves closer to the left wall, there is a pair of upward pressure gradients: one on the left side of the channel from mid-height to SGA and one on the right side from SGB to mid-height. On the other hand, a pair of downward pressure gradients develops on the left side from mid-height to SGB and on the right side from SGA to mid-height. These two pairs of gradients are responsible for generating the observed global pulsating axial flows.

In Sec. 2.3 we have observed how both, axial and cross velocities show a threshold behavior depending on K . In order to investigate this behavior we will try to link the threshold values of K to critical values given in literature. The experimental matrix considered in this work only takes into account 2 β values (rod diameter stays constant and 2 excitation frequencies are analyzed). Furthermore at $f = 5.35$ Hz, K is far enough from threshold to imagine that the flow acts without instabilities, therefore we can consider just Mode 1: $f = 1.30$ Hz. From Eq. 2.3 and 2.4 we can calculate the threshold K_{thr} respectively for Hall and Sarpkaya models. An empirical way to retrieve a critical value $K_{cr,em}$, is based on the Keulegan-Carpenter parameter's physical meaning. The meaning of this parameter is the ratio of the distance traveled by a fluid particle during half cycle to the rod diameter. We call K_{em} the Keulegan-Carpenter number calculated with this definition, to distinguished from the K used in Eq. 2.2. K_{em} is defined in Eq. 2.8, where l is the distance traveled by the particle.

$$K_{em} := \pi \frac{l}{d} \qquad l = \frac{K_{em} d}{\pi} \qquad (2.8)$$

This definition has been formulated from Keulegan and Carpenter for a single rod, but we now have a confined rod bundle, which implies that there are some spaces where the distance a particle can travel is limited, namely, in the Intraline plane the maximum distance that a particle can travel is the total gap g from one rod edge to its next. g represents the first constraint imposed by the rod bundle; passing from rod to rod, and being parallel to the confinement wall, the maximum distance a particle can travel varies from the gap g to the pitch p , in the Interline plane. Because of the rod bundle symmetry, in the Interline plane, a particle could travel a maximum path equal to p . Therefore we can apply K_{em} definition in a rod bundle and define a minimum critical number $K_{cr,min}$ for which $l = g$ and a maximum $K_{cr,max}$ critical number where $l = p$, as defined by Eq. 2.9:

$$K_{cr,min} = \pi \frac{g}{d} \qquad K_{cr,max} = \pi \frac{p}{d}. \qquad (2.9)$$

Tab. 2.3 shows the different K_{thr} threshold values depending on their definition. We can see that $K_{cr,min}$ calculated for the rod bundle is in good agreement with Hall and

Table 2.3: Threshold Keulegan-Carpenter

	Hall	Sarpkaya	$K_{cr,min}$	$K_{cr,max}$
K_{thr}	1.48	1.33	1.05	4.19

Table 2.4: Parameters for K_{em} calculations

Case	K	l [mm]	$g - l$ [mm]	$K/K_{cr,min}$	$K/K_{cr,max}$
1	0.17	0.78	3.97	0.16	0.04
4	0.30	1.38	3.37	0.29	0.07
5	0.41	1.84	2.91	0.39	0.10
6	0.49	2.22	2.53	0.47	0.12
7, 10	0.82	3.70	1.05	0.78	0.19
8, 11	1.13	5.12	-0.37	1.08	0.27
9, 12	1.50	6.80	-2.05	1.43	0.36
13	1.80	8.18	-3.43	1.72	0.43
14	2.07	9.38	-4.63	1.97	0.49

Sarpkaya critical value for a single rod, while $K_{cr,max}$ is quite larger. These parameters should be deeper investigated or even better defined for the case of a rod bundle, taking in account firstly the number of rods and the p/d ratio, or eventually even the lattice of the bundle. In Tab. 2.4 we reported the values for l and the ratios $K/K_{cr,min}$ and $K/K_{cr,max}$ for the experiments at $f = 1.30$ Hz.

Taking into account the K_{thr} values from Tab. 2.3, we have two results: the behaviour corresponding to over-threshold are actually referring to cases where $K > K_{cr,min}$ and K_{thr} is almost equal to $K_{cr,min}$, $K_{thr} = 1.08 \cdot K_{cr,min}$ justifying the threshold effects. We can see how the instabilities start when the free path l become larger than maximum allowable path in the Intraline g . On the other hand, none of our experiments has $K > K_{cr,max}$, meaning that for our definition of K_{em} in the rod bundle, the fluid is always sub-threshold on FOVs Interline. This is in contrast with the results showed in Sec. 2.3.3.

The instabilities found in Intraline for $K > K_{cr,min}$ can be explained with Honji [1981] model. Honji introduces a streak spacing λ , that is constant with β and decreases with amplitude. λ can be seen as a vertical length that divided two consecutive streak lines along which vortices travel. According to Fig. 2.15 and 2.16a these λ are in the range [10, 21] mm suggesting this fluid behaviour is somehow dictated by the rod diameter. K - β map of Elston et al. [2006] does not report the flow regimes for our frequency parameter $\beta = 272$ and, in any case, it does not take into account the presence of more than one rod; a rod bundle K - β map with a new definition of key parameters is necessary to deepen rod bundle oscillating analysis. Indeed, it is difficult to say if our K and β parameters will actually fall into one regime or, depending on pitch/diameter ratio and the number of rods present in the bundle, these regimes could merge or disappear. Furthermore the two-dimensional symmetry has different meaning for a confined rod bundle compared to a single rod. First a rod bundle does not necessarily have a point or axis of symmetry. For a

rod bundle definition of global and local symmetries are necessary and useful in order to better understand the fluid-structure interactions. For example our FOV Intraline, due to its position, sees some local symmetry effect but not the global symmetry present at real center of the assembly. Therefore, those effects would be less enhanced as the number of rods increases and would be stronger as the confinement reduces.

Finally we observed that for FOV Interline the velocities are higher than for FOV Intraline at $K > K_{thr}$. Around the rods, however, some instabilities have been created without shedding. We can imagine that these fluid instabilities result in a virtual enlargement of the rod diameter. In Interline, this effect would correspond to a shrinking of the passage section and an increase in velocity, producing a sort of jet. This behaviour has been reported by both Ricciardi and Boccaccio [2014], Weichselbaum [2016]. Another reason of these higher velocities is linked to the position of our FOV. Indeed the fluid is mostly affected by the rod-bundle oscillation in the xz plane. The fluid is free to follow the vibration along x in the Interline, while in the Intraline it has to circumvent the rods. Hence on FOV Intraline the fluid velocity is also moving along the z -axis, entering to the page (or exiting), while in the Interline the fluid velocity is moving mostly along x direction.

2.5 Conclusions

We have presented some unique results made with flying PIV in MIR condition to measure the flow velocities in the inner part of a confined rod bundle under vibration. To the author's knowledge only this facility is capable of such a study. We showed that the behavior of velocities induced by the assembly oscillation varied in relation to the amplitude of the vibration itself, resulting in a threshold for which three-dimensional fluid structures broke planar symmetry. These fluid instabilities affect the energy transmission from the structure to the fluid, hence, the fluid-structure interactions. Therefore, it is important to determine when these instabilities begin. To predict the Keulegan-Carpenter number threshold for a rod bundle, one could think to use $K_{em,min}$ value we proposed in this chapter. It is actually inspired from the very definition that Keulegan and Carpenter gave to this number, using the gap between the rod as maximum distance a fluid particle can travel in half a cycle. We have show how the instabilities begin in the inner part of the assembly and in the Intraline plane before than in the Interline. Rod bundle vibration in still fluid need more investigations in order to better understand the dependencies of the hydraulic forces from the fluid-dynamics and to be able to estimate better drag and mass coefficients. A new step in this direction will be done with the successor of SBF which will allow us to measure the forces acting on the rod bundle and experimentally link force coefficients to the fluid dynamic.

Drag coefficient estimation in FSI for PWR fuel assembly bowing

Contents

3.1 Introduction	53
3.2 Experimental methods	54
3.2.1 Eudore	56
3.2.2 Force measurements	57
3.2.3 Laser Doppler Velocimetry	59
3.3 Experimental results	63
3.3.1 Force	63
3.3.2 Velocity	67
3.4 Analytical model and identification of coefficients	71
3.4.1 Line load model	73
3.4.2 Displacement field under line load u_1 and punctual force u_2	73
3.4.3 Resolution: finding c_N from measurements	74
3.5 Porous Medium Approach	75
3.6 FSCORE numerical resolution	78
3.6.1 Comparison of experimental and numerical results	79
3.7 Conclusions	81

Summary

In the previous chapter we have investigated Keulegan-Carpenter instabilities for a rod-bundle. Their connection with the drag coefficient for an assembly is beyond the analysis presented in this document. However, the development of fluid instabilities affects all the mechanical phenomena in the fluid-structure interaction, such as the added damping, added mass, rigidity, etc. In that sense, the analysis of Keulegan-Carpenter instabilities

on small scale can lead to define the drag coefficient for the rod in the bundle. On the contrary, in this chapter we discuss a method to retrieve the drag coefficient for a rod in the bundle starting from force and velocity measurements for the whole assembly.

In a PWR core, assembly bowing can be a serious problem for managing the power during normal operation or for periodical maintenance. One of the causes of this phenomenon is the transverse flow in the core, generated by the nonuniformity of the axial flow which the assemblies are subjected to. The fluid force acting on the assembly depends on drag and inertia coefficients. Studying the fluid-structure interaction in the core for design or maintenance, nuclear industries need to be able to evaluate the fluid force coefficients. Modeling the mechanical behaviour of a PWR core is even more difficult because of the complex geometry and the numerous friction points that lead to non-linearities. A simple but efficient way to deal with these issues is the porous medium model proposed by [Ricciardi et al. \[2009a\]](#). In this model, the equations used at the fluid-structure interface require empirical parameters such as the added mass coefficient, the axial and the normal drag coefficients.

These coefficients are empirical and retrieved on experimental basis. In this chapter we will introduce a new experimental setup at CEA, Eudore, which hosts 3 half-scale PWR surrogate fuel assemblies in a line. Eudore is a adjustable facility with several of different configurations. This test section is linked to two hydraulic pistons and lies on 2 rails. It is connected to a pump by a hydraulic loop called Mercure 400, which allows a maximum flowrate of 400 m³/h. Thus, in Eudore the assemblies can be subjected to a high flow-rate. The 2 hydraulic pistons allow two kind of experiments on Eudore: Static and Dynamic. On Static experiments the pistons are stationary and there is no external vibrational solicitation imposed, whereas in Dynamics an oscillation is imposed to the test section. This chapter is dedicated to Static experiments, Dynamic experiments being studied in the next one.

Eudore is equipped with force and displacement sensors. A set of diaphragms can impose different inlet flow-rate independently for each assembly in the line. Finally, several windows are disposed all along the test section in order to perform non intrusive velocimetry or displacement measurements. For all these peculiarities, Eudore is unique and represents the state of the art of fluid structure interaction facilities with a plurality of assemblies under axial flow with the possibility to impose a vibrating external force.

This chapter covers forces acting on the assemblies by a non-uniform flow profile. By mean of the Laser Doppler Velocimetry (LDV), the velocity profile along Eudore height is retrieved. Force results show a parabolic dependence on the flow-rate. By mean of LDV measurements one can see how the presence of the rods is an important hydraulic resistance for the flow-rate. The flow-rate is almost completely homogenized at about one quarter of Eudore height (Plan B in the chapter). After showing the experimental results, we discuss an analytical model to retrieve the normal drag coefficient starting from the measured forces and velocities. This coefficient is then used in FSCORE, the numerical software based on the porous medium approach. Finally a comparison between experimental and numerical

data is shown. Two cases are considered: the first with an average drag coefficient equal for all the assemblies, the second with a dedicated drag coefficient for each assembly. Since the geometry is the same for every assembly, one would opt to use the same drag coefficient for each assembly. However, the assembly confinement plays a role in the fluid structure interaction, above-all on Eudore confinement values. In the selected Eudore configuration, the confinement is smaller than the gap. Therefore the lateral assemblies are more affected by the confinement than the central assembly. This could explain the difference in the drag coefficient.

3.1 Introduction

The problem of bowing in PWR assemblies has been known for some time. [Andersson et al. \[2005\]](#), [Gabrielsson et al. \[2018\]](#) describe what was the first documented case of assembly buckling in 1994 at the nuclear power plant Ringhals. In that case, the physical phenomenon was noticed after an incomplete rod insertion (IRI) accident of a control rod. The deformation of the assembly had deformed the guide thimbles, increasing friction and preventing the nominal insertion of the control rod.

During power plant maintenance, assemblies are regularly extracted and reinserted into the core. The study of the hydrodynamic forces on the assemblies aims at optimizing this operation, preventing or reducing assembly deformation. [Andersson et al. \[2005\]](#) found the largest deformation to be 20 mm, a length comparable to the nominal gap between 2 assemblies. Assembly bowing may also induce a power tilt, a common issue due to a permanent asymmetry of the power distribution [[de Lambert et al., 2019](#)]. Thus, assembly bowing can be a serious problem not only to manage the power during normal operation but also during periodical maintenance.

[Wanninger et al. \[2018\]](#) carried out a sensitivity analysis, enlightening the different physical phenomena that can induce assembly deformation. The three most relevant phenomena are: irradiation creep, assembly growth, and hydraulic lateral forces. The authors describe the structural and material behaviour, covering the first two phenomena causing assembly bow. This paper focuses instead on the third one: lateral forces and flow redistribution. We hypothesise that lateral hydraulic forces arise mainly from inhomogeneities of the inlet flow rates. [Horváth and Dressel \[2013\]](#), [Wanninger \[2018\]](#) have analysed the flow redistribution between the inlet and the outlet and their results suggest that assembly bowing is itself a cause of lateral flows. Hence, bowing and lateral flows may amplify each other.

Modelling the mechanical behaviour of a PWR core is complicated by the complex geometry and the numerous friction points that lead to non-linear phenomena. [Ricciardi et al. \[2009a\]](#) proposed to model a PWR core as a porous medium, averaging over the entire core domain the structure and fluid equations. Lately [de Lambert et al. \[2021\]](#) proposed different 1D hydraulic models to reproduce the flow redistribution upstream from the grids for two fuel assemblies separated by a water gap that are not taken into account

in the porous medium approach of Ricciardi et al. [2009a] and that may be responsible for important fluid-structure interactions. On the same note, Ricciardi et al. [2022] analysed the flow on a rod array for a non-zero angle of attack. These approach that account for lateral flow can, in principle, be integrated into the porous medium approach to improve its predictions. However, the equations used at the fluid-structure interface in the porous model are empirical [Païdoussis, 2003] and they require empirical coefficients that account for the effect of a lateral flow. To evaluate these coefficients, Joly et al. [2018], used the 2D TLP model, based on the works of Taylor [1952], Lighthill [1960], Païdoussis [1966a] and on the more recent work of Divaret et al. [2014].

Another approach to estimate these coefficients is to measure them experimentally. At the CEA in Cadarache, many experimental setups have been built in the last 30 years, with the aim of studying assemblies mechanical behaviour when interacting with the water flow. There have been full-scale [Collard et al., 2005, Ricciardi and Boccaccio, 2014] and reduced-scale setups, created to study transverse flow effect [Peybernes, 2005] or coupling between assemblies [Ricciardi et al., 2010], [Capanna et al., 2019]. However, neither the flow velocity profile through the assemblies nor the hydraulic forces acting on them were measured during these experiments. The state-of-the-art setup is Eudore, a new facility hosting 3 half-scale fuel assemblies in a line. It allows us to study experimentally the effects of a flow redistribution on the assembly by measuring both the fluid forces acting on the assemblies and the flow profile. The purpose of this chapter is to use the experimental data of Eudore to derive, through an analytical model, the normal drag coefficient. Then one can use this coefficient to numerically solve the fluid-structure interaction problem with porous medium approach. The comparison between the experimental and numerical results estimates how well the simulations approximate the behaviour of the assemblies.

The chapter is organized as follows. The next section introduces Eudore, enlightening its major features and how the force and velocities are measured. The LDV technique is briefly illustrated. Force and velocity results are shown. The analytical model is presented to retrieve the normal drag coefficient based on the experimental data. The porous medium approach is introduced summarizing the model's main equations. A sensitivity analysis on the porous medium numerical code is performed before showing comparison between numerical and experimental results.

3.2 Experimental methods

In order to be able to fully understand the force and velocity measurements results, one needs to be acquainted with the experimental methods. This includes the basis of the velocimetry technique and the description of the experimental facility, Eudore, which is the key-tool of this analysis.

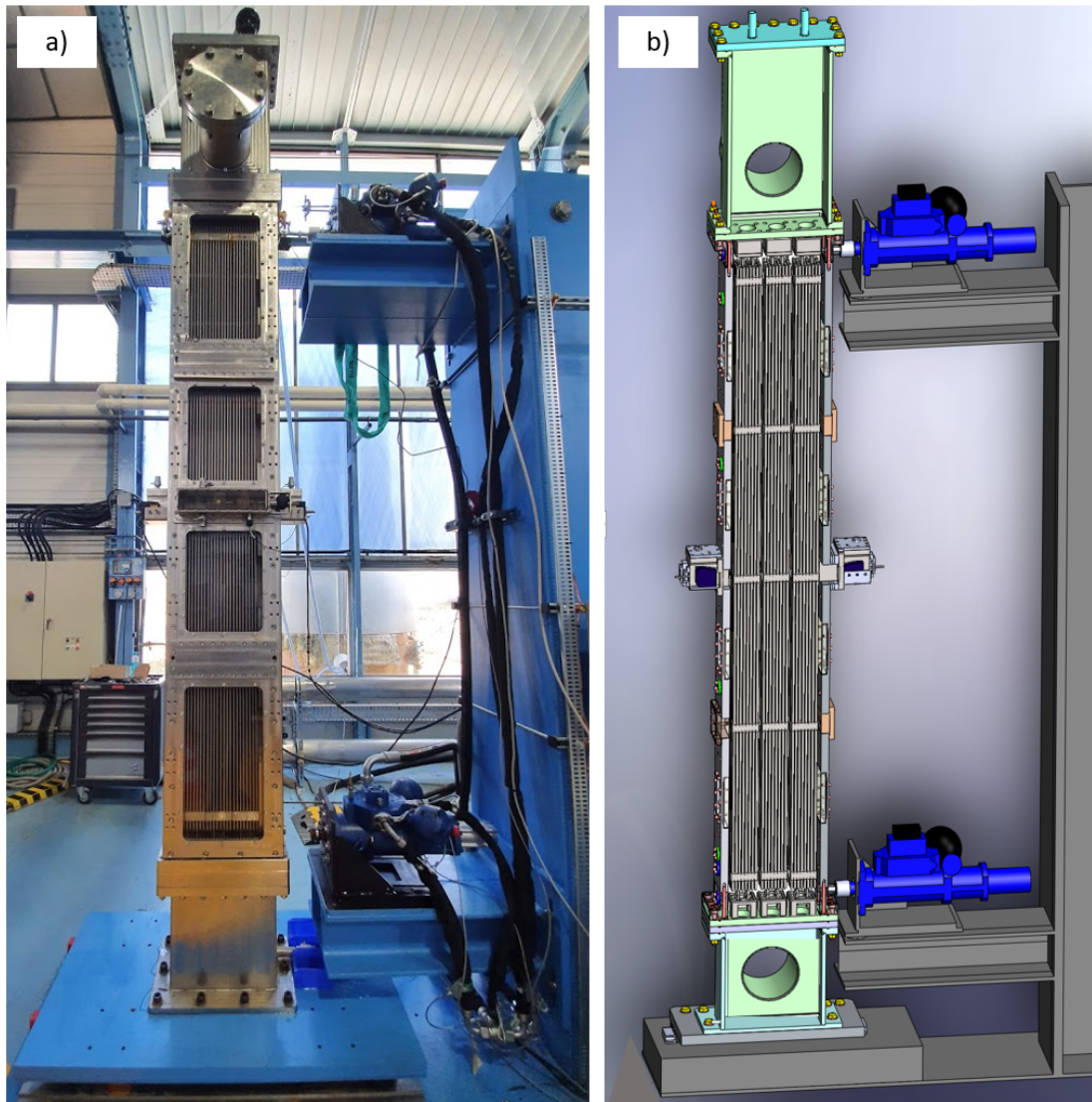


Figure 3.1: Eudore experimental facility: a) picture, b) 3D model.

3.2.1 Eudore

Eudore is an adjustable test section that can host a row of 3 half-scale fuel assemblies under axial flow (Fig. 3.1). The experiments presented in this document have been performed with 2 mm confinement, i.e. the distance between two assemblies or between an assembly and the walls is 2 mm. Other confinement possibilities on Eudore are: 4, 8 and 12 mm. The different confinements are possible by means of vertical slabs used to reduce the cross section. Since this analysis focuses only on 2 mm confinement, the vertical added slabs are considered as part of the test section walls. Each fuel assembly consists of 60 fuel rods and 4 guide tubes in a square lattice 8×8 . Both the fuel rods and guide tubes are in stainless steel and their diameter is $d = 9$ mm. The height of the fuel rods is 2512 mm while the guide tubes are 82 mm longer, adding 41 mm at the bottom and at the top of the assembly. Along the height of the assembly, there are 5 spacer grids welded to the guide tubes; the grids are spaced regularly along the rod length. Each grid is 101 mm wide and 32 mm tall, with a plate thickness of 0.5 mm, hence lateral size of the fuel assemblies at the grid level is 101 mm, while the pin pitch is $p = 12.5$ mm. This choice gives a pitch/rod diameter ratio $P = 1.39$, similar to the nominal one of a prototypical assembly as for SBF. The fuel rods are trapped in the spacing grids by means of several springs. The assemblies are clamped at the bottom to the LCP (Lower Core Plate) and at the top to the UPC (Upper Core Plate). These surrogate fuel bundles have been designed for Icare facility: for a deeper description the reader is addressed to Clément [2014].

The main feature of Eudore, is the link of the test section to two external pistons, as shown in Fig. 3.1. The pistons are connected at the height of the interlocking point of the assemblies on the LCP and UCP. Eudore lies on two rails and by means of the lateral pistons, a vibrating external load can be imposed. The purpose of imposing this solicitation is to reproduce a seismic event. Therefore, two main kinds of experiments are possible on Eudore: Static and Dynamic. As their names suggest, for Static experiments no external load is applied to the structure. In Static experiments, the hydraulic pistons are disconnected from the test section and the only structure vibrations are induced by the flow-rate. In Dynamic experiments the pistons are linked to Eudore and an external load is imposed, resulting in the vibration of the entire test section. In this chapter only Static experiments are investigated, leaving the Dynamic experiments to the next chapter.

Along the test section there are 12 portholes, 4 on the frontal wall and 4 for each lateral wall of Eudore. These portholes allow us to perform non intrusive measurements on the flow velocity field using lasers and cameras. The first and the fifth grid can be considered as motionless because they are very close to the interlocking point (41 mm) as illustrated in Fig. 3.1b and 3.2a. Another feature of this setup is the possibility to change the diameter of the diaphragms located at the inlet and at the outlet of each assembly, so as to influence the flow. For this experiment we decided to use the set of diaphragm diameters shown in Tab. 3.1. The inlet diaphragms diameter grows from left to right. The outlet diaphragms are identical and equal to the diameter of the central inlet. These boundary conditions

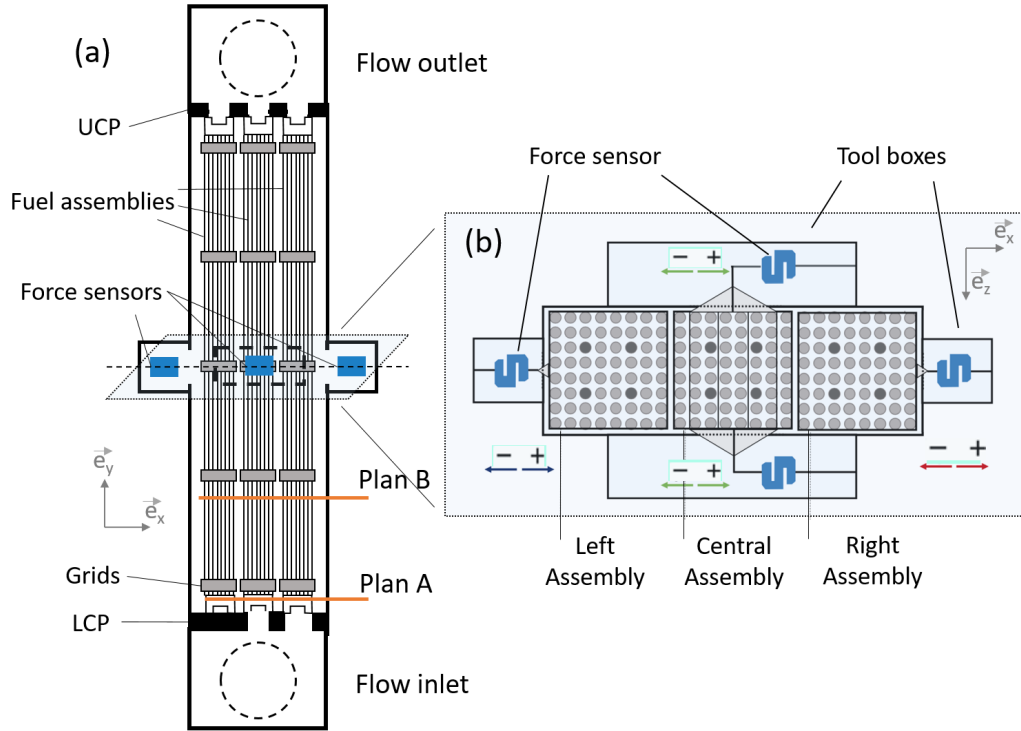


Figure 3.2: Eudore test section configuration for Static experiments: (a) Vertical section. (b) Cross-section at the 3rd grid level; plus and minus arrows indicate the reference system of the sensors.

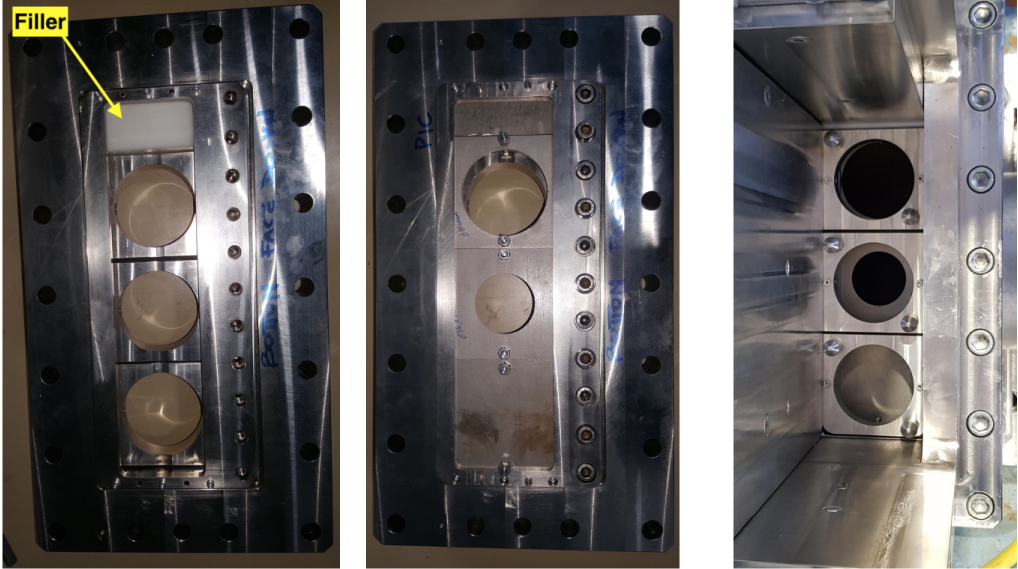
Table 3.1: Diaphragm sizes per assembly.

Position	Size	Left	Central	Right
LCP	Diameter [cm]	0.00	5.65	8.00
	Area [cm ²]	0.00	25.07	50.27
UCP	Diameter [cm]	5.65	5.65	5.65
	Area [cm ²]	25.07	25.07	25.07

generate a transverse flow from right to left (along $-\vec{e}_x$ in Fig. 3.2a). The diaphragms on the LCP are shown in Fig. 3.3. The filler shown in Fig. 3.3a allows to setup the LCP for 2 mm confinement configuration on Eudore. The LCP and the UCP are adjustable too, and one can change the diaphragms as well as the distance between the diaphragms.

3.2.2 Force measurements

At the 2nd, 3rd and 4th grids height, toolboxes can be installed in order to measure the fluid force acting on the assemblies and the assemblies displacement. Fig. 3.4 shows a lateral toolbox used to acquire displacement and force data on lateral assemblies. Fig. 3.5 shows the system designed to collect force data on the central assembly. For Static experiments, the left and right assemblies are connected to the force sensors by means of preloaded pistons. If the fluid force exceeds the preload, the sensor will not be linked to the grid



(a) Assembling LCP. (b) LCP completed. (c) LCP installed.

Figure 3.3: LCP configuration for static test Eudore in campaign 3.



Figure 3.4: Lateral toolbox on Eudore.

anymore, resulting in erroneous measurements. Therefore, the preload has to be larger than the measured force, without being too large to impose a significant deflection of the fuel assembly affecting the flow. For the present analysis the measurements have been performed only on the third grid height.

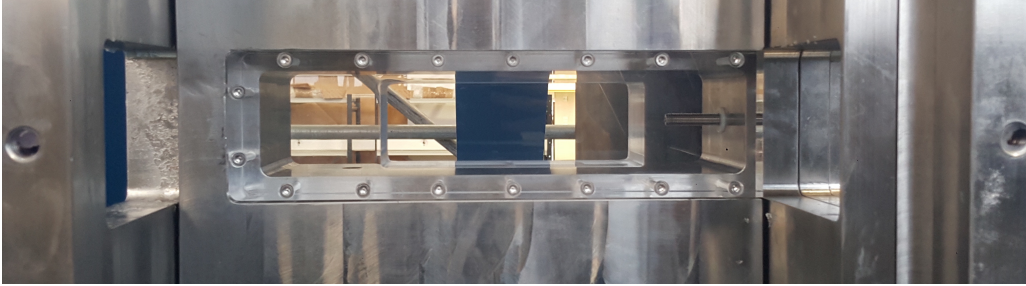
The central assembly is connected to the front and rear force sensors, “door” (Fig. 3.5d) and “back” (Fig. 3.5c), by means of an interlocking clamp (Fig. 3.5b). The clamp passes through the fuel rods and hooks the assembly from side to side as shown in Fig. ??b. The force sensors used for Static experiments have a range of 500 N and sensitivity $s = 0.6$ N; they are stiff enough to block the assemblies’ displacements. The total force on the central assembly is obtained by adding the values recorded by the “back” and “door” sensors, as they act in parallel on the central assembly.

3.2.3 Laser Doppler Velocimetry

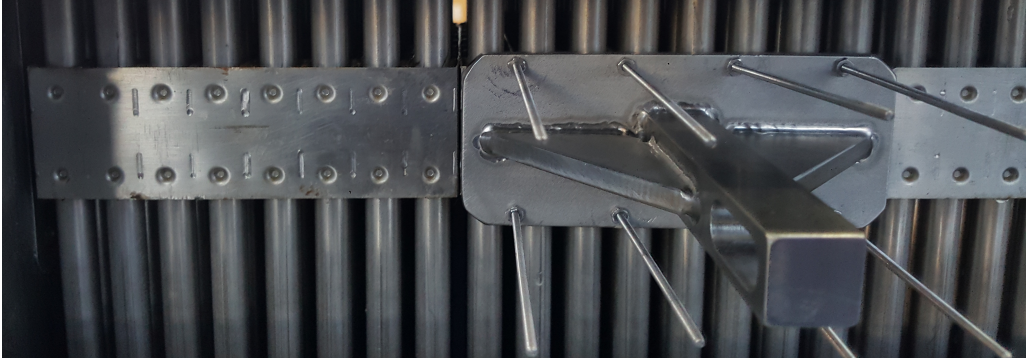
As recalled in the previous chapter, optical velocimetry techniques are of great use in fluid-dynamics measurements. They allow to measure the flow field non-intrusively, without interfering with it. As lasers and opto-eletronic devices are the main characters in this field, optical velocimetry techniques have become more and more common in the latest decades. Laser Doppler Velocimetry (LDV) is a simpler technique than PIV, involving less dangerous lasers and a photo-detector instead of a camera. Its efficiency lies in the possibility of measuring larger volumes than with PIV in a given time. The measures are punctual and less complicated to process.

Also LDV technique, as PIV, is based on the assumption that seeding particles will follow closely the fluid dynamic without interfering with it. Laser Doppler Velocimetry uses the Doppler effect to measure the velocities of the particles in a flow. The classic example of Doppler effect in sound waves applied to everyday life is the change of sound when a siren approaches and then moves away from the observer. Even for electromagnetic waves, the Doppler effect describes the wave frequency shift due to the velocity of the source itself. In LDV the source is the light reflected by the seeding particles. With the development of lasers, Doppler effect on electromagnetic waves has become possible to measure.

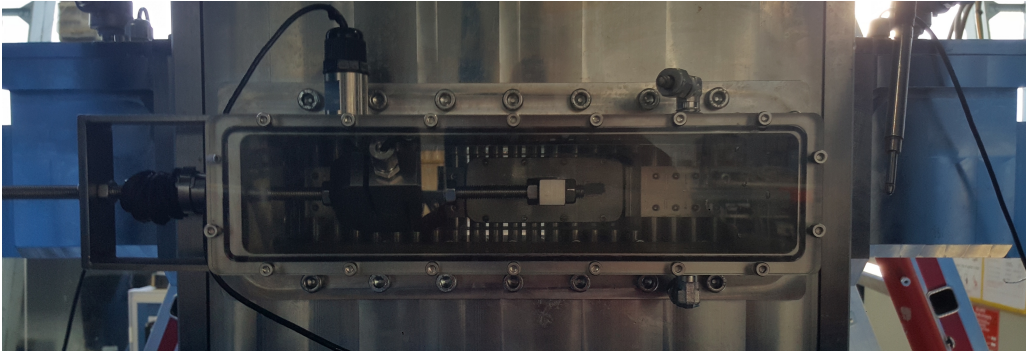
As for PIV, different methods are available when using LDV. In our case of interest, there are two incident laser beams on the same axis and a photodetector to collect the backscattered light as it is shown in Fig. 3.6. The two incident laser beams create an interference volume: when the particle passes through this volume, it reflects the light. The backscattered light is caught in a photomultiplier and sent in the photodetector. By means of the photodetector it is possible to measure the frequency shift and therefore to obtain the velocities of the particles. In LDV 2 laser beams allow to measure the velocity in one direction. In order to understand if the fluid particle is moving upstream or downstream,



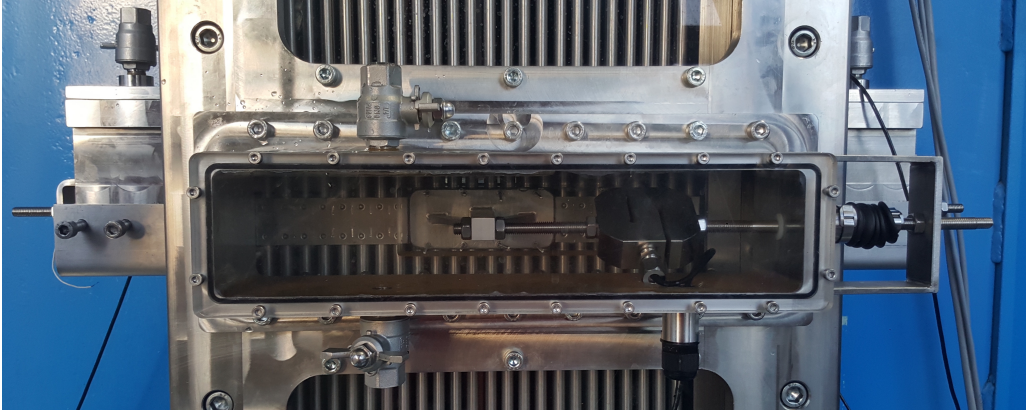
(a) Back manhole



(b) Central assembly clamp



(c) Toolbox on the back of Eudore.



(d) Toolbox on the door of Eudore.

Figure 3.5: Manholes and toolboxes.

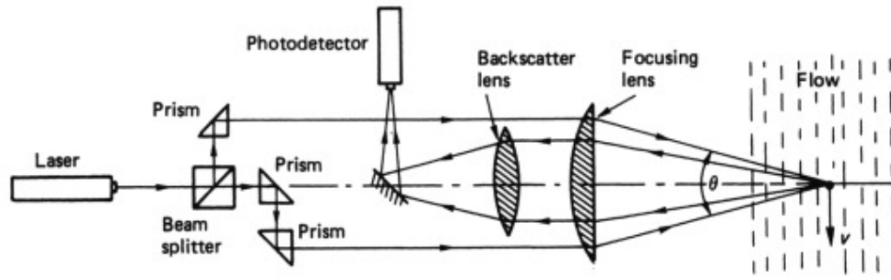


Figure 3.6: Backscattered LDV scheme. This figure is in [Carlton, 2018]

the two laser beams are different in their frequencies by $\Delta\nu$. The two frequencies are:

$$\nu_{i,1} \quad \text{and} \quad \nu_{i,2} = \nu_{i,1} + \Delta\nu$$

Taking only the first beam as example, assuming it propagates along direction is $\vec{l}_{i,1}$ and that it intercepts the particle with velocity \vec{v} . The backscattered light will be characterized by a frequency:

$$\nu_{s,1} = \nu_{i,1} + \frac{\vec{v}}{\lambda_{i,1}} \cdot (\vec{l}_{s,1} - \vec{l}_{i,1})$$

where $\vec{l}_{s,1}$ is the propagation direction of the scattered beam. The same holds for the second beam. As the frequency shift $\Delta\nu$ is very small, the Doppler frequency can be approximated as:

$$\nu_D = \nu_{s,2} - \nu_{s,1} \sim \Delta\nu + \frac{\vec{v}}{\lambda_{i,1}} \cdot (\vec{l}_{i,1} - \vec{l}_{i,2}) \quad (3.1)$$

The measures do not depend any longer on the propagation direction of the reflected beams since $\vec{l}_{s,1} = \vec{l}_{s,2}$ (there is only one receiver). The velocity of the particle, that under no-slip condition coincides with the velocity of the fluid, is easily obtained from Eq. 3.1. From the frequency shift $\Delta\nu$ one can understand the sign of the particle velocity on the vertical direction:

$$\begin{aligned} \nu_D = \Delta\nu &\quad \longrightarrow \quad \vec{u} \cdot (\vec{l}_{s,1} - \vec{l}_{s,2}) = 0 \\ \nu_D > \Delta\nu &\quad \longrightarrow \quad \vec{u} \cdot (\vec{l}_{s,1} - \vec{l}_{s,2}) > 0 \\ \nu_D < \Delta\nu &\quad \longrightarrow \quad \vec{u} \cdot (\vec{l}_{s,1} - \vec{l}_{s,2}) < 0 \end{aligned}$$

For further information on LDV techniques the reader is addressed to [Kalkert and Kayser, 2006, Zhu, 1996, Albrecht et al., 2013].

In order to be homogeneous for each measuring point, LDV measurements are performed respecting two threshold: the time of the measurement and the number of particles detected. The measurement lasts for a maximum time or a minimum number of detected particles. In the case the flow is slow, the number of particles backscattering counted by

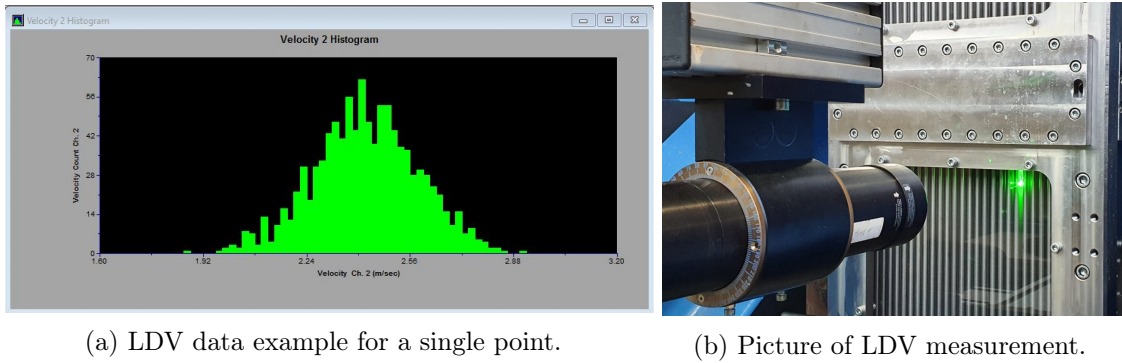


Figure 3.7: LDV measurement on Eudore.

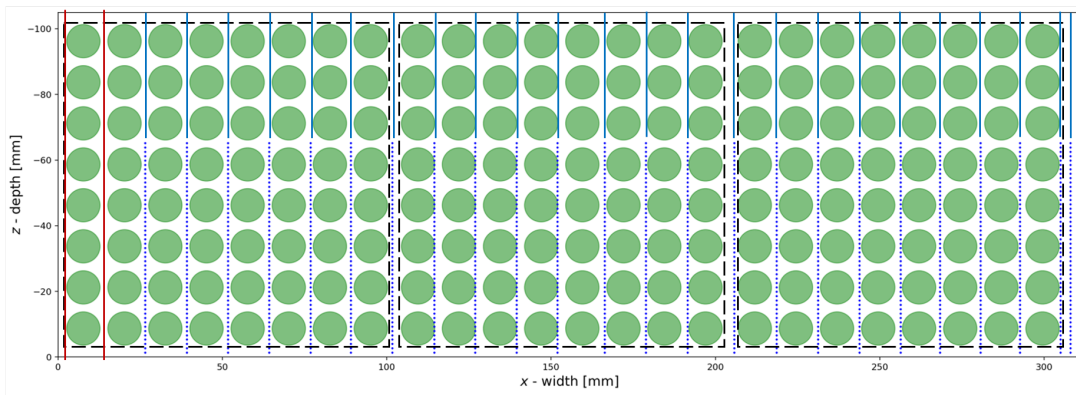


Figure 3.8: LDV measurement points on Eudore. Blue points are measured, blue lines are retrieved by symmetry, red lines are extrapolated.

the photo-detector grows slowly, hence one needs to fix a maximum time for the measurement. Otherwise, at high flow-rate, the photo-detector stops collecting data as soon as a minimum number of particles has been detected. Each detected particle has its own axial velocity. The ensemble of the velocity recorded for all the particles in a single measuring point is normal distributed on the average velocity for that point (Fig. 3.7a). The average velocity is then taken as the fluid velocity in that point, with a standard deviation given by the normal distribution.

Fig. 3.7b shows a LDV measurement on Eudore. The velocimetry campaign was conducted at a single flow rate, $171.2 \text{ m}^3/\text{h}$, involving two measurement planes A and B represented in Fig. 3.2a. Velocity measurements have been performed on \vec{e}_y axis. Plane A is 27 mm above the bottom of the fuel rods and 13 mm before the first grid. Plane B is 505 mm above plane A, 460 mm after the first grid and 108 mm from the second grid. Each plane contains several points distributed along the horizontal section: starting from the right assembly, along the width of the experimental section, the measuring points were taken in every bypass of the first 23 rods, while in depth points are spaced 1.33 mm apart up to a depth of 50.54 mm for plane A and 65.17 mm for plane B.

Fig. 3.8 shows the measuring points for LDV for plan B. Due to technical issues, the

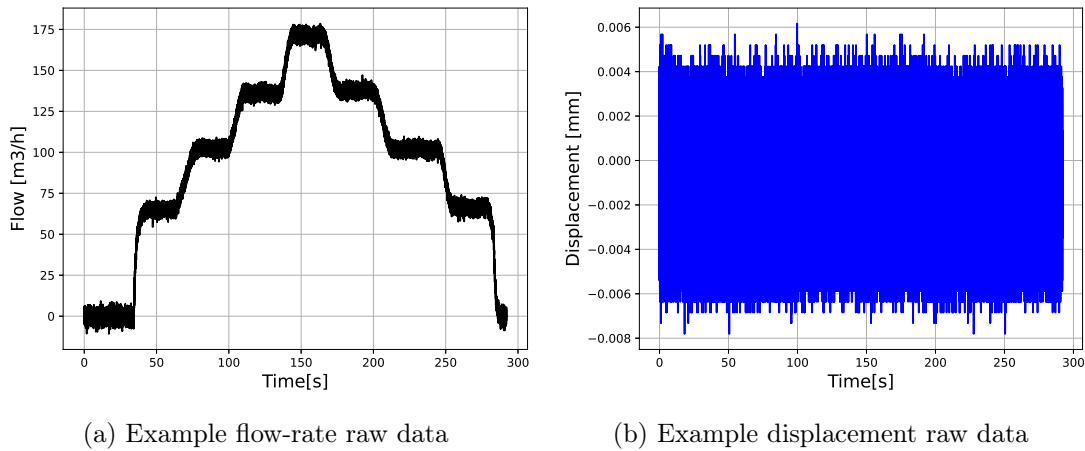


Figure 3.9: flow-rate and displacement raw data for each experiment on Eudore.

measuring section is smaller than Eudore horizontal section. Measurements in depth have a limitation due to the reflection of the laser beam by the rear wall of Eudore. Eudore is in stainless steel, hence once the measuring point reaches a certain depth, the reflection on the rear wall was too important for the photo-detector to be neglected, resulting in an impossibility to perform measurements. On the left side, the limitation is structural. The central windows present on the door of Eudore are not as large as the inner section. Therefore, measurements on the rear part of the horizontal section of Eudore have been substituted with their dual on the frontal part, assuming the flow is symmetrical on the horizontal axis centered on the section on the \vec{e}_z direction. For the lateral missing part, the velocity values have been linearly extrapolated. Extrapolation up to the 5th order have been performed and are shown in the Annex D. Linear extrapolation has been chosen because it was the only one which was physically admissible.

3.3 Experimental results

The transverse flow generated by the diaphragms exerts a force on the assemblies. By varying the flow rate, the transverse flow and therefore the force felt by the assemblies changes. The experimental campaigns allowed us to measure these forces with the force sensors, while Laser Doppler Velocimetry (LDV) allowed us to estimate the average axial and transverse components of the flow along the length of the 3 assemblies.

3.3.1 Force

Force measurements have been performed on 4 campaigns: the first two were used to calibrate the sensors and to optimize Eudore control and data acquisition softwares. Campaigns 3 and 4 are the real experimental campaigns. In campaign 3 the diaphragms are settled as illustrated in Sec. 3.2.1, with the left assembly seeing no inlet flow, the right assembly having a completely opened inlet diaphragm and the central assembly having a

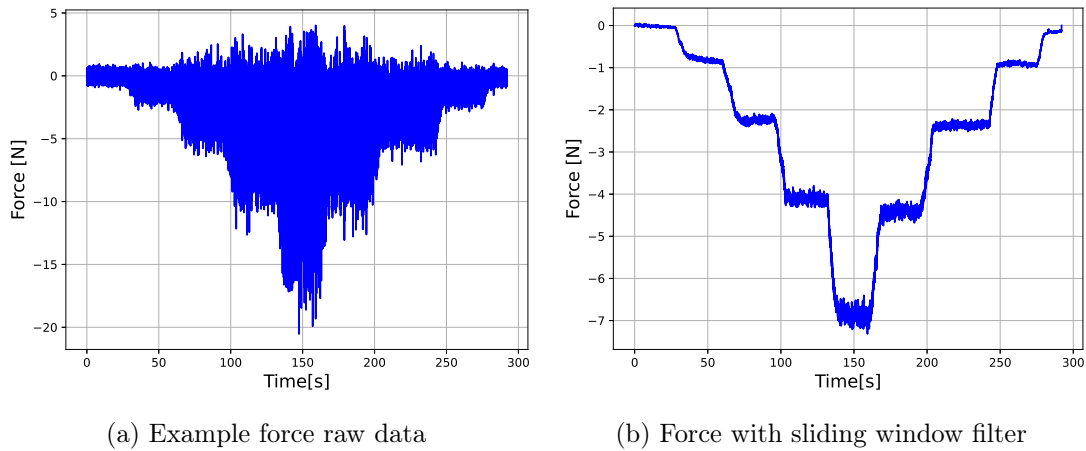


Figure 3.10: Force data for each experiment on Eudore.

half-opened diaphragm.

The experiments were conducted varying the hydraulic pump frequency f by steps of 5 Hz starting from 5 Hz. The flow-rate fr within Eudore varies according to the pump frequency. The ratio flow-rate/frequency on the hydraulic pump has been previously calibrated as $fr = 0.14 \cdot f + 0.92$ (with f in [Hz] and fr in [m^3/h]). Each flow-rate plateau on the ramp lasted about 30 s while the flow variation lasted 10 s.

Fig. 3.9 and 3.10 show the raw data collected for an experiment. Fig. 3.9a is the varying flow-rate during the experiment. Fig. 3.10a and 3.9b respectively show the force and displacement data for Left assembly. Fig. 3.10b shows the force variation after a sliding window filter of 500 ms has been applied to data. Displacement data for Static experiments are not useful even after the sliding window filtering, hence they have not been post-processed nor analysed. In Fig. 3.10b one can notice how, during the experiment the recorded force measurements slightly change for the same flow-rate before and after the peak ramp. This is due mainly to 2 reasons. The first is that the flow-rate depends not only on the pump frequency but also on the quantity of gases presents in the hydraulic loop. Before the beginning of each experiment, the water loop is degassed but, augmenting the pump frequency and the flow-rate, cavitation phenomena arise. Decreasing the flow-rate the presence of gases affects the flow-rate. Therefore, during the descending ramp of the experiments the flow-rate - pump frequency ratio is slightly different than in the ascending ramp. At a fixed pump frequency correspond slightly different flow-rates, for ascending and descending ramps. The second reasons behind different force values is more important and is connected to a hysteresis phenomenon typical of the assembly.

Clément [2014] has documented the hysteresis phenomenon for the very same assemblies used on another facility, Icare. In Fig. 3.11 we can see the results of a quasi-static experiment where an assembly was connected to a small hydraulic jack controlling its displacement. The physical reason behind the hysteresis is intuitive. The rods in the assembly are held by the spacer grids by means of springs and dimples. The vibrations induced by

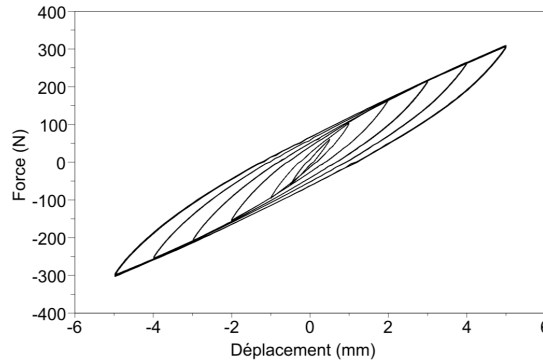


Figure 3.11: Assembly hysteresis phenomena. Displacement (x axis) vs Force (y axis). Plot from Clément [2014].

the flow can slightly displace the rod axial positions in the assembly. Springs and dimples are designed to prevent the rods to fall due to gravity while allowing their extraction from the bottom to the top. Hence the axial movement of the rods in the assembly has a preferential direction from bottom to the top. The rod displacement can be seen as a plastic deformation of the assembly. Furthermore, since the induced cross flow is above-all at the bottom of the test section, the induced vibrations on the rod are homogeneous along the assembly height. Once the rods move upward or downward in the assembly, the mechanical characteristics of the rod-bundle change. From the ensemble of these phenomena the mechanical hysteresis arises.

For this reason, only the ascendant part of the ramp will be considered in the following. For each flow-rate plateau the force value is the averaged force in the central 10 s of the plateau. The same is valid for the flow-rate. Measurement errors are calculated from the variance on the different campaigns: absolute error Δ is the square root of the sum of the measurement variance σ^2 and the quadratic value of the sensor sensibility s ; relative error δ is the ratio between the absolute error and the mean force value \bar{F} .

$$\Delta = \sqrt{\sigma^2 + s^2} \qquad \delta = \frac{\Delta}{\bar{F}} \qquad (3.2)$$

Campaign 3 and 4

In campaign 3, 36 experiments were performed. Among these, 10 were successful, while the others had problems during execution, e.g. too much cavitation, water leaks, inadequate piston preload, etc. For campaign 4, 30 experiments have been performed and 8 only were kept for the same reasons. The difference between campaign 3 and 4 is the order of the inlet diaphragms: left and right diaphragms were inverted. In campaign 3, the right assembly was the one mostly subjected to the axial flow, while in campaign 4, the left assembly was the most subjected to the axial flow. For campaign 3, the left assembly did not see any inlet axial flow and its force measurements were the cleanest

3.3. EXPERIMENTAL RESULTS

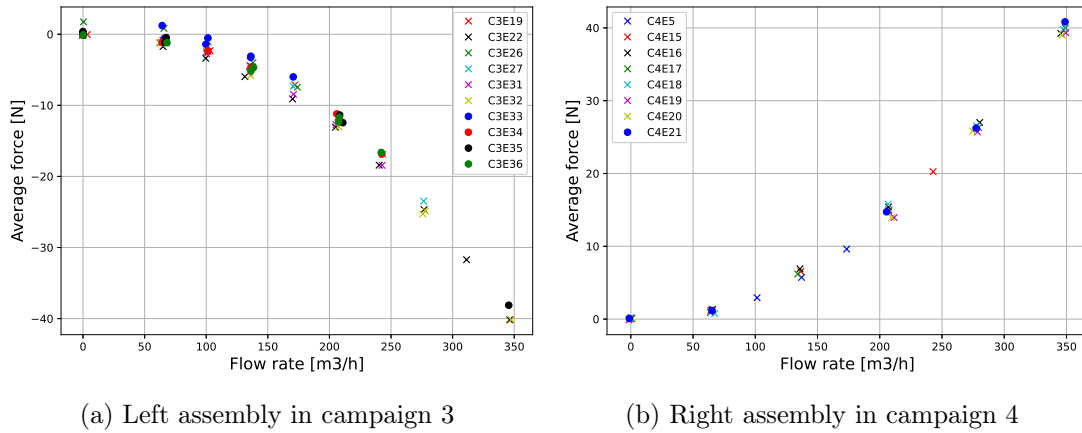


Figure 3.12: Comparison of campaigns 3 and 4, opposite assemblies.

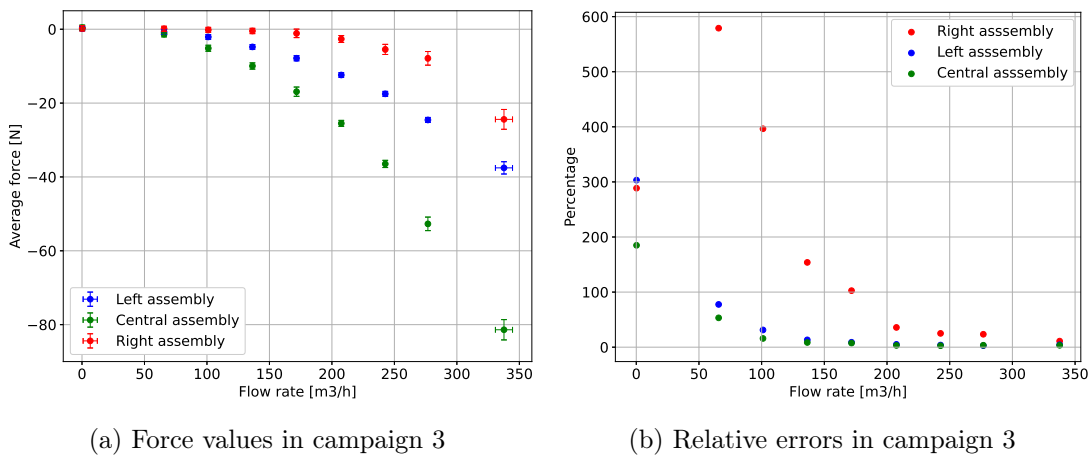


Figure 3.13: Force results for Campaign 3. Force value per assembly versus flow-rate with absolute errors and relative errors versus flow-rate.

among the 3 assemblies. For campaign 4, the cleanest measures have been obtained on the right assembly. Fig. 3.12 shows the force measurements for left assembly in campaign 3 and right assembly for campaign 4. Since the transverse flow-rate was opposite in one campaign to the other, also the sign of the force values is the opposite between campaign 3 and 4. Nevertheless, the force values show a perfect match on the two campaigns.

Fig. 3.13 and 3.14 show how the force varies with the total flow rate for campaigns 3 and 4. In absolute values, the assembly subjected to most important traverse flow is the central one for every flow-rate. In contrast, for campaign 3 (4) the right (left) assembly experiences the least fluid load and the least transverse flow. It must be considered, however, that the right (left) assembly is the one subjected to the largest inlet flow rate; its behaviour with respect to lateral flow is therefore affected by the important axial flow. Absolute errors are small enough to indicate a good repeatability of the experiments and hence a good reliability on the experimental data. However, the relative errors in Fig. 3.13b (3.14b) show a large uncertainty on the right (left) assembly at low flow rates. This uncertainty

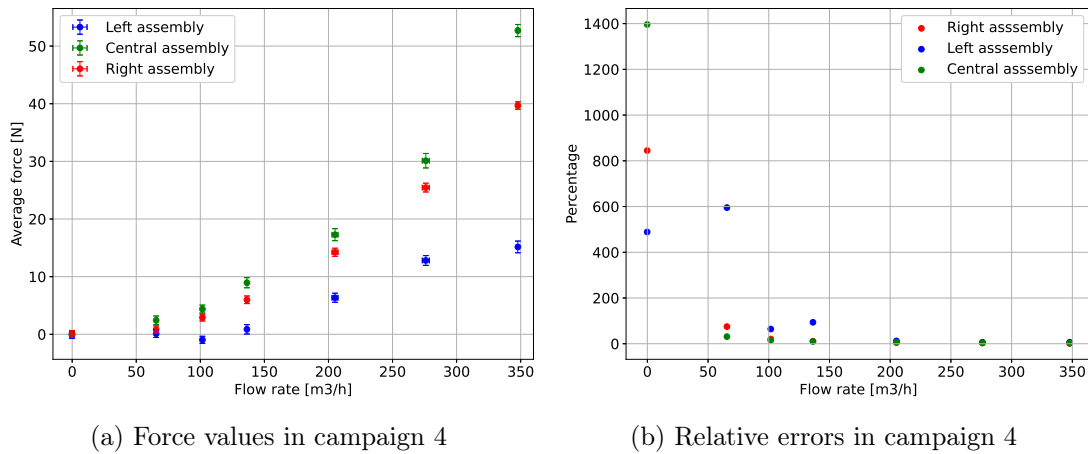


Figure 3.14: Force results for Campaign 4. Force value per assembly versus flow-rate with absolute errors and relative errors versus flow-rate.

could be due to an insufficient preload of the force sensor. Even if the relative errors are very large at low flow-rate, one should keep in mind that the mean values and the absolute errors at low flow-rate are really small. Thus, even an absolute error of 0.5 N could give an huge relative error if the mean value is 0.05 N.

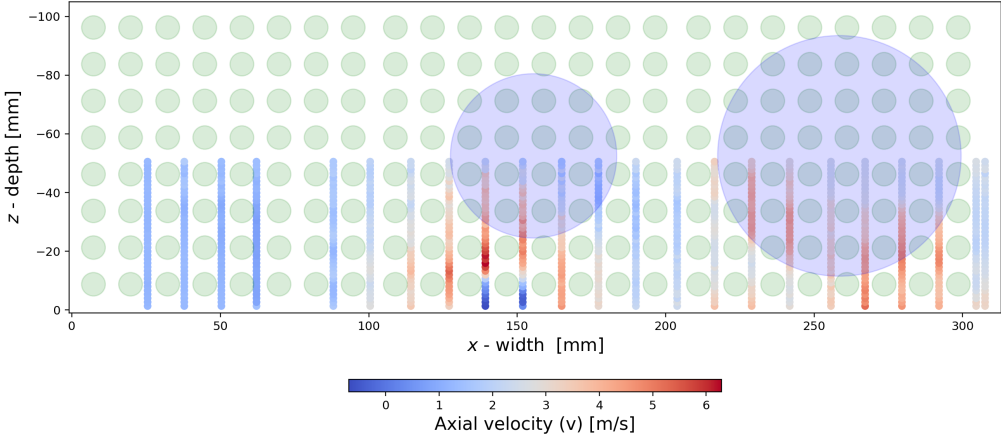
While left and right assemblies respectively for campaign 3 and 4 show a perfect match, the other assemblies (central and right-left) are subjected to a smaller fluid load. An LDV campaign has been conducted for the experiments in campaign 3 configuration and indicated the necessity of a changing the rear slab of Eudore. Since the confinement slab was metallic, the laser light was reflected interfering with the measurement. Thus, changing configuration for campaign 4, the rear slab has been substituted with a black opaque slab. After some measurement we saw the new rear confinement slab left less than 2 mm confinement on the third grid. This could explain the lower force value for central and left assemblies in campaign 4.

For this reason, only the left and central force values in campaign 3 will be taken as reference in the following analysis.

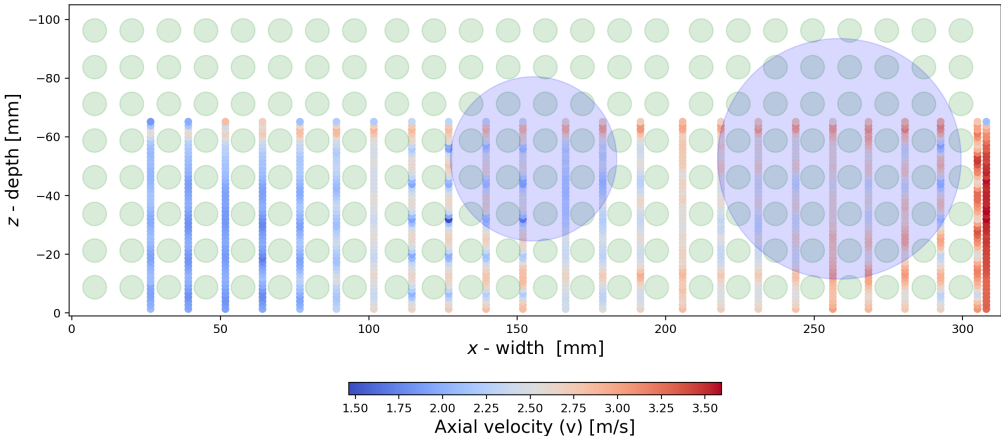
3.3.2 Velocity

LDV campaign concerns only campaign 3 configuration on 2 planes: A and B. Using the LDV technique, the axial velocity was measured for each LDV measuring point presented in Fig. 3.8. The graph in Fig. 3.15 is generated by taking into account the actual position of the measurement volumes.

As previously mentioned, LDV measurements have a Gaussian trend centered on the mean velocity and whose dispersion depends on a standard deviation. Given the large number of measurement points and since our work focuses on the average flow rate per assembly more than the actual local velocity, we will simply say that for plane A we have an average standard deviation over all points of 1.05 m/s and an average velocity of 3.39 m/s,



(a) LDV measures on plane A



(b) LDV measures on plane B

Figure 3.15: Measured axial velocity profiles [m/s] on planes A (a) and B (b). Blue circles represent the LCP diaphragms.

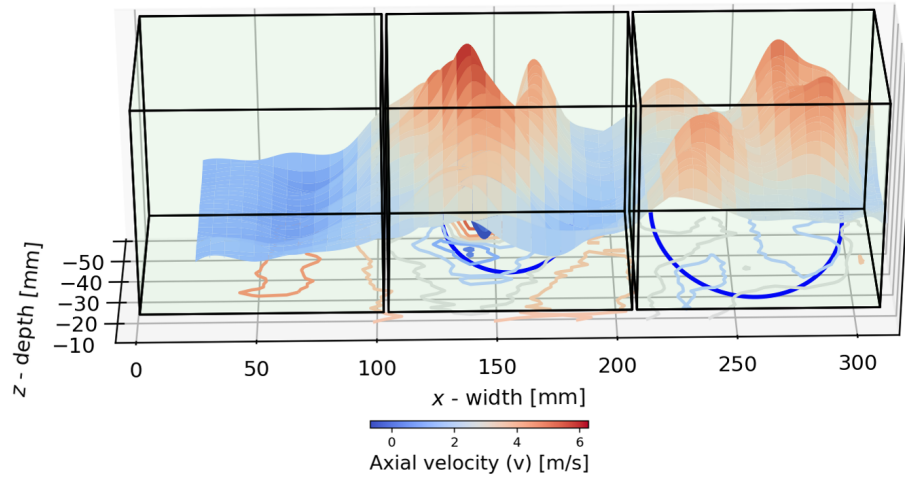


Figure 3.16: Axial velocity profile 3D reconstruction on plane A

while on plane B we find an average standard deviation of 0.23 m/s for an average velocity of 2.96 m/s. Dwelling on these numbers for a moment, we can see that the average velocity varies by about ten percentage points and that the average standard deviation is far greater in plane A than in plane B, indicating a more homogeneous flow in the latter.

Fig. 3.16 and 3.17 show the 3D reconstruction of the axial flow in Eudore on the 2 measurement planes. The reconstruction is made just on the measured domain. One should have in mind that this profile gives us just an indication on the velocity fields inside Eudore, because it does not take into account the presence of the rods. Hence only qualitative information can be retrieved. For example we can see how on plane B, just before the second grid, the axial flow is almost homogeneous, while at plane A, before the first grid, the velocity field is vastly heterogeneous even with negative velocities. In addition to technical limitations, two drawbacks affected the measurement. On plane A, one of the front rods of the left assembly was misaligned with the others, thus obstructing the space on which the measurement could be made. Furthermore, there is a void in the center of the second assembly surrounded by maximum velocity peaks: unfortunately a rubber gasket that fell into the hydraulic loop, got stuck right at LCP central assembly inlet channel during measurements. This causes a vortex and hence a local flow recirculation. The presence of the gasket may explain the difference in average velocities. However, fortunately the gasket was in a position (central assembly inlet channel) where the flow was already turbulent and as shown in the next paragraph, both technical limitations and problems did not have a major influence on the measurements. Beyond these observations, Fig. 3.16 and 3.17 show a velocity gradient in both measurement planes: the one in plane B is smaller, which is consistent with a more uniform flow profile as the flow develops away from the inlet, as expected.

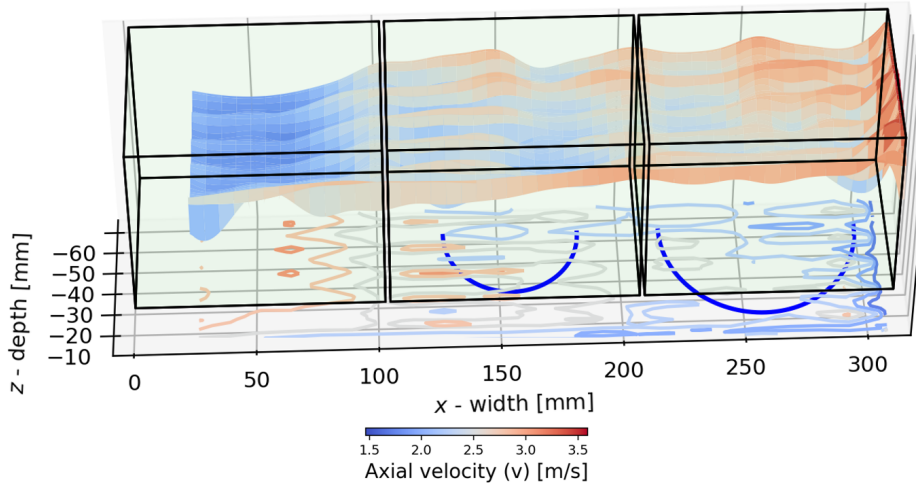


Figure 3.17: Axial velocity profile 3D reconstruction on plane B

Average axial and cross flows estimation

As previously explained, to retrieve the full axial flow in a horizontal plane, two assumptions are needed: axial symmetry with respect to a vertical plane (\vec{e}_x, \vec{e}_y) centered within the depth of the channel and linear extrapolation for widths greater than 285.5 mm. The total flow rate calculated with these assumptions for plane A is 178.8 m³/h, for plane B 174.2 m³/h while the flow rate set by the pump is 171.2 m³/h. This good agreement shows that our assumptions are valid.

We can now retrieve the average axial flow-rate for each assembly on plane A and B. Thus the velocity for each assembly at height A and B is simply retrieved by dividing the flow-rate by the free cross section of each assembly. We want to estimate the axial and cross velocity trend along the length of the assemblies. We can make another assumption on the outlet plane of Eudore. Since the diaphragms are identical on the UCP, L , and since the presence of the rods homogenizes the axial flow-rate already at plane B height, we can assume that at L height the flow-rate is the same for each assembly. Furthermore inside the UCP there is no transverse flow, all the flow-rate is axial flow-rate. This assumption gives the information on the outlet velocity for each assembly. We can assume that all the assembly on the outlet channel see a third of the total flow-rate. Thus the velocity is calculated dividing by the free cross section. With two points of measure, A and B, where we know the average axial velocity, and a third point at L , where we can assume the axial velocity, we can retrieve the axial velocity profile for each assembly along \vec{e}_y : the mean velocity along the height of each assembly is estimated with a exponential interpolation of the data (Fig. 3.19a).

A simple model is then used to estimate the transverse flows starting from the axial flows. Eudore section is divided into 9 sections (Fig. 3.18), 3 for each assembly, divided in height by 4 planes: O (Origin), A, B and L (length of the section). In practice, section Right

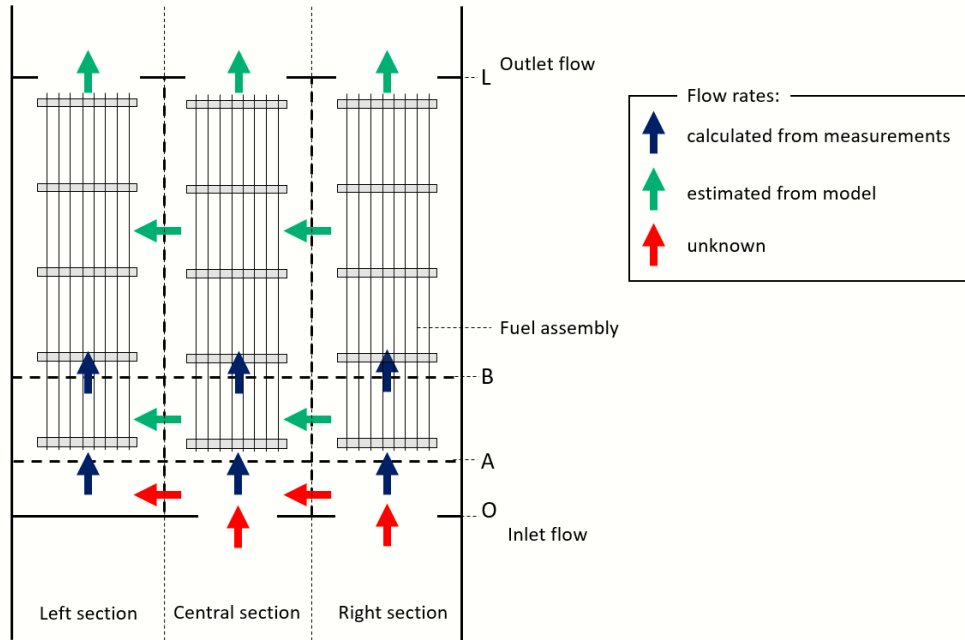


Figure 3.18: Axial and Transverse flow rates model.

A-B has one known flow input in plane A, one known flow output in plane B, which allows us to calculate the transverse flow towards the central assembly. This reasoning allows us to estimate the average cross flow between the three assemblies above plane A. Below, it is not possible because we do not know the inlet flow rates. Using the impermeability condition on the lateral wall and again a polynomial interpolation of the data, we can estimate the cross flow along \vec{e}_x and along \vec{e}_y (Fig. 3.19b and 3.19c). Axial and cross flows variations along the height can be approximated by an exponential, which shows a quick homogenisation away from the inlet channels.

3.4 Analytical model and identification of coefficients

This section proposes an analytical model, which will relate the line load $f_j(y)$ applied by the fluid on the j -th assembly to the force F_{Cj} measured by each force sensor at y_C height.

To this aim, Eudore fuel assemblies are modelled as Euler-Bernoulli beams. Each beam has 3 supports: the interlocks on the LCP and UCP that clamp both beam ends and the force sensor on the third grid which acts as a pinned condition (Fig 3.20). Hence the problem is hyperstatic and must be solved using 2 steps: first, each beam is considered as clamped at both ends receiving line load $f_j(y)$, hence implying a displacement $u_1(y)$. Then, each beam is considered as clamped at both ends and receiving a force F_{Cj} at y_C , hence implying a displacement $u_2(y)$. The line load $f_j(y)$ will be tuned such that:

$$u(y_C) = 0 \text{ with } u(y) = u_1(y) + u_2(y). \quad (3.3)$$

3.4. ANALYTICAL MODEL AND IDENTIFICATION OF COEFFICIENTS

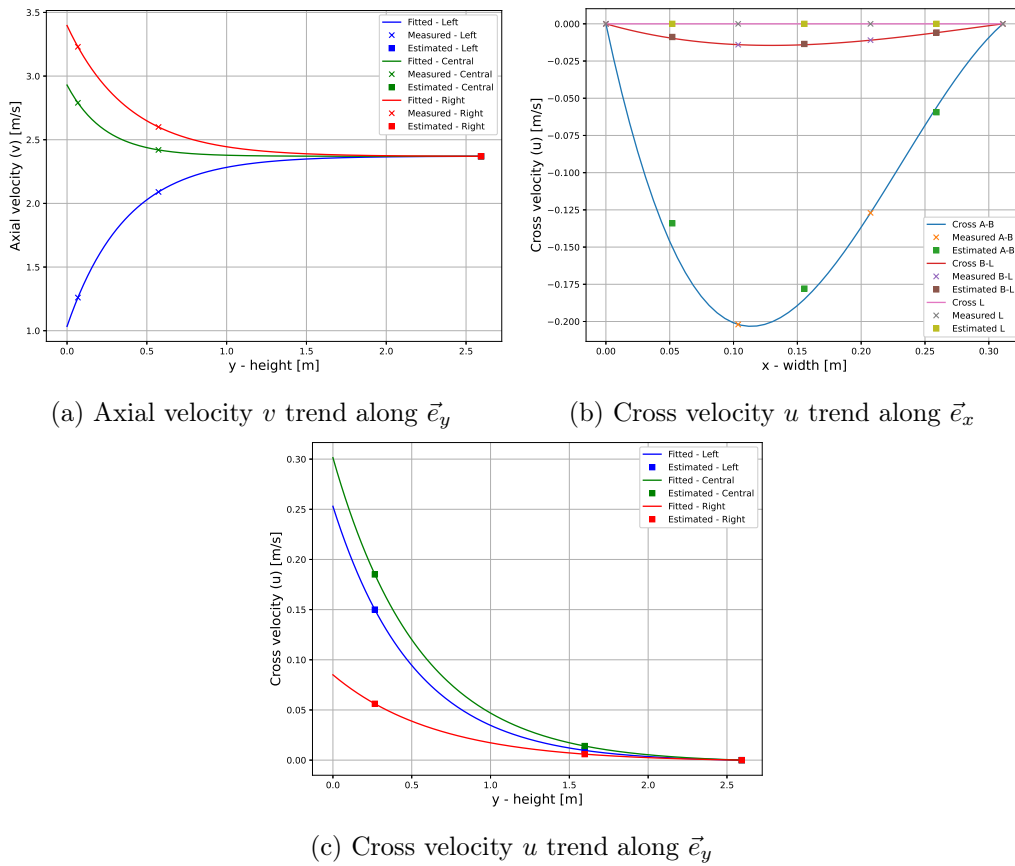


Figure 3.19: Axial velocity v and cross velocity u profiles estimation in Eudore for each assembly.

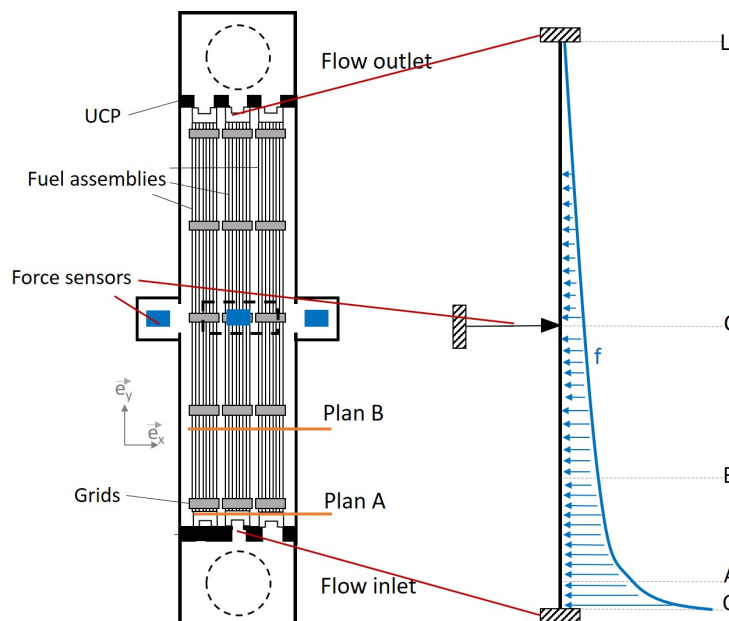


Figure 3.20: Graphic model for 1 assembly with the transversal line load f indicated.

3.4.1 Line load model

In our model the assemblies are 1D beams centered at half depth along \vec{e}_z lying on the same plane. The symmetry of the problem allows us to reduce the space to the xy plane. The empirical model used to estimate the line load over the fuel assembly is the one proposed by Païdoussis [1966a] for a cylinder submerged in an axial flow also used by Ricciardi et al. [2009a]. The line load model in \vec{e}_x direction is then

$$\vec{f}_{\text{fluid} \rightarrow \text{A}} = 64 \times (\vec{f}_I + \vec{f}_N), \quad (3.4)$$

where \vec{f}_I is the inertial term due to the added mass, while \vec{f}_N is a force term due to the normal drag acting on one rod. With the assumption that the assembly is not moving and the flow is in stationary condition, these contributions have the following expressions:

$$\vec{f}_I = m_f 2V_y \frac{\partial V_x}{\partial y} \vec{e}_x = m_f f_{m_f} \vec{e}_x, \quad \vec{f}_N = \frac{1}{2} \rho d c_N V_x V_y \vec{e}_x = c_N f_{c_N} \vec{e}_x, \quad (3.5)$$

where d is the fuel rod diameter, m_f is the added mass per unit length, c_N is the normal drag coefficient, V_x is the velocity component along \vec{e}_x (cross velocity), and V_y along \vec{e}_y (axial velocity). The coefficients m_f and c_N depend on the geometry of the structure, its roughness, the material, and the casing. The product between the axial and transverse velocity appears in the expression of the normal drag force (Eq. 3.5) due to the small angle approximation proposed in Ricciardi et al. [2009a]. Indeed, the normal drag force is one among the normal components of the viscous forces acting on the rods in the empirical model proposed by Païdoussis [1966a]. In that model the only flow is axial but taking in account a small cross flow, the transverse component of the structure velocity in the expression is replaced by the transverse structure velocity relative to the fluid cross flow. The axial velocity multiplies then the transverse structure velocity relative to the fluid cross flow. Since our immobility assumption for the assembly, the transverse structure velocity is null and the cross flow velocity remains to be multiplied by the axial flow velocity. For a deeper analysis the reader is addressed to Ricciardi et al. [2009a].

3.4.2 Displacement field under line load u_1 and punctual force u_2

Based on V_x and V_y estimations for the j -th assembly, functions f_{m_f} and f_{c_N} appearing in Eq. 3.5 can be evaluated. To compute the fluid force on each assembly, one needs to estimate the coefficients m_f and c_N , which are the weights for these functions in Eq. 3.5.

The Euler-Bernoulli equations for a clamped beam in equilibrium under a generic load

$l(y)$ are:

$$\begin{array}{ll}
 EI\partial_{yyyy}u(y) = l(y) & \text{Static equilibrium for } y \in]0, L[, \\
 u(0) = 0 & \text{Null displacement at } y = 0, \\
 \partial_y u(0) = 0 & \text{Null section rotation at } y = 0, \\
 u(L) = 0 & \text{Null displacement at } y = L, \\
 \partial_y u(L) = 0 & \text{Null section rotation at } y = L,
 \end{array}$$

where $\partial_y u = \frac{\partial u}{\partial y}$.

When the load is the fluid force, $l(y) = m_f f_{m_f}(y) + c_N f_{c_N}(y)$ and its resolution gives a displacement $u_1(y)$:

$$u_1(y; m_f, c_N) = \frac{1}{EI} \left(m_f F_{m_f}^4(y) + c_N F_{c_N}^4(y) + \frac{a}{6}y^3 + \frac{b}{2}y^2 + cy + d \right), \quad (3.6)$$

where F_{\bullet}^4 denotes the fourth primitive of f_{\bullet} ($F_{\bullet}^4 = \int \int \int \int f_{\bullet}$) and the boundary conditions provide a way to determine the coefficients a , b , c and d .

When the load is the punctual force applied by a force sensor, $l(y) = F_{Cj}\delta_{y_C}$. This implies a displacement $u_2(y)$:

$$u_2(y) = \frac{1}{EI} \left(\frac{\alpha}{6}y^3 + \frac{\beta}{2}y^2 + \gamma y + \delta \right) \quad y < y_C, \quad (3.7)$$

$$u_2(y) = \frac{1}{EI} \left(\frac{\alpha + F_{Cj}}{6}y^3 + \frac{\beta'}{2}y^2 + \gamma' y + \delta' \right) \quad y \geq y_C. \quad (3.8)$$

Boundary conditions in conjunction with the two conditions implying equal displacement and equal section rotation at y_C allow us to determine α , β , β' , γ , γ' , δ and δ' .

3.4.3 Resolution: finding c_N from measurements

Capanna et al. [2021b] used fuel assemblies of identical shape and size to those used in Eudore, albeit in larger confinement (4 mm gap between assemblies). They derived a value of the linear added mass density for an assembly $m_{f_A} = 7.78 \text{ kg.m}^{-1}$, or $m_f = 0.12 \text{ kg.m}^{-1}$ for a single rod. To reduce the unknowns to c_N only, we use this value for m_f .

Having $u_1(y_C; c_N)$ parameterised by c_N only and $u_2(y_C)$ evaluated via the measured force, Eq. 3.3 can be solved, allowing us to estimate a value for c_N for each assembly. Computed values are displayed in Tab. 3.2 (force measurements for the right assembly were discarded as explained in Sec. 3.2.2).

Table 3.2: c_N values evaluated for left and central assemblies.

Left	Central	Average
0.48	0.84	0.66

Recently, [Moussou et al. \[2017\]](#) found that c_N is in the range $[0.3; 0.5]$ for a scale-one assembly. This is of the same order of magnitude than the range in [Tab. 3.2](#) although our two values differ by 43%. This is surprising as the assemblies are identical in shape and material and one would expect to retrieve the same value for the normal drag coefficient c_N . This difference can be explained by the boundary conditions and the presence of the grids. The cross flow through the central assembly encounters a homogeneous space in the \vec{e}_x direction, while in the left assembly this is not valid anymore. The presence of the wall affects the velocity field, so that its gradient along \vec{e}_x is larger in magnitude compared to the one in the central assembly. In [Sec. 3.4.1](#) the average velocity over each assembly was used to derive the average fluid force on each rod. This approximation works better when this gradient is small, but this is not true for the lateral assemblies, which could explain the observed discrepancy on c_N .

3.5 Porous Medium Approach

The porous medium model was developed to simulate the mechanical behaviour of an entire nuclear reactor core. The aim was to keep the number of degrees of freedom low to reduce computational costs, while accounting for the major fluid-structure interactions.

First the equations for the fluid and structure motion are established individually. Then through a porosity coefficient, equivalent fluid and structure are defined, over the whole core domain. Finally the empirical model proposed by [Païdoussis \[1966a\]](#) is used to couple the two systems of equations.

The model starts with 5 assumptions:

- H1: The fluid is viscous, incompressible and Newtonian.
- H2: Gravity effects are neglected.
- H3: The rod section does not deform.
- H4: Distance between two rods remains constant.
- H5: Turbulent kinetic energy is negligible in comparison with turbulent diffusion.

From these 5 assumptions the model develops as summarised below. The equations of motion for the fluid are written in the ALE (Arbitrary Lagrangian-Eulerian) approach, to be matched later with those for the motion of the structure written with a Lagrangian approach.

Equivalent fluid motion equation

The fluid is described by the Navier-Stokes equations for an incompressible fluid and neglecting gravitational effects (H1, H2). A total control volume $\Omega_t(x, y, z)$ is then defined as the union of the fluid and structure domains, $\Omega_t(x, y, z) = \Omega_f(x, y, z) \cup \Omega_s(x, y, z)$.

This control volume is centered at a point $M(x, y, z)$ and is defined with an infinitesimal square-based volume of side p and height dz , where p is the pitch between the fuel rods.

From H3 and H4 it follows that the fluid volume $V_{\Omega_f}(x, y, z)$ present in the control volume $\Omega_t(x, y, z)$ does not depend on the position M , and that the structure volume $V_{\Omega_s}(x, y, z)$ present in $\Omega_t(x, y, z)$ is equal to the one of a rod with infinitesimal height dz :

$$V_{\Omega_t}(x, y, z) = V_{\Omega_f}(x, y, z) + V_{\Omega_s}(x, y, z), \quad (3.9)$$

$$V_{\Omega_t}(x, y, z) = V_{\Omega_t}, \quad V_{\Omega_f}(x, y, z) = V_{\Omega_f} \quad \text{and} \quad V_{\Omega_s}(x, y, z) = V_{\Omega_s}. \quad (3.10)$$

At this point the spatial averaging operation is done by integrating the Navier-Stokes equations in the fluid domain $\Omega_f(x, y, z)$, resulting in:

$$\rho \frac{1}{V_{\Omega_t}} \int_{\Omega_f(x, y, z)} \left(\frac{\partial \vec{V}}{\partial t} + \left(\vec{V} - \frac{\partial \vec{u}}{\partial t} \right) \cdot \nabla \vec{V} \right) d\Omega = \frac{1}{V_{\Omega_t}} \int_{\Omega_f(x, y, z)} \vec{\nabla} \cdot \underline{\underline{\sigma}}_f d\Omega, \quad (3.11)$$

$$\frac{1}{V_{\Omega_t}} \int_{\Omega_f(x, y, z)} \vec{\nabla} \cdot \vec{V} d\Omega = 0, \quad (3.12)$$

where ρ is the fluid density, \vec{V} is the fluid velocity, \vec{u} is a vector field that coincides with the structure displacement and, since H1, $\underline{\underline{\sigma}}_f$ is the classic Cauchy stress tensor for a Newtonian fluid whose variables are the fluid pressure P and the viscosity μ .

Ricciardi et al. [2009a] chose a constant \vec{u} in the fluid domain and models turbulence by taking into account spatial fluctuations, neglecting turbulent kinetic energy (H5). The turbulent viscosity μ_T is chosen constant in space and time justified by the homogeneity of the flow of a PWR.

Finally the equivalent fluid with variables \vec{V}_{eq} and P_{eq} is defined:

$$\vec{V}_{eq} = \frac{1}{V_{\Omega_f}} \int_{\Omega_f(x, y, z)} \vec{V} d\Omega, \quad P_{eq} = \phi \frac{1}{V_{\Omega_f}} \int_{\Omega_f(x, y, z)} P d\Omega. \quad (3.13)$$

where $\phi = V_{\Omega_f}/V_{\Omega_t}$ is the porosity.

Structure model

In order to transform the 3D equilibrium equations into beam equations, the Timoshenko beam model is used. Defining ρ_s as the structure density, $\underline{\underline{\sigma}}_s$ as the Cauchy-stress tensor and \vec{u} as the structure displacement, assumptions H3 and H4 lead to:

$$(1 - \phi) \rho_s \frac{\partial^2}{\partial t^2} \left(\frac{1}{V_{\Omega_s}} \int_{\Omega_s(x, y, z)} \vec{u} d\Omega \right) = (1 - \phi) \vec{\nabla} \cdot \left(\frac{1}{V_{\Omega_s}} \int_{\Omega_s(x, y, z)} \underline{\underline{\sigma}}_s d\Omega \right) + \underbrace{\frac{1}{V_{\Omega_t}} \int_{\partial\Omega_s(x, y, z)} \underline{\underline{\sigma}}_s \cdot \vec{n} dS}_{\vec{f}_{\text{fluid} \rightarrow \text{structure}}}. \quad (3.14)$$

Then the equivalent variables for structure are defined as:

$$\vec{u}_{eq} = \frac{1}{V_{\Omega_s}} \int_{\Omega_s(x,y,z)} \vec{u} d\Omega, \quad \underline{\underline{\sigma}}_{eq} = \frac{1}{V_{\Omega_s}} \int_{\Omega_s(x,y,z)} \underline{\underline{\sigma}}_s d\Omega. \quad (3.15)$$

Therefore Eq. 3.14 is the classical Newton's law for continuous structure. Indeed, defining $\rho_{seq} = (1 - \beta)\rho_s$ we have:

$$\rho_{seq} \frac{\partial^2 \vec{u}_{eq}}{\partial t^2} = (1 - \phi) \vec{\nabla} \cdot \underline{\underline{\sigma}}_{eq} + \vec{f}_{\text{fluid} \rightarrow \text{structure}}. \quad (3.16)$$

Without going into the details of this model we will provide the system equations in the following section.

Coupled model

Defining the equivalent density $\rho_{eq} = \phi\rho$, the equivalent turbulent viscosity $\mu_{T_{eq}} = \phi(\mu_T + \mu)$ and the assembly mass per unit length m_A , the equations describing the coupled system are:

$$\rho_{eq} \frac{\partial \vec{V}_{eq}}{\partial t} + \rho_{eq} \nabla \cdot (\vec{V}_{eq} \otimes \vec{V}_{eq}) = -\nabla P_{eq} + \mu_{T_{eq}} \Delta \vec{V}_{eq} + 2\rho_{eq} \frac{\partial \vec{u}}{\partial t} \cdot \nabla \vec{V}_{eq} - \rho_{eq} \vec{V}_{eq} \cdot \nabla \frac{\partial \vec{u}}{\partial t} + \underbrace{\frac{1}{V_{\Omega_t}} \int_{\partial\Omega_s(x,y,z)} \underline{\underline{\sigma}} \vec{n} dS}_{\vec{f}_{\text{structure} \rightarrow \text{fluid}}}, \quad (3.17)$$

$$\nabla \cdot \vec{V}_{eq} = 0, \quad (3.18)$$

$$m_A \frac{\partial^2 u_{eqx}}{\partial t^2} = \frac{\partial Q_x}{\partial y} + T_0 \frac{\partial^2 u_{eqx}}{\partial y^2} + \frac{1}{S_A} \int_{S_A} \left(f_{I_x} + f_{N_x} - y f_{L_x} \frac{\partial^2 u_{eqx}}{\partial y^2} \right) dS, \quad (3.19)$$

$$m_A \frac{\partial^2 u_{eqz}}{\partial t^2} = \frac{\partial Q_z}{\partial y} + T_0 \frac{\partial^2 u_{eqz}}{\partial y^2} + \frac{1}{S_A} \int_{S_A} \left(f_{I_z} + f_{N_z} - y f_{L_z} \frac{\partial^2 u_{eqz}}{\partial y^2} \right) dS, \quad (3.20)$$

$$I_{fA} \frac{\partial^2 \vec{\theta}_{eq}}{\partial t^2} = \frac{\partial \vec{M}}{\partial x} + \vec{e}_y \wedge \vec{Q} + \vec{M}_{\text{fluid} \rightarrow A}. \quad (3.21)$$

\vec{Q} is the shear force, \vec{f}_L is the axial drag function, \vec{T}_0 is the tension force at the bottom of the fuel assembly, I_{fA} is the inertial moment per unit length of a fuel assembly, $\vec{\theta}_{eq}$ is the section rotation and \vec{M} is the bending moment. The fluid-structure interaction term $\vec{f}_{\text{structure} \rightarrow \text{fluid}}$ is integrated over the fluid-solid frontier surface $\partial\Omega_s$ and can be decomposed as follows:

$$\vec{f}_{\text{structure} \rightarrow \text{fluid}} = -\frac{1}{S_A} (\vec{f}_I + \vec{f}_N + \vec{f}_L). \quad (3.22)$$

$\vec{f}_L = \frac{1}{2} \rho d_{\text{rod}} c_T V_y^2 \vec{e}_y$ is the lift term present in the Paidoussis model. It takes into account the axial drag and acts on the y direction. It was not considered in the 1D model in

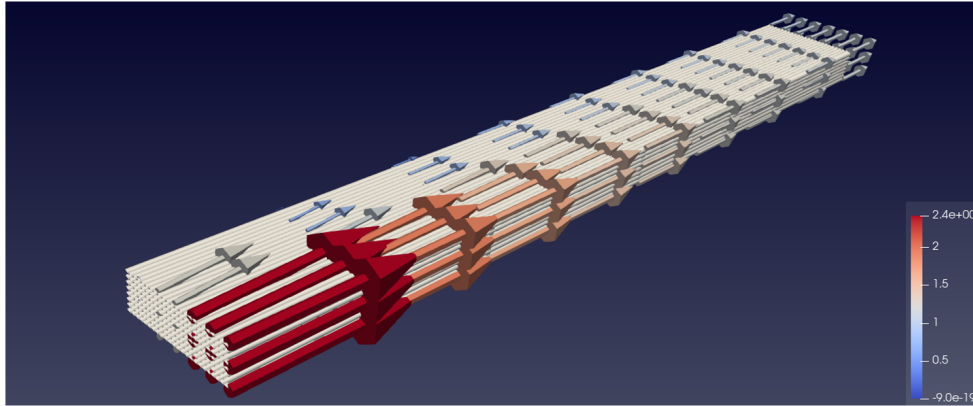


Figure 3.21: Simulation with FSCORE for a line of 3 Eudore-like assemblies.

Sec. 3.4.1 which takes into account forces in \vec{e}_x direction only. This force implies another geometric coefficient c_T . From pressure loss related experiments in Ricciardi [2020], a value $c_T = 0.02$ was determined. This value accounts for the effect of the grids on the pressure drop.

3.6 FSCORE numerical resolution

Numerical simulations are implemented in EUROPLEXUS framework (abbreviated EPX, see <http://www-epx.cea.fr> for details) via a submodule named FS-CORE. EPX is a software developed for transient analyses involving nuclear reactors. FS-CORE is EPX application implementing the “porous medium” approach compatible with parallel processing. The theoretical foundations of the model are briefly recalled in the next paragraph. Faucher et al. [2021] validated this numerical software on PWR fuel assemblies under dynamic excitation by comparing the numerical results with experiments carried out on 4 fuel assemblies geometrically identical to those of Eudore.

Fig. 3.21 shows the reproduction of a simulation for the line of 3 assemblies as in Eudore facility. The configuration for the simulation is the one corresponding to campaign 3, with the right assembly seeing the most of the axial flow. The mesh is implemented in Cast3M and was built with 15 equispaced nodes along the height of each assembly, 3 nodes in width and 3 nodes in depth. Increasing by 50% the number of nodes, the computational time dilates with a factor almost 300% passing from 5000 s to 14500 s for a simulation of 6.5 s.

At the initial time the axial velocity is 0 for each assembly. The boundary conditions are set at the inlet of the assemblies. The inlet velocities follow a ramp of about 4 s before reaching a steady state plateau. Fig. 3.22a shows the resultant axial velocity on the second grid of each assembly. The effect of the diaphragms is taken into account by imposing different inlet velocities for each fuel assembly based on exponential interpolation depicted in Fig. 3.19 at $y = 0$ obtained for a flow rate of 172 m³/h. The ratio of axial flow rate between the fuel assemblies is kept constant for other flow rates. One would expect no

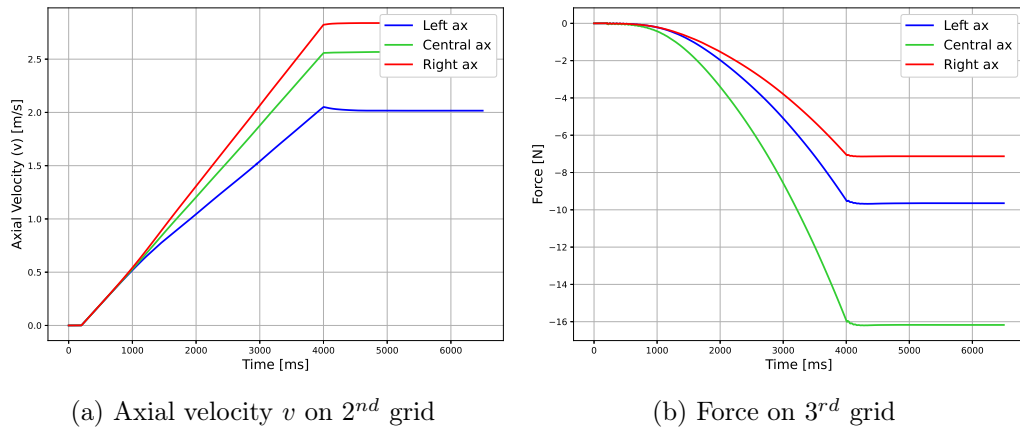


Figure 3.22: Simulated data

axial flow at the bottom of the left fuel assembly since the diaphragm is completely closed, but the LDV measurements show a significant axial flow at that location. This is due to the possibility for the fluid to freely redistribute in the space between the lower core plate and the bottom of the fuel assemblies.

Fig. 3.22b shows the force value at the third grid of each assembly during the numerical resolution. One can see how both the plateau for axial velocity and horizontal force are in steady state. Contrary to the experiment, each simulation has only one ramp and one plateau for the total flow-rate. Several simulation have been performed imposing each time a different total flow-rate. A sensitivity analysis on FSCORE for static simulations is presented in Annex B.

3.6.1 Comparison of experimental and numerical results

The numerical simulations are performed on FS-CORE using values of m_f , c_N estimated in Sec. 3.4.3. Empirical value of c_N follow in the range [0.3; 0.5] [Moussou et al., 2017], while c_T is an order of magnitude smaller [Ricciardi, 2020]. For the axial drag term $c_T = 0.02$ has been chosen. Since the heterogeneity for c_N , two kind of simulations have been run: one with the homogeneous c_N and one with the heterogeneous c_N . In the heterogeneous case, for the right assembly the c_N coefficient is set equal to the left one. A null cross velocity is imposed on the boundaries. Flow values are retrieved at planes A and B level for V_y . Fig. 3.23 illustrates how the measured and simulated data present the same behaviour for the axial velocity field.

Using two different c_N values of Tab. 3.2 for laterals and central assemblies (heterogeneous set), or using the average value $c_N = 0.66$ (homogeneous set) for all the assemblies does not noticeably affect these values.

Fig. 3.24 shows the numerical axial and cross velocity profiles for the whole Eudore frontal section. This allows to have an idea of the velocity gradient and how it changes for each assembly. Fig. 3.24a shows a non homogeneous axial velocity profile at section end

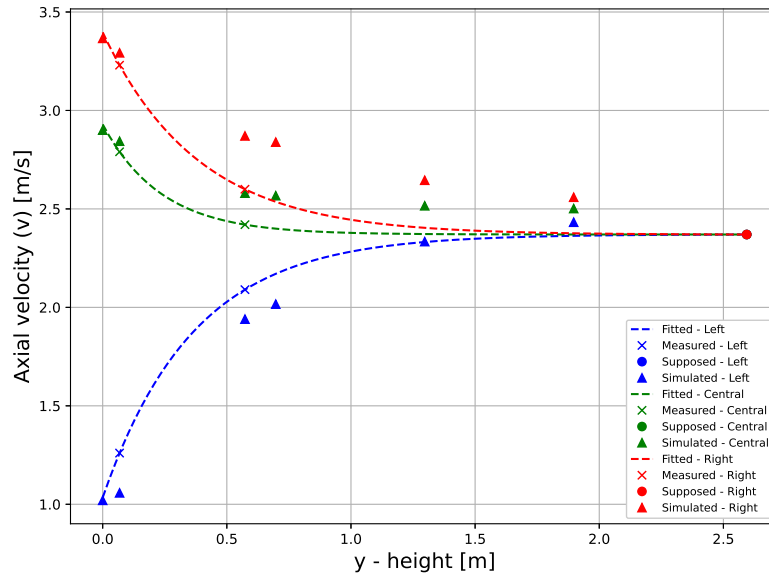


Figure 3.23: Axial velocity profiles [m/s] measured and simulated with homogeneous $c_N = 0.66$.

$y = L$. However, variations along the section width are very small, indeed the standard deviation is less than 5 %. This validates the assumptions in Sec. 3.3.2 used to derive average flow profiles. Fig. 3.24b exhibits a non symmetrical cross flow with respect to the section width which is consistent with experimental results depicted in Fig. 3.19b.

Fig. 3.25 compares measured and computed force values on the third grid for both c_N values sets. Fig. 3.25a, 3.25c and 3.25e show data for different c_N values for lateral and central assemblies, as retrieved in Sec. 3.4.3. Meanwhile Fig. 3.25b, 3.25d and 3.25f show the numerical and experimental data with the average $c_N = 0.66$ value for the three assemblies. These results show a good agreement between numerical and experimental results in both cases with discrepancies at high flow rates for left and central assemblies. Discrepancies are observed for the right assemblies even for low flow rates, confirming the assumption of erroneous experimental data formulated in Sec. 3.2.2. Maximum and average absolute errors for each assembly are shown in Tab. 3.3. Simulations and experimental data lie on parabolic curves, so at higher flow rates one might expect more important differences. However, much higher flow rates would exceed the typical PWR velocities, hence they are beyond the interest of this study.

A sensitivity analysis to m_f and c_N parameters was conducted via simulations. Further simulations were run using $c_N = 0.74$ for all assemblies. When compared to the results obtained for $c_N = 0.66$ that is a 12% increase, the force on the grids increase similarly (about 15%). m_f value was then increased or decreased by 17% of its original value $m_f = 0.12$. This led to a decrease (when m_f is increased) or an increase of only 2.5% of the forces exerted on the grids. This sensitivity analysis points out the importance of a correct estimate of the normal drag coefficient c_N for a proper evaluation of forces induced

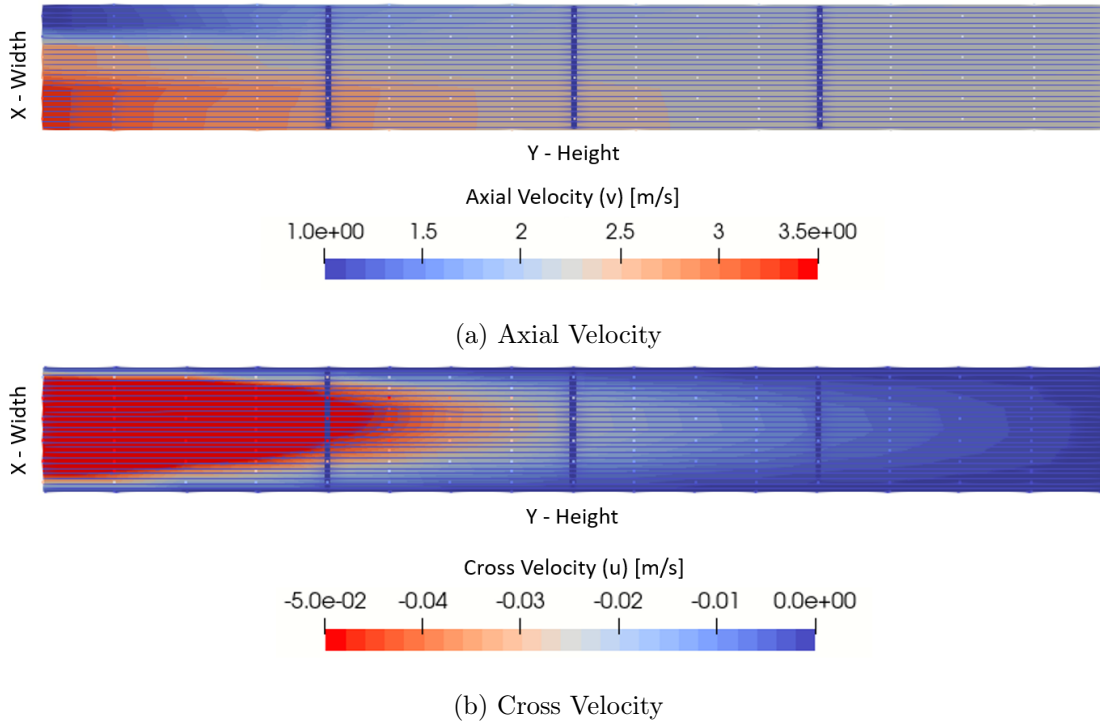


Figure 3.24: Numerical simulation of velocity fields $V_y(x, y)$ (a) and $V_x(x, y)$ (b) for a $172 \text{ m}^3/\text{h}$ flow and $c_N = 0.66$.

Table 3.3: Data differences between simulations and experiments.

Assembly	Heterogeneous c_N			Homogeneous c_N		
	Left	Central	Right	Left	Central	Right
max abs error [N]	11.99	6.04	5.58	1.79	19.94	10.40
average error [N]	3.56	3.40	3.50	1.10	4.99	5.35

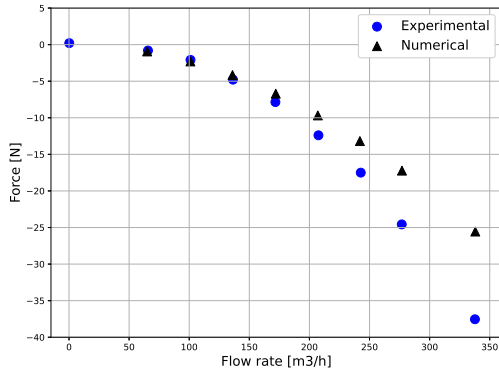
by cross flow and hence the bowing of the assemblies.

The differences between simulations and experiments are probably related to the presence of the grids, that are not taken into account in the numerical resolutions. The grids play a non negligible role in the flow redistribution, as shown for instance by [de Lambert et al. \[2021\]](#). Further experimental investigations are desirable to evaluate these effects such as measuring the pressure drop due to the presence of the grid or even adding more grids on the assemblies and measuring how the fluid forces vary.

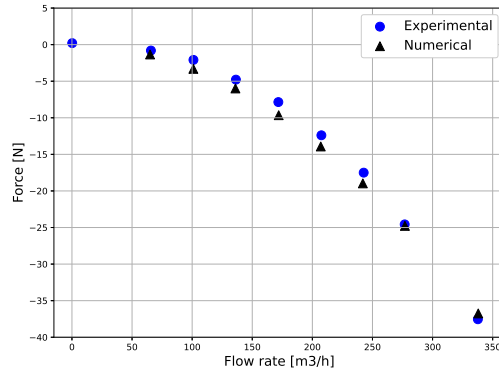
3.7 Conclusions

In this chapter we have presented a study on the drag coefficient which is a major parameter of the fluid interaction structure for PWR fuel assemblies, which is a concern for the nuclear industry.

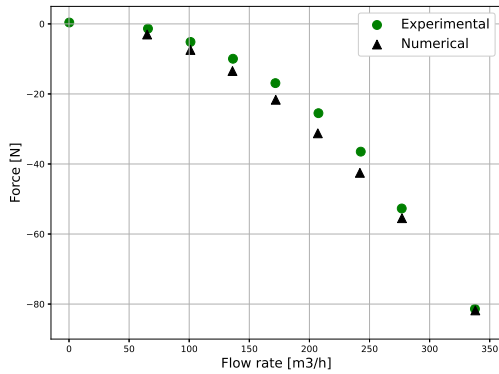
A new experimental set-up named Eudore which aims at studying fluid-structure in-



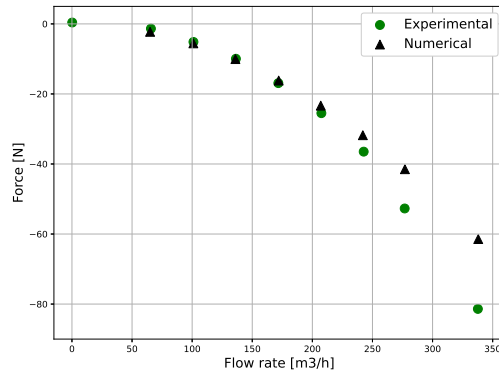
(a) Left assembly $c_N = 0.48$



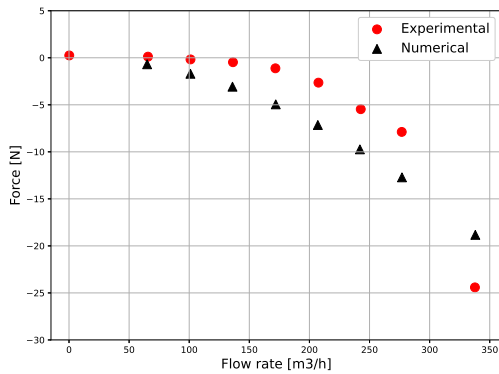
(b) Left assembly $c_N = 0.66$



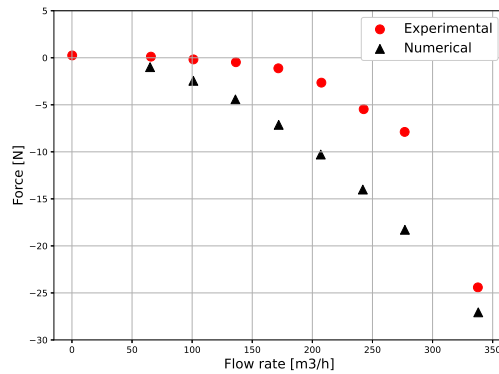
(c) Central assembly $c_N = 0.84$



(d) Central assembly $c_N = 0.66$



(e) Right assembly $c_N = 0.48$



(f) Right assembly $c_N = 0.66$

Figure 3.25: Comparison of force values from simulations and experiments for two different sets of c_N values: left column (a,c,e) separate values for each assembly; right column (b,d,f) identical average value for all assemblies.

teraction was presented. It involves three in line half-scale PWR assemblies and different diaphragms at the inlet section to generate a cross flow. Instrumented with both force sensors and LDV equipments, it provided a characterization of the hydraulic forces due to a flow redistribution at different flow rates.

Based on LDV measures, average axial and cross velocities profiles were derived for each assembly. These results were used in conjunction with an analytical model to estimate drag force coefficients. Numerical simulation based on the porous model approach showed a good agreement between experimental and numerical results as well as the great influence of the drag force coefficient on the fluid force acting on the assembly, and hence, their possible bowing.

Future experimental work will involve measurements with assemblies already bowed or free to move as well as new experiments with other types of diaphragms on the LCP or UCP. With the structure moving and the assemblies free to move, the fluid-structure interaction equations are enriched with terms regarding the velocity of the assemblies with respect to the fluid, while different diaphragms at the inlet and outlet will dictate new boundary conditions. Further investigations are desirable to evaluate the grid effect, measuring the pressure drop due to their presence or even adding more grids on the assemblies and measuring how the fluid forces vary accordingly.

Eudore offers the possibility of carrying out all these kind of experiments, i.e. it has a broad set of diaphragms, it allows to bend the assemblies and even to leave them free to move and put under vibration the whole structure simulating a seismic event. It would be interesting to see how much the drag coefficient varies with more or less transverse flow, understanding the sensibility of this investigation to the flow and to the structure conditions. This would finally show if normal drag coefficient range of values presented in this paper can predict the force values in the assembly-wall and assembly-assembly impacts.

The setup limitations will be improved. In fact, new velocimetry campaigns involve using an opaque black slab on the rear wall of Eudore so that there are no problems with laser light reflection.

On the numerical hand, the next step will be to take into account the presence of the grids and improve the prediction on the mechanical behavior of the reactor core. Subsequently the porous medium approach can be incorporated into a multiphysics model that takes into account fission reactions, the presence of radiation and their effects on material behavior. In this way it would be possible to obtain a model that takes into account the three main phenomena responsible for the deformation of the assemblies (irradiation creep, assembly growing and hydraulic lateral forces) and that can be used in the design phase to improve the assemblies mechanical performances.

Assembly vibrations under seismic-like load

Contents

4.1	Introduction	85
4.2	Eudore configuration for dynamical experiment	88
4.3	Experimental results and discussion	91
4.4	Numerical model for the Dynamic experiments	98
4.5	Comparison of experimental and numerical results	101
4.6	Conclusions and perspectives	105

Summary

In the previous chapters, we addressed the vibrations of an assembly in an stagnant fluid and the deformations suffered by assemblies due to transverse flow. In Chapter 2, on KC instabilities, the sinusoidal motion of the assembly was only taken into account as the amplitude of oscillation and the analysis was done on millimetre scale displacement fields. In Chapter 3, on the other hand, we considered the assemblies as static. In this chapter, we want to investigate the kinematics and dynamics of vibrating assemblies in the presence of an axial flow. We want to use the Eudore experimental setup and study the amplitudes of vibration induced and the impact forces between the assemblies and the walls. Since the experimental setup used is the same as in Chapter 3, the reader is referred to the description there. In the present case, however, no transverse flow is purposely induced, no diaphragms are used and the inlet and outlet flow channels are identical. The analyses of this chapter are of the dynamic type, i.e. a seismic load is simulated by means of the piston connected to Eudore. Since we are interested in the kinematics of the assemblies, we do not want them to be blocked by force sensors. The lateral force sensors were therefore set back from the rest position of the assemblies and they were brought on the wall, so as to interfere the least possible with the flow and the assemblies. The central force sensors and the connection clamp were removed and therefore no data could be retrieved on the central

assembly. We used different flow velocities and different vibration amplitudes imposed to the structure. The context of this work is to improve the predictability of numerical models aimed at simulating the kinematics and dynamics of a nuclear reactor core. We used the porous medium approach used in Chapter 3. The model is extended by considering the motion of the assemblies. We used the drag coefficient obtained in the previous chapter in the dynamic simulations. The comparison between dynamic experiments and simulations is provided at the end of the chapter. At low excitation amplitudes, the comparison shows good agreement, confirming how the drag coefficient found with Static experiments can also be used on numerical simulations for Dynamic experiments.

4.1 Introduction

The dynamic behaviour of the PWR (Pressurized Water Reactor) assemblies is generally non-linear. This non-linearity has two origins: the internal friction of the structure and the fluid-coupling effects induced by the axial flow. For the nuclear industry, the study of the dynamical behavior of the assemblies is fundamental: in the defined hypothetical transient of an accident, such as seismic shocks or sudden drops in water level (LOCA, Loss Of Coolant Accident), the assemblies would be subjected to strong vibrations. These vibrations can induce a collision between the assemblies. The mechanical behavior of the damaged assembly is affected and its correct functioning is no longer guaranteed. It is therefore crucial to evaluate the hydrodynamic interactions between assemblies in the design phase. Fuel assemblies are designed with large allowances for this type of events and the study of these accidental events can optimize their design.

Engineers need special tools to design and maintain reactor cores. These tools usually involve structural modeling accounting for added mass and added damping effects induced by fluid–structure interactions. They are of major concern since the fuel assembly response and thus the grids integrity will directly depend on them. The problematic of fuel assemblies vibrations was first investigated by [Chen \[1975\]](#), who previously investigated the vibration induced by a parallel flow on a rod [[Chen and Wambsganss, 1972](#)]. He proposed a method to analyze the rod assembly vibrations in a fluid that takes into account fluid coupling among the other force components. Since the flow strongly modifies the dynamical behaviour of the fuel assemblies [[Collard et al., 2005](#)], the identification of the fluid forces is important to provide a relevant modeling of the fuel assemblies behaviour. The first approximation of the fluid forces is to consider them as added mass and added damping [[Viallet et al., 2003](#), [Rigaudeau et al., 1997](#)]. [Païdoussis \[2003\]](#) proposed a more complex expression of these fluid forces, in which the velocity and the relative direction of the flow with respect to the fuel assembly are accounted for. Based on Païdoussis theory, [Ricciardi \[2008\]](#) proposed a porous media approach. These models, and in particular the porous medium approach, have their utility in many applications in nuclear industry, but also in other industrial fields, such as in heat exchangers, petroleum reservoirs or biomechanics. Practically these simplified approaches are used in every application where reproducing the

exact geometry implies large computational time.

The validity of the model simulating fuel assemblies vibrations need to be demonstrated by seismic experiments. Regarding seismic behavior of fuel bundles, some experimental studies have been performed in the latest three decades. [Queval et al. \[1991b\]](#) first investigated the impact forces on a row of fuel assemblies. He used a monoaxial shaking table, Vesuve, supporting a line of 5 or 13 fuel assemblies in air or still water, confined or unconfined. He showed how the response of the assemblies increases with the excitation and with the number of assemblies at high level excitation. The presence of still water increases the response of the unconfined assemblies and decreases the response of the confined line, with respect to the in air condition. [Queval et al. \[1991a\]](#) used these experimental results to validate two models: one with a single beam per assembly and one with 2 beams per assembly, which is more precise.

[Collard and Vallory \[2001\]](#) used Echasse facility to measure impact forces. This mock-up hosted 2 half-scale fuel assemblies. One of them could be bended and then released in order to impact on the other assembly, simulating large amplitude motion induced by seismic excitations. The forces were measured between the fuel assembly and the test section. With Echasse, other than air and still water condition, there was the possibility to impose an axial flow. Collard's experimental results show the importance of the axial flow on the impact forces: when the axial flow velocity increases, the impact forces decrease. [Ricciardi et al. \[2009b\]](#) validated a porous medium approach on a line of six full-scale fuel assemblies immersed in still water. Recently, [\[Faucher et al., 2021\]](#) validated the FSCore application, based on Ricciardi porous medium model, with experiments performed on Icare facility [\[Capanna et al., 2019\]](#).

[Clément \[2014\]](#) and [Boccaccio \[2015\]](#) retrieved modal characteristics of assemblies used in Icare. In that particular configuration, the Icare facility hosted 2 reduced-scale assemblies with an axial flow. The fuel assemblies used in Icare are the same mock-up fuel assemblies as the one used in Eudore. The nominal confinement is of 8.0 mm, larger than the one used in Eudore (2.0 mm). The right assembly is connected to a small hydraulic jack on the 4th grid, therefore the test section is still and only one assembly is forced. Icare was equipped with LVDT displacement sensors on the 2nd, 3rd and 4th grid of each assembly, in two directions: tangent and perpendicular to the oscillating direction. Furthermore, the hydraulic jack was equipped with a force sensor. The analysis of both force and displacement values provided the structural characteristic of the assembly shown in [Fig. 4.1](#). The experiments have been performed by forcing the assembly with a sinusoidal signal at different amplitudes and frequencies, with different flow rates. This study shows how the natural frequency of the assembly decreases with oscillating amplitude, but is not affected by the flow-rate. The modal mass (mass + added mass) does not show any significant variation with amplitude, but decreases with the flow rate, and at 2 m/s it is equal to the modal mass without water. The assembly rigidity decreases as the natural frequency with both amplitude and flow-rate increase. Finally, damping increases with both amplitude and flow-rate increase.

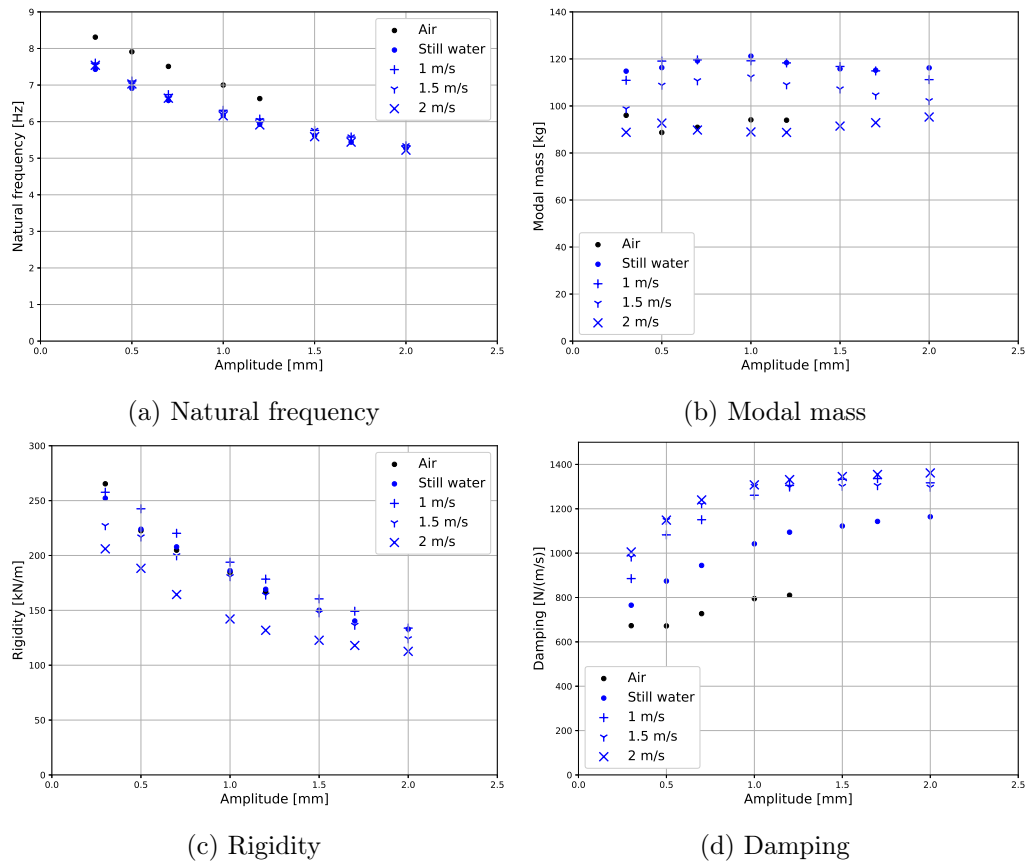


Figure 4.1: Structural characteristics of Eudore assemblies in Icare facility: 2 inline assemblies with 8 mm confinement [Boccaccio, 2015]. These graphs show how the natural frequency (a), the modal mass (b), the rigidity (c), and the damping (d) of an assembly varies as a function of the vibration amplitude and flow rates.

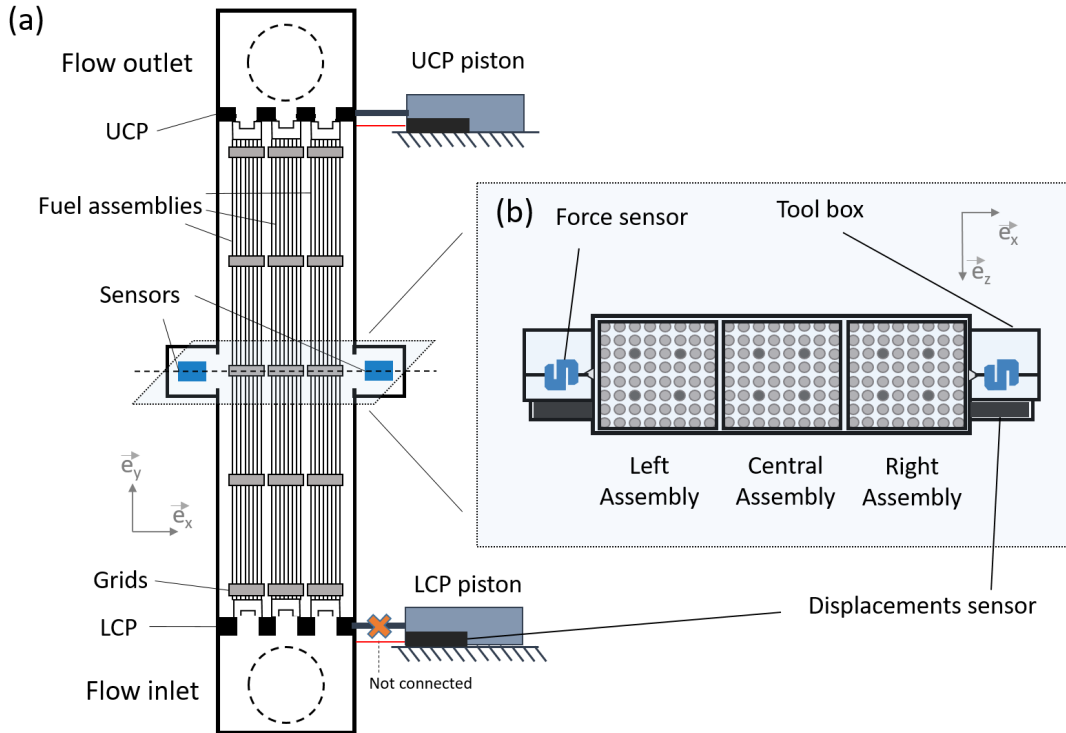


Figure 4.2: Eudore test section configuration for Dynamic experiments: (a) Vertical section. (b) Cross-section at the 3rd grid level.

[Ricciardi, 2018] performed a parametric study with the porous medium approach on a row of three fuel assemblies. In his study the coupling due to the axial flow was not affected by the confinement of the assemblies. In this chapter we will experimentally investigate the dynamics of a line of three fuel assemblies in Eudore. We will focus on the effects of the flow rate and the vibrating amplitude on the displacements and impact forces. With the Eudore facility we can study simultaneously an axial flow and an external seismic-like load on a line of 3 assemblies. To the author knowledge, measurements of forces and displacements on a line of assemblies under axial flow and seismic solicitation have never been presented in the literature before. We will complement these experimental observation with comparison to numerical results obtained using the porous medium approach.

4.2 Eudore configuration for dynamical experiment

In this chapter we use a line of three half-scale assemblies hosted in Eudore facility (Sec. 3.2.1). The test section rests on two rails and is linked to two lateral pistons on its right side (Fig. 4.2). Those can set in motion the entire test section in the rail direction. The connection to the Mercure 400 hydraulic loop is ensured by 6 flexible tubes, three upstream the LCP (Lower Core Plate) and three downstream the UCP (Upper Core Plate). The upper piston is connected to the UCP and the lower piston is connected to the LCP. Displacement sensors are installed on the pistons bases in order to record Eudore motion at

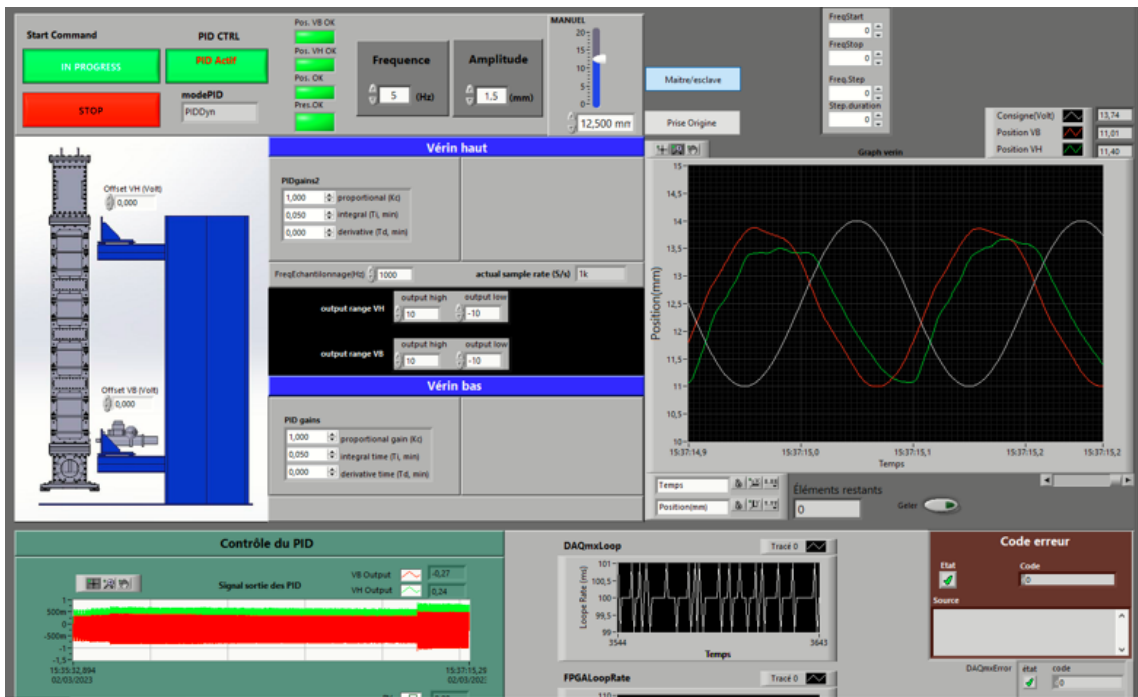


Figure 4.3: Control-command software for Dynamic experiments.

Table 4.1: Flow-rate conditions for dynamical experiments

Flowrate [m^3/h]	114.5	194.5	240.5	305.5	<i>Air</i>
Velocity [m/s]	1.56	2.64	3.26	4.14	<i>Air</i>

the UCP and LCP levels. The analysis presented in this chapter focuses on understanding assemblies displacements and impact forces in a seismic-like event. This kind of experiments is called Dynamic experiments.

Fig. 4.3 shows the latest implementation of the control-command software we developed on LabView to perform these Dynamic experiments. We can see the imposed signal and the displacement of the two hydraulic jacks: UCP and LCP (sinusoidal-like signals). As a first attempt, the control software has been operated in open loop, with no automatic feedback. Only the upper hydraulic piston is commanded in order to avoid synchronization problems that may arise with two pistons operating in open loop. During the experiments, the operator checked the displacement on LCP and UCP. When an unwanted motion raised on the displacement signals, the operator manually increased or decreased two adjustment coefficients changing the tension sent to the piston. In open loop, the PID controller (Proportional-Integrative-Derivative controller) was not active.

As shown in Fig. 4.4, for Dynamic experiments, the lateral force sensors were aligned with the inner walls, while the central force sensors and the clamp were removed (Fig. 3.5). The inlet and outlet channels for each assembly have been set to their widest opening, at 80 mm of diameter (Fig. 4.2).

The Dynamic experiments were conducted in two stages: first a flow rate was set on

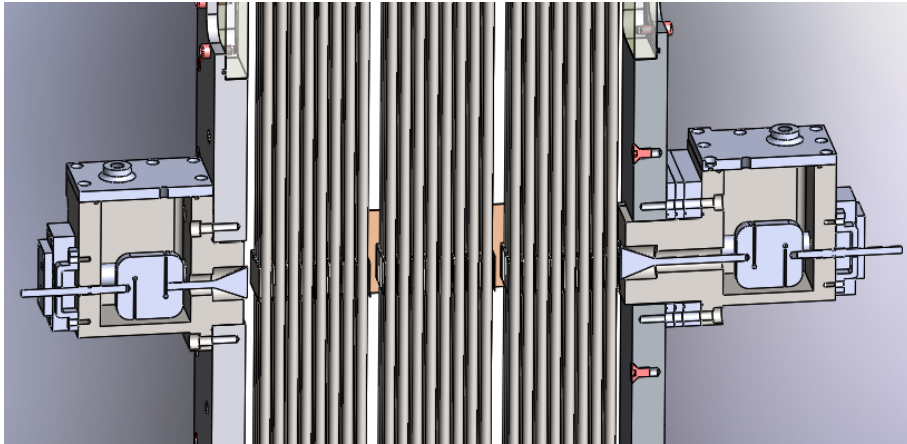


Figure 4.4: Force sensor in Dynamic experiment configuration

the hydraulic pump of the Mercure 400 loop, then the desired oscillation frequency and amplitude were set on the control-command software. As for the experiments with SBF in Chapter 2, each experiment has been performed at constant frequency. The desired frequency was first used at a relatively small amplitude, 0.5 mm, to avoid any sudden motion of the test section and the assemblies. The vibration amplitude then varied in steps of 0.5 mm. Each step counted several periods of oscillation, in a range from 40 to 65 periods. The number of periods differs for each experiments depending on the motion of the Eudore test section. We recorded measurements for as many periods as possible without large displacement variations that could arise due to the open-loop control.

Two oscillation frequencies, 5 Hz and 4 Hz, and four flow rates reported in Tab 4.1, have been investigated. Flow-rates were set by changing the frequency on the Mercure 400 pump. The velocity is the average axial velocity obtained by dividing the flow rate by the cross section in Eudore. The cross section, 0.02 m^2 is calculated subtracting from the whole horizontal section, $311 \times 105 \text{ mm}^2$, the area occupied by the rods 0.012 m^2 (64 rods with a diameter of 9 mm for 3 assemblies). The free test section does not take into account the presence of the grid or the inlet diaphragms area (0.015 mm^2 for the three channels).

Fig. 4.5 shows an example of displacement measurements in a dynamical experiment. Compared to UCP, the LCP moves smoothly and slightly out of phase. LCP is not linked to the lower piston so it can oscillate freely on the rails. The two signals have different amplitudes; since the LCP is smoother and sinusoidal, we will take its amplitude as reference in the following analysis. The experiments are controlled in open loop and the measurements at different flow rates or frequencies do not share exactly the same LCP amplitude; those are always in the range $[0.78, 3.18]$ mm. In Fig. 4.5 Left and Right refer respectively to the third grid of the left and right assemblies (see Fig. 4.2). We can see that they move with different amplitudes because of the different confinements of the assemblies. Nominally, the confinement in Eudore test section is set to 2 mm between each assembly and between each assembly and the walls (even for frontal and rear walls). During the configuration changing phase of Eudore from Static to Dynamic, the test section was mounted slightly

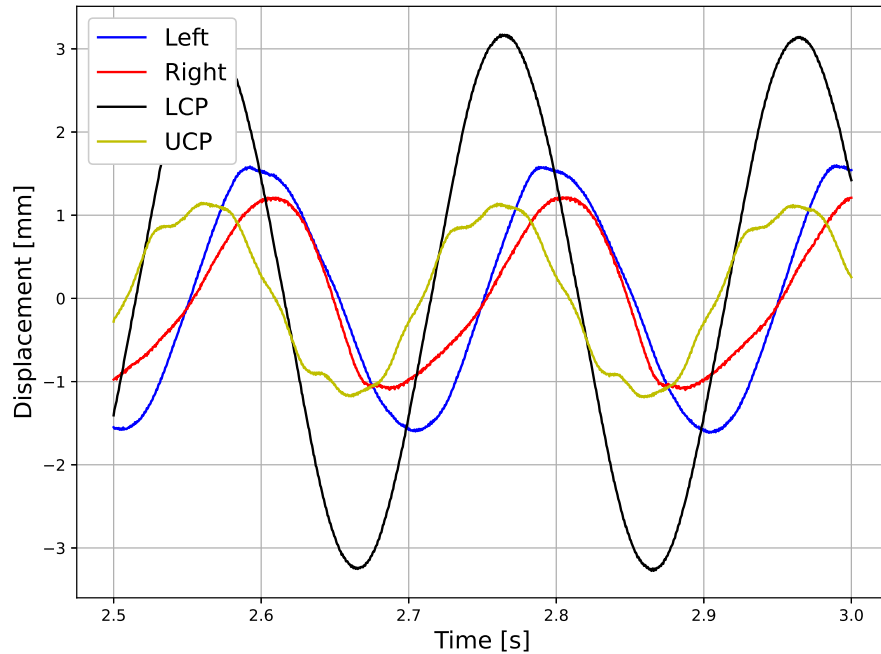


Figure 4.5: Displacement data example for dynamic experiments. Experiment at 5 Hz and $305.5 \text{ m}^3/\text{h}$. Left is the displacement for the third grid of the left assembly, Right is the displacement for the third grid of the right assembly.

misaligned with the LCP. This caused a change in the lateral gaps that were not exactly of 2 mm. Furthermore, the assemblies are elongated structures which can bow and whose side surfaces may not be exactly parallel. Therefore even the inner gap values differ from the nominal value of 2 mm. In particular, the left assembly has a larger confinement than the right assembly, justifying a larger amplitude as we will see in the next section.

4.3 Experimental results and discussion

In this section we will analyze the experimental measurements of the third grid of the lateral assemblies. The third grid is at half height of the assembly. Since the oscillation frequency is close to the natural frequency of the assembly (Fig. 4.1a), we will assume that the assemblies oscillate with the classical D-shape of the first proper mode for a clamped-clamped beam. The half-height point is a node for eigen even vibration modes, hence we are not able to directly observe these modes by measuring the displacements of the mid-height grid. In the following, we will refer to the motion of the assembly at mid-height as the motion of the lateral assembly itself, both for Left and Right.

Fig. 4.6 shows the displacements and impact forces measured with displacement and force sensors present on the lateral walls for assemblies Left and Right at different solicitation amplitudes (frequency is 5 Hz and flow-rate $114.5 \text{ m}^3/\text{h}$). As said above, for this experimental campaign, assembly Right is closer to the right wall than assembly Left to the left wall. We can see how, even for small oscillation amplitudes, the right assembly

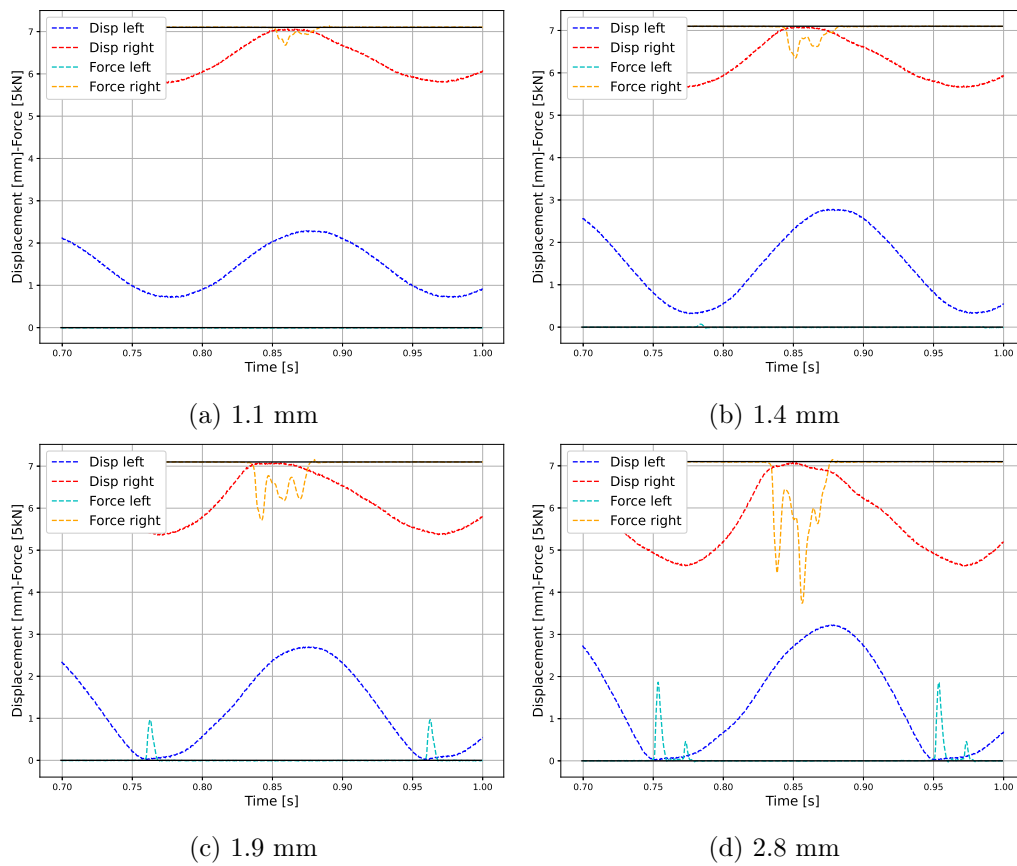


Figure 4.6: Displacements and impact forces for left and right assemblies solicited at 5 Hz with a flowrate of $114.5 \text{ m}^3/\text{h}$ and different amplitudes for LCP.

impacts on the wall, while the left assembly oscillates freely. One can also see that the assemblies do not always oscillate sinusoidally. The displacements, u_L and u_R , are the distances ran by the third grid from the closest to furthest point of the reference wall, left or right. In this sense, Fig. 4.6 has to be intended qualitatively and not quantitatively. We can talk of equivalent amplitudes for the assemblies $a_{e,L}$ and $a_{e,R}$, and it would correspond to half their displacement $2 \times a_{e,L} = u_L$ and $2 \times a_{e,R} = u_R$.

From the assembly displacements at different LCP amplitudes and flow rates, we can identify the available gaps between the lateral walls and the lateral assemblies (i.e. the maximum equivalent amplitude without impact). We identify the left gap, between the left wall and the left assembly, as 1.5 mm, and the right gap, between the right assembly and the right wall, as 0.6 mm. When the oscillation amplitude¹ of the LCP approaches 1.4 mm the left assembly impacts the left wall and its motion is not smooth any more (Fig. 4.6b). The impact force peak is barely visible in Fig. 4.6b and the displacement signal still appears sinusoidal. One should have in mind that even if the force sensors are aligned with the lateral wall (Fig. 4.5), they protrude a few tenths of millimetre into the section. In this way the grid impacts on the sensor and not directly on the wall and we are able to measure the impact force. That few tenths of millimetre are probably the reason why we do not see any effect on displacement signal in Fig. 4.6b.

Fig. 4.7 shows the variation of displacements and impact forces with forcing amplitude and flow-rate for assemblies Left and Right. The induced displacements u_L and u_R increase when the LCP amplitude a_{LCP} increases and decrease when increasing the flow-rate. This is a direct effect of the added mass and added damping induced by the flow rate. From Fig. 4.7a one can define a threshold LCP amplitude at which the left assembly start impacting the left wall. This threshold LCP amplitude increases with the flow rate. The flow rate effect is more evident for assembly Left because of the larger confinement and because assembly Right impacts on the wall at each amplitude and flow rate. We can see the impact force values increasing with amplitude and decreasing with flow rate (Fig. 4.7a and 4.7b). Referring to the analysis of Boccaccio [2015], in Fig. 4.1b and 4.1d, one can see that the added mass effect decreases and the damping increases when the flow velocity increases. Since in this work we used higher velocities², we can expect an enhancement of these effects. In summary, increasing the flow rate the damping increases, the added mass decreases and, by consequence, the overall impact forces and induced displacements decrease.

At the time of impact with the lateral walls, the displacement signal is almost flat and does not help understanding the impact dynamic. Fig. 4.8 shows the different impact peaks shapes for left and right assemblies, with a flow-rate of 114.5 m³/h, forcing frequency of 4 and 5 Hz and different amplitudes. By comparing assemblies Left and Right, we can see

¹We refer to the experimental amplitudes we have performed. We are not able to identify the maximum oscillation amplitude without impacts, but only the maximum oscillation amplitude without impacts among the amplitudes we performed.

²It is not appropriate to talk about flow-rate because the test sections Icare and Eudore have different cross-sections.

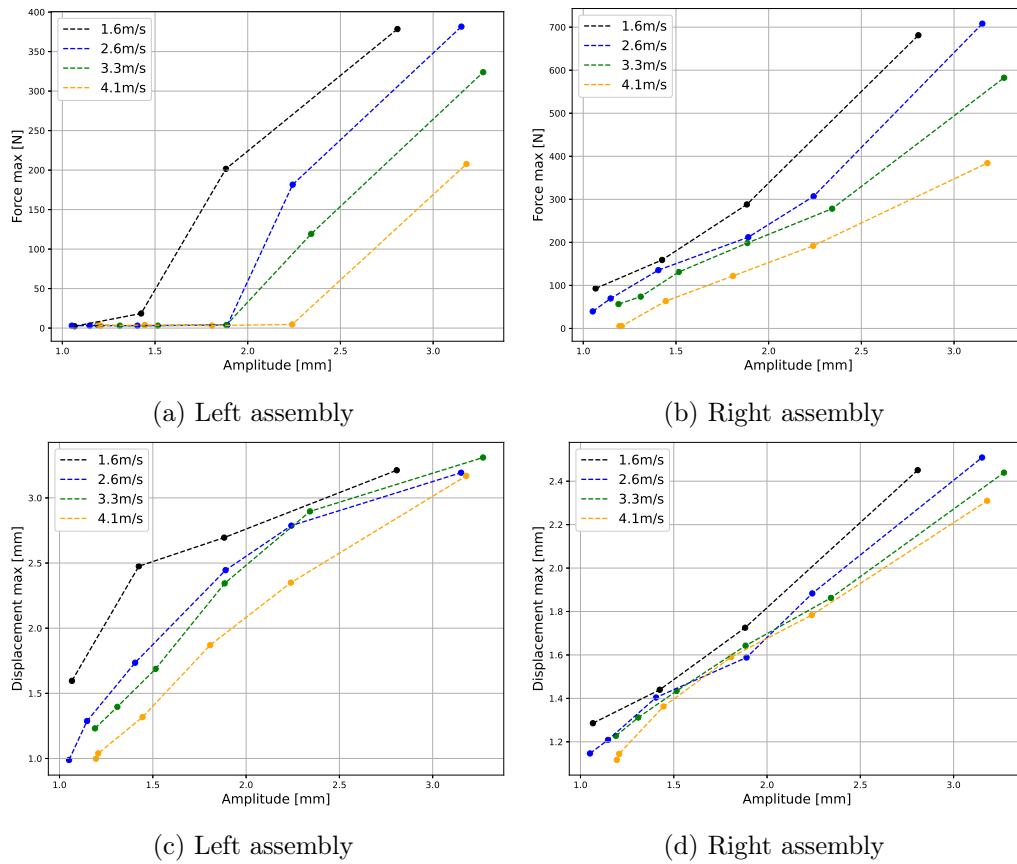


Figure 4.7: Impact forces and displacement variations with amplitude and flow-rates at 5 Hz.

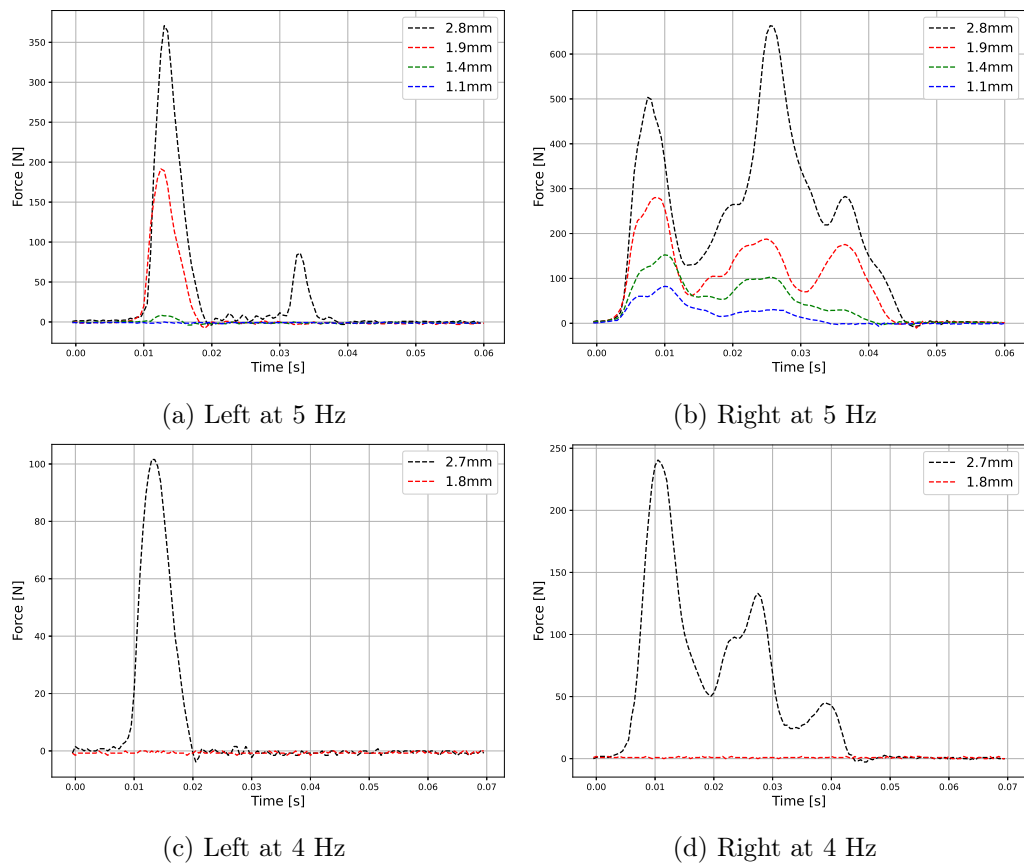


Figure 4.8: Impact forces for left and right assemblies at 4 and 5 Hz with a flow-rate of 114.5 m³/h for different LCP amplitudes.

Table 4.2: Number of impact peaks per LCP amplitude at 5 Hz and 114.5 m³/h.

a_{LCP} [mm]	$a_{e,L}$ [mm]	$a_{e,R}$ [mm]	# peaks L	# peaks R
1.1	0.8	0.7	0	1
1.4	1.3	0.8	1	2
1.9	1.4	0.9	1	3
2.8	1.6	1.2	2	3

how the forces measured at impact are different. This underlines a different dynamic during the impact shocks. As seen previously, at 5 Hz, assembly Left impacts starting at LCP amplitude $a_{LCP} = 1.4$ mm, while its displacement is $u_L = 2.5$ mm ($a_{e,L} = 1.25$ mm). At $a_{LCP} = 1.9$ mm there is again a single impact peak while for $a_{LCP} = 2.8$ mm we can see a second smaller impact peak arising after 0.02 s. For assembly Right (Fig. 4.8b), the second smaller peak is already visible for $a_{LCP} = 1.1$ mm. It increases up to $a_{LCP} = 1.9$ mm where a smaller shoulder peak appears before the second peak and a third peak appears, of about the same intensity of the second peak. At higher amplitude, $a_{LCP} = 2.8$ mm, the shoulder peak and the third peak have the same intensity, but the second peak is now stronger than the first peak.

Tab. 4.2 reports equivalent amplitudes and number of peaks for assemblies Left and Right per LCP amplitude at 5 Hz and 114.5 m³/h. One can see one impact peak arises as soon as the equivalent amplitude ($a_{e,L}$ or $a_{e,R}$) is greater than the relative gap (assembly to left wall 1.5 mm or right wall 0.6 mm) subtracted of the few tens of millimetre due to the force sensor thickness. To retrieve the real dynamic, we would need at least the measurements on the central assembly displacement. Without those measurements, we can make some hypothesis to explain the evolution of other peaks. We can make three hypotheses for the presence of the second peak:

1. Assembly Right touches the force sensor for the first impact, other higher frequencies are excited and the assembly, as it is vibrating, hits on the force sensor again.
2. Once the right assembly moves away after the first impact, the central assembly impacts on the right assembly and pushes it back to the right wall: at the time of the second peak the right assembly is in contact with both the central assembly and the right force sensor.
3. Once the right assembly moves away after the first impact, the central assembly impacts on the right assembly: the impact between the assemblies is instantaneous and only the right assembly moves toward the right wall hitting the force sensor again.

In hypotheses 2 and 3, the central assembly hits the lateral assembly causing the second peak. In case 2 the central assembly hits the lateral assembly and then it changes displacement direction. The lateral assembly is then pushed to hit the wall. In case 3, once the central assembly hits the lateral one, both of them proceed in the same direction and on

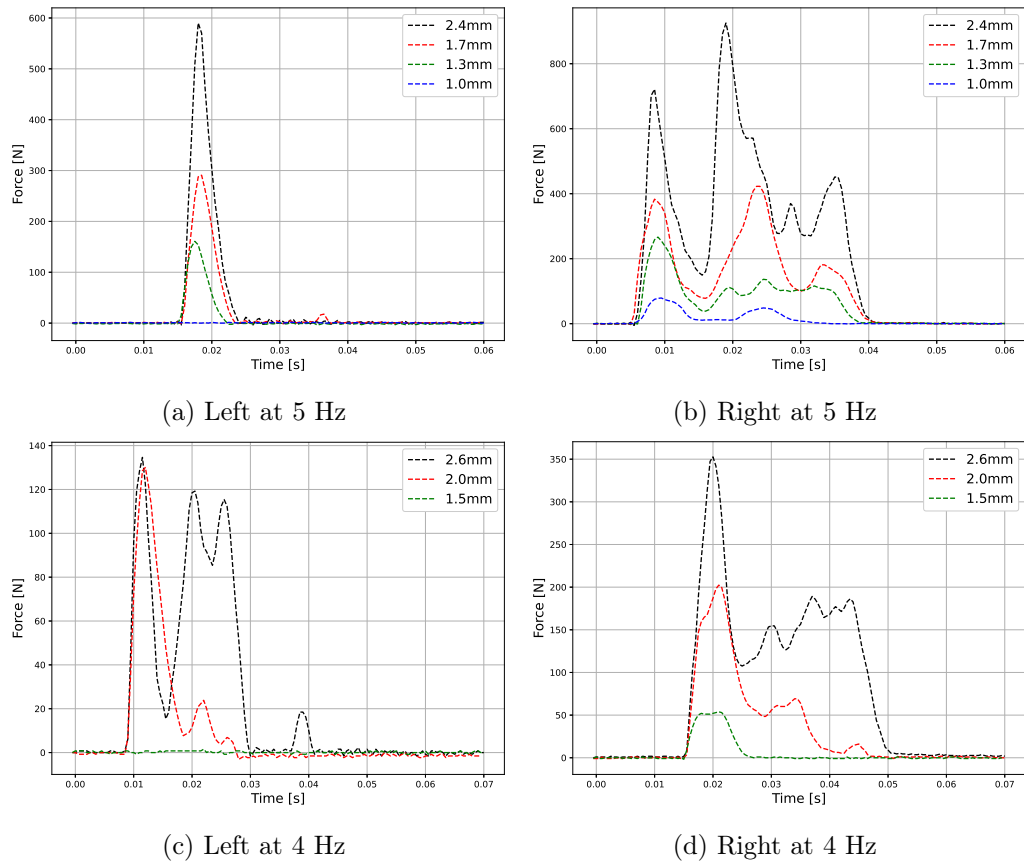


Figure 4.9: Impact forces for left and right assemblies at 4 and 5 Hz in air.

the impact moment the central assembly is pushing the lateral against the force sensor. We have seen that assembly Left has larger displacements, hence we can assume that the central assembly does not affect significantly the dynamics of the left assembly. Since the presence of the second peak is seen for both lateral assemblies, Left and Right, hypothesis 1 seems more probable, because in this case the central assembly does not contribute to the second peak. In hypothesis 1, when the lateral assembly hits the wall, higher frequencies and higher vibration modes are excited, causing a second hit on the wall. On the contrary, when the third peak appears, the central assembly likely affects the dynamics, causing the shoulder peak and strengthening the second peak. The shoulder peak could be a sign of an impact with the central assembly as in case 2, while when the second peak is stronger than the first one, the impact would be as the one described in case 3. The third peak would be due to the rebound of the only lateral assembly as we assume it is at lower LCP amplitudes.

At 4 Hz the excitation frequency is further away from the natural frequency of the assemblies. The assembly displacements in those cases are smaller and the motion of the assemblies is closer to Eudore translation than the D-shape vibration. Fig. 4.9 shows the force measurements at impact for the experiments in air at 4 and 5 Hz. We can see how the

Table 4.3: Force peaks at 4 Hz for different flow-rates

Flowrate [m^3/h]	Amplitude [mm]	Force [N]		
		Left	1 st Right	2 nd Right
<i>Air</i>	2.6	135	350	190
114.5	2.7	100	240	130
194.5	3.0	-	175	110
240.5	3.0	-	205	90
305.5	2.9	-	115	45

Table 4.4: Force peaks at 5 Hz for different flow-rates

Flowrate [m^3/h]	Amplitude [mm]	Force [N]		
		Left	1 st Right	2 nd Right
<i>Air</i>	2.4	600	745	950
114.5	2.8	375	500	650
194.5	3.2	365	560	690
240.5	3.3	330	470	570
305.5	3.2	180	380	280

dynamics change due to the absence of the hydrodynamic coupling between the assemblies. Furthermore, without water the added damping and mass effects are not present, resulting in stronger impact forces. Tab. 4.3 and 4.4 show the peak values at highest performed LCP amplitude for different flow-rates. We can see how the impact forces in air are stronger than in water with the presence of a flow rate. We can also see they are stronger at 5 Hz than at 4 Hz.

4.4 Numerical model for the Dynamic experiments

As explained in Chapter 3, the porous medium approach describes the FSI problem as an equivalent fluid model and an equivalent structure model, both defined in the whole domain. The fuel assemblies are modeled as an equivalent porous beam (Fig. 4.10). Motion equations for both equivalent entities, fluid and structure, are established separately. For the equivalent fluid model, the Navier-Stokes equation are spatially averaged in an Arbitrary Lagrangian-Euler reference, ALE, (Eq. 3.11 and 3.12). The resulting equivalent velocities and pressure are defined in the whole domain (Eq. 3.13). Fluid related effects on the structure are accounted for through a body force, which is again defined in the whole domain. In our case the whole domain corresponds to the inner part of Eudore test section, but it can be applied to the entire nuclear reactor core.

In Chapter 3, the assemblies were considered static and fluid forces acting on them were represented in Eq. 3.4. In the static case, only two force components have been accounted for: the inertial and the normal drag. The expressions for the force components in Eq. 3.5 are simplified expressions valid only for the static case. For the dynamic case, since the assemblies are free to move, there are 4 force components present in the porous medium

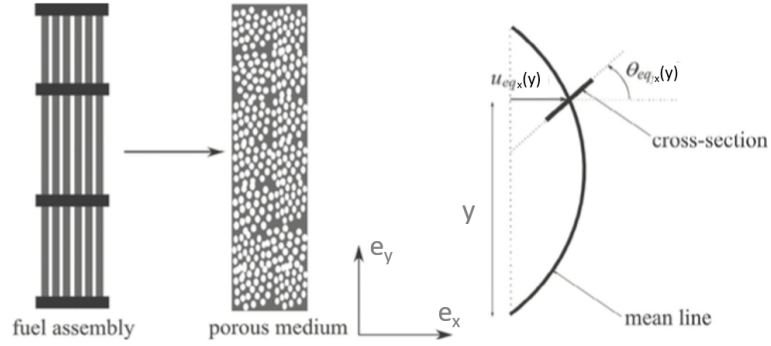


Figure 4.10: Fuel assembly seen as an equivalent porous beam [Faucher et al., 2021].

approach proposed by Ricciardi et al. [2009a]. In 3 dimensions, the force terms are:

$$\begin{aligned} \vec{f}_I &= -m_f \left(\frac{\partial}{\partial t} \left(\frac{\partial u_x}{\partial t} - V_x \right) + V_y^2 \frac{\partial^2 u_x}{\partial y^2} + 2V_y \frac{\partial}{\partial y} \left(\frac{\partial u_x}{\partial t} - V_x \right) \right) \vec{e}_x \\ &\quad - m_f \left(\frac{\partial}{\partial t} \left(\frac{\partial u_z}{\partial t} - V_z \right) + V_y^2 \frac{\partial^2 u_z}{\partial y^2} + 2V_y \frac{\partial}{\partial y} \left(\frac{\partial u_z}{\partial t} - V_z \right) \right) \vec{e}_z \end{aligned} \quad (4.1)$$

$$\vec{f}_N = -\frac{1}{2} \rho d V_y c_N \left(\frac{\partial u_x}{\partial t} - V_x + V_x \frac{\partial u_x}{\partial y} \right) \vec{e}_x - \frac{1}{2} \rho d V_y c_N \left(\frac{\partial u_z}{\partial t} - V_z + V_z \frac{\partial u_z}{\partial y} \right) \vec{e}_z \quad (4.2)$$

$$\vec{f}_L = +\frac{1}{2} \rho d c_T V_y^2 \vec{e}_y \quad (4.3)$$

$$\vec{f}_D = -c \left(\frac{\partial u_x}{\partial t} - V_x \right) \vec{e}_x - c \left(\frac{\partial u_z}{\partial t} - V_z \right) \vec{e}_z. \quad (4.4)$$

\vec{f}_I is the inertial term, \vec{f}_N is the normal drag term, \vec{f}_L is the tangential drag or lift term and \vec{f}_D is the damping term, characterized by the damping coefficient c . The notation u_i refers to the assembly displacement along i , while V_i denotes fluid velocity along i . Even if the damping term is actually present in the numerical model, we rely on the normal drag term to account for the damping effect. Therefore we decided to not consider the damping term in the numerical simulations, using in practice $c = 0$. As stated in Chapter 3, m_f is the added mass per unit length, c_N and c_T are the normal and tangential drag coefficients.

It is important to come back to the coupled model seen in Chapter 3 (Eq. 3.17). At that time, we did not discuss the dynamics because the assemblies bowed statically.

$$\rho_{eq} \frac{\partial \vec{V}_{eq}}{\partial t} + \rho_{eq} \nabla \cdot (\vec{V}_{eq} \otimes \vec{V}_{eq}) = -\nabla P_{eq} + \mu_{T_{eq}} \Delta \vec{V}_{eq} + 2\rho_{eq} \frac{\partial \vec{u}}{\partial t} \cdot \nabla \vec{V}_{eq} - \rho_{eq} \vec{V}_{eq} \cdot \nabla \frac{\partial \vec{u}}{\partial t} + \underbrace{\frac{1}{V_{\Omega_t}} \int_{\partial \Omega_s(x,y,z)} \underline{\underline{\sigma}} \vec{n} dS}_{\vec{f}_{\text{structure} \rightarrow \text{fluid}}}, \quad (4.5)$$

$$\nabla \cdot \vec{V}_{eq} = 0, \quad (4.6)$$

$$m_A \frac{\partial^2 u_{eqx}}{\partial t^2} = \frac{\partial Q_x}{\partial y} + T_0 \frac{\partial^2 u_{eqx}}{\partial y^2} + \frac{1}{p^2} \int_{S_A} \left(f_{I_x} + f_{N_x} + f_{D_x} - y f_{L_x} \frac{\partial^2 u_{eqx}}{\partial y^2} \right) dS, \quad (4.7)$$

$$m_A \frac{\partial^2 u_{eqz}}{\partial t^2} = \frac{\partial Q_z}{\partial y} + T_0 \frac{\partial^2 u_{eqz}}{\partial y^2} + \frac{1}{p^2} \int_{S_A} \left(f_{I_z} + f_{N_z} + f_{D_z} - y f_{L_z} \frac{\partial^2 u_{eqz}}{\partial y^2} \right) dS, \quad (4.8)$$

$$I_{fA} \frac{\partial^2 \vec{\theta}_{eq}}{\partial t^2} = \frac{\partial \vec{M}}{\partial x} + \vec{e}_y \wedge \vec{Q} + \vec{M}_{\text{fluid} \rightarrow A}. \quad (4.9)$$

In these equations, the structure motion is accounted by the equivalent displacement u_{eqx} and by the equivalent rotation angle of the rod section $\vec{\theta}_{eq}$. m_A and I_{fA} are the mass and second moment of inertia per unit length of an assembly, T_0 is the tension force at the bottom of the assembly, p is the rod center-center pitch, S_A is the cross-section area of the equivalent beam, \vec{Q} is the shear force and \vec{M} is the bending moment. The expression for these two last quantities gives the constitutive law of the assembly:

$$\vec{Q} = G_{eq} S_A \left(\frac{\partial \vec{u}}{\partial y} - \theta \right) + \mu_G S_A \frac{\partial}{\partial t} \left(\frac{\partial \vec{u}}{\partial y} - \theta \right) \quad (4.10)$$

$$\vec{M} = E_{eq} I_{fA} \frac{\partial \theta}{\partial y} + \mu_E I_{fA} \frac{\partial^2 \theta}{\partial t \partial y} + \vec{M}_{fr} \quad (4.11)$$

where G_{eq} is the shear modulus, E_{eq} is the Young modulus, and μ_G and μ_E are viscoelastic damping coefficients. Coupling coefficients used in the numerical simulations are reported in Tab. 4.5. In Eq. 4.11 \vec{M}_{fr} is a term accounting for the non-linear contact between rods and grids. It considers the difference between the rotation angle of the rods and the friction angle θ_f . Their expression are:

$$M_{fr_{x/z}} = M_{0_{x/z}} + \begin{cases} \frac{N_e^2 K_d d_f^2}{12} (\theta_{x/z} - \theta_{0_{x/z}}) & \text{if } (\theta_{x/z} - \theta_{0_{x/z}}) < \theta_f \\ \frac{N_c^1 F_{ri} d_x}{4} - \frac{N_p F_x^3}{3d_x K_c^2} \frac{1}{(\theta_{x/z} - \theta_{0_{x/z}})^2} & \text{if } (\theta_{x/z} - \theta_{0_{x/z}}) > \theta_f \end{cases}, \quad (4.12)$$

$$\theta_f = \frac{2F_{ri}}{N_p d_g K_c}. \quad (4.13)$$

$$(4.14)$$

$M_{fr_{x/z}}$ and $\theta_{0_{x/z}}$ correspond to the moment and the angle when the fuel assembly changes direction (hence at its maximum bow). N_p is the number of fuel rods in the excitation direction, K_c is the fuel rod axial stiffness and F_{ri} is the friction force caused by the pushing springs in the grid cell on the rod. The friction angle θ_f is deduced from the comparison of the rod axial force to the rod-to-grid friction limit F_{ri} for the peripheral rods in the assemblies. The model is described by [Faucher et al. \[2021\]](#).

4.5 Comparison of experimental and numerical results

The model equations are rich of parameters that need to be measured. [Faucher et al. \[2021\]](#) validated the porous medium approach in the FSCORE application using the experiments performed on Icare (Sec. 1.4). As we have seen, even if the fuel assemblies are the same, their arrangement changes. Icare hosts 2 or 4 assemblies in 1×2 or 2×2 lattices. In Icare only one lateral assembly was displaced by an hydraulic jack connected to the 4th spacer grid.

Fig. 4.11 shows the transfer function between the hydraulic jack displacement and the force applied to move the assembly. The transfer function is retrieved from experimental data and computed by the numerical code for both Icare configurations (2 and 4 assemblies), in stagnant water and with a 2 m/s flow velocity. This dynamic test on Icare was performed applying a swept sine between 0 and 10 Hz at a constant displacement amplitude.

We can see that the simulations can reproduce accurately the experimental results. From the transfer function we can see that the porous medium approach has been validated and how it correctly predicts the resonance frequency, the rigidity and the damping of the fuel assembly. We can also see how simulations reproduce the increase of damping as the fluid velocity increases. Numerical simulations also show good results also on the hydraulic coupling between the assemblies. Overall, simulations reproduce fairly well the global dynamics of the Icare system. We will use most parameters identified by [Faucher et al. \[2021\]](#) in the FSCORE validation in order to reproduce Eudore Dynamic experiments. More precisely, we will use all parameters except the fluid-structure coupling parameters. For these parameters we will use the values measured in Chapter 3.

Tab. 4.5 contains the values used in the numerical simulations for fluid-structure coupling. As said above, the real gap values between assemblies differ from the nominal ones.

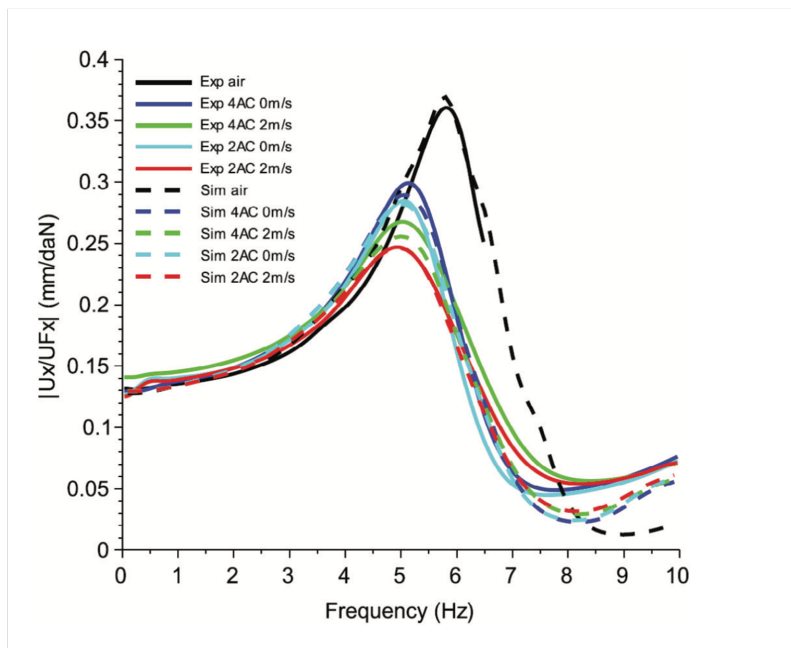


Figure 4.11: Transfer function of Eudore fuel assembly [Faucher et al., 2021].

Table 4.5: Coefficient for the fluid-structure coupling

Added mass	Normal drag	Tangent drag	Still water damping coefficient
$m_f = 0.12$	$c_N = 0.84$	$c_T = 0.02$	$c = 0.0 \text{ kg}/(\text{m}\cdot\text{s})$

Table 4.6: Gaps value for numerical simulations

1 st gap	2 nd gap	3 rd gap	4 th gap
1.5 mm	3.8 mm	1.2 mm	0.6 mm

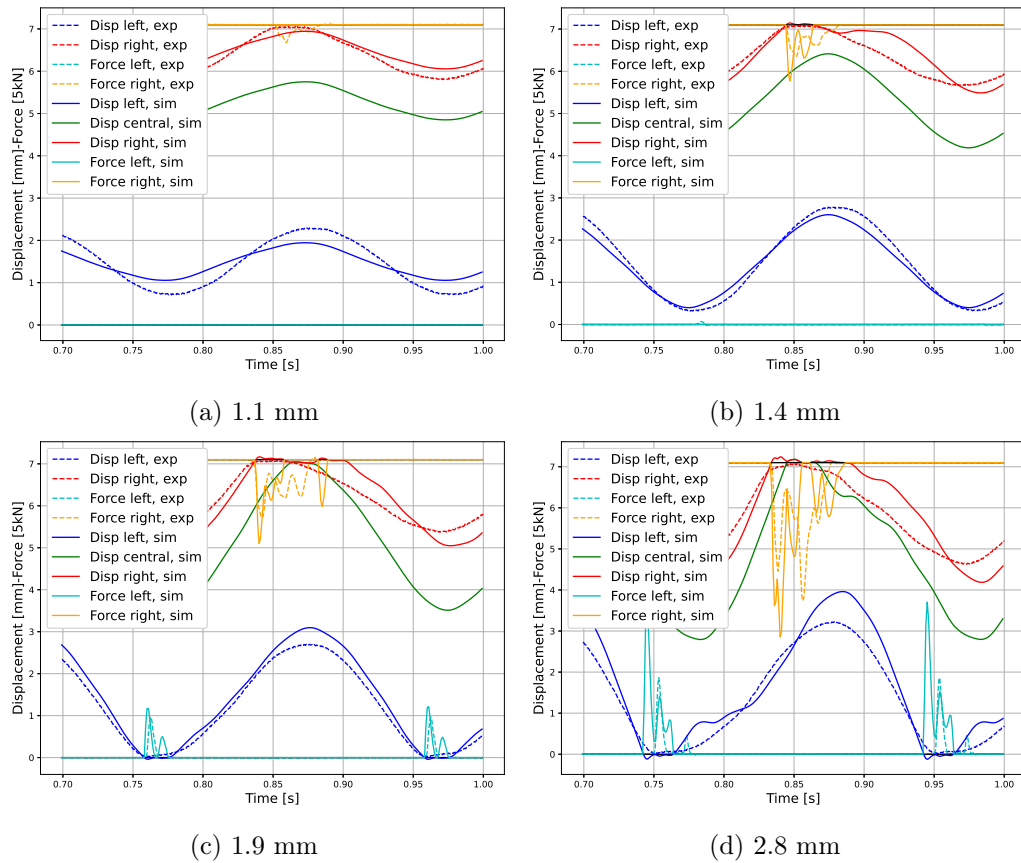


Figure 4.12: Numerical and experimental values for displacements and impact forces for assemblies solicited at 5 Hz with a flowrate of $114.5 \text{ m}^3/\text{h}$ and different LCP amplitudes.

With the experimental analysis we measured the lateral gap values. By performing the numerical simulations, we identified the other 2 gaps in Eudore test section: between the left and central assemblies (2^{nd} gap), and between the central and right assemblies (3^{rd} gap). We tried different simulations to reproduce the experimental behavior of assemblies Left and Right. This led to gap values given in Tab. 4.6.

Fig. 4.12 shows numerical and experimental data for assemblies forced at 5 Hz with a flow rate of $114.5 \text{ m}^3/\text{h}$ at different LCP amplitudes. In the numerical simulations the LCP amplitude is actually the whole test section amplitude, since there is no difference between the UCP and LCP motions. Motion for assemblies Left and Right is well reproduced in simulations for low amplitudes (Fig. 4.12b and 4.12d). With the numerical model, we can simulate also the central assembly motion. At high amplitudes (Fig. 4.12c and 4.12d), precisely when the the central assembly starts hitting one of the lateral assemblies, the numerical kinematics of the lateral assembly hit slightly differs from the experimental measurements. If the kinematics of the central assembly is accurate, we can see that, as we assumed in Sec. 4.3, the central assembly is not involved in the second peak.

Fig. 4.13 compares the simulated and measured displacements and maximum impact forces and their dependence from the vibrating section amplitude. The comparisons are

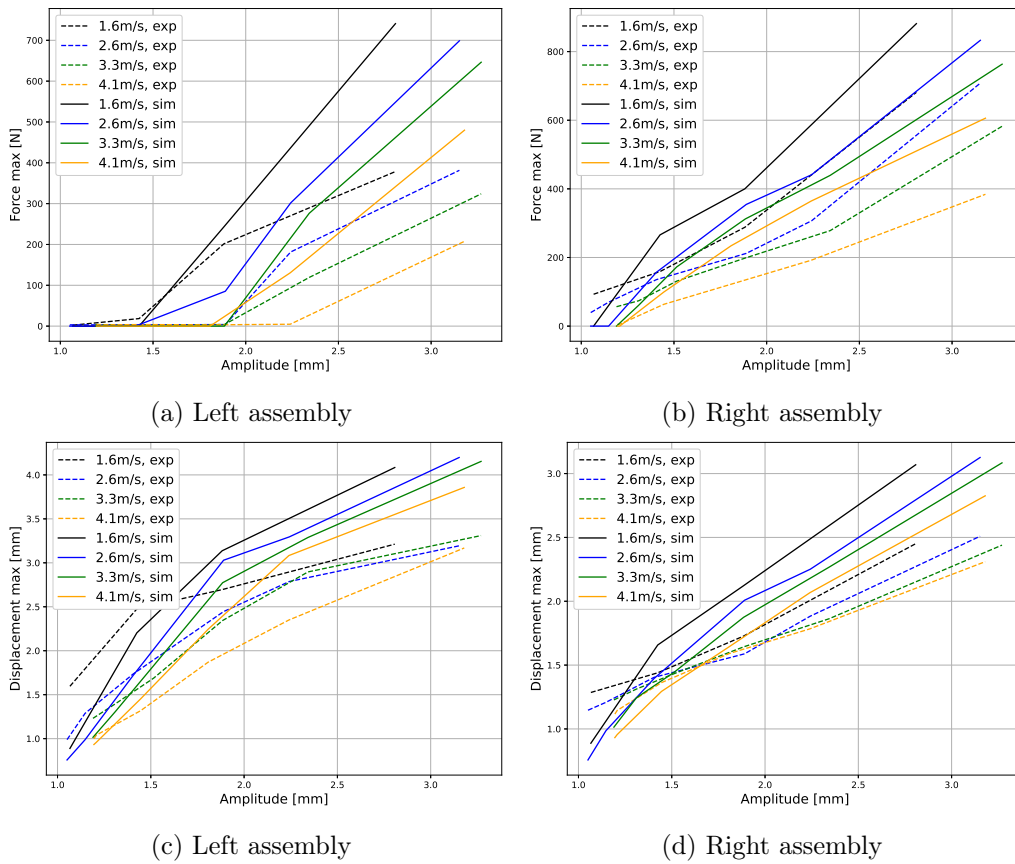


Figure 4.13: Impact forces and displacement variations with amplitude and flow-rates at 5 Hz.

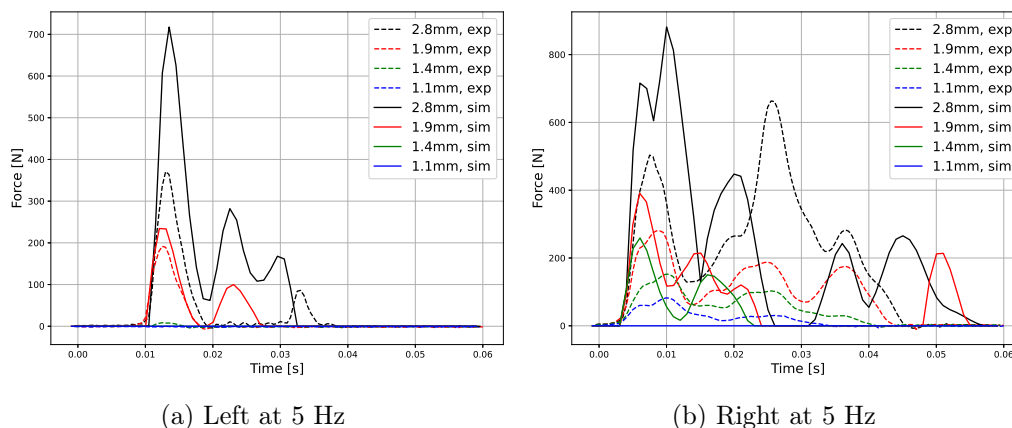


Figure 4.14: Numerical and experimental values of impact forces for left and right assemblies at 5 Hz with a flow-rate of $114.5 \text{ m}^3/\text{h}$.

for both lateral assemblies for different flow rates at 5 Hz. Numerical simulations show a good qualitative agreement with experiments, although they tend to overestimate both the forces and the displacements at large forcing amplitudes. Left impact forces are more overestimated than Right, probably because of the larger displacements (due to the larger gap). Furthermore, we should have in mind that experimental LCP amplitudes were larger than UCP amplitudes which is not the case in the simulations. At third grid level, where the measurements have been taken, amplitude is higher than for UCP but lower than for LCP. Imposing the LCP amplitude everywhere in the numerical model leads to larger displacements than in the experiments and this may explain why simulations tend to overestimate the displacements and the impact forces.

In Fig. 4.14 we compare the simulated and measured impact forces for left and right assemblies at 5 Hz with a flow rate of $114.5 \text{ m}^3/\text{h}$. For assembly Right, simulations and experiments both exhibit the arising of the third peak at high amplitudes but impact time is more rapid and a fourth and fifth peaks arise which are not present in the experiment. These differences could be due to the larger forcing amplitude in the simulations, but it could also be due to non-linear effects that are taken into account in the model (both structural ones and fluid ones).

4.6 Conclusions and perspectives

The objective of this chapter is to better understand the behavior of the PWR fuel assemblies when vibrations can cause collisions between them. This can happen during an earthquake or because of a LOCA. The study was carried out in the experimental test section EUDORE and was complemented by a numerical model based on porous medium approach. The experimental results give the opportunity to observe the behavior of the assemblies, in Eudore configuration for different frequencies, amplitudes and flow rates. The different behaviors of the lateral assemblies, Left and Right, has been attributed to

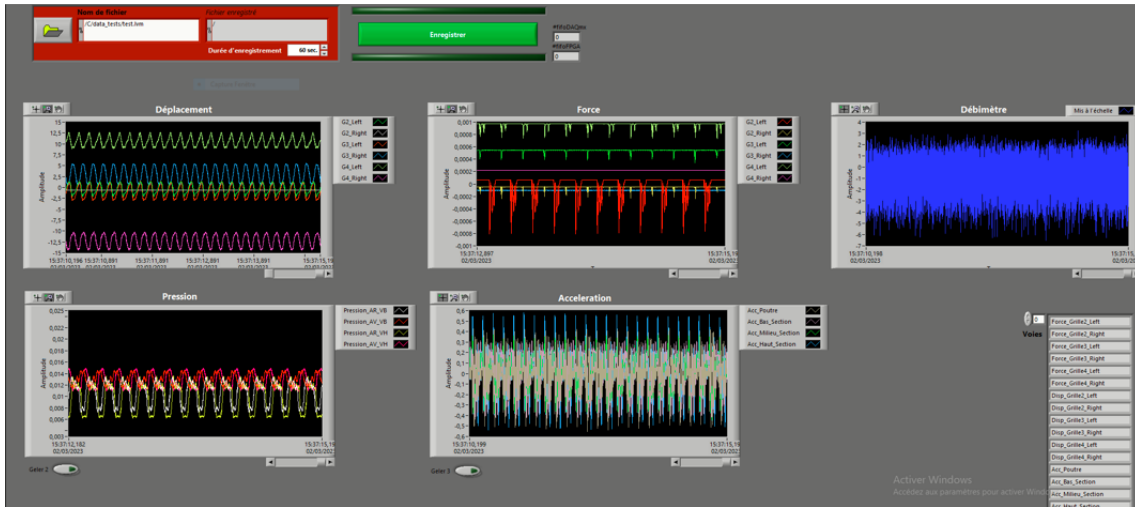


Figure 4.15: Data acquisition software for Dynamic and Static experiments.

the different confinements.

We found that the displacements induced on the assemblies increase with the forcing amplitude, but decrease with flow rate because of an increase of damping effect. The same can be said for the impact forces, which depend on the assemblies displacements. An explanation of the impact force time-variation is proposed. It involves the central assembly when high amplitude are imposed on the test section. Simulation results show that impact forces and displacements are overestimated at high forcing amplitude. At low amplitude simulations and experiments show good agreement. The dynamic of the impacts on the wall is faster in simulations, underling the necessity of a further implementation of the numerical model in cases of impact.

Perspectives It is planned to install 4 new toolboxes connected to the second and fourth grids of assemblies Left and Right. Eudore will have up to six lateral toolboxes, three for each side. With the latest configuration on Eudore we will be able to measure displacements and impact forces on the second, third and fourth grids of the lateral assemblies. Fig. 4.15 shows the latest version of the acquisition part of the software. It will be used with the new toolboxes. Accelerometers and pressure sensors are present on different parts of the test section too. Accelerometers deepen the understanding of the dynamic phenomena for the test section and pressure sensors allow to evaluate the pressure losses for different part of the assemblies, such as one grid, the 64 rods or the complete assembly, 64 rods and 5 grids. Measuring the displacements on the second and fourth grids, we can now detect also the even vibrational modes. Finally, six fast cameras record the motion of the second, third and fourth grids of the three assemblies inside Eudore. The camera are positioned frontally to the test section, two for each grid level. Thanks to the portholes present on Eudore door, they can trace the motion of the grids. Displacement sensors and cameras will help understanding the dynamics of the assemblies during the impacts on the walls and the impacts between the assemblies.

All these new measurement sensors will collect data during the next experimental campaigns. With the close loop control system we will be able to perform experiments at higher frequencies and amplitudes. The identification of higher proper modes for fuel assemblies will be possible as well as a deeper analysis on the impact dynamics for fuel assemblies under axial flow and seismic solicitation.

General conclusion

In this thesis report we looked at the subjects I worked on during my doctoral project. In the three main chapters of this document, we investigated three different aspects of the fluid-structure interaction for nuclear fuel assemblies. We have been focused on the Keulegan-Carpenter instabilities for rod-assembly, assembly bowing and assembly oscillations. The academic purpose of this research matched the practical needs of nuclear industry in:

- the identification of numerical code parameters capable of resolving assemblies and fluid dynamics in a reactor core;
- the analysis of assemblies bow and the dynamic of impacts for assemblies vibrating under axial flow.

The document has been divided in three main chapters after the general introduction. The second, the third and fourth chapter are conceived to be independent. Each of them investigates a particular aspect of the research. Our study has a strong experimental component, 2 experimental facilities have been presented: SBF and Eudore.

In the second chapter we faced Keulegan-Carpenter instabilities for a rod-bundle. We have focused our analysis on a particular set of experiments retrieved with SBF where the fluid was stagnant. The analysis reveals that the fluid instabilities arise firstly in the inner volume of the assemblies and after in the gaps between the assembly and the external confinement. The instabilities arise after a threshold amplitude. By definition of Keulegan-Carpenter number, this dimensionless number is strictly linked to the oscillation amplitude of a single rod. We proposed a definition of Keulegan-Carpenter number for the rod-assembly, $K_{cr,min}$, related to the physical meaning of the dimensionless number. This definition of the number has a solid physical base and matches the experimental results. Effects of fluid structure instabilities need to be deeper studied for a good correlation with viscous effects on assembly mechanical behavior. The correlation between the magnitude of instabilities to assembly oscillation amplitudes or rod diameter represent a path to be investigated in order to improve the design of fuel assemblies. Investigation of displacement

forces needed to set in oscillation the rod-bundle are suitable to be performed. Studying the correlation between the force behavior before and after Keulegan-Carpenter instabilities arise and develop, will deepen our knowledge on this subject. To this aim, a new setup will replace SBF at the George Washington University. In this new setup, only the assembly will be solicited, while the test section will stay at rest. A force sensor will be installed on the assembly actuator. Finally but yet important, PIV in MIR condition are not always possible. Other non-intrusive measuring techniques are also at study. They will involve MTV (Molecular Tracking Velocimetry) combined with the use of a borescope inside an instrumented rod. The general idea is to be able to reach high vibration frequencies and amplitudes, in closed space where laser or camera field of view are difficult to be stabilized.

The third and fourth chapters concern experiments performed on Eudore facility on two different configurations. In the third chapter the analysis has focused on assembly bowing due to an induced cross-flow. LDV measurements on Eudore has been performed. Exploiting these results, we have retrieved the axial and cross flow velocities profiles along Eudore height. The induced cross flow exerts a load, bowing the assemblies. We proposed an analytical model to retrieve drag coefficient starting from velocities and force data, based on Ricciardi's porous medium model for fluid load. Numerical results have been presented in the chapter showing good agreement with experimental results. These results were published in a peer-reviewed journal [Longo et al., 2022]. Different induced cross-flow will be implemented and force measures on other grid levels will be performed. Further investigations need to be done in order to better understand the differences between heterogeneous and homogeneous drag coefficients, and how the axial flow and the confinement affect assemblies bow when a cross-flow is induced using inlet diaphragms.

In the fourth chapter, we have presented Eudore in the Dynamic configuration. Seismic-like experiments have been presented, their results have been showed and discussed. A model to explain the shapes of the impact forces has been developed and presented. We used homogeneous drag coefficient retrieved with Static experiments to perform numerical simulation on Dynamic experiments. Numerical results have been showed and discussed, showing good agreement with the experimental ones. The numerical model well represents the assemblies vibration dynamics but underestimates the damping effect at high amplitudes. Further investigations on this subject would imply a better characterization of vibrating phenomena at higher frequencies. With new Eudore configurations we will be able to measure the motion of all the assemblies, not only of the laterals, on different grid levels. Measuring impact forces on other grids levels of the lateral assemblies will be possible too. Tracking assemblies motion at different grid levels is interesting in order to better understand the impact dynamics. We will be able to detect higher modes and stacking phenomena during impacts. Finally, on Eudore it is possible to perform experiments in stagnant water, with PIV measures, as the ones performed on SBF. This will give the possibility to investigate Keulegan Carpenter instabilities with a different assembly configuration, recording impact forces. An incipit of this investigation is given in Annex A.

Nomenclature

Δ	force absolute error, [N]
δ	force relative error, [-]
$\nu_{i,1}$	LDV laser frequency, [Hz]
s	force sensor sensitivity, [N]
β	Stokes parameter, frequency parameter
λ_l	laser wavelength, [nm]
$\mathcal{F}(x)$	Fourier transform of x
f	in-line hydraulic load, [N/m]
f_p	penalty force term, [N/m]
m	inertial penalty coefficient, [-]
p	damping penalty coefficient, [-]
u	displacement, [m]
ν	kinematic viscosity, [m ² /s]
ϕ	porosity coefficient, [-]
ρ	fluid density, [Kg/m ³]
σ_x	standard deviation of x
$\underline{\underline{\sigma}}_s$	Cauchy-stress tensor, [kg/m s ²]
\vec{f}_I	inertial force term, [N/m]
\vec{f}_L	lift force term, [N/m]

\vec{f}_N	normal drag force term, [N/m]
$\vec{\theta}_{eq}$	section rotation, [rad]
\vec{M}	bending moment, [N/m]
\vec{Q}	shear force, [N/m]
\vec{T}_0	tension force at the bottom of the fuel assembly, [N · m]
\vec{u}_{eq}	equivalent displacement, [m]
A	bundle oscillating amplitude, [m]
$a_{e,L}$	equivalent amplitude for assembly Left, [mm]
$a_{e,R}$	equivalent amplitude for assembly Right, [mm]
a_{LCP}	LCP amplitude, [mm]
A_{sbf}	table oscillating amplitude, [m]
c_D	drag coefficient, [-]
C_g	ad hoc geometrical coefficient, [-]
c_M	mass coefficient, [-]
c_N	normal drag coefficient, [-]
d	rod diameter, [m]
d_b	equivalent bundle diameter, [m]
F	force, [N]
f	frequency, [Hz]
f_{acq}	camera sampling frequency, [fps]
G	g/d
g	gap, [m]
I_{fA}	inertial moment per unit length of a fuel assembly, [kg · m]
K	Keulegan Carpenter number, period parameter
K_{thr}	threshold K
m_f	added mass per unit length, [Kg/m]
n_D	refractive index

P	p/d
p	pitch, [m]
$PSD(x)$	Power spectral density of x
Re	Reynolds number
T	period, [s]
u_L	displacement for assembly Left, [mm]
u_R	displacement for assembly Right, [mm]
u_m	velocity oscillations magnitude, [m/s]
FOV	Field Of View
FSI	Fluid Structure Interaction
LCP	Lower Core Plate
LDV	Laser Doppler Velocimetry
LOCA	Loss Of Coolant Accident
MIR	Matching Indexes of Refraction
NPP	Nuclear Power Plant
PIV	Particle Image Velocimetry
PWR	Pressurize Nuclear Reactor
UCP	Upper Core Plate

Bibliography

- R. J. Adrian. Particle-imaging techniques for experimental fluid mechanics. *Annual review of fluid mechanics*, 23(1):261–304, 1991.
- H.-E. Albrecht, N. Damaschke, M. Borys, and C. Tropea. *Laser Doppler and phase Doppler measurement techniques*. Springer Science & Business Media, 2013.
- B. Anderson, M. Hassan, and A. Mohany. Modelling of fluidelastic instability in a square inline tube array including the boundary layer effect. *Journal of Fluids and Structures*, 48:362–375, 2014.
- T. Andersson, J. Almberger, and L. Björnkvist. A decade of assembly bow management at ringhals. In *Proceedings of IAEA Technical Meeting on Structural Behaviour of Fuel Assemblies for Water Cooled Reactors, Cadarache, 2004, IAEA-TECDOC*, volume 1454, pages 129–136, 2005.
- P. Bardet and G. Ricciardi. Validation data and model development for fuel assembly response to seismic loads. Technical report, George Washington Univ., Washington, DC (United States), 2016.
- R. Boccaccio. *Etude expérimentale du comportement sous séisme de quatre assemblages combustibles à échelle réduite sur ICARE*. Master’s thesis, ENSIAME, 2015.
- B. Brenneman, S. Shah, G. Williams, and J. Strumpell. Water confinement effects on fuel assembly motion and damping. 2003.
- D. Broc, J. C. Queval, J. Rigaudeau, and E. Viallet. Analysis of confinement effects for in water seismic tests on pwr fuel assemblies. 2001.
- D. Brochard, A. Benjedidia, F. Gantenbein, and R. Gibert. Dynamic modelling of pwr fuel assembly for seismic behaviour. Technical report, CEA Centre d’Etudes de Saclay, 1993.
- R. Capanna. *Modelling of fluid structure interaction by potential flow theory in a PWR under seismic excitation*. PhD thesis, Ecole Centrale Marseille, 2018.

-
- R. Capanna, G. Ricciardi, E. Sarrouy, and C. Eloy. Experimental study of fluid structure interaction on fuel assemblies on the icare experimental facility. *Nuclear Engineering and Design*, 352:110146, 2019.
- R. Capanna, L. Longo, F. Bazin, G. Ricciardi, and P. M. Bardet. Deployment of time-resolved particle image velocimetry between two pwr surrogate bundles. *Nuclear Engineering and Design*, 382:111375, 2021a.
- R. Capanna, G. Ricciardi, E. Sarrouy, and C. Eloy. Seismic response of cylinder assemblies in axial flow. *arXiv preprint arXiv:2110.15924*, 2021b.
- R. Capanna, E. Sarrouy, G. Ricciardi, and P. M. Bardet. Modal contribution of bundle oscillation to induced flow. *Journal of Fluids and Structures*, 111:103557, 2022.
- J. Carlton. *Marine propellers and propulsion*. Butterworth-Heinemann, 2018.
- D.-i. Chang and S. Tavoularis. Numerical simulation of turbulent flow in a 37-rod bundle. *Nuclear Engineering and Design*, 237(6):575–590, 2007.
- S.-S. Chen. Vibration of nuclear fuel bundles. *Nuclear Engineering and Design*, 35(3):399–422, 1975.
- S.-s. Chen and M. W. Wambsganss. Parallel-flow-induced vibration of fuel rods. *Nuclear engineering and design*, 18(2):253–278, 1972.
- Y.-S. Chen, Y.-R. Yuann, L.-C. Dai, and Y.-P. Lin. Pressure and temperature analyses using gothic for mark i containment of the chinshan nuclear power plant. *Nuclear Engineering and Design*, 241(5):1548–1558, 2011.
- S. Clément. *Mise en oeuvre expérimentale et analyse vibratoire non-linéaire d'un dispositif à quatre maquettes d'assemblages combustibles sous écoulement axial*. PhD thesis, Aix-Marseille, 2014.
- B. Collard and J. Vallory. Impact forces on a core shroud of an excited pwr fuel assembly. 2001.
- B. Collard, S. Pisapia, S. Bellizzi, and D. Broc. Flow induced damping of a pwr fuel assembly. In *Structural behaviour of fuel assemblies for water cooled reactors: proceedings of technical meeting*. Vienna, pages 279–288, 2005.
- S. de Lambert, G. Campioni, V. Faucher, B. Leturcq, and J. Cardolaccia. Modeling the consequences of fuel assembly bowing on pwr core neutronics using a monte-carlo code. *Annals of Nuclear Energy*, 134:330–341, 2019.
- S. de Lambert, J. Cardolaccia, V. Faucher, O. Thomine, B. Leturcq, and G. Campioni. Semi-analytical modeling of the flow redistribution upstream from the mixing grids in a context of nuclear fuel assembly bow. *Nuclear Engineering and Design*, 371:110940, 2021.

-
- E. de Langre, M. Païdoussis, O. Doaré, and Y. Modarres-Sadeghi. Flutter of long flexible cylinders in axial flow. *Journal of Fluid Mechanics*, 571:371–389, 2007.
- J. De Ridder, J. Degroote, K. Van Tichelen, P. Schuurmans, and J. Vierendeels. Modal characteristics of a flexible cylinder in turbulent axial flow from numerical simulations. *Journal of Fluids and Structures*, 43:110–123, 2013.
- J. De Ridder, O. Doaré, J. Degroote, K. Van Tichelen, P. Schuurmans, and J. Vierendeels. Simulating the fluid forces and fluid-elastic instabilities of a clamped–clamped cylinder in turbulent axial flow. *Journal of Fluids and Structures*, 55:139–154, 2015.
- J. De Ridder, J. Degroote, K. Van Tichelen, and J. Vierendeels. Predicting modal characteristics of a cluster of cylinders in axial flow: From potential flow solutions to coupled cfd–csm calculations. *Journal of Fluids and Structures*, 74:90–110, 2017.
- C. Demazière, A. Rouchon, and A. Zoia. Understanding the neutron noise induced by fuel assembly vibrations in linear theory. *Annals of Nuclear Energy*, 175:109169, 2022.
- L. Divaret, O. Cadot, P. Moussou, and O. Doaré. Normal forces exerted upon a long cylinder oscillating in an axial flow. *Journal of Fluid Mechanics*, 752:649–669, 2014.
- E. Dominguez-Ontiveros, C. Estrada-Perez, and Y. Hassan. Non-intrusive experimental investigation of flow behavior inside a 5x5 rod bundle with spacer grids using piv and mir. In *International Conference on Nuclear Engineering*, volume 43543, pages 351–360, 2009.
- M. Duclercq, D. Broc, and O. Cadot. Characterization of long time fluctuations of forces exerted on an oscillating circular cylinder at $kc=10$. *Journal of Fluids and Structures*, 27(4): 596–610, 2011. ISSN 0889-9746. doi: <https://doi.org/10.1016/j.jfluidstructs.2011.01.004>. URL <https://www.sciencedirect.com/science/article/pii/S0889974611000168>.
- J. R. Elston, J. Sheridan, and H. M. Blackburn. Two-dimensional floquet stability analysis of the flow produced by an oscillating circular cylinder in quiescent fluid. *European Journal of Mechanics-B/Fluids*, 23(1):99–106, 2004.
- J. R. Elston, H. M. Blackburn, and J. Sheridan. The primary and secondary instabilities of flow generated by an oscillating circular cylinder. *Journal of Fluid Mechanics*, 550: 359–389, 2006.
- V. Faucher, G. Ricciardi, R. Boccaccio, K. Cruz, T. Lohez, and S. A. Clément. Numerical implementation and validation of a porous approach for fluid–structure interaction applied to pressurized water reactors fuel assemblies under axial water flow and dynamic excitation. *International Journal for Numerical Methods in Engineering*, 122(10): 2417–2445, 2021.

-
- G. Ferrari, P. Balasubramanian, S. Le Guisquet, L. Piccagli, K. Karazis, B. Painter, and M. Amabili. Non-linear vibrations of nuclear fuel rods. *Nuclear Engineering and Design*, 338:269–283, 2018.
- G. Ferrari, G. Franchini, L. Faedo, F. Giovanniello, S. Le Guisquet, P. Balasubramanian, K. Karazis, and M. Amabili. Nonlinear vibrations of a 3×3 reduced scale pwr fuel assembly supported by spacer grids. *Nuclear Engineering and Design*, 364:110674, 2020.
- B. Fontaine and I. Politopoulos. A non linear model for the pwr fuel assembly seismic analysis. *Nuclear engineering and design*, 195(3):321–329, 2000.
- C. Fort, C. D. Fu, N. A. Weichselbaum, and P. M. Bardet. Refractive index and solubility control of para-cymene solutions for index-matched fluid–structure interaction studies. *Experiments in Fluids*, 56(12):1–11, 2015.
- P. Gabrielsson, D. Schrire, E. Suvdantsetseg, and M. Malmberg. Investigation of the development of fuel assembly bow in ringhals 3 and 4. In *Proc Int Conf Top Fuel'18*. Prague, Czech Republic, 2018.
- P. Hall, M. R. Malik, and D. Poll. On the stability of an infinite swept attachment line boundary layer. *Proceedings of the Royal Society of London. A. Mathematical and Physical Sciences*, 395(1809):229–245, 1984.
- H. Honji. Streaked flow around an oscillating circular cylinder. *Journal of Fluid Mechanics*, 107:509–520, 1981.
- Á. Horváth and B. Dressel. On numerical simulation of fuel assembly bow in pressurized water reactors. *Nuclear Engineering and Design*, 265:814–825, 2013.
- IAEA. <https://www.iaea.org/topics/water-cooled-reactors>.
- A. Joly, P. Badel, N. d. B. de Chasse, O. Cadot, A. Martin, P. Moussou, and L. Pastur. Experimental investigation of a 2-d model of fluid forces upon a cylinder array in axial flow. In *FIV2018 Conference*, 2018.
- A. Joly, N. de Buretel de Chasse, A. Martin, O. Cadot, L. Pastur, and P. Moussou. Direct measurement of steady fluid forces upon a deformed cylinder in confined axial flow. *Journal of Fluids and Structures*, 104:103326, 2021. ISSN 0889-9746. doi: <https://doi.org/10.1016/j.jfluidstructs.2021.103326>. URL <https://www.sciencedirect.com/science/article/pii/S0889974621001092>.
- C. Kalkert and J. Kayser. Laser doppler velocimetry. *San Diego: PHYS173*, 2006.
- G. H. Keulegan and L. H. Carpenter. Forces on cylinders and plates in an oscillating fluid. *Journal of research of the National Bureau of Standards*, 60(5):423–440, 1958.

-
- J. Kim, U. Borsdorf, and G. Stern. Comparison of theoretical and experimental examinations on pwr-fuel-assemblies under external loads. In *Structural mechanics in reactor technology. Vol. C/D*. 1981.
- V. Lamirand, P. Frajtag, D. Godat, O. Pakari, A. Laureau, A. Rais, M. Hursin, G. Hursin, C. Fiorina, and A. Pautz. The colibri experimental program in the crocus reactor: characterization of the fuel rods oscillator. In *EPJ Web of Conferences*, volume 225, page 04020. EDP Sciences, 2020a.
- V. Lamirand, A. Rais, S. Hübner, C. Lange, J. Pohlus, U. Paquee, C. Pohl, O. Pakari, P. Frajtag, D. Godat, et al. Neutron noise experiments in the akr-2 and crocus reactors for the european project cortex. In *EPJ Web of Conferences*, volume 225, page 04023. EDP Sciences, 2020b.
- C. Y. Lee, C. H. Shin, J. Y. Park, and W. K. In. An experimental investigation on turbulent flow mixing in a simulated 3×3 dual-cooled annular fuel bundle using particle image velocimetry. *Nuclear Engineering and Design*, 260:134–144, 2013.
- E. E. Lewis. *Fundamentals of nuclear reactor physics*. Elsevier, 2008.
- M. Lighthill. Note on the swimming of slender fish. *Journal of fluid Mechanics*, 9(2): 305–317, 1960.
- C. Lombardi. *Impianti nucleari*. Polipress, 2012.
- L. Longo, K. Cruz, N. Cadot, E. Sarrouy, G. Ricciardi, and C. Eloy. Drag coefficient estimation in fsi for pwr fuel assembly bowing. *Nuclear Engineering and Design*, 399: 111995, 2022. ISSN 0029-5493.
- J. Morison, J. Johnson, and S. Schaaf. The force exerted by surface waves on piles. *Journal of Petroleum Technology*, 2(05):149–154, 1950.
- P. Moussou, A. Guilloux, E. Boccaccio, and G. Ricciardi. Fluid damping in fuel assemblies. In *Pressure Vessels and Piping Conference*, volume 57977, page V004T04A048. American Society of Mechanical Engineers, 2017.
- R. Murray and K. E. Holbert. *Nuclear energy: an introduction to the concepts, systems, and applications of nuclear processes*. Elsevier, 2014.
- M. Nagargoje. An introduction to particle image velocimetry (piv) technique, 11 2017.
- T. Nguyen, N. Goth, P. Jones, R. Vaghetto, and Y. Hassan. Stereoscopic piv measurements of near-wall flow in a tightly packed rod bundle with wire spacers. *Experimental Thermal and Fluid Science*, 92:420–435, 2018.
- M. Païdoussis. Dynamics of flexible slender cylinders in axial flow part 1. theory. *Journal of Fluid Mechanics*, 26(4):717–736, 1966a.

-
- M. Païdoussis. Dynamics of flexible slender cylinders in axial flow part 2. experiments. *Journal of Fluid Mechanics*, 1966b.
- M. Païdoussis. Dynamics of cylindrical structures subjected to axial flow. *Journal of sound and vibration*, 29(3):365–385, 1973.
- M. Païdoussis and M. Pettigrew. Dynamics of flexible cylinders in axisymmetrically confined axial flow. *Journal of Applied Mechanics*, 46:37–44, 1979.
- M. Païdoussis and S. Suss. Stability of a cluster of flexible cylinders in bounded axial flow. 1977.
- M. Païdoussis, S. Suss, and M. Pustejovsky. Free vibration of clusters of cylinders in liquid-filled channels. *Journal of Sound and Vibration*, 55(3):443–459, 1977.
- D. Papini, D. Grgić, A. Cammi, and M. E. Ricotti. Analysis of different containment models for iris small break loca, using gothic and relap5 codes. *Nuclear Engineering and Design*, 241(4):1152–1164, 2011.
- M. Païdoussis. *Fluid–Structure Interactions: Slender Structures and Axial Flow*. Elsevier, Academic Press, London, 2003.
- J. Peybernes. Evaluation of the forces generated by cross-flow on pwr fuel assembly. *IAEA-TECDO*, 1454:13citation_URL_Access_Date, 2005.
- S. Pisapia. *Etude du comportement vibratoire non-linéaire d’un assemblage combustible de Réacteur à Eau Pressurisé (REP)*. PhD thesis, Université Aix-Marseille II, 2004.
- S. Price. A review of theoretical models for fluidelastic instability of cylinder arrays in cross-flow. *Journal of Fluids and Structures*, 9(5):463–518, 1995.
- J. Queval and D. Brochard. Analysis of impact phenomena between pwr fuel assemblies in earthquake situations. Technical report, CEA Centre d’Etudes Nucleaires de Saclay, 1988.
- J. Queval, F. Gantenbein, D. Brochard, and J. Rigaudeau. Seismic behavior of pwr fuel assemblies model and its validation. 1991a.
- J. Queval, F. Gantenbein, and J. Rigaudeau. Experimental studies on seismic behaviour of pwr fuel assembly rows. Technical report, CEA Centre d’Etudes de Saclay, 1991b.
- J. C. Queval, D. Broc, J. Rigaudeau, and E. Viallet. Seismic tests of interacting scale one fuel assemblies on shaking table. 2001.
- M. Raffel, C. E. Willert, F. Scarano, C. J. Kähler, S. T. Wereley, and J. Kompenhans. *Techniques for 3D-PIV*, pages 309–365. Springer International Publishing, Cham, 2018. ISBN 978-3-319-68852-7. doi: 10.1007/978-3-319-68852-7_9. URL https://doi.org/10.1007/978-3-319-68852-7_9.

-
- M. Rahman and D. Bhatta. Evaluation of added mass and damping coefficient of an oscillating circular cylinder. *Applied Mathematical Modelling*, 17(2):70–79, 1993.
- G. Ricciardi. *Une approche milieu poreux pour la modélisation de l'interaction fluide-structure des assemblages combustibles dans un coeur de réacteur à eau pressurisée: simulation et expérimentation*. PhD thesis, Université de Provence-Aix-Marseille I, 2008.
- G. Ricciardi. Fluid–structure interaction modelling of a pwr fuel assembly subjected to axial flow. *Journal of Fluids and Structures*, 62:156–171, 2016.
- G. Ricciardi. Hydraulic coupling of fuel assemblies under axial flow, confinement effect. *Nuclear Engineering and Design*, 326:190–201, 2018.
- G. Ricciardi. Numerical investigation of fluid forces acting on a confined cylinder with obstacle subjected to axial flow. *Science and Technology of Nuclear Installations*, 2020, 2020.
- G. Ricciardi and E. Boccaccio. Measurements of fluid fluctuations around an oscillating nuclear fuel assembly. *Journal of Fluids and Structures*, 48:332–346, 2014.
- G. Ricciardi and E. Boccaccio. Modelling of the flow induced stiffness of a pwr fuel assembly. *Nuclear Engineering and Design*, 282:8–14, 2015.
- G. Ricciardi, S. Bellizzi, B. Collard, and B. Cochelin. Modelling pressurized water reactor cores in terms of porous media. *Journal of Fluids and Structures*, 25(1):112–133, 2009a.
- G. Ricciardi, S. Bellizzi, B. Collard, and B. Cochelin. Row of fuel assemblies analysis under seismic loading: Modelling and experimental validation. *Nuclear engineering and design*, 239(12):2692–2704, 2009b.
- G. Ricciardi, S. Bellizzi, B. Collard, and B. Cochelin. Fluid-structure interaction in a 3-by-3 reduced-scale fuel assembly network. *Science and Technology of Nuclear Installations*, 2010, 2010.
- G. Ricciardi, J. Peybernes, and V. Faucher. Analytical model of transverse pressure loss in a rod array. *Nuclear Engineering and Technology*, 2022.
- J. Rigaudeau, E. Labarriere, and B. Ladouceur. Flow induced vibration analysis for preventing pwr fuel rods from excessive fretting wear. 1997.
- T. Sarpkaya. Force on a circular cylinder in viscous oscillatory flow at low keulegan—carpenter numbers. *Journal of Fluid Mechanics*, 165:61–71, 1986.
- T. Sarpkaya. Experiments on the stability of sinusoidal flow over a circular cylinder. *Journal of Fluid Mechanics*, 457:157–180, 2002.
- T. Sarpkaya. On the parameter $b = re/kc = d^2/vt$. *Journal of Fluids and Structures*, 21: 435–440, 2005.

-
- M.-K. Shin, H.-A. Lee, J.-J. Lee, K.-N. Song, and G.-J. Park. Optimization of a nuclear fuel spacer grid spring using homology constraints. *Nuclear Engineering and Design*, 238 (10):2624–2634, 2008.
- G. Spykman and J. Pattberg. Pwr fuel assembly bow. In *Proceedings of the 45th Annual Meeting on Nuclear Technology (AMNT 2014), Frankfurt, Germany, May 6-8 2014*, 2014.
- R. Stephenson. *Introduction to Nuclear Engineering*. McGraw-Hill, 1958.
- G. G. Stokes. On the effect of the internal friction of fluids on the motion of pendulums. 1851.
- M. Tanaka, K. Fujita, A. Hotta, and N. Kono. Parallel flow induced damping of pwr fuel assembly. In *Damping-1988*. 1988.
- M. Tatsuno and P. Bearman. A visual study of the flow around an oscillating circular cylinder at low keulegan–carpenter numbers and low stokes numbers. *Journal of Fluid Mechanics*, 211:157–182, 1990.
- G. I. Taylor. Analysis of the swimming of long and narrow animals. *Proceedings of the Royal Society of London. Series A. Mathematical and Physical Sciences*, 214(1117):158–183, 1952.
- F. Tong, L. Cheng, M. Zhao, and H. An. Oscillatory flow regimes around four cylinders in a square arrangement under small and conditions. *Journal of Fluid Mechanics*, 769: 298–336, 2015.
- N. Turankok, T. Lohez, F. Bazin, V. Biscay, and L. Rossi. Exploration of frequencies peaks observed on local wall pressure measurements by time-resolved velocity field measurements in complex flows. *Experiments in Fluids*, 62(2):1–13, 2021.
- USNRC. Westinghouse technology system manual. Technical report, USNRC Human Resources Training & Development, 2012.
- M. Valette, J. Pouvreau, D. Bestion, and P. Emonot. Revisiting large break loca with the cathare-3 three-field model. *Nuclear engineering and design*, 241(11):4487–4496, 2011.
- J. Vallory. *Rapport des essais d’impact d’assemblages sur une paroi.*, 1999. Note Technique.
- J. Vallory. *Compte rendu des essais d’impact de deux assemblages entre eux et sur la paroi sous écoulement.*, 2000. Note Technique.
- E. Viallet, G. Bolsee, B. Ladouceur, T. Goubin, and J. Rigau. Validation of pwr core seismic models with shaking table tests on interacting scale 1 fuel assemblies. 2003.
- C.-Y. Wang. On high-frequency oscillatory viscous flows. *Journal of Fluid Mechanics*, 32 (1):55–68, 1968.

-
- A. Wanninger. *Mechanical Analysis of the Bow Deformation of Fuel Assemblies in a Pressurized Water Reactor Core*. PhD thesis, Technische Universität München, 2018.
- A. Wanninger, M. Seidl, and R. Macián-Juan. Mechanical analysis of the bow deformation of a row of fuel assemblies in a pwr core. *Nuclear Engineering and Technology*, 50(2): 297–305, 2018.
- N. A. Weichselbaum. *Non-intrusive experimental study on nuclear fuel assembly response to seismic loads*. PhD thesis, The George Washington University, 2016.
- N. A. Weichselbaum, S. Hussain, M. R. Abkenar, M. T. Manzari, and P. M. Bardet. 3d volumetric fluid-structure interaction measurements with non-intrusive optical measurement techniques on an earthquake shake table.
- N. A. Weichselbaum, M. Rahimi Abkenar, M. Vanella, M. T. Manzari, E. Balaras, and P. M. Bardet. Validation facility and model development for nuclear fuel assembly response to seismic loading. *Journal of Nuclear Engineering and Radiation Science*, 1(4), 2015.
- N. A. Weichselbaum, M. A. André, M. Rahimi-Abkenar, M. T. Manzari, and P. M. Bardet. High-resolution flying-piv with optical fiber laser delivery. *Experiments in Fluids*, 57(5): 1–20, 2016a.
- N. A. Weichselbaum, S. Hussain, M. Rahimi-Abkenar, M. T. Manzari, and P. M. Bardet. Fuel assembly oscillation-induced flow in initially stagnant fluid. *Nuclear Technology*, 195(1):98–104, 2016b.
- P. Yvon, R. Schill, P. Coffre, X. Averty, J. Rigaudeau, B. d’Uston, A. Billerey, and E. SEPTEN. Results of crush tests performed on irradiated pwr zircaloy-4 spacer grids. *IAEA-Tecdoc-1454, Structural behaviour of fuel assemblies for water cooled reactors*, pages 289–296, 2005.
- J. Zhu. *Laser doppler velocimetry for flow measurements in pulp and paper research*. 1996.

KC threshold for Dynamic experiments

A.1 Introduction

One could have notice that Eudore, presented in Chapter 3 and 4, gives the possibility for dynamic experiment also in stagnant water condition. Furthermore the presence of the three assemblies is an option, experiment with just one assembly are possible too. Here we find the conditions to recreate the experiments performed on SBF, presented in Chapter 2, with a setup such Eudore that allows impact force measurements. This is interesting also because Eudore's assemblies are different from SBF's assembly for number of rods, rod dimensions and pitch. PIV experiments with one assembly on Eudore, could test the validity of K numbers proposed for the assembly in Chapter 2, $K_{cr,min}$. Relating fluid instabilities recorded with PIV and damping effect retrieved by the impact force measures in an important step possible with Eudore.

Eudore is not designed to perform PIV experiments in MIR (Refractive index match) conditions, hence only the Intraline planes can be investigated. For this reason, next SBF configuration will be developed at Thermo-fluid lab at GWU. The new configuration of SBF will have a displacement actuator just for the assembly, hence the test section will not move and there will not be a vibrating table. On the assembly actuator a force sensor will be installed in order to record force values for each oscillation amplitude. With the new configuration for SBF a complete analysis for both, fluid instabilities and forces, will be possible.

In this Annex we will show the results obtained on Eudore in stagnant water and we will calculate the $K_{cr,min}$ and another keulegan-Carpenter number \bar{K} , based on geometrical considerations. We will relate the impact force measures to the fluid instabilities in a first approximation.

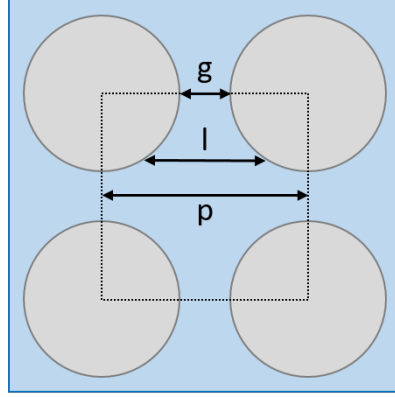


Figure A.1: Averaged l .

A.2 Geometrical considerations on Keulegan-Carpenter definition for rod-bundle

Working on Intraline or Interline planes in Chapter 2, gives us some hints on the fluid dynamics inside the rod-bundle. The data collected and presented in this analysis concern only one facility with a defined lattice, therefore, the next considerations are to be intended as only speculative.

One can think to define average coefficients that set a general bundle threshold for fluid instabilities. Those would involve the p/d ratio, the number of rods n and the rod-bundle lattice. Based on simple geometrical assumptions, an ad hoc coefficient C_g would define a new characteristic length d_b as an equivalent bundle-diameter, as in Eq. A.1.

$$d \rightarrow d_b = C_g \cdot d \qquad C_g = \left(1 + \frac{d}{p}(\sqrt{n} - 1)\right)^\phi \qquad (\text{A.1})$$

Here n is under square root assuming the rods in the bundle will have a 2D lattice and hence only \sqrt{n} will affect d_b , while n will affect the total horizontal cross section. In order to take into account the lattice, ϕ could be the porosity coefficient, hence in our case $\phi = \pi d^2/4p^2$. One could note that $C_g = 1$ for $n = 1$ and $C_g \rightarrow 1$ for $p/d \rightarrow \infty$. In the first case $d_b = d$, that is coherent since there is no bundle but only a single rod. In the second case the presence of other rods in the bundle would not affect the fluid dynamic interaction around a single rod, since p/d is large. Contrariwise, for $p/d \rightarrow 1$ the flow would see a structure having a characteristic length $d_b = \sqrt{n}^\phi \cdot d$. Then K , Re and β would change accordingly.

Along the same line of thought, one might think of using an average quantity instead of the gap g or pitch p . This quantity \bar{l} is a characteristic average length of the bundle and can be obtained as shown in Eq. A.3 and shown in Fig. A.1. We can use d_b and \bar{l} in

Table A.1: SBF mean critical Keulegan Carpenter number

P	ϕ	n	C_g	d_b [mm]	\bar{l} [mm]	$\overline{K_{cr}}$
1.33	0.44	36	1.98	28.3	10.6	1.18

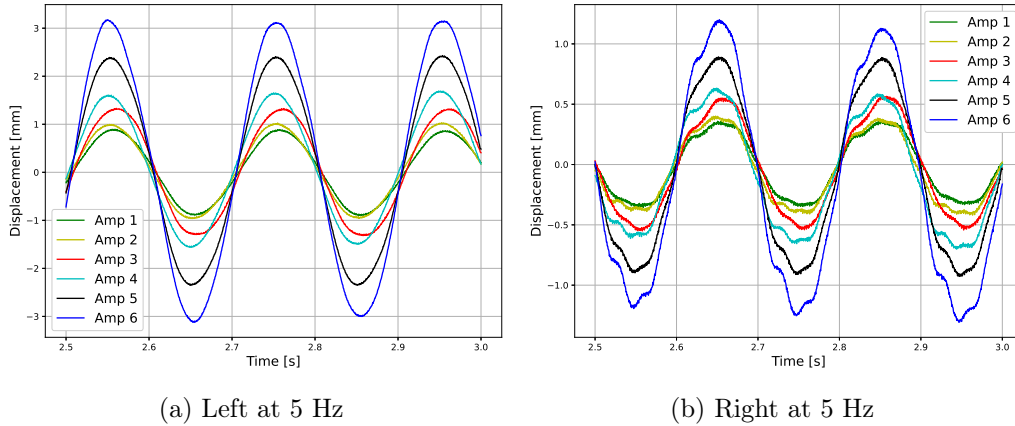


Figure A.2: Comparison Left and Right assemblies displacement in stagnant water at different LCP amplitudes.

K_{em} definition to obtain a mean critical value of $\overline{K_{cr}}$ valid for our assembly (Eq. A.3), as shown in Tab. A.1.

$$\bar{l} = \frac{4p^2 - \pi d^2}{4p} \qquad \overline{K_{cr}} = \pi \frac{\bar{l}}{d_b} \qquad (A.2)$$

Experimental results show that instabilities in the rod-bundle occur when $K \sim 1.13$. Using the mean quantities defined ad hoc only on geometric considerations (C_g , d_b and \bar{l}) for the rod-bundle, we retrieve a mean critical $\overline{K_{cr}}$ number for SBF. The experimental results fits with this critical value $\overline{K_{cr}} = 1.18$. The validation of this analysis needs other experiments with different n , p/d and lattice matrix.

A.3 Dynamic experiments in stagnant water

We performed experiment in still fluid also in Eudore. Even if there are 3 assemblies in the test section, assembly Left can be considered independent. Indeed its gaps allow the assembly to move almost without impacting on wall or Central assembly. Thus, one can think to study on assembly Left motion the KC threshold for these experiment too. Fig. A.2 shows the assemblies motion in stagnant water. We can see the freely motion of assembly Left. Contrary to assembly Right, displacement signal from assembly Left is completely sinusoidal and clean from strong impact.

Left assembly impacts with left wall starting from amplitude 3, but the impact is not so strong to visibly modify the displacement signal. This allows to calculate K number as

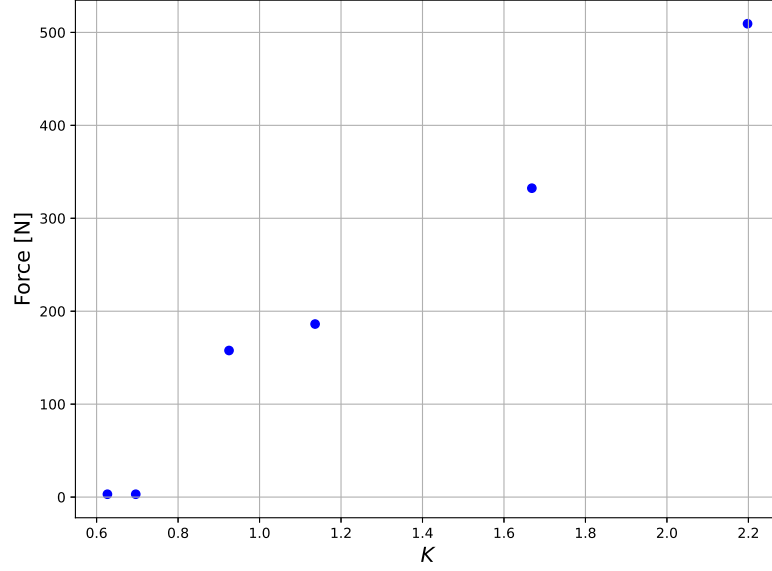


Figure A.3: Impact forces for Left assembly in stagnant water.

Table A.2: SBF mean critical Keulegan Carpenter number

d [mm]	g [mm]	P	ϕ	n	C_g	d_b [mm]	\bar{l} [mm]	$K_{cr,min}$	$\overline{K_{cr}}$
9.0	3.5	1.39	0.41	64	2.08	18.72	7.41	1.22	1.24

we have done for SBF using the equations from Chapter 2:

$$\begin{aligned}
K_{cr,min} &= \pi \frac{g}{d} & \phi &= \frac{\pi d^2}{4p^2} & C_g &= \left(1 + \frac{d}{p}(\sqrt{n} - 1)\right)^\phi \\
d_b &= C_g \cdot d & \bar{l} &= \frac{4p^2 - \pi d^2}{4p} & \overline{K_{cr}} &= \pi \frac{\bar{l}}{d_b}
\end{aligned} \tag{A.3}$$

Tab. A.2 reports the principal data for Eudore. We recall: d is the rod diameter, g is the gap between the rod in the assembly, $P = p/d$ is the dimensionless pitch, ϕ is the porosity, n is the number of rods in the assembly, C_g is the ad-hoc geometrical coefficient to calculate the equivalent bundle-diameter, d_b is the equivalent bundle-diameter and \bar{l} is the characteristic average length in the assembly.

We do not have experimental measures on the fluid for Eudore Dynamic experiments, hence we cannot detect fluid instabilities. Therefore, the next considerations are just speculative. If instabilities arise, from Fig. A.2 we can imagine this happens between $K = 1.2$ and $K = 1.6$. Indeed, the slope of forces versus K seems to change before and after this range. We do not consider the first two K numbers because assembly Left does not impact on the wall, hence we cannot retrieve the force values. If we consider a linear dependence between force and K , we can trace the 2 slope and calculate the intersection point which results $K = 1.29$.

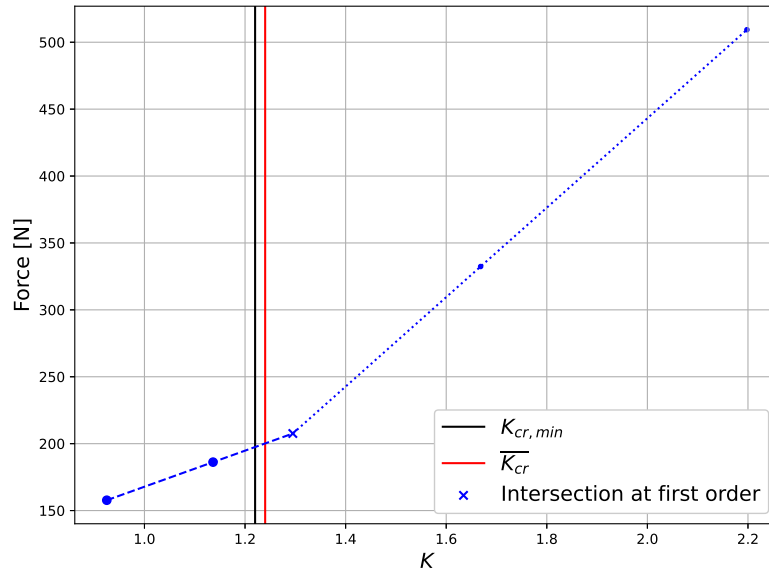


Figure A.4: Zoom on impact forces for Left assembly in stagnant water.

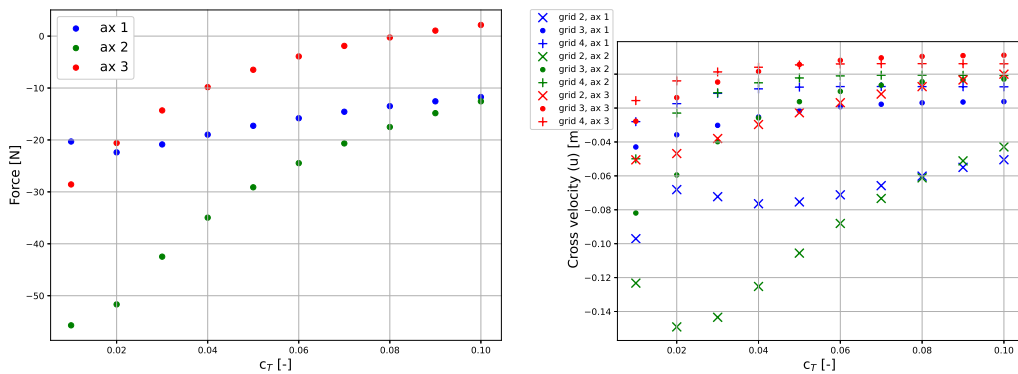
Fig. A.4 shows the zoom on the impact forces for assembly Left on the K where we can retrieve the values. In the figure we can see the linear interpolation of the points assuming a slope change in range $K \in [1.2, 1.6]$. The intersection point $K = 1.29$ is shown. We cannot establish a clear behaviour because we have too few points. In any case, the proposed $K_{cr,min}$ and \bar{K}_{cr} numbers are in good agreement with the linear interpolation on the force values. If experimental measures on fluid instabilities will be performed on Eudore and if these measures confirm the that the instabilities arise around these K values, it would strengthened our proposition on threshold K number for the assembly.

Sensitivity analysis for static simulations

In this annex we show a brief sensitivity study of the numerical results to the variation of c_N and c_T and to a penalty coefficient p . The numerical results presented in Chapter 3 were obtained by canceling the penalty term $p = 0$, however, the numerical code offers the possibility of using it and it is therefore useful to know the sensitivity of the results from this coefficient.

The simulations need non zero value for m_f , c_N and c_T . Empirical value of c_N follow in the range $[0.3; 0.5]$ [Moussou et al., 2017], while c_T is an order of magnitude smaller [Ricciardi, 2020]. Fig.s B.1 and B.3 show the sensitivity of the numerical results to the variation of these two force coefficients. Here Left, Central and Right assembly are denoted ax 1, ax 2 and ax 3.

Simulations on Fig. B.1 have been performed using $c_N = 0.5$. Increasing c_T the force acting along \vec{e}_y increases too. The cross velocity increases for all the assemblies and all the grids except for the second grid of assembly Left and Central. The cross velocity on the second grid of the central assembly has a minimum at $c_T = 0.02$, while for the left assembly the minimum is a $c_T = 0.04$. It seems the values of both force and velocities



(a) Force on 3rd grid

(b) Cross velocity

Figure B.1: Simulated data for different c_T , .

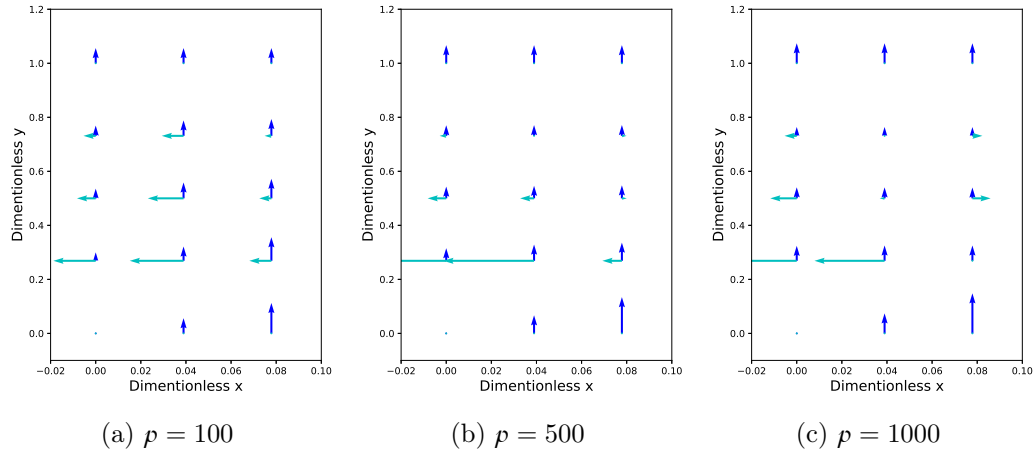


Figure B.2: Simulated velocity field on Eudore for different penalty coefficients.

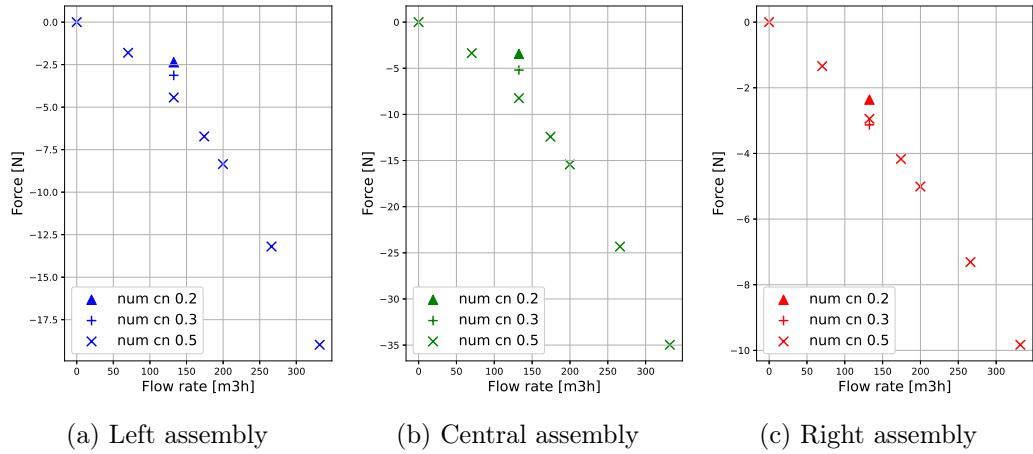


Figure B.3: Forces on 3rd grid for different flow-rates and c_N .

approach an asymptotic value when $c_T \approx 0.1$.

Fig. B.2 helps to understand why the behaviour of force and velocity is different changing the axial drag term.

Fig. B.3 shows the horizontal force values for the third grid of each assembly at $c_T = 0.04$. c_N has been set at 0.2, 0.3 and 0.5. The tendency is that the maximum absolute value for the force is at $c_N = 0.5$, except for the right assembly where $c_N = 0.3$ show a slightly higher absolute value for the force.

Penalty coefficients All the previous simulations hide 2 other coefficients, p and m . These are penalty coefficients used in the numerical resolution. p is a damping coefficient and m is an inertial coefficient. The first one is related to the velocity and the second one to the acceleration of the cross flow creating a penalty force term f_p . This penalty force term f_p is used to avoid lateral leakages of fluid on the porous medium lateral walls. In order to simplify the sensitivity analysis, the ratio p/m is fix to 10. Therefore, in the next

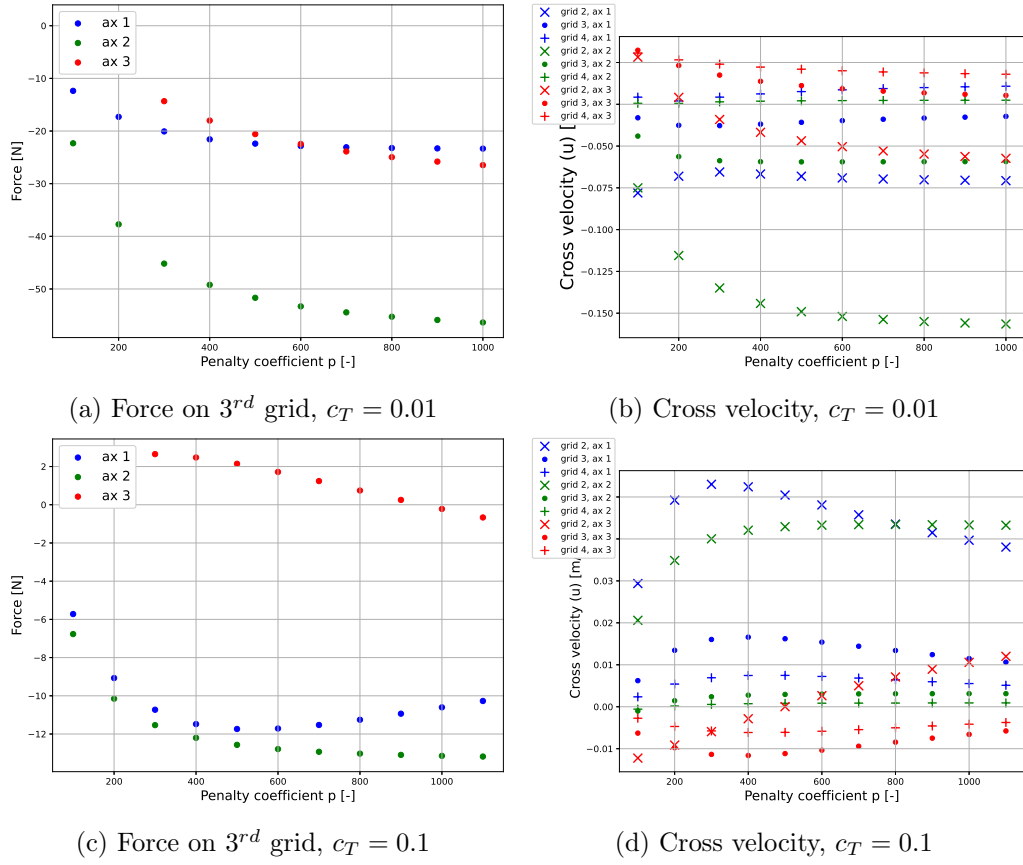


Figure B.4: Simulated data for different penalty coefficient ρ .

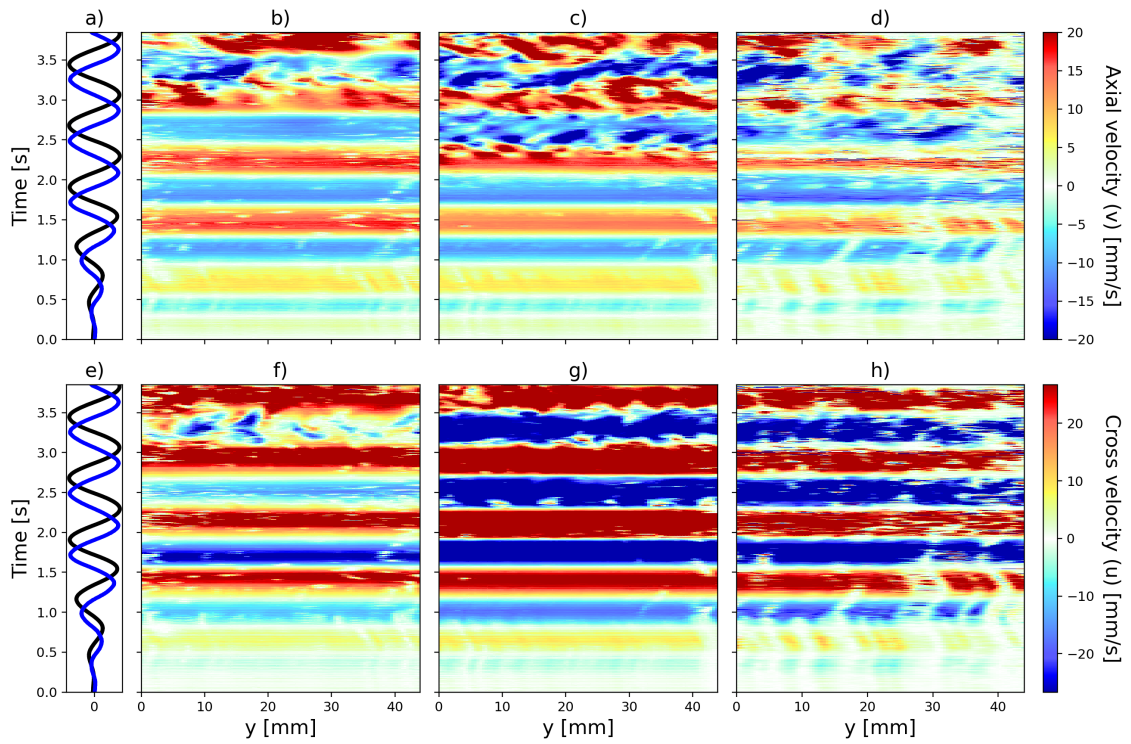
plots both ρ and m changes but only ρ phase direction is shown.

Fig. B.4 shows the sensibility of the numerical results to ρ . For $c_T = 0.01$, Figs B.4a and B.4b, there is an asymptotic value reached once $\rho \approx 500$. This behaviour is common at low c_T . On the other hand, at $c_T = 0.1$ the asymptotic value seems to be after $\rho \approx 1000$ (Fig. B.4c and B.4d).

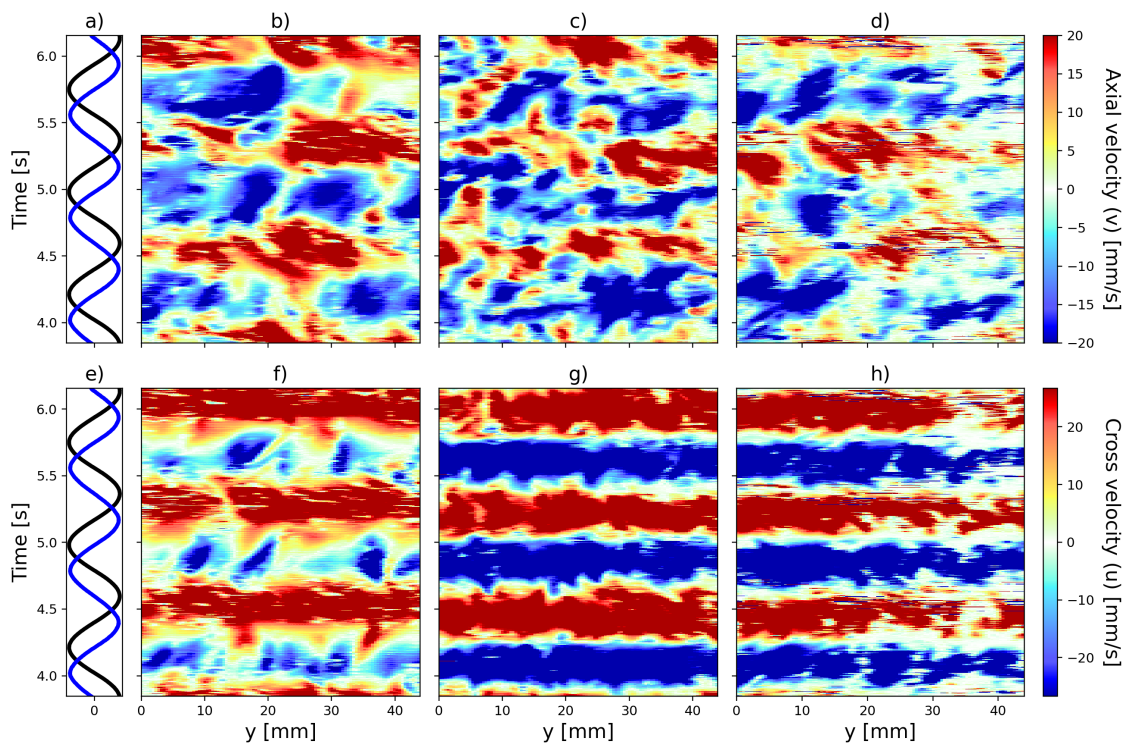


More results from SBF

In this Annex we present more results concerning the investigation performed in Chapter [2](#) for a deepen comprehension of the analysis.

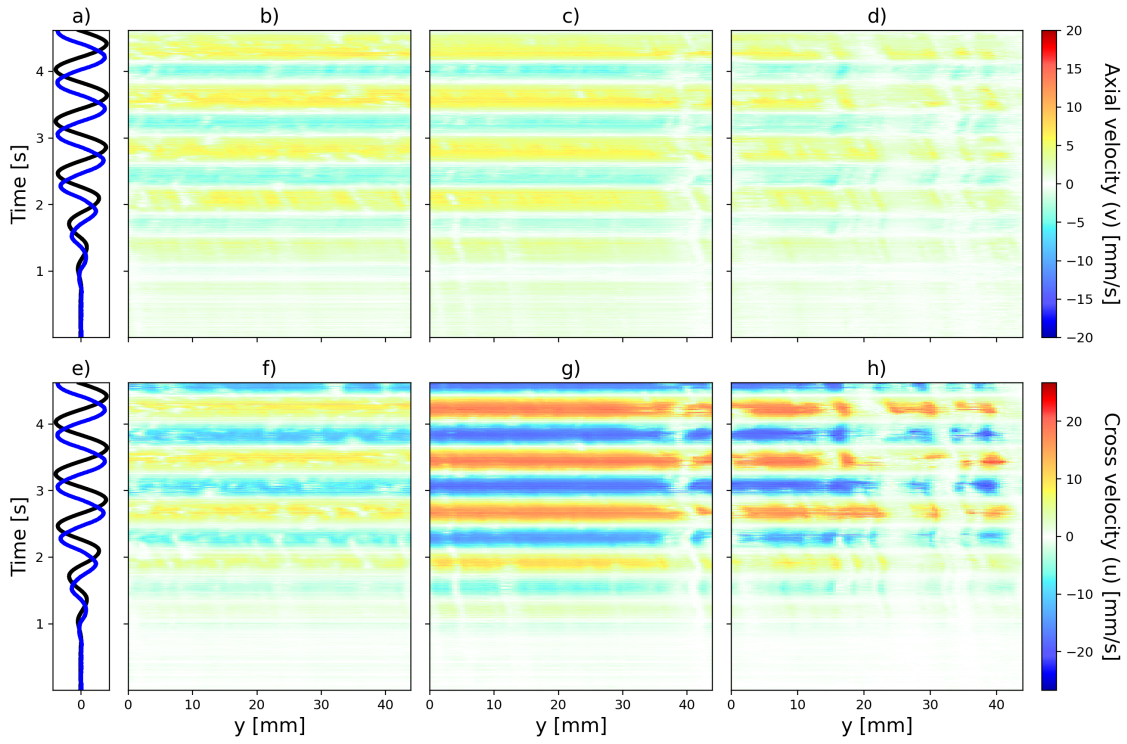


(a) $K = 2.07$ transient

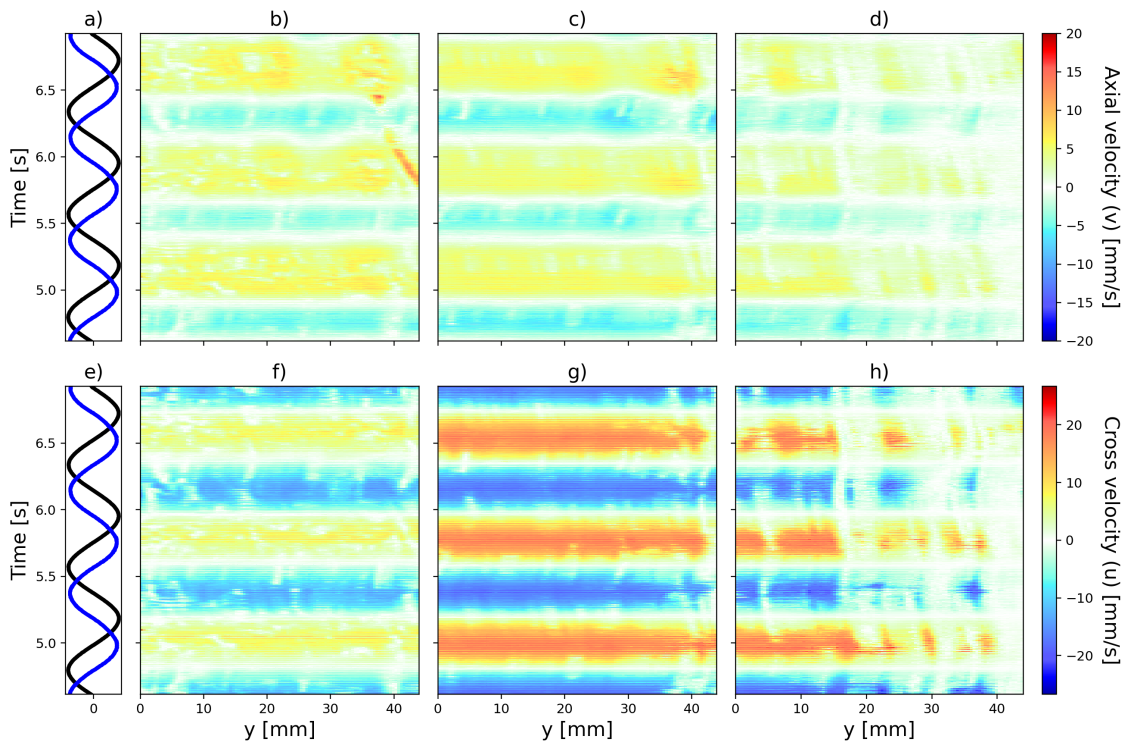


(b) $K = 2.07$ steady state

Figure C.1: Case 14, $K = 2.07$ Intraline evolution.

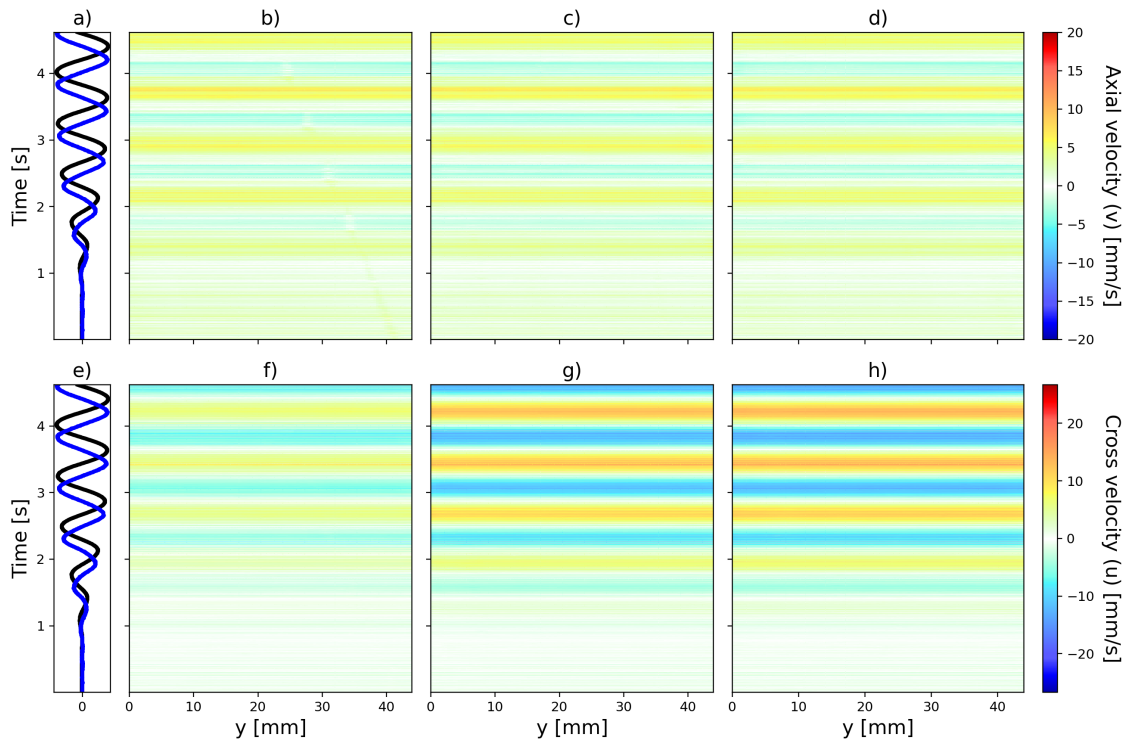


(a) $K = 1.13$ transient

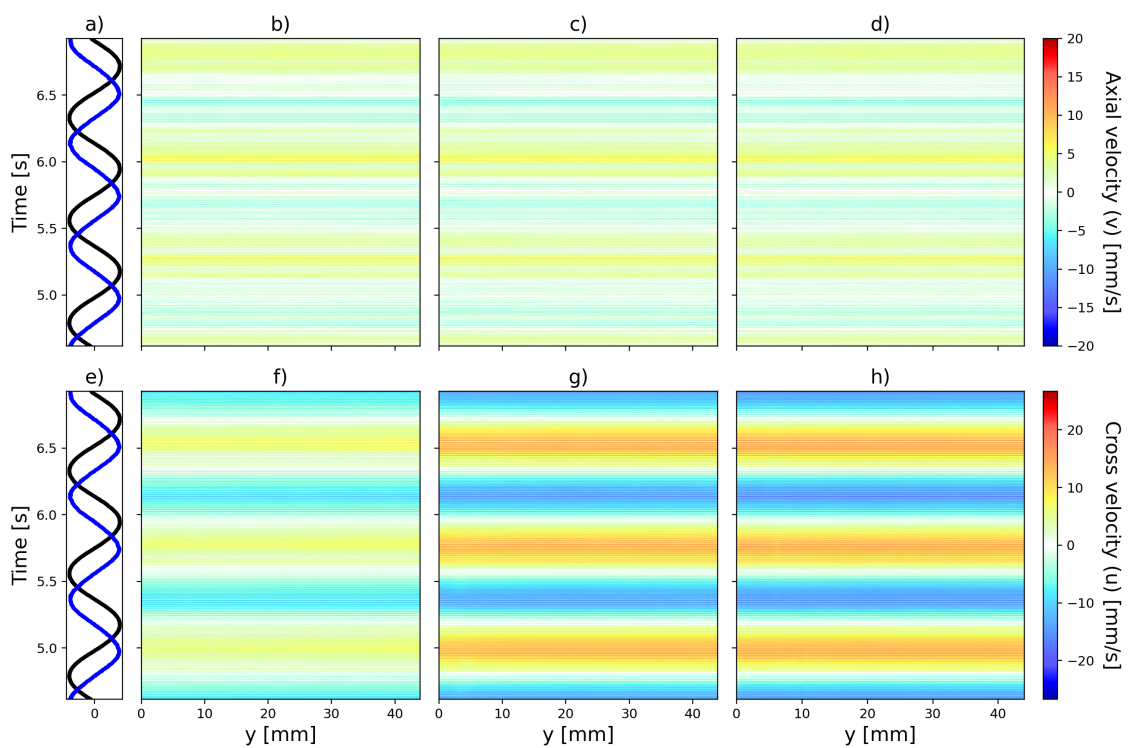


(b) $K = 1.13$ steady state

Figure C.2: Case 8, $K = 1.13$ Intraline evolution.

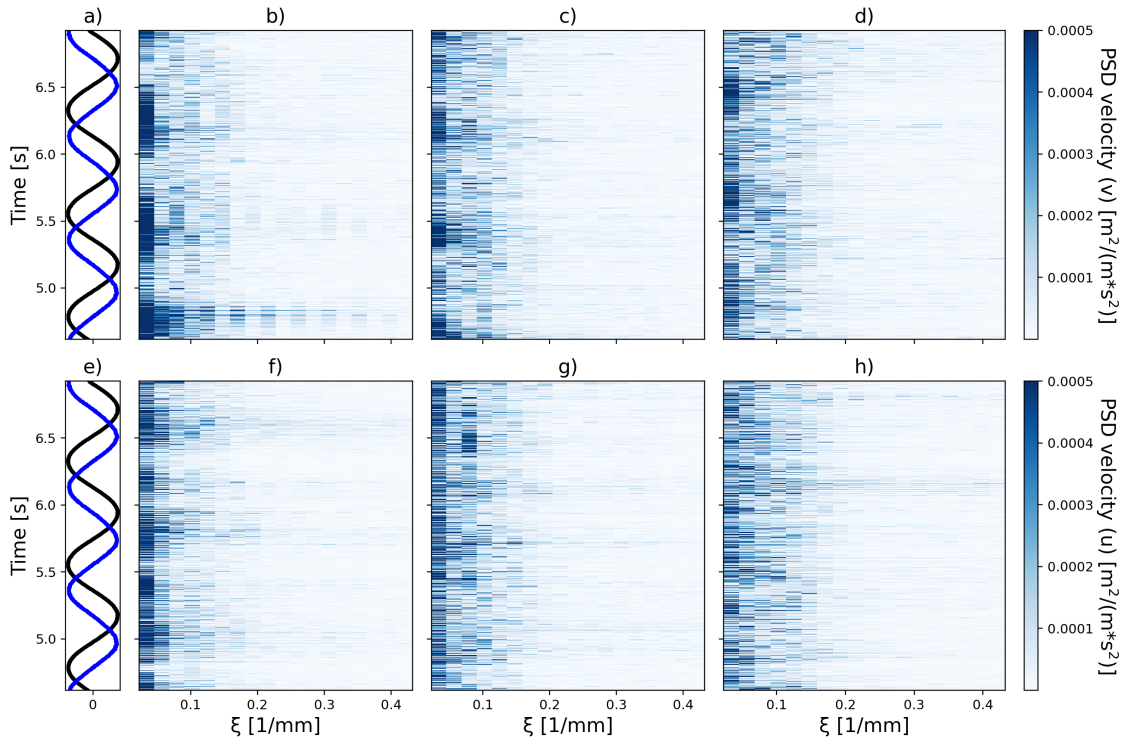


(a) $K = 0.82$ transient

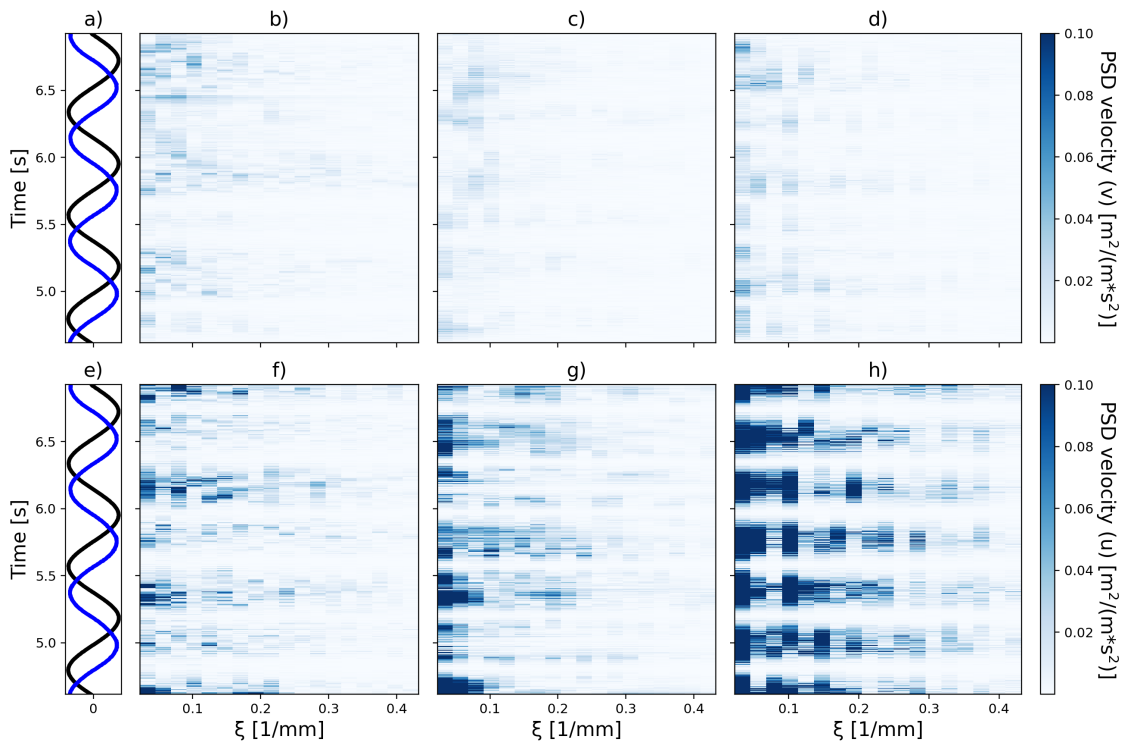


(b) $K = 0.82$ steady state

Figure C.3: Case 7, $K = 0.82$ Intraline evolution.



(a) Case 7, $K = 0.82$ steady state



(b) Case 8, $K = 1.13$ steady state

Figure C.4: PSD for case 7 ($K = 0.82$) and 8 ($K = 1.13$) Intraline at steady state.

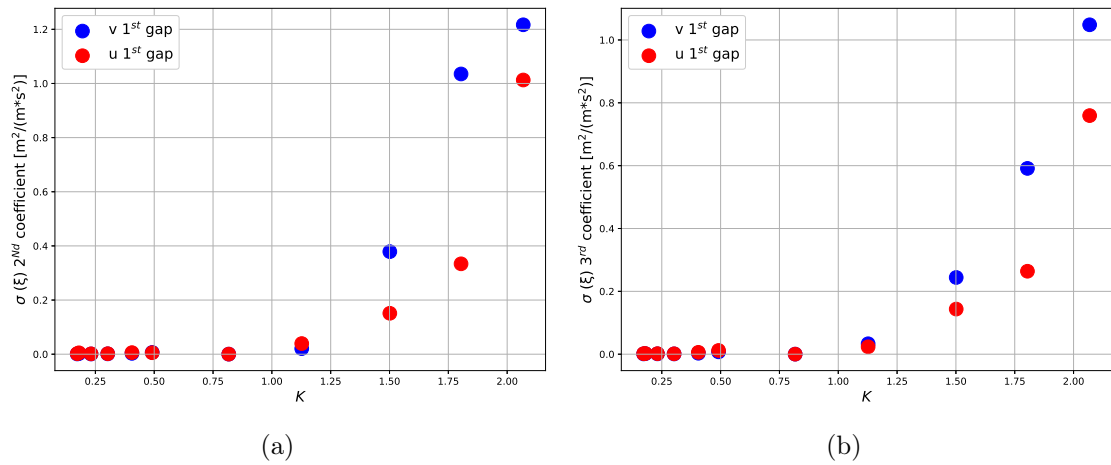


Figure C.5: Standard deviation for 2nd (a) and 3rd (b) coefficients.

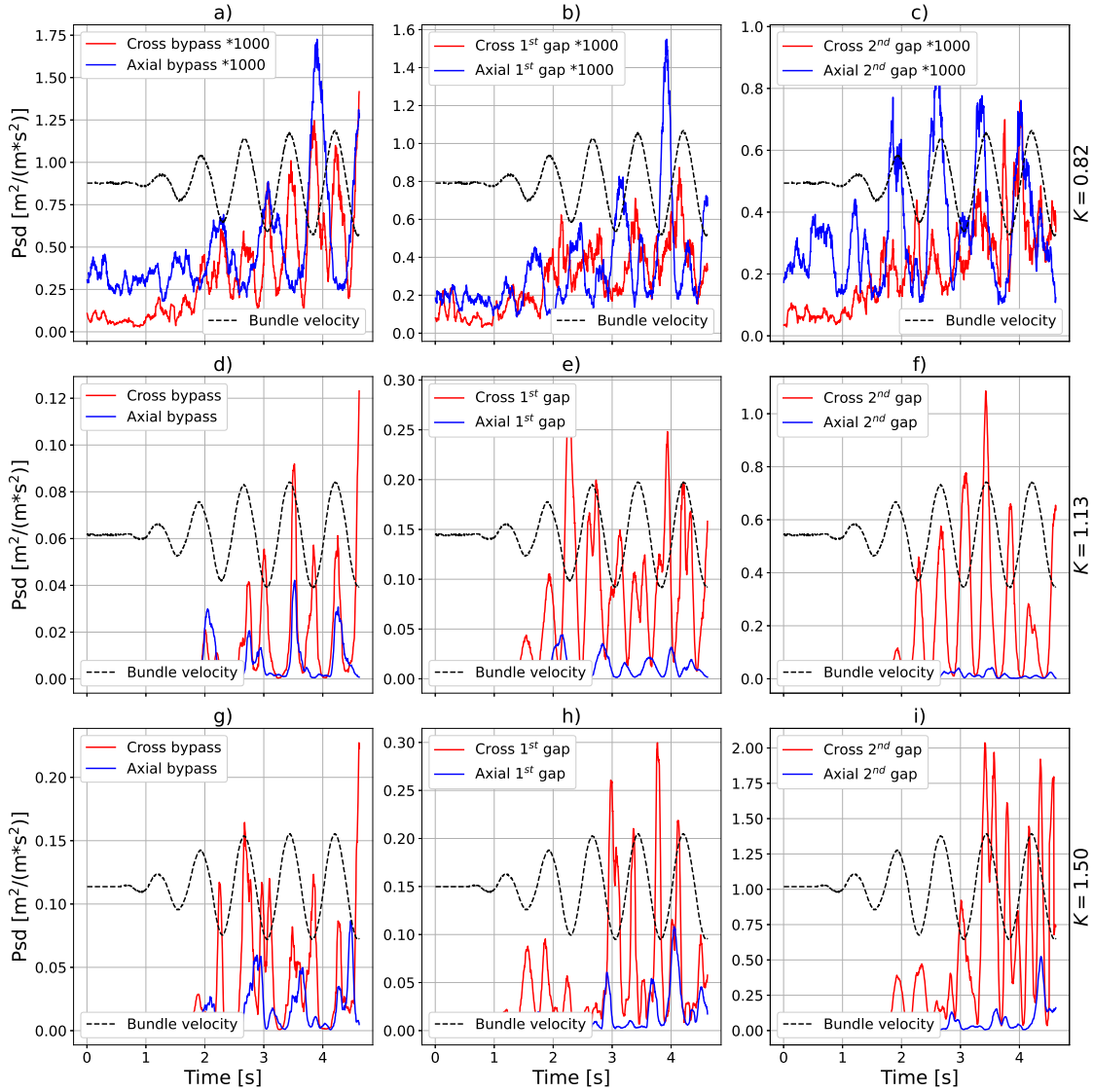


Figure C.6: 1^{st} Coefficient evolution for axial and cross velocities. a) Case 7 ($K = 0.82$), Bypass line. b) Case 7 ($K = 0.82$), 1^{st} Gap line. c) Case 7 ($K = 0.82$), 2^{nd} Gap line. d) Case 8 ($K = 1.13$), Bypass line. e) Case 8 ($K = 1.13$), 1^{st} Gap line. f) Case 8 ($K = 1.13$), 2^{nd} Gap line. g) Case 9 ($K = 1.50$), Bypass line. h) Case 9 ($K = 1.50$), 1^{st} Gap line. i) Case 9 ($K = 1.50$), 2^{nd} Gap line.

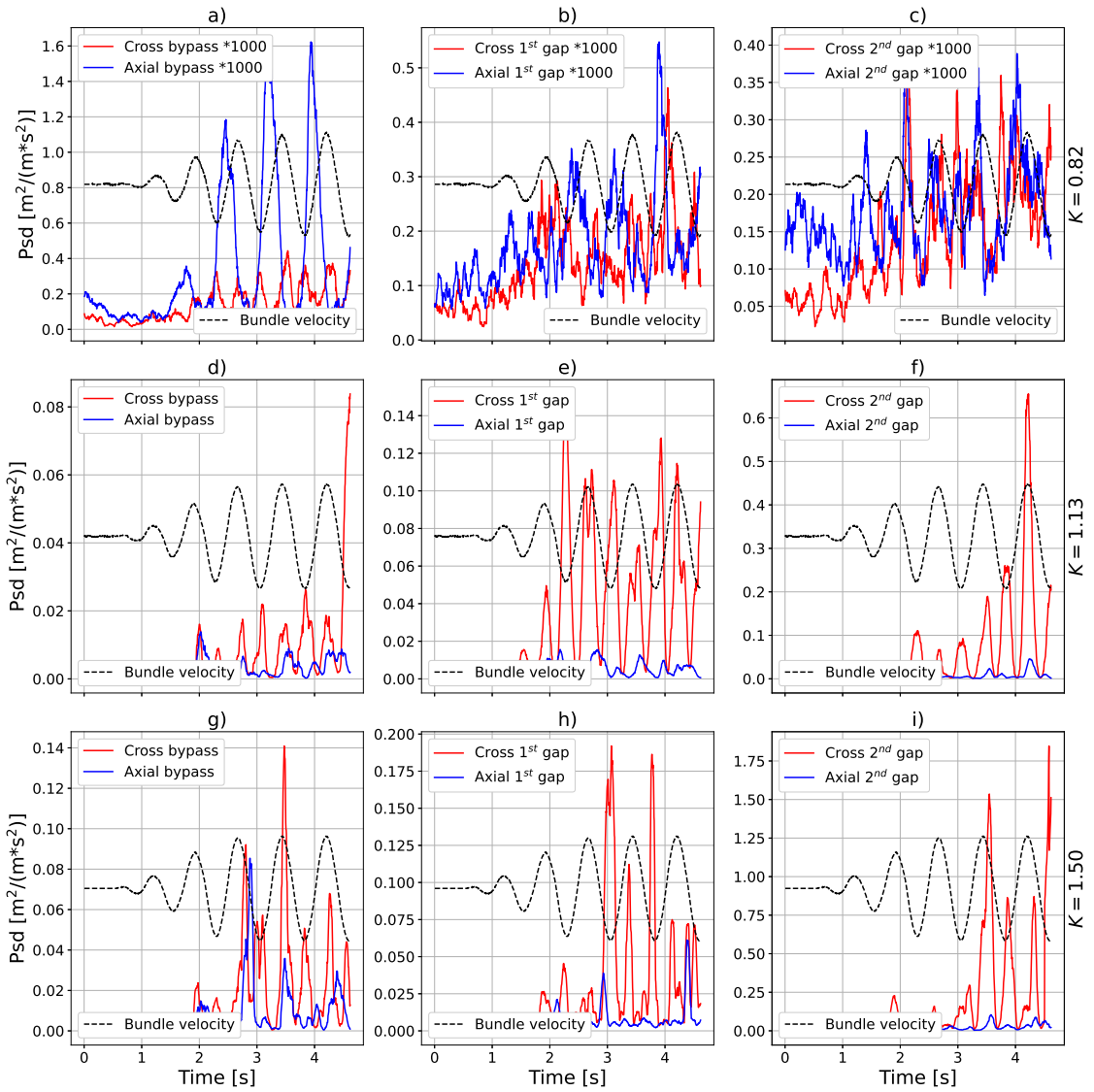


Figure C.7: 2^{nd} Coefficient evolution for axial and cross velocities. a) Case 7 ($K = 0.82$), Bypass line. b) Case 7 ($K = 0.82$), 1^{st} Gap line. c) Case 7 ($K = 0.82$), 2^{nd} Gap line. d) Case 8 ($K = 1.13$), Bypass line. e) Case 8 ($K = 1.13$), 1^{st} Gap line. f) Case 8 ($K = 1.13$), 2^{nd} Gap line. g) Case 9 ($K = 1.50$), Bypass line. h) Case 9 ($K = 1.50$), 1^{st} Gap line. i) Case 9 ($K = 1.50$), 2^{nd} Gap line.

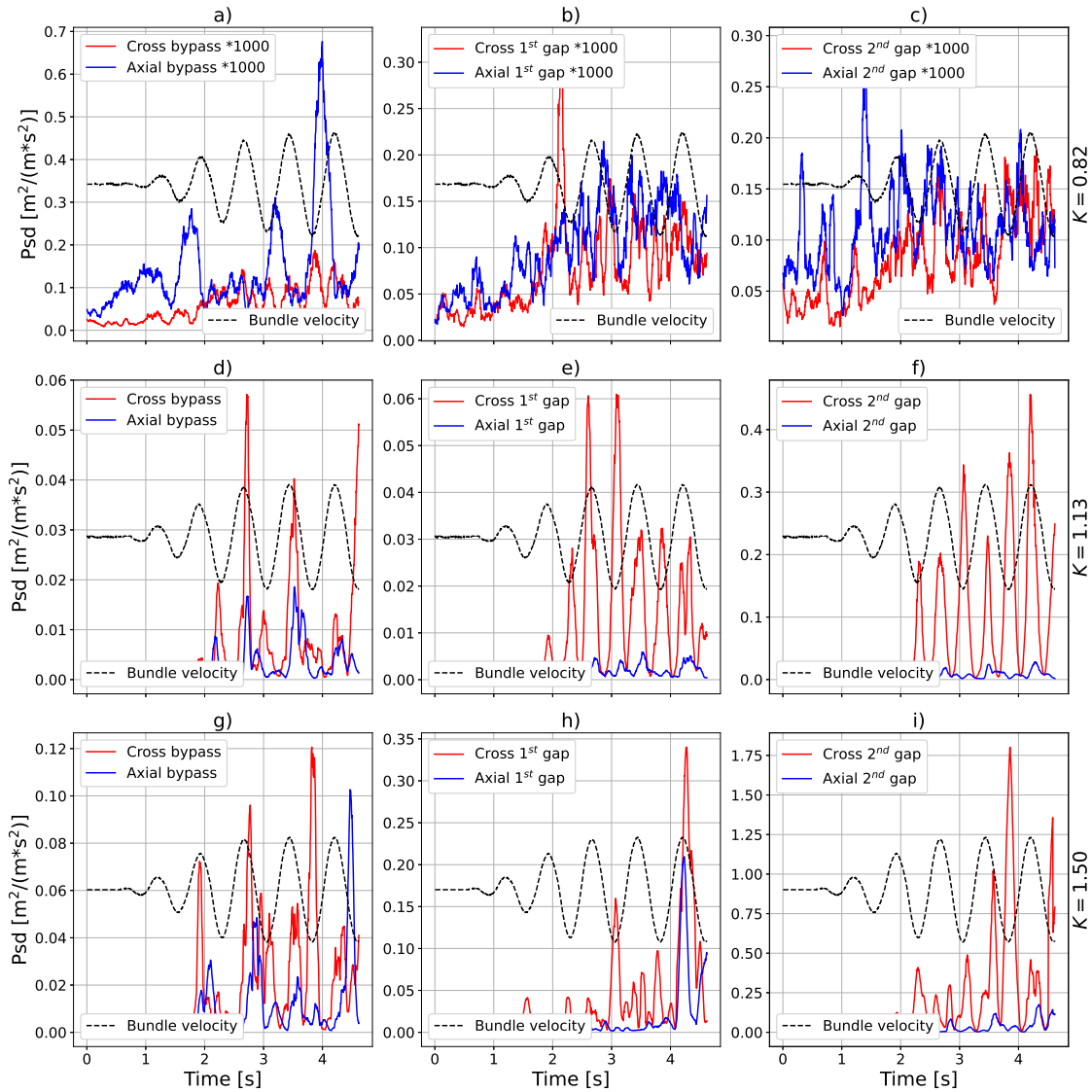
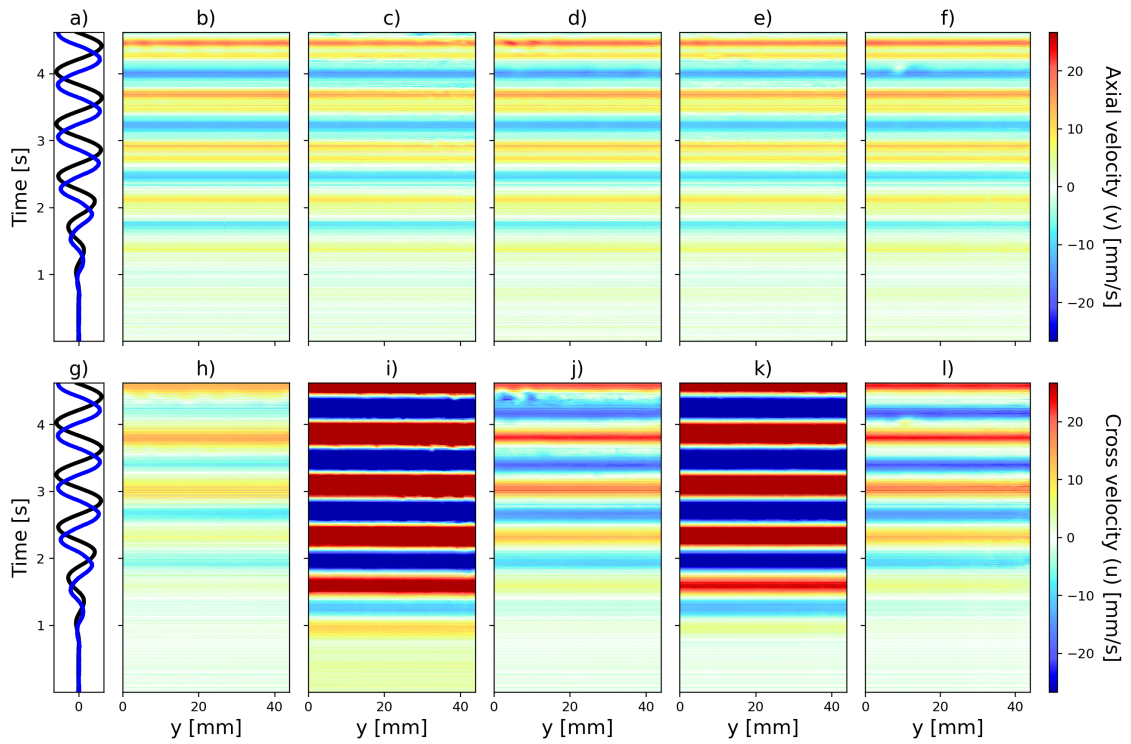
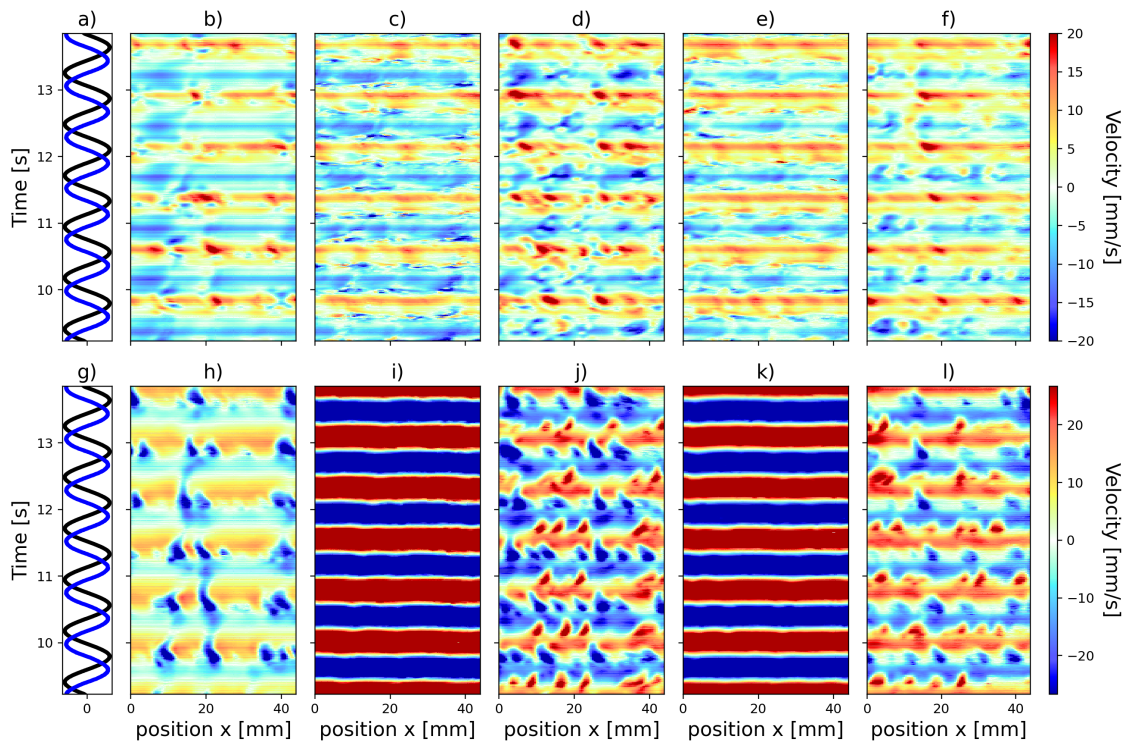


Figure C.8: 3^{rd} Coefficient evolution for axial and cross velocities. a) Case 7 ($K = 0.82$), Bypass line. b) Case 7 ($K = 0.82$), 1^{st} Gap line. c) Case 7 ($K = 0.82$), 2^{nd} Gap line. d) Case 8 ($K = 1.13$), Bypass line. e) Case 8 ($K = 1.13$), 1^{st} Gap line. f) Case 8 ($K = 1.13$), 2^{nd} Gap line. g) Case 9 ($K = 1.50$), Bypass line. h) Case 9 ($K = 1.50$), 1^{st} Gap line. i) Case 9 ($K = 1.50$), 2^{nd} Gap line.

Figure C.9: Other coefficients.

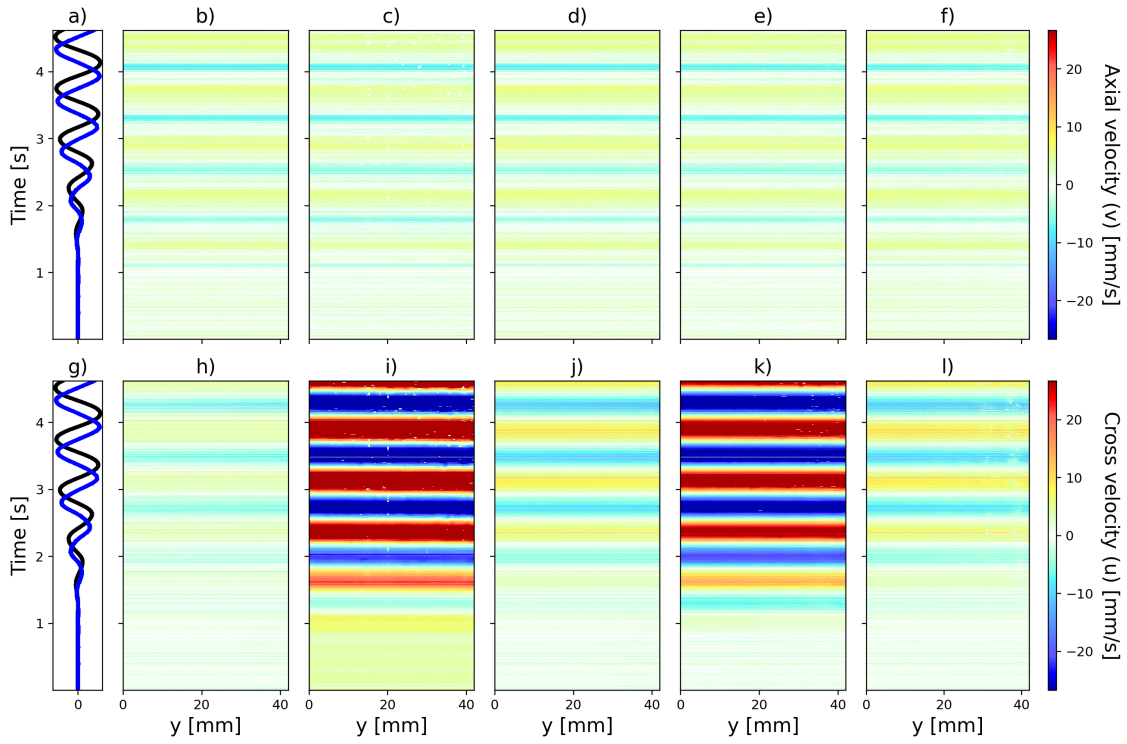


(a) $K = 1.13$ transient

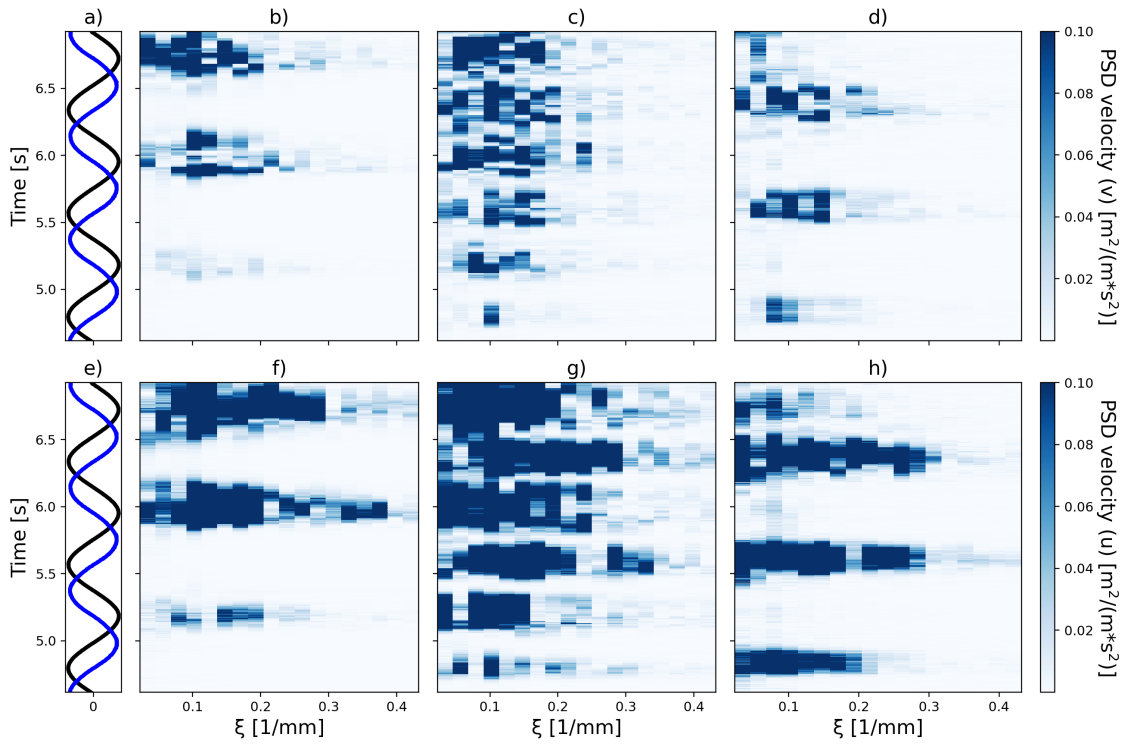


(b) $K = 1.13$ steady state

Figure C.10: Case 11 ($K = 1.13$), Interline evolution.



(a) Case 10 ($K = 0.82$) Interline transient



(b) Case 11 ($K = 1.13$) PSD Interline steady state

Figure C.11: Other Interline results.

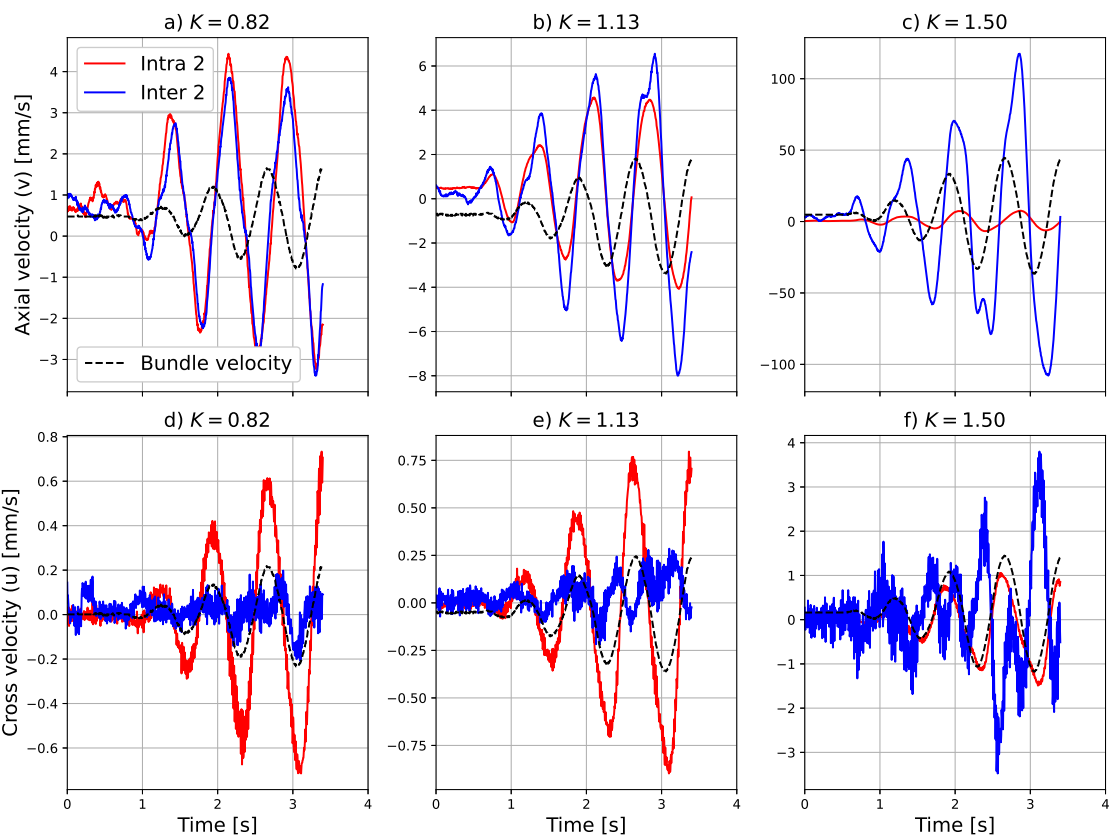
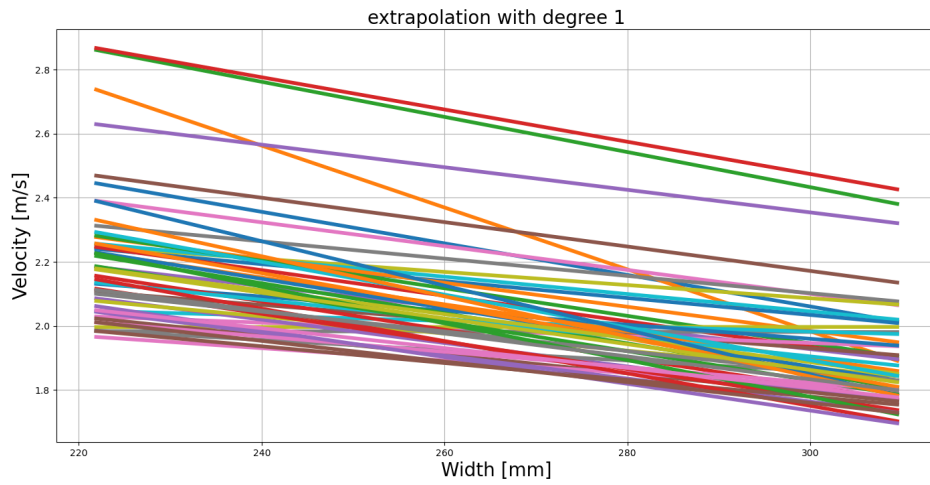


Figure C.12: Superposition of Intraline and Interline averaged velocities for 2^{nd} bypass line for $K = 0.82$, $K = 1.13$ and $K = 1.50$.

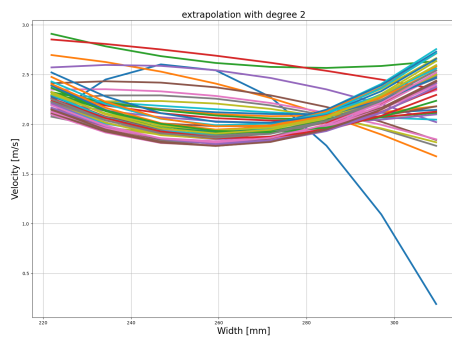


LDV extrapolation

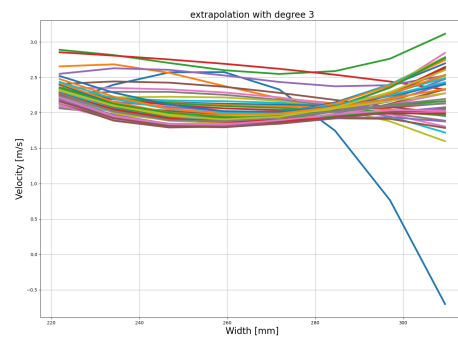
In sec. 3.2.3 we have extrapolated the velocity values for points that are not accessible by LDV on Eudore section. Fig. D.1 shows the extrapolation at first and higher orders. One should noted that here the system of coordinates is inverted. Point 311 here coincides with point 0 in chapter 3 and vice-versa.



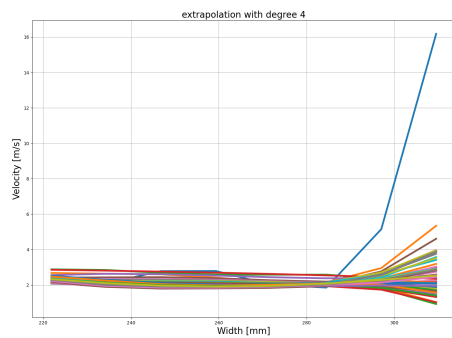
(a) Polynomial extrapolation of order 1



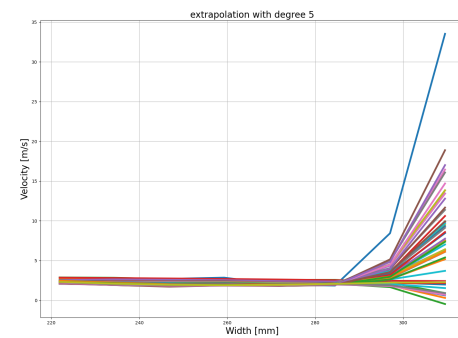
(b) Polynomial extrapolation of order 2



(c) Polynomial extrapolation of order 3



(d) Polynomial extrapolation of order 4



(e) Polynomial extrapolation of order 5

Figure D.1: Polynomial extrapolation of different orders



More results from Eudore Dynamic experiments

In this Annex we present more results concerning the investigation performed in Chapter 4 for a deepen comprehension of the analysis.

Table E.1: Force peaks at 4 Hz

Flowrate [m^3/h]	Amplitude [mm]	Force [N]		
		Left	1 st Right	2 nd Right
<i>Air</i>	2.6	135	350	190
114.5	2.7	100	240	130
194.5	3.0	-	175	110
240.5	3.0	-	205	90
305.5	2.9	-	115	45

Table E.2: Force peaks at 5 Hz

Flowrate [m^3/h]	Amplitude [mm]	Force [N]		
		Left	1 st Right	2 nd Right
<i>Air</i>	2.4	600	745	950
114.5	2.8	375	500	650
194.5	3.2	365	560	690
240.5	3.3	330	470	570
305.5	3.2	180	380	280

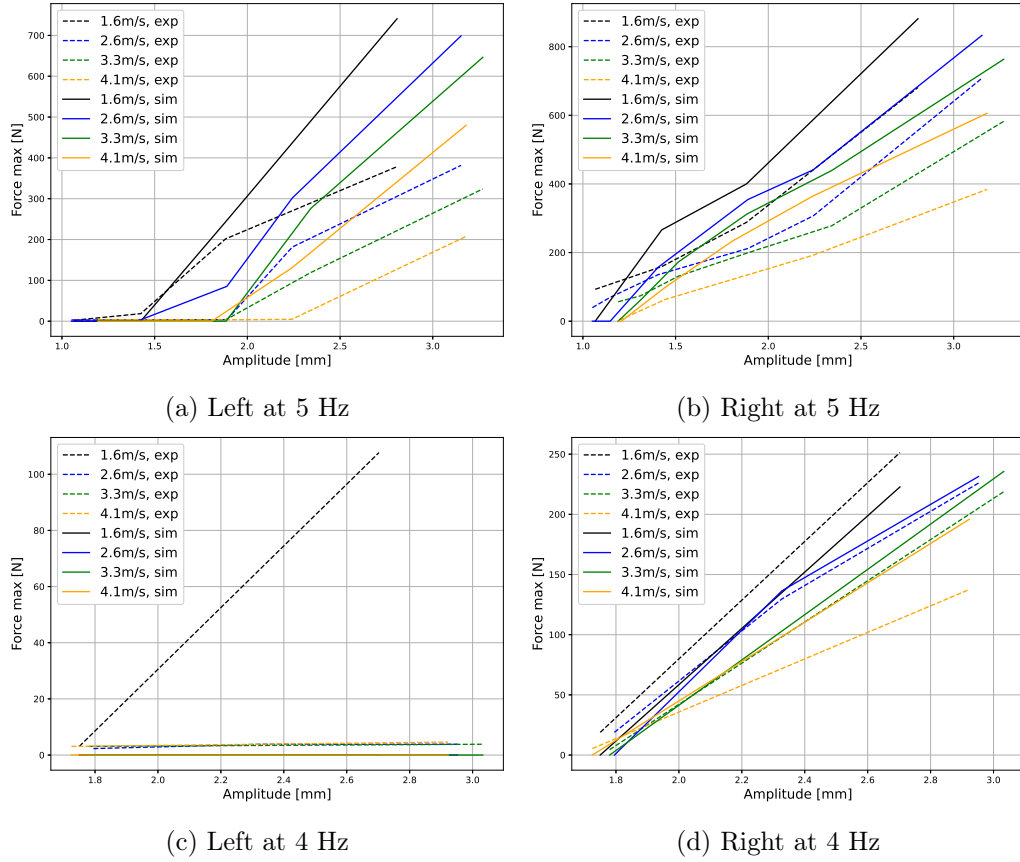
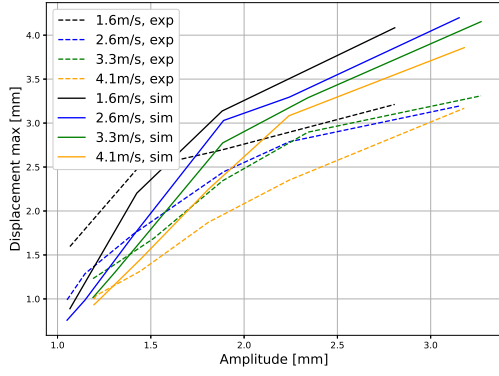


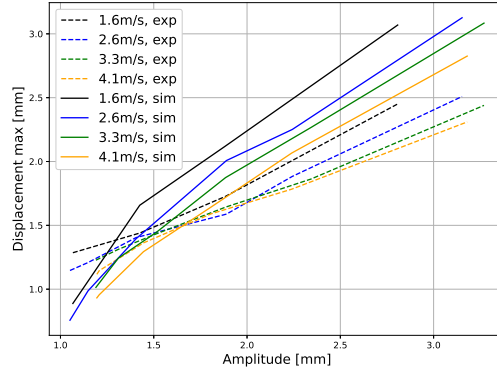
Figure E.1: Force vs amplitudes for Left and Right for 4 and 5 Hz, experimental.

Table E.3: Displacement in *Air*, 5 Hz [mm]

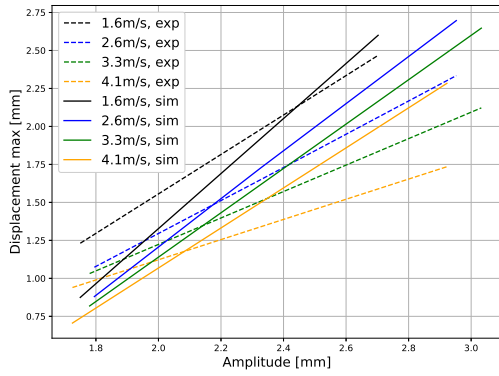
UCP	LCP	Left assembly	Right assembly
0.36	0.78	0.96	0.51
0.40	0.85	1.62	0.64
0.46	0.98	1.39	0.67
0.65	1.31	1.42	0.83
0.76	1.65	1.65	1.00
0.99	2.42	2.13	1.28



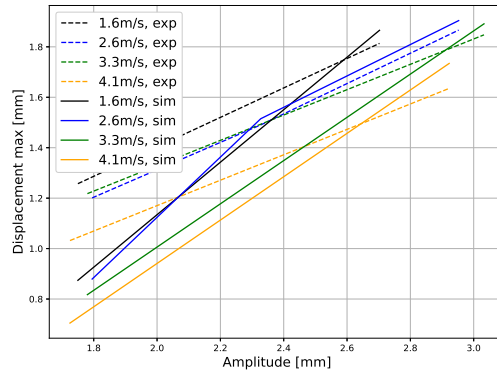
(a) Left at 5 Hz



(b) Right at 5 Hz



(c) Left at 4 Hz



(d) Right at 4 Hz

Figure E.2: Displacement vs amplitudes for Left and Right for 4 and 5 Hz, experimental.

Table E.4: Displacement in *Air*, 4 Hz [mm]

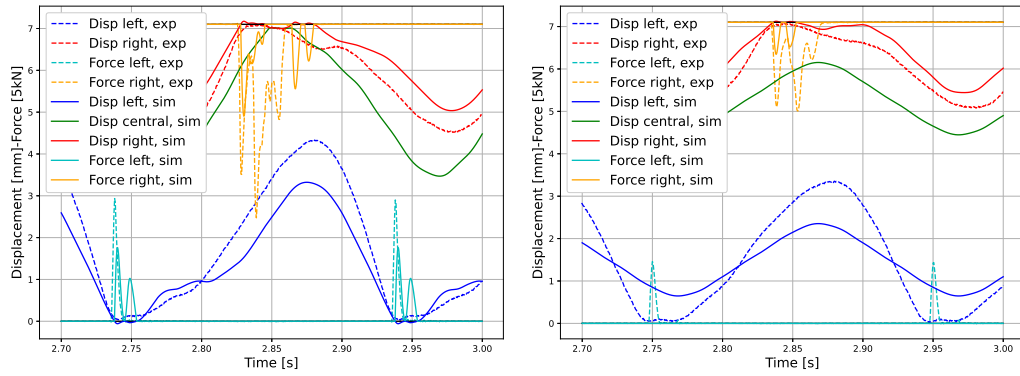
UCP	LCP	Left assembly	Right assembly
1.13	1.50	0.91	0.78
1.47	2.08	1.35	1.14
1.80	2.60	1.53	1.31

Table E.5: Displacement in $114.5m^3/h$, 5 Hz [mm]

UCP	LCP	Left assembly	Right assembly
0.45	1.07	0.78	0.63
0.62	1.44	1.24	0.72
0.79	1.90	1.34	0.87
1.11	2.82	1.59	1.22

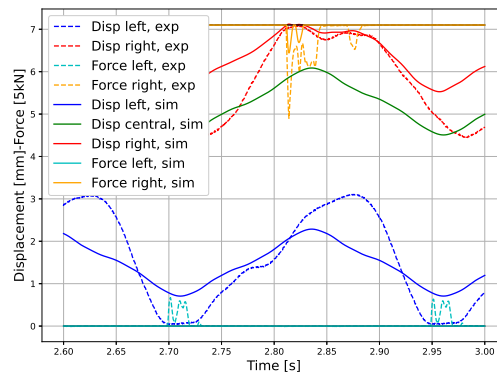
Table E.6: Displacement in $114.5m^3/h$, 4 Hz [mm]

UCP	LCP	Left assembly	Right assembly
1.02	1.66	0.58	0.62
1.66	2.73	1.23	0.91
1.66	2.73	1.23	0.91



(a) Amplitude 6, 5 Hz

(b) Amplitude 5, 5 Hz



(c) Amplitude 3, 4 Hz

Figure E.3: Comparison simulations and experiments in air for 4 and 5 Hz, experimental.

Table E.7: Displacement in $194.5m^3/h$, 5 Hz [mm]

UCP	LCP	Left assembly	Right assembly
0.41	1.07	0.49	0.56
0.47	1.13	0.60	0.60
0.58	1.42	0.86	0.69
0.73	1.89	1.22	0.80
0.90	2.23	1.38	0.93
1.25	3.18	1.59	1.23

Table E.8: Displacement in $194.5m^3/h$, 4 Hz [mm]

UCP	LCP	Left assembly	Right assembly
1.11	1.80	0.52	0.59
1.43	2.36	0.81	0.74
1.76	2.96	1.16	0.93

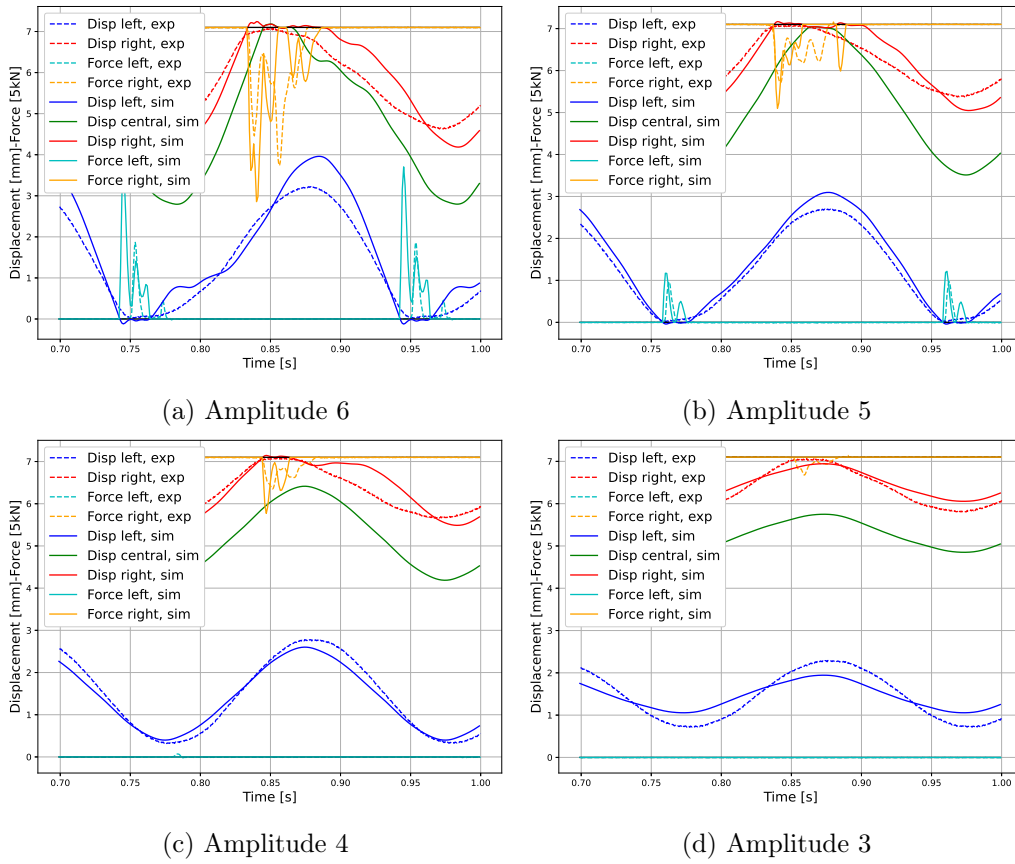


Figure E.4: Comparison simulations and experiments at $114.5 \text{ m}^3/\text{h}$ at 5 Hz .

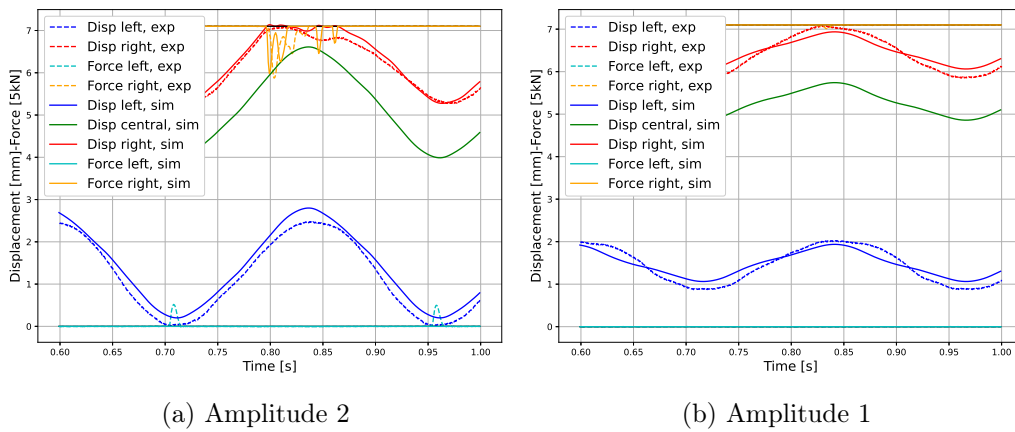


Figure E.5: Comparison simulations and experiments at $114.5 \text{ m}^3/\text{h}$ at 4 Hz .

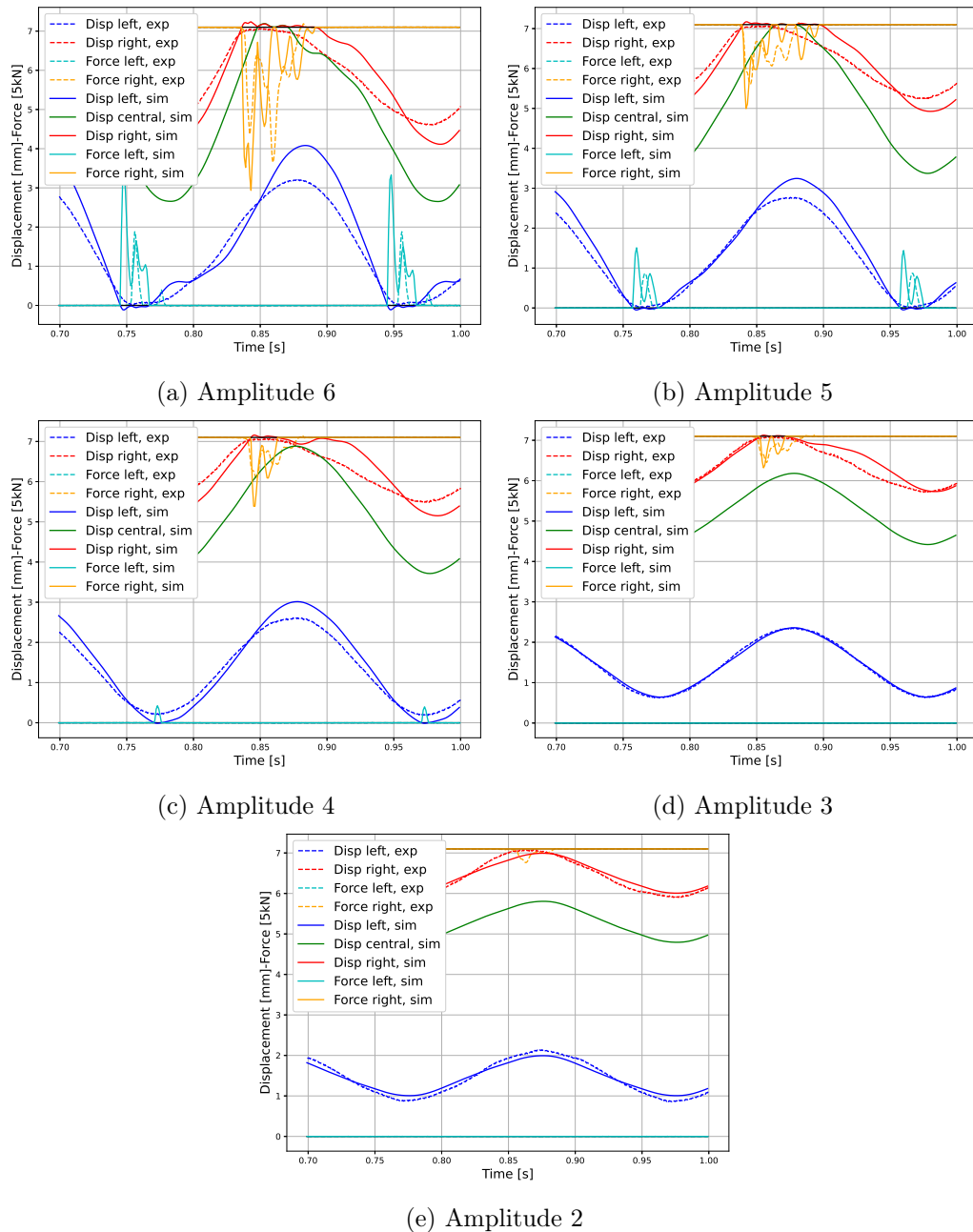


Figure E.6: Comparison simulations and experiments at $194.5 \text{ m}^3/\text{h}$ at 5 Hz.

Table E.9: Displacement in $240.5 \text{ m}^3/\text{h}$, 5 Hz [mm]

UCP	LCP	Left assembly	Right assembly
0.50	1.19	0.58	0.60
0.55	1.32	0.68	0.65
0.62	1.51	0.83	0.70
0.77	1.91	1.17	0.81
0.93	2.36	1.44	0.93
1.25	3.28	1.62	1.20

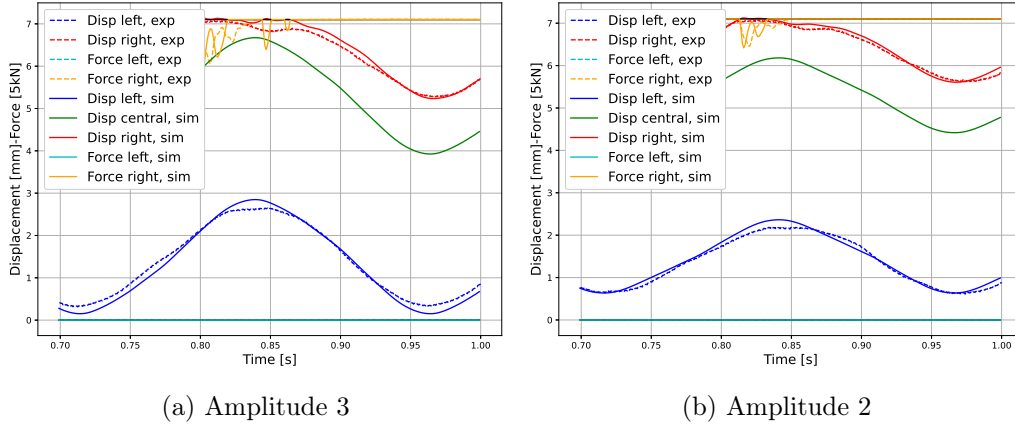


Figure E.7: Comparison simulations and experiments at $194.5 \text{ m}^3/\text{h}$ at 4 Hz.

Table E.10: Displacement in $240.5 \text{ m}^3/\text{h}$, 4 Hz [mm]

UCP	LCP	Left assembly	Right assembly
1.14	1.79	0.52	0.57
1.83	3.05	1.08	0.93

Table E.11: Displacement in $305.5 \text{ m}^3/\text{h}$, 5 Hz [mm]

UCP	LCP	Left assembly	Right assembly
0.46	1.16	0.47	0.52
0.49	1.23	0.52	0.57
0.57	1.45	0.65	0.66
0.69	1.81	0.89	0.77
0.85	2.24	1.15	0.88
1.16	3.17	1.58	1.16

Table E.12: Displacement in $305.5 \text{ m}^3/\text{h}$, 4 Hz [mm]

UCP	LCP	Left assembly	Right assembly
1.10	1.76	0.45	0.50
1.75	2.96	0.87	0.81

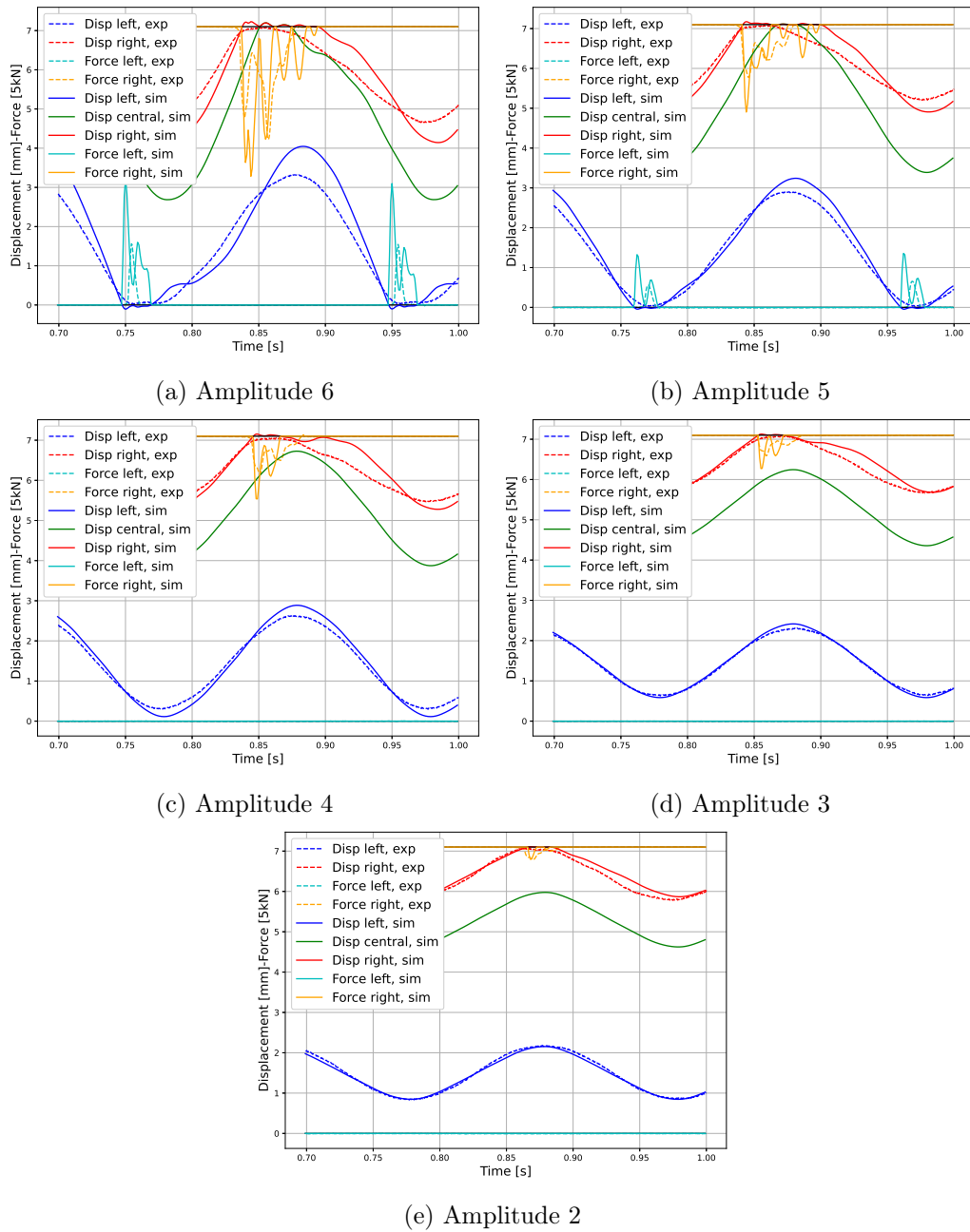
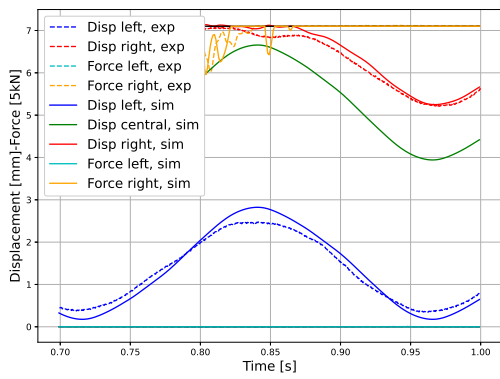
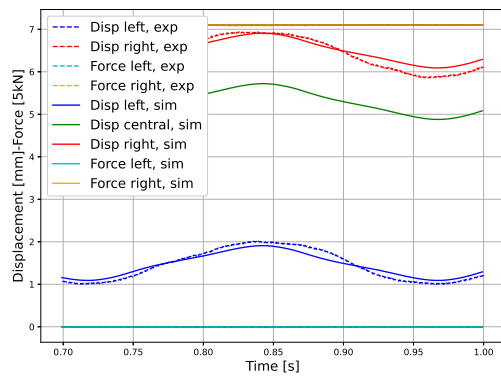


Figure E.8: Comparison simulations and experiments at $240.5 \text{ m}^3/\text{h}$ at 5 Hz .

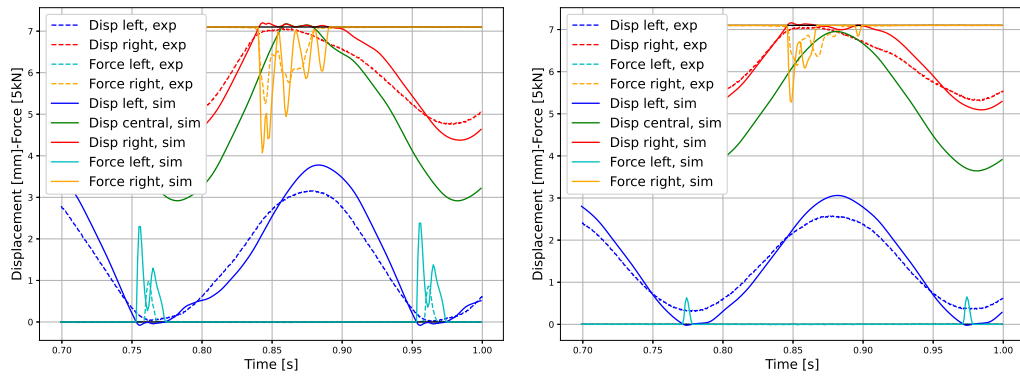


(a) Amplitude 3



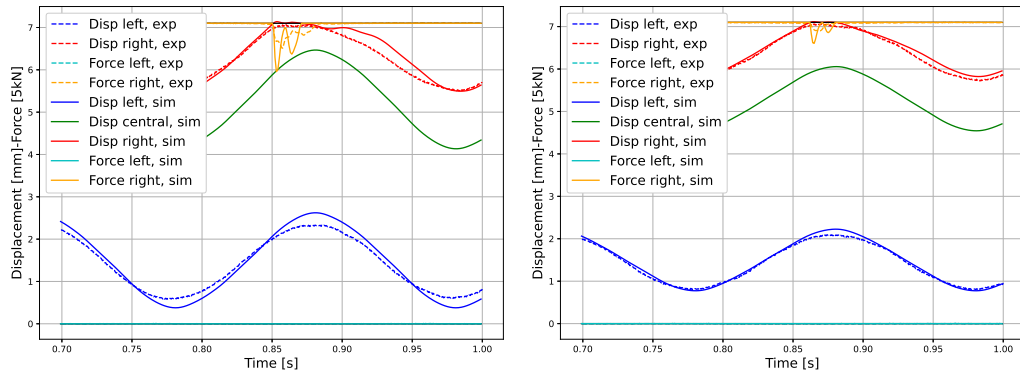
(b) Amplitude 1

Figure E.9: Comparison simulations and experiments at $240.5 \text{ m}^3/\text{h}$ at 4 Hz .



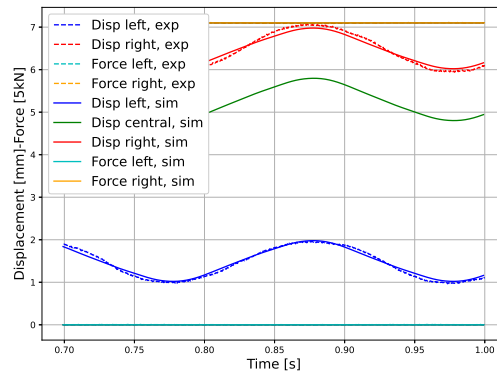
(a) Amplitude 6

(b) Amplitude 5



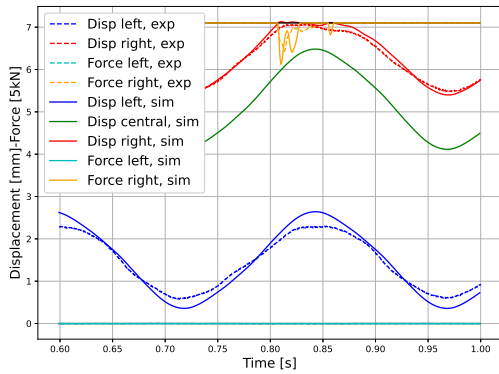
(c) Amplitude 4

(d) Amplitude 3

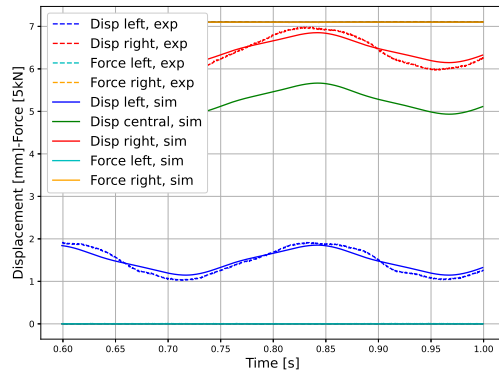


(e) Amplitude 2

Figure E.10: Comparison simulations and experiments at $305.5 \text{ m}^3/\text{h}$ at 5 Hz.

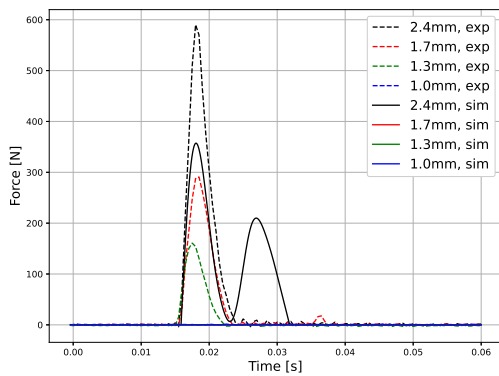


(a) Amplitude 3

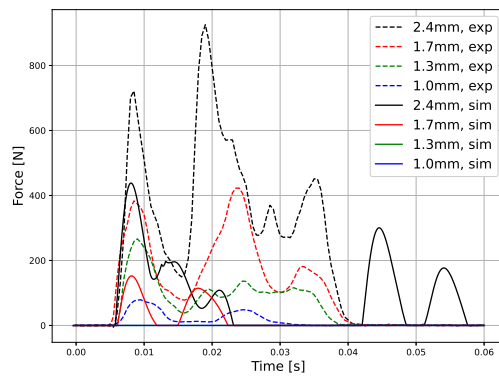


(b) Amplitude 1

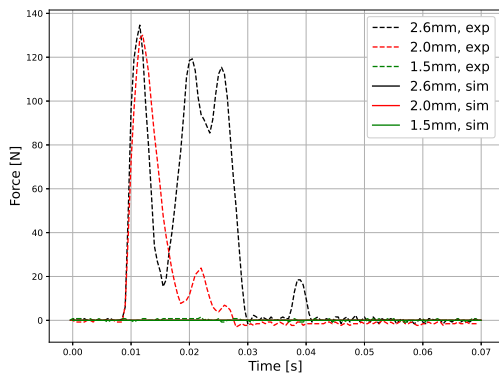
Figure E.11: Comparison simulations and experiments at $305.5 \text{ m}^3/\text{h}$ at 4 Hz.



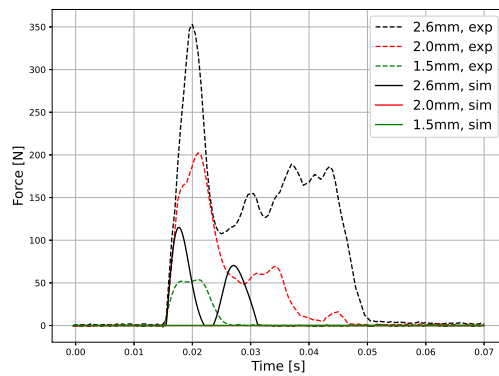
(a) Left at 5 Hz



(b) Right at 5 Hz



(c) Left at 4 Hz



(d) Right at 4 Hz

Figure E.12: Impact forces in air for different amplitudes for Left and Right for 4 and 5 Hz, experimental.

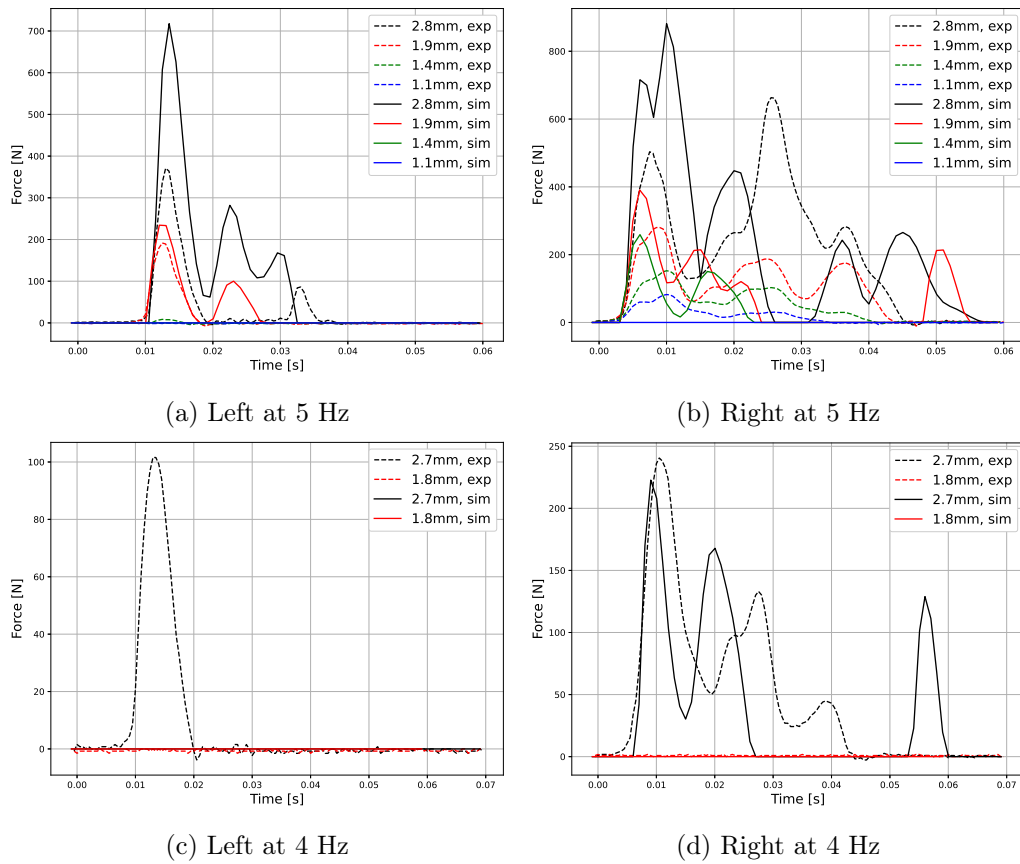
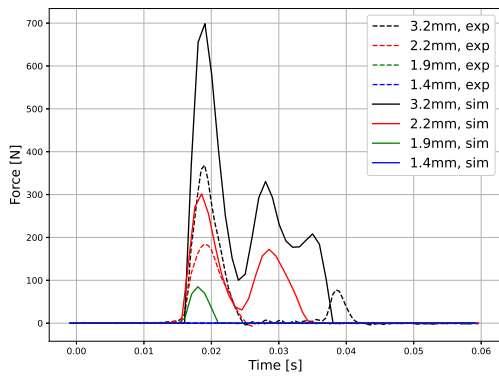
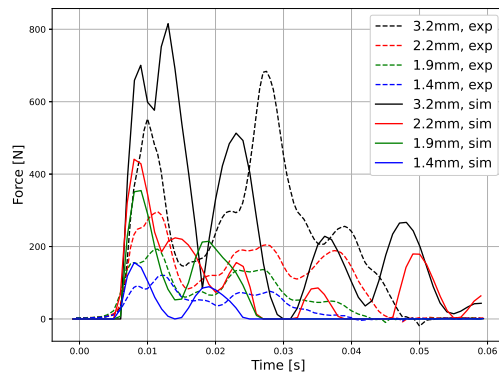


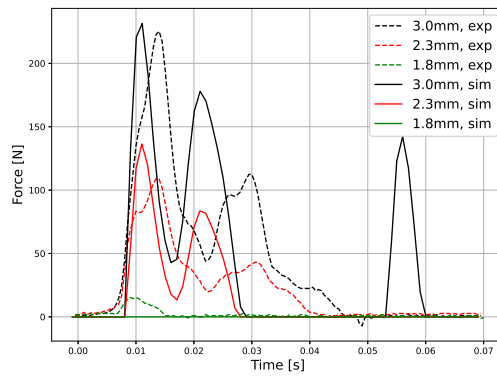
Figure E.13: Impact forces at $114.5 \text{ m}^3/\text{h}$ for different amplitudes for Left and Right for 4 and 5 Hz, experimental.



(a) Left at 5 Hz

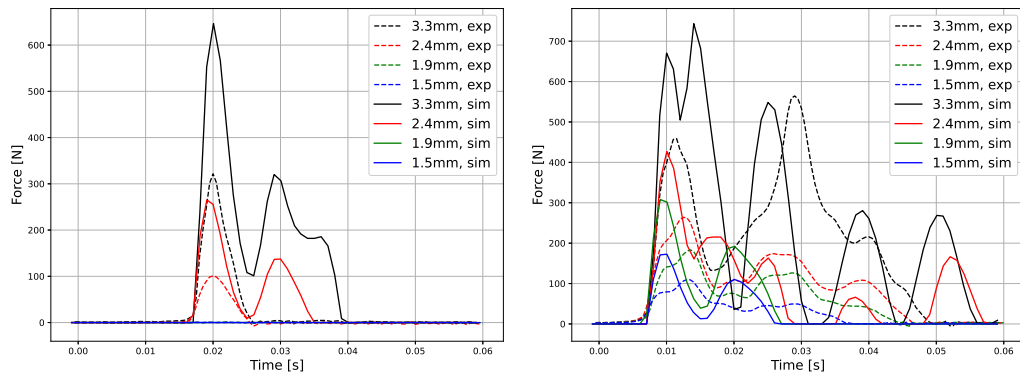


(b) Right at 5 Hz



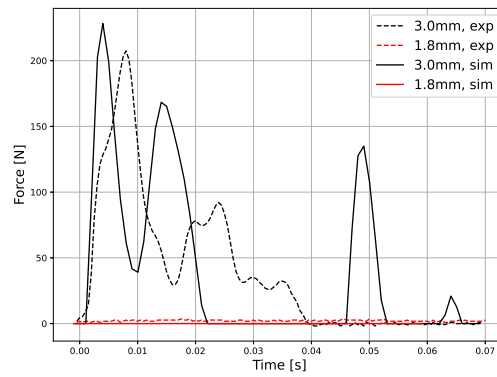
(c) Right at 4 Hz

Figure E.14: Impact forces at $194.5 \text{ m}^3/\text{h}$ for different amplitudes for Left and Right for 4 and 5 Hz, experimental.



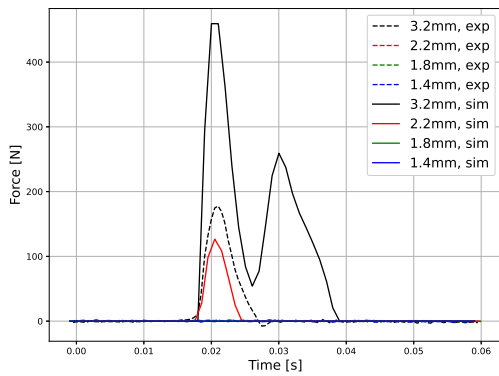
(a) Left at 5 Hz

(b) Right at 5 Hz

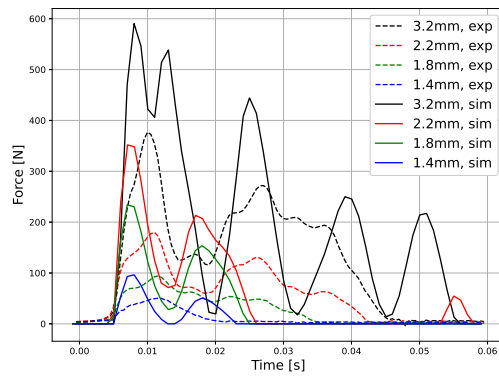


(c) Right at 4 Hz

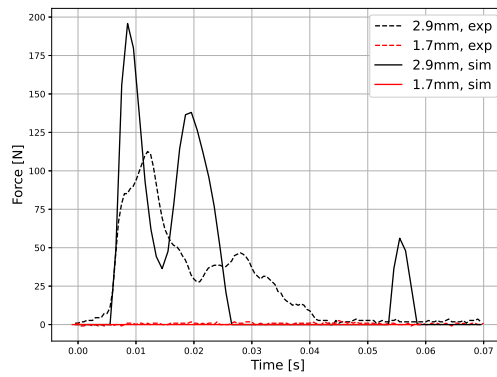
Figure E.15: Impact forces at $240.5 \text{ m}^3/\text{h}$ for different amplitudes for Left and Right for 4 and 5 Hz, experimental.



(a) Left at 5 Hz



(b) Right at 5 Hz



(c) Right at 4 Hz

Figure E.16: Impact forces at $305.5 \text{ m}^3/\text{h}$ for different amplitudes for Left and Right for 4 and 5 Hz, experimental.